

Operating Regimes and Automated Control of
Holmium and Thulium Non-linear Polarisation
Rotation Mode-locked Fibre Optic Lasers

David McAfee

Thesis submitted for the degree of

Master of Philosophy

in

Physics

at The University of Adelaide

Faculty of Sciences, School of Physical Sciences

June 2020



THE UNIVERSITY
of ADELAIDE

Contents

Abstract	xix
Signed Statement	xxi
Acknowledgements	xxiii
Dedication	xxv
1 Introduction	1
1.1 Mode-locked Lasers	1
1.2 Applications of Mode-locked Sources	2
1.2.1 Seed Sources	2
1.2.2 Soft x-rays via Higher Harmonic Generation (HHG)	3
1.2.3 Supercontinuum Generation	4
1.2.4 Mode-locking at 3 μm	5
1.3 Mode-locking Techniques	6
1.4 Demonstrated Mode-locked Sources	11
1.4.1 SA Mode-locked Fibre Lasers	11
1.4.2 NLPR Mode-locked Fibre Lasers	11
1.4.3 Hybrid NLPR/SESAM Mode-locked Fibre Lasers	12
1.4.4 NALM Mode-locked Fibre Lasers	13
1.5 Objectives	13
1.6 Mode-locked Automation Techniques	14
1.7 Outline of Thesis	14

2	Background	17
2.1	Introduction	17
2.2	Optical Fibres	18
2.2.1	Introduction to Fibres	18
2.2.2	Doped Fibres	21
2.2.3	Pumping Schemes	23
2.3	Polarisation	25
2.3.1	Polarisation States	25
2.3.2	Polarisation Controllers	26
2.4	Optical Pulses	28
2.4.1	Introduction to Pulses	28
2.4.2	Time-Bandwidth Product	30
2.4.3	Gain Bandwidth	31
2.4.4	Dispersion	32
2.5	Non-linear Effects	35
2.5.1	Non-linear Optical Propagation	35
2.5.2	Non-linear Schrödinger Equation	36
2.5.3	Self Phase Modulation	39
2.5.4	Cross Polarisation Modulation	41
2.5.5	Non-linear Polarisation Evolution	42
2.6	Mode-locking	43
2.6.1	Introduction to Mode-locking	43
2.6.2	Non-linear Polarisation Rotation Mode-locking	46
2.7	NLPR Regimes	47
2.7.1	Q-switched Mode-locked	48
2.7.2	Multi-pulsed Mode-locked	49
2.7.3	Background CW (non-pulsed)	51
2.7.4	Simultaneous CW and Continuously Mode-locked	51
2.8	Summary	54

3	Mode-locking Measurement Techniques	55
3.1	Introduction	55
3.2	Erbium Fibre Laser	56
3.2.1	Cavity Configuration	56
3.2.2	Characterisation Overview	57
3.3	Results	59
3.3.1	Temporal Characterisation	59
3.3.2	Radio Frequency (RF) Spectrum	63
3.3.3	Optical Spectrum	68
3.3.4	Autocorrelator	71
3.4	Summary	80
4	Automation Metric Testing using a Thulium NLPR Fibre Laser	83
4.1	Introduction	83
4.2	Mode-locked Thulium Fibre Laser	84
4.2.1	Cavity Configuration	84
4.3	Results	85
4.3.1	Continuously Mode-locked (CML)	86
4.3.2	Q-switched Mode-locked (QML)	89
4.3.3	Continuously Mode-locked with CW Background (CMLCW)	92
4.3.4	Multi-pulsed Mode-locked (MPML)	95
4.4	Automation Techniques Investigation	99
4.4.1	Literature Review	99
4.4.2	Stokes Parameters	102
4.4.3	Two Photon Absorption (TPA) Diagnostic	111
4.4.4	RF Spectrum Diagnostic	114
4.5	Automation Discussion	118
4.6	Summary	120
5	Automation of a Diode-pumped Holmium NLPR Fibre Laser	123
5.1	Introduction	123
5.2	Mode-locked Holmium Fibre Laser	125

5.2.1	Cavity Configuration	125
5.2.2	Results	126
5.2.3	Discussion	130
5.3	Automation	130
5.3.1	Overview	130
5.3.2	RF Spectrum Collection	132
5.3.3	Baseline RF Spectrum	132
5.3.4	Categorising the Laser Output using RF Spectra	133
5.3.5	Adjusting Polarisation Controller Voltages	134
5.3.6	Automation GUI	135
5.4	Automation Results	136
5.4.1	Automation Discussion	139
5.5	Summary	140
6	Conclusion	141
6.1	Introduction	141
6.2	Summary	143
6.2.1	Sources Developed and Characterised	143
6.2.2	Automation Metric Summary	145
6.3	Future Work	146
6.3.1	Component Selection	146
6.3.2	Removing Q-switched Instabilities	147
6.3.3	Dispersion Management	148
6.3.4	Automation Algorithm Refinements	151
6.4	Final Remarks	153
A	Stokes Parameters	155
B	Kerr Coefficient Derivation	159
C	Tensor Simplification	163
D	Frequency Resolved Optical Gating (FROG)	165

<i>Contents</i>	vii
E Theoretical roll-off	169
F Alignment of an autocorrelator using collinear and non-collinear mode	173
G Angular Acceptance of Type I Phase Matching with SHG	177
H Power Measurements from Polarising Beamsplitter	179
I Interfacing MATLAB Code	181
J RF Spectrum Output File	185
K Regime Classification Code	187
L Interfacing with Piezoelectric Polarisation Controller	193
M Q-switched Mode-locked Piezo Incrementation	195
N Continuous Mode-locked Piezo Incrementation	201
O Continuous Mode-locked Piezo Incrementation Part II	207
P Dispersion Compensation in the Literature	213
Q List of Publications	217
Q.1 Conference Presentation and Proceedings	217
References	219

List of Tables

1.1	Table of summary characteristics for a range of SESAM mode-locked fibre lasers.	11
1.2	Table of summary characteristics for a range of NLPR mode-locked fibre lasers.	12
1.3	Table of summary characteristics for hybrid NLPR and SESAM mode-locked fibre lasers.	12
1.4	Table of summary characteristics for NALM mode-locked fibre lasers.	13
2.1	Table featuring cross sections and the refractive index profile for a range of different fibre types.	18
2.2	Table of typical properties for SM and PM fibres [2,3].	21
2.3	Advantages of each of the pumping schemes.	25
2.4	Table with gain bandwidth and corresponding pulse durations (Equation 2.10) for a range of rare-earth ion doped amplifiers – erbium, holmium and thulium.	32
3.1	Table summarising the role of each diagnostic instrument.	80
3.2	Table of summary characteristics for erbium source in a CML state.	81
4.1	Side-by-side depiction of temporal and RF traces for a range of stable and unstable MPML regimes.	97
4.2	Advantages and disadvantages of using $\langle S_1 \rangle$ discontinuity measurement as a diagnostic for automated mode-locking.	110
4.3	Average 2 μm and TPA power for different regimes	112

4.4	Advantages and disadvantages of using a TPA power measurement as a diagnostic for automated mode-locking.	114
4.5	Table containing RF spectrum traces of the laser train output for different regimes and the amplitude modulation (peak-height) metric across groups of harmonics.	116
4.6	Advantages and disadvantages of using RF spectrum amplitude modulation as a diagnostic for automated mode-locking.	118
4.7	Table of summary statistics for thulium source in highest power, stable CML state.	121
5.1	Table featuring temporal and RF spectrum traces as the piezoelectric controller is changed to sweep into a CML regime.	138
5.2	Summary of holmium source in highest power, stable CML state.	140
5.3	Summary of diode-pumped mode-locked holmium sources.	140
6.1	Table of summary statistics for holmium source in highest power, stable CML state.	143
6.2	Summary of CML state performance of all laser sources developed.	144
M.1	Table featuring temporal and RF spectrum traces for every step of the piezoelectric voltages while sweeping into a QML regime.	196
N.1	Table featuring temporal and RF spectrum traces for every step of the piezoelectric voltages while sweeping into a CML regime.	202
O.1	Table featuring temporal and RF spectrum traces as the piezoelectric controller is changed to sweep back into a CML regime upon previously exiting.	208

List of Figures

1.1	General schematic of a ring SESAM mode-locked fibre cavity. Light propagates in a clockwise direction around the cavity. Light reflected off the SESAM passes back to the circulator and exits through port 3. Figure originally presented in [56]. SMF = single mode fibre, PC = polarisation controller, WDM = wavelength division multiplexer, SESAM = semiconductor saturable absorber mirror. Many of these components will be introduced in later chapters (Chapters 2-3). . . .	8
1.2	General schematic of a linear SESAM mode-locked fibre cavity. Figure adapted from [57]. FC/APC = fibre connector, FBG = fibre Bragg grating.	8
2.1	Energy level diagrams for trivalent erbium (Er), thulium (Tm) and holmium (Ho) ions in silica showing transitions that yield light around 1.5 μm and 2 μm [4, 10-13].	22
2.2	(a): Absorption and emission cross-section of erbium. Figure reproduced from [7]. (b): Absorption and emission cross-section of thulium and holmium. Figure reproduced from [13].	22
2.3	Refractive index profile and schematic of core-pumped (top), and cladding-pumped (bottom) fibre geometries. Black represents the pump input, and red represents the signal output. Pump light is converted to signal through transitions (as outlined in the previous section). Based off a similar image presented in [17].	24

2.4	The Poincaré sphere with the three axes representing S_1 , S_2 and S_3 . Polarisation states at the poles and the equator correspond to circular and linear polarisations respectively. LCP = Left Circularly Polarised, RCP = Right Circularly Polarised, LVP = Linear Vertically Polarised, LHP = Linear Horizontally Polarised, L-45 = Linearly Polarised at -45° , L+45 = Linearly Polarised at $+45^\circ$	26
2.5	Schematic of the Newport manual polarisation controller. Image adapted from [22].	27
2.6	Schematic of the actuators inside the General Photonics electronic polarisation controller. Image adapted from [23]. Squeezers labelled from 1 (foreground) to 4 (background). Squeezer 4 was not included in the specific controller used in this project.	27
2.7	Carrier and envelope schematic for an optical pulse.	28
2.8	A plot of the material dispersion curve and waveguide dispersion curve for a silica optical fibre. Image initially presented in [36].	34
2.9	Temporal plot of pulse intensity for an initially unchirped pulse and the corresponding chirp it experiences due to self phase modulation. An upchirp is experienced at the centre of the pulse when $\frac{d\omega}{dt} = 0$. Note that the lower curve is the derivative of the upper curve. Image adapted from [7].	40
2.10	Graphic depicting polarisation rotation across the intensity profile of a pulse.	42
2.11	A general (theoretical) schematic for a NLPR mode-locked fibre laser. Non-PM passive fibre is spliced between all components and is spliced to the active fibre. An in-line polariser could be used in lieu of an isolator as the mode-locking element.	46
2.12	Temporal trace of a CML laser output	48
2.13	Temporal trace of a QML laser output	49
2.14	Temporal trace of a stable MPML laser output where pulses are out-coupled twice per round trip	50
2.15	Temporal trace of an unstable MPML laser output	51

2.16	Temporal trace of a CMLCW laser output	52
2.17	Temporal trace of a noisy CMLCW laser output	53
2.18	Temporal trace of another noisy CMLCW laser output	53
2.19	Flowchart outlining the connection between physical concepts and NLPR mode-locking, which forms the basis for the background information presented in this chapter.	54
3.1	A schematic of the NLPR mode-locked EDFL cavity. WDM = wavelength division multiplexer, PC = polarisation controller and x marks the position of splices or fibre connectors.	57
3.2	Diagnostics used for characterisation of the mode-locked EDFL. Connections from the laser are optical fibre splitters which launch light into the diagnostic instruments. The output of the second 50% splitter was beam dumped. The photodiode in the second arm was removed when using the OSA.	58
3.3	Oscilloscope trace of pulse train output in a CML regime. Amplitude variation between subsequent pulses was around 8% over eleven pulses.	60
3.4	Oscilloscope trace of noise between pulses. Periodic patterns are evident albeit small, indicating fairly good stability.	60
3.5	Oscilloscope trace of pulse train output in a QML regime.	61
3.6	Oscilloscope trace of pulse train output in a MPML regime.	62
3.7	Oscilloscope trace of pulse train output in a MPML regime. Amplitude variation between subsequent pulses was of the order of 9% over eleven pulses.	63
3.8	Diagram showing the relationship between time and frequency domains for (a) a theoretical CML regime, (b) an experimental CML regime with occasional instabilities and (c) a competing experimental (MPML) regime with irregular instabilities. Instabilities include amplitude noise and timing jitter.	65
3.9	RF spectrum of erbium NLPR operating in CML regime.	67
3.10	RF spectrum of erbium NLPR operating in QML regime.	67

3.11	RF spectrum of erbium NLPR operating in a MPML regime.	68
3.12	Optical spectrum of NLPR mode-locked EDFL operating in CML regime.	69
3.13	Optical spectrum of NLPR mode-locked EDFL operating in QML regime.	70
3.14	Optical spectrum of NLPR mode-locked EDFL operating in a MPML regime.	71
3.15	Schematic of a field autocorrelator	72
3.16	Schematic of a second harmonic generation (SHG) autocorrelator aligned for an intensity autocorrelation (non-collinear mode). A curved mirror is used to focus a beam waist in the SHG crystal. . .	73
3.17	A set of different pulse intensity profiles that have similar autocorrelation functions.	75
3.18	A set of noisy pulses and their corresponding autocorrelation traces. A pulse that has more noise tends towards a coherence spike upon an envelope.	76
3.19	Autocorrelation trace (150 ps span) of NLPR mode-locked EDFL output operating in a CML regime with 70 mW average power. . .	77
3.20	Autocorrelation trace (5 ps span) of NLPR mode-locked EDFL output operating in a CML regime with 70 mW average power.	78
3.21	Fitted profiles for the ACF trace presented in Fig. 3.20.	78
3.22	Autocorrelation trace (left: 5 ps span and right: 150 ps span) of NLPR mode-locked EDFL operating in a Q-switched mode-locked regime.	79
4.1	A schematic of the NLPR mode-locked TDFL cavity. WDM = wavelength division multiplexer, PC = polarisation controller and x marks the position of splices or fibre connectors.	84
4.2	Temporal trace of a CML pulse train	86
4.3	Broadband RF spectrum of a CML pulse train	87
4.4	Optical spectrum for a CML regime	87

4.5	Autocorrelation trace (150 ps span) taken while operating in a CML regime. Trace collected after removing a filter from the photodetector module. Average power of CML output launched into autocorrelator was 80 mW.	88
4.6	Autocorrelation trace (5 ps span) taken while operating in a CML regime. Average power of CML output launched into autocorrelator was 80 mW.	89
4.7	Oscilloscope traces of a QML envelope. The output intensity varies with time considerably. The plot is produced from stitching 4 shorter temporal windows together.	90
4.8	Broadband RF spectrum of the QML pulse train.	91
4.9	Optical spectrum for a QML regime.	91
4.10	Autocorrelation trace (150 ps span) taken while in a QML regime.	92
4.11	Autocorrelation trace (15 ps span) taken while in a QML regime.	92
4.12	Temporal trace of a CML pulse train with a CW optical power component.	93
4.13	Broadband RF spectrum of the CML mode-locked pulse train with an optical CW component.	94
4.14	Optical spectrum for a CML regime with a CW optical power component.	94
4.15	Autocorrelation trace (5 ps span) taken while laser operating in a CML regime with an optical CW component.	95
4.16	Optical spectrum for the stable MPML regime.	98
4.17	Autocorrelation trace (150 ps span) taken while in a stable MPML regime.	98
4.18	Autocorrelation trace (5 ps span) taken while in a stable MPML regime.	99
4.19	Plot of $\langle S_1 \rangle$ as a function of angle relative to the polariser axis, θ . Entire figure reproduced including the original caption from [7]. The authors have used the abbreviation EDF for erbium doped fibre (the active fibre).	101

4.20	Two-photon absorption energy level diagram showing how two photons can bridge the energy gap in a semiconductor.	101
4.21	Schematic diagram of measurement and diagnostic equipment for Stokes Parameter discontinuities. The remaining 50% power from the second splitter was beam-dumped.	102
4.22	A flowchart with an iterative process to determine when mode-locking is achieved based on changes in the Stokes parameter $\langle S_1 \rangle$. S'_1 is simply the new value of S_1 at some given point in time when analysing the signal.	103
4.23	Plot of $\langle S_1 \rangle$ as a function of voltage on CH1. The insets shows the pulse train temporal trace before and after entering the QML regime. A discontinuity in $\langle S_1 \rangle$ was found to coincide with a regime transition (background CW regime to QML).	104
4.24	A plot of photodetector voltages (left) and S_1 parameter (right) for CH1 voltage: 64.5 V.	105
4.25	A plot of photodetector voltages (left) and S_1 parameter (right) for CH1 voltage: 64.6 V.	106
4.26	A plot of photodetector voltages (left) and S_1 parameter (right) for CH1 voltage: 64.7 V.	107
4.27	A plot of photodetector voltages (left) and S_1 parameter (right) for CH1 voltage: 64.8 V.	107
4.28	A plot of photodetector voltages (left) and S_1 parameter (right) for CH1 voltage: 65.0 V.	108
4.29	A plot of photodetector voltages (left) and S_1 parameter (right) for CH1 voltage: 65.1 V.	108
4.30	A plot of photodetector voltages (left) and S_1 parameter (right) for CH3 voltage: 6.3 V.	109
4.31	A plot of photodetector voltages (left) and S_1 parameter (right) for CH3 voltage: 6.4 V.	110
4.32	Schematic diagram of measurement and diagnostic equipment for two-photon absorption.	111

4.33	Responsivity curve for a silicon photodetector. Diagram originally from [11].	112
4.34	Simulation of TPA pulses in the CML regime using a 2 μm trace.	113
4.35	Simulation of TPA pulses in the QML regime based on a 2 μm trace. Note that there were oscillations outside the main envelope.	113
5.1	A schematic of the NLPR mode-locked HDFL cavity. WDM = wavelength division multiplexer, PC = polarisation controller and x marks the position of fibre splices or fibre connectors.	125
5.2	Temporal trace of a CML pulse train.	127
5.3	Broadband RF spectrum of a CML pulse train with 200 s sweep time.	127
5.4	Optical spectrum for the holmium NLPR operating in a CML regime.	128
5.5	Autocorrelation trace (5 ps span) for holmium NLPR operating in a CML regime taken for an average power of 4.2 mW.	129
5.6	Autocorrelation trace (150 ps span) for holmium NLPR operating in a CML regime.	129
5.7	A flowchart of an iterative process to determine when mode-locking is achieved based on amplitude variation in radio-frequency (RF) spectra of the pulsed train laser output.	131
5.8	Diagnostics used for the automation of an NLPR mode-locked HDFL using RF spectrum analyser metrics.	131
5.9	Broadband RF spectrum of a measured CML pulse train with 2-second sweep time. The PRF was 17 MHz.	133
5.10	A screenshot of the MATLAB GUI used for automation.	136
6.1	A plot of the total dispersion curves for a variety of different optical fibres – standard single-mode, non-zero dispersion-shifted and dispersion-compensating. Image from [10].	149
6.2	A plot of material dispersion coefficient as a function of wavelength for silica and ZBLAN glasses. Figure originally presented in [14].	151
E.1	Diagram of an RF spectrum envelope for a mode-locked pulse train with two points documented.	170

F.1	Schematic of a second harmonic generation (SHG) autocorrelator aligned for an interferometric autocorrelation (collinear mode). Note that the beams overlap outside the crystal (along the path to the mirror after the beamsplitter).	174
G.1	Schematic of type-I phase matching in a non-linear crystal	177
J.1	ASCII output of the RF spectrum trace.	186

Abstract

Mode-locked fibre lasers have applications in research, defence, biological science, manufacturing and spectroscopy. The aim of this research was to investigate automatic control of a passive mode-locking technique known as non-linear polarisation rotation (NLPR) that exploits polarisation differences across a pulse's profile that manifest due to different intensities. This research seeks to focus on how NLPR laser sources can be made stable, especially at longer wavelengths (such as 2 μm).

Three different fibre lasers were developed to investigate different aspects of NLPR. An erbium mode-locked source was used to explore measurement techniques and competing operating regimes. The operating regimes were controlled using a manual polarisation controller. Characterisation revealed that the source produced 570 fs pulses with a central wavelength of 1567 nm, repetition rate of 17 MHz and pulse energy of 3 nJ.

A thulium NLPR source was developed to further explore possible automation metrics and characterise a range of additional undesired operating regimes. Automation metrics tested to determine if the laser was continuously mode-locked included discontinuities in Stokes parameters, two-photon absorption signals and amplitude modulation across the radio-frequency spectrum of the laser. Characterisation revealed that the source produced 1.15 ps pulses with a central wavelength of 1990 nm, repetition rate of 21 MHz and pulse energy of 5 nJ.

Lastly, a holmium NLPR source with electronic control of the intra-cavity polarisation state was built. To the best of our knowledge, this is the first diode-pumped

NLPR mode-locked holmium source in the $2\mu\text{m}$ waveband. An automation mechanism was devised and implemented. Characterisation revealed that the source produced 770 fs pulses with a central wavelength of 2061 nm, a repetition rate of 17 MHz and pulse energy of 0.41 nJ.

Signed Statement

I certify that this work contains no material which has been accepted for the award of any other degree or diploma in my name, in any university or other tertiary institution and, to the best of my knowledge and belief, contains no material previously published or written by another person, except where due reference has been made in the text.

In addition, I certify that no part of this work will, in the future, be used in a submission in my name, for any other degree or diploma in any university or other tertiary institution without the prior approval of the University of Adelaide and where applicable, any partner institution responsible for the joint-award of this degree.

I acknowledge that copyright of published works contained within this thesis resides with the copyright holder(s) of those works.

I also give permission for the digital version of my thesis to be made available on the web, via the University's digital research repository, the Library Search and also through web search engines, unless permission has been granted by the University to restrict access for a period of time.

I acknowledge the support I have received for my research through the provision of an Australian Government Research Training Program Scholarship.

Signed: 

Date:26/06/2020

Acknowledgements

This research was supported by the Defence Science and Technology Group (DST Group). I would like to thank them for the financial and academic support they provided through both a Defence Science Partnering Deed and a Cadetship.

First and foremost, I would like to thank my external (DST Group) supervisors - Keiron Boyd, Nikita Simakov and Miftar Ganija. Their support and contribution to the project - from building fibre lasers to providing insight and guidance – has been greatly appreciated. I could not have asked for a more attentive, patient and resourceful supervision team. I am thankful for the critical roles that each of them have played in developing my scientific understanding, laboratory skills and research practices.

I would like to thank my primary supervisor, Peter Veitch, for his vital role in improving my thesis. His support and efforts have helped me become a better writer and communicator.

I also wish to thank Alexander Hemming and John Haub for their ongoing support of the project.

I am grateful to Neil Carmody, and Jesper Munch for their helpful discussions regarding experiments and for providing laboratory equipment.

To my colleagues Adam, Jamie, James, Lily and Nick, thank you for your support. I enjoyed the discussions we had about physics throughout completing our projects

and coursework.

I would also like to thank the School of Physical Sciences and the DST Group Cadetship Program Managers for providing funding to attend and present at ACOFT 2018 in Perth and ACOFT 2019 in Melbourne.

Finally, I would like to thank my family and friends. I appreciate the support and understanding they have provided me with throughout my candidature.

Dedication

I dedicate this thesis to my parents - Michael and Tracy - for the support they have given me throughout my life.

Chapter 1

Introduction

1.1 Mode-locked Lasers

A laser can generate ultra-short pulses (picosecond and femtosecond duration) by utilising one or more different mode-locking techniques [1]. Mode-locking relies on inducing a fixed phase relationship between longitudinal cavity modes. Constructive interference between these phase-fixed modes results in pulse formation [1]. A laser cavity may support a single or multiple circulating pulses when it enters a mode-locked state [1].

Mode-locked fibre lasers have applications in research [2, 3], defence [1], biological science [4], manufacturing [5] and spectroscopy [6]. Their use as seed sources, producing stable (albeit low energy) continuously mode-locked (CML) pulse trains, that can be amplified are a particular area of interest. The output of the amplifier can be used for higher harmonic generation and the generation of supercontinua. Recent research into mid-IR (MIR) mode-locked sources is also introduced in this Chapter. This Chapter seeks to provide a quick overview of the field of mode-locking.

1.2 Applications of Mode-locked Sources

1.2.1 Seed Sources

Seed sources are small laser devices whose optical output enters one or more amplifiers [7]. Amplification systems are valuable for power scaling while maintaining a specific pulse property (such as pulse duration, linewidth, wavelength tuning) [7, 8]. Care must be taken to avoid broadening the linewidth during amplification [9]. Pulse duration can also increase if dispersion is not adequately accounted for [10, 11].

To increase gain, light can either pass through the same gain medium several times (multi-pass amplifier), or it passes through several amplifiers (amplifier chain) [7].

Regenerative amplification has become a popular amplification technique for ultra-short pulses [12]. It is similar to multi-pass amplification; however, an optical switch (i.e. an electro-optic (EO) modulator and a polariser) controls the number of round trips made by a pulse [12]. Initially, the gain medium is pumped to store energy. A pulse is then injected into the resonator using a switch. The pulse completes many round trips in the cavity [13]. A high gain manifests from having a large number of passes through the gain medium. The switch is then also used to release the pulse from the resonator [13]. Pulse energies in the mJ range or larger can be formed using this technique [14].

Hinkelmann *et al.* presented a linear amplifier with a Ho:YLF gain medium [15]. The laser operated at $2.05 \mu\text{m}$ and produced mJ-level pulse energies with high repetition rates (1 kHz to 100 kHz). Rezvani *et al.* reported on 1.35 mJ pulses using regenerative amplification from a diode-pumped Tm:YAP ring cavity [16]. The peak power was 2 GW, and the repetition rate was 1 kHz. The output had a central wavelength of 1937 nm. Pulses completed 45 round trips before out-coupling and were measured to have a duration of 360 fs [16].

Amplifiers are adversely affected by any noise from the seed that passes through the amplifier [17]. Noise can take the form of fluctuations in optical intensity or even offset satellite pulses from a primary pulse train [17]. The desired lasing signal may be diluted upon amplification of the noise. Consequently, seed sources must be stable and have low noise. Amplifiers can also be affected by amplified spontaneous emission (ASE) and internal stray reflections [18].

Seed sources seldom need to be of high power. Stability and output characteristics are often more crucial to avoid amplification of an imperfect signal.

1.2.2 Soft x-rays via Higher Harmonic Generation (HHG)

High peak power pulsed lasers can be used to generate soft x-rays through the process of higher harmonic generation (HHG). Ultrashort pulsed lasers have fields with high optical intensities. High intensities lead to large electron displacement perturbations as photons pass through a dielectric medium [19]. These large displacements generate light at a range of different wavelengths that are a fraction of the incident lasing wavelength (harmonics). The relative intensity of the n^{th} harmonic is generally less than that of the $n - 1^{\text{th}}$ harmonic, especially for higher order harmonics [20].

For visible lasing wavelengths, the average energy of an electron perturbed by the light field (ponderomotive energy) is quite small, meaning few harmonics have any meaningful intensity. Near-infrared (NIR) and mid-infrared (MIR) photons can accelerate electrons to much higher energies due to the λ^2 (wavelength) dependency in ponderomotive energy, leading to greater yield at higher harmonics. Experimentally, MIR lasers have led to the generation of hundreds of harmonics using HHG, forming soft x-rays out to 600 eV energies and beyond [21].

Soft x-rays have a variety of different applications in nuclear physics including ultrafast electronic and structural dynamics, medical and pharmaceutical analysis,

spectroscopy in the water window (a portion of the electromagnetic spectrum that water is transparent to), nuclear inner-shell spectroscopy, thin-film property measurements, imaging, microscopy and metrology [22, 23, 24, 25]. The water window (2.2 - 4.4 nm) is unique as it houses absorption edges for a range of different elements, including carbon and oxygen [26].

The generation of soft x-rays highlights the need for stable mode-locked sources at two micron. High peak powers are required meaning that amplification of the source is necessary.

1.2.3 Supercontinuum Generation

Supercontinuum light generation exploits non-linear effects in materials of high non-linearity [2]. It has a broad, and often continuous, optical spectrum [2]. The principle of supercontinuum generation has been around since the 1970s in bulk fibre lasers [2]. Fibre lasers have the benefit of longer interaction lengths [2]. Stable short (nanosecond) and ultrashort pulses (picosecond and femtosecond) allow for supercontinuum generation. High peak powers drive temporal breakup of short pulses that, combined with non-linear effects, generate optical spectra that can span beyond one octave.

Medical imaging is one application for supercontinuum light sources. Stimulated emission depletion (STED) microscopy can provide a better resolution than $\lambda/50$ [27]. Increased resolution can overcome the optical diffraction limit that plagues confocal microscopes [28]. STED utilises a synchronised pair of laser pulses to excite a substance that can fluoresce [29]. A depletion pulse, at a lower frequency, follows the excitation pulse yielding light through stimulated emission [29]. Picosecond pulses are preferable as they provide the most efficient de-excitation [30].

OCT is another imaging technique. Imaging biological matter often uses light with wavelengths of 800 – 1300 nm due to water absorption and tissue scattering [31].

However, optical scattering decreases as wavelength increases [32]. Painted and opaque surfaces readily scatter light and do not contain substantial amounts of water [32]. Two micron appears to be a suitable wavelength for the analysis of such materials. Authors have reported on using broadband supercontinuum in the two-micron range to resolve individual layers of paint on a surface [32].

Supercontinuum also plays a vital role in MIR spectroscopy. Many molecules have characteristic absorption features (fingerprints) in the MIR due to fundamental and harmonic (overtone) molecular vibrations [33, 34]. Chemical substances are identifiable from absorption features at different wavelengths [34, 35]. MIR spectroscopy can hence be useful as a quality control measure in chemical and pharmaceutical production. Concentrations and the presence of impurities are quantifiable by measuring absorbance [35].

Additionally, MIR spectroscopy has applications in standoff detection [36], determining octane levels in biofuels [37] and environmental sensing [38]. MIR spectroscopy is compelling as an analysis technique as absorption bands of different chemical components are isolatable [39]. Additionally, NIR spectroscopy often relies on weaker absorption features, as overtones are used [39].

1.2.4 Mode-locking at 3 μm

This project will specifically focus on mode-locking at wavelengths around 2 μm , which is categorised as the NIR. There is also an increasing demand for compact and stable mode-locked laser sources in the MIR at wavelengths near 3 μm and beyond [40]. Such sources enable a range of applications, including breath analysis and laser surgery [40].

Fluoride ZBLAN glasses, discussed in Section 6.3.3, doped with erbium and holmium are known to generate light in the 2.7 – 2.9 μm region [41, 42]. Trivalent dysprosium is another dopant that can result in lasing at 2.8 – 3.4 μm [43].

Fuerbach *et al.* generated ultrashort pulses at $2.875 \mu\text{m}$ from a holmium-praseodymium co-doped ZBLAN fibre laser [40]. The output of the ring cavity had a short length of As_2S_3 step-index chalcogenide fibre [40]. This highly non-linear fibre resulted in spectral broadening to generate MIR supercontinuum. The final pulses obtained had a 3 dB spectral width of 141 nm and a temporal full-width-half-maximum (FWHM) of 804 fs [40].

Henderson-Sapir *et al.* demonstrated an acousto-optic tunable mode-locked laser, a technique discussed in Section 1.3, based on erbium-doped zirconium fluoride fibres. The source developed could lase at wavelengths up to 3162 nm and presently holds the record for longest wavelength from a rare-earth doped mode-locked fibre laser [44].

Zhang *et al.* modelled soliton non-linear polarisation (NLPR) mode-locking, a technique discussed in Section 1.3, at $3 \mu\text{m}$ using the coupled Ginzburg-Landau equation [42]. They noted that the low modulation depth of commercial-grade MIR saturable absorber mirrors, another mode-locking technique also discussed in Section 1.3, for Er^{3+} systems limit pulse durations to the picosecond scale [42]. The artificial saturable absorber effect of NLPR would yield a faster response time and higher damage thresholds [42]. Their model utilised two waveplates for polarisation control. Their findings indicated that a 5 m intra-cavity fibre length could theoretically yield sub-600 fs pulses. [42]

1.3 Mode-locking Techniques

There are several mechanisms that can be used to mode-lock a laser. These mechanisms can be broadly categorised as either active or passive [45]. Active mode-locking involves inserting an intra-cavity component that modulates the pulse amplitude or frequency [45]. Passive mode-locking involves inserting an intra-cavity component that favours high intensities [45].

There are a range of active mode-locking techniques including acousto-optic (AO) modulation [46], liquid-crystal modulators [47], and electro-optic modulation [48]. AO mode-locking often utilises an electrical signal tuned to a modulation frequency that matches the round-trip time of the laser cavity [46]. In some systems, a frequency shifting element is sufficient [46]. Optical power passes through the modulator when losses are minimal yielding a short pulse. The variable loss manifests as a result of a sinusoidal density from acoustic waves that alter the medium's refractive index [46].

EO modulation involves applying a voltage to a medium to change the polarisation state of light passing through. Pulses can be outcoupled based on their polarisation using a polariser (for example) [48]. Pulse durations attainable from active techniques are generally affected by gain narrowing and chromatic dispersion [49]. These concepts are introduced in Sections 2.4.3 and 2.4.4 respectively.

Passive mode-locking techniques include semiconductor saturable absorber mirrors (SESAMs) [50], Mamyshev mode-locking [51], non-linear polarisation rotation (NLPR) [52], and non-linear amplifying loop mirrors (NALMs) [53, 54]. Section 1.4 includes a review of demonstrated passive mode-locked fibre lasers at wavelengths up to 2 μm .

SESAMs, and saturable absorbers (SA's), are fabricated from materials that exhibit a greater absorption when incident fluence is small. Saturation from intense fields reduces absorption and results in an increased reflectivity [55]. Increased reflectivity leads to a preference for a high intensity, low loss configuration in the cavity enabling short pulse generation [55]. SESAMs can be introduced to a fibre ring cavity using an optical circulator, as depicted in Fig. 1.1.

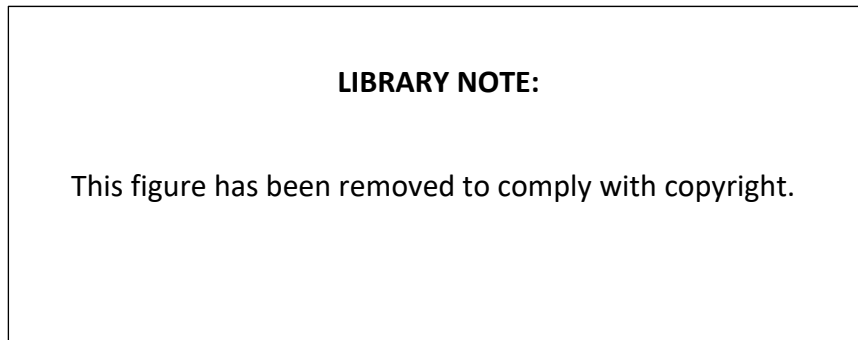


Figure 1.1: General schematic of a ring SESAM mode-locked fibre cavity. Light propagates in a clockwise direction around the cavity. Light reflected off the SESAM passes back to the circulator and exits through port 3. Figure originally presented in [56]. SMF = single mode fibre, PC = polarisation controller, WDM = wavelength division multiplexer, SESAM = semiconductor saturable absorber mirror. Many of these components will be introduced in later chapters (Chapters 2-3).

SESAMs can also be used in linear fibre laser cavities, as depicted in Fig. 1.2.

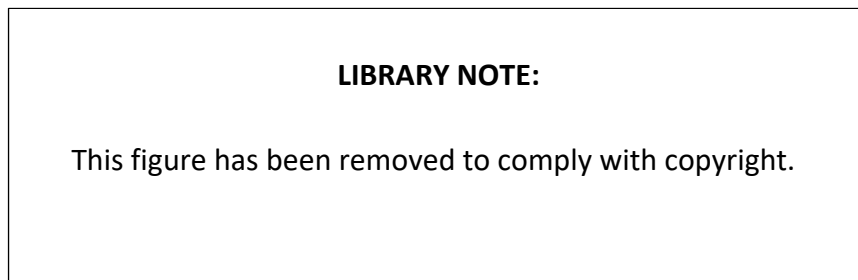


Figure 1.2: General schematic of a linear SESAM mode-locked fibre cavity. Figure adapted from [57]. FC/APC = fibre connector, FBG = fibre Bragg grating.

Pulses from SA mode-locking have durations that are limited by properties of the absorber and dispersion from propagating through optical fibres.

Mamyshev mode-locking is achieved using two bandpass filters with non-overlapping bands [58]. Non-linear effects, in particular Self Phase Modulation (SPM) discussed in Section 2.5.3, aid in the transition between the two spectral bands [59]. Low intensity pulses are blocked by the offset filter as they experience less SPM whereas high intensity components pass through [59]. The filter combination hence acts as an artificial saturable absorber, which forces the laser into a pulsed state [59].

NLPR and NALM mode-locking exploit the intensity dependence in a light field's polarisation state [60]. Polarisation dependent losses while propagating through fibre enable short pulse formation. These techniques will be described in more detail in Chapter 2. NALM and NLPR fibre lasers have pulse duration's limited by the time-bandwidth product (Section 2.4.2), gain narrowing (Section 2.4.3), the Optical Kerr Effect (Section 2.5.1) and intra-cavity dispersion (Section 2.4.4).

In recent years, there has been a demand for mode-locked sources at wavelengths near $2 \mu\text{m}$. One driving force behind the demand is a water absorption peak around this wavelength. Sources that lase near this peak are useful for medical applications due to a lower penetration depth in human tissue [61]. Difficulty arises from developing these sources in a way that a stable output is attained.

SA mode-locked fibre cavities at $2 \mu\text{m}$ provide stable outputs but require either of the following:

- A commercially-available component which has a relaxation time that currently limits pulse duration to the picosecond level, as documented in Section 1.4 [62]
- A component built in house which requires advanced fabrication techniques, prototyping and semiconductor knowledge [63]
- Graphene saturable absorbers

Contrastingly, NLPR should be able to yield shorter pulses than lasers manufactured with currently available commercial SESAMs and without the need for advanced fabrication techniques. However, a trade-off is the instability associated with NLPR sources.

NLPR often relies on the adjustment of intra-cavity devices to generate short pulses. Manual adjustment of polarisation can often be difficult, and even if a stable mode-locking regime is found, it may not persist for seconds or minutes at a time. Thermal

or mechanical fluctuations in the laser cavity can change the polarisation conditions and force the laser to go into a range of undesired competing lasing regimes (as will be explored in Section 2.7) [64]. The prevalence of competing regimes has driven demand for sources that can automatically find an appropriate regime for operation by exploiting feedback from diagnostic tools [65].

It is important to note that there are many other mode-locking techniques that have not been discussed in this Section [66, 67].

1.4 Demonstrated Mode-locked Sources

1.4.1 SA Mode-locked Fibre Lasers

A summary of recent results from custom-built and commercial SA and SESAM mode-locked lasers is presented in Table 1.1.

Sotor *et al.* explored the fabrication and use of a graphene saturable absorber to obtain sub-ps pulses [68]. Hinkelmann *et al.* reported on the generation of 1.16 ps pulses using a commercial Batop SESAM in a linear oscillator connected to a thulium-doped amplifier [69]. Grzes *et al.* used a SESAM mode-locked laser as a seed for a Tm-doped amplifier system providing over 20 W at 2 micron [70].

Table 1.1: Table of summary characteristics for a range of SESAM mode-locked fibre lasers.

Lead author	Dopant	Central wavelength, (nm)	Pulse duration (fs)	Repetition rate (MHz)	Average power (mW)	Peak power (kW)	Pulse energy (nJ)
Lin [71]	Yb	1050	69	109	-	-	-
Wang [72]	Tm	1945	152	25.7	4.85	1.2	0.19
Grzes [70]	Tm	1994	23 ps	81	20 W 17 mW (pre-amp)	9.6	250
Wang [73]	Tm, Ho	2015	52	86	376	79	44
Hinkelmann [69]	Ho	2052	1160	27.3	10	0.30	0.37
Pawliszewska [74]	Ho	2058	190	21	18	4.2	0.86
Sotor [68]	Ho	2078	811	38	7	0.21	0.18
Tolstik [75]	Ho	2094	2230	7.8	28	1.51	3.6

1.4.2 NLPR Mode-locked Fibre Lasers

A summary of recent results from NLPR mode-locked lasers is presented in Table 1.2. Voropaev *et al.* developed a manually controlled NLPR holmium laser with dispersion management that yielded 142 fs pulses with a 370 mW average power and 1950 nm central wavelength [76]. NLPR has generated pulses that are

less than 50 fs for wavelengths near two micron [77]. In general, the pulse energies reported on in the literature and presented in Table 1.2 for NLPR mode-locked sources exceed that attained from a SESAM mode-locked source (Table 1.1).

Table 1.2: Table of summary characteristics for a range of NLPR mode-locked fibre lasers.

Lead author	Dopant	Central wavelength, (nm)	Pulse duration (fs)	Repetition rate (MHz)	Average power (mW)	Peak power (kW)	Pulse energy (nJ)
Chen [78]	Yb	1030	84-113	50	220	49	4
Li [79]	Er	1568	88 ¹	38.6	18.8	7.9	0.49
Nomura [77]	Tm	1880	50 ²	67.5	13	50	2.7
Gao [80]	Tm	1890	350	11.3	90	22.3	7.8
Voropaev [76]	Tm	1950	143	11.5	370	222	31
Lin [81]	Tm	1985	663	28	-	-	-
Li [82]	Ho	2060	98	35	40	11	1.1

¹ Wings of autocorrelation trace reveal excess intensity suggesting the pulse has a noise-like structure.

² A small satellite pulse with an amplitude of 10% of the primary pulse was observed with a 100 fs offset from the FROG pulse profile.

1.4.3 Hybrid NLPR/SESAM Mode-locked Fibre Lasers

Authors have often utilised a combination of SESAMs and NLPR in mode-locked fibre cavities. A summary of these hybrid mode-locked devices is presented in Table 1.3. Haxsen *et al.* produced 482 fs pulses (once dechirped) using a combination of the mode-locking techniques [83]. Li *et al.* produced 37 nJ pulses from a hybrid system [84].

Table 1.3: Table of summary characteristics for hybrid NLPR and SESAM mode-locked fibre lasers.

Lead author	Dopant	Central wavelength, (nm)	Pulse duration (fs)	Repetition rate (MHz)	Average power (mW)	Peak power (kW)	Pulse energy (nJ)
Li [84]	Yb	1030	960	83.7	3.2 W	37	37
Wu [85]	Er	1550	713	4.65	5	1.4	1.1
Chen [87]	Er	1570	680	28	4	197	0.14
Dvoretzkiy [86]	Er	1575	382	25	4	0.22	0.16
Haxsen [83]	Tm	1927	482	19.7	13.2	1.3	0.67

1.4.4 NALM Mode-locked Fibre Lasers

NALMs are capable of producing sub-picosecond duration pulses. A summary of recent results from NALM mode-locked lasers is presented in Table 1.4. Similar pulse energies and durations are attainable to that of mode-locking with NLPR (Table 1.2).

Table 1.4: Table of summary characteristics for NALM mode-locked fibre lasers.

Lead author	Dopant	Central wavelength, (nm)	Pulse duration (fs)	Repetition rate (MHz)	Average power (mW)	Peak power (kW)	Pulse energy (nJ)
Liu [88]	Yb	1028	215	700	150	0.94	0.21
Deng [89]	Yb	1035	195 ¹	8.7	61	33.8	7
Guo [90]	Er	1550	2700	1.8	11.7	2.3	6.5
Khagai [91]	Bi	1700	630 ²	3.6	20.5	8.5	5.7
Michalska [92]	Tm	1988	534 ¹	10.6	189	-	-

¹ Broad wings suggest that pulse formation is noisy with the autocorrelation trace consisting of a coherence spike atop a broader envelope.

² After amplification from a bismuth amplifier followed by compression.

1.5 Objectives

This thesis aims to investigate non-linear polarisation rotation (NLPR) as a mode-locking technique at different wavelengths. Analysis over a range of wavelengths was deemed important to explore the non-ideal lasing behaviour/regimes that hinder stable mode-locking [95]. Part of the focus of our research is to devise a method to automate mode-locking at wavelengths near $2 \mu\text{m}$.

The research presented in this thesis seeks to address the following objectives:

- A detailed characterisation of NLPR sources operating in different (ideal and non-ideal) regimes at a variety of different wavelengths – erbium (1560 nm), thulium (1990 nm) and holmium (2060 nm)

- An exploration of appropriate metrics to automate an NLPR laser around two micron
- Demonstration of the first diode-pumped NLPR holmium-doped mode-locked source at $2\ \mu\text{m}$
- The development of a fully automated NLPR source

1.6 Mode-locked Automation Techniques

NLPR sources have been developed with automation diagnostics to correct for unideal lasing states. Many authors have reported on automated erbium-doped mode-locked fibre laser systems, however there is an absence of such reports for $2\ \mu\text{m}$ systems. Common approaches for automating erbium NLPR lasers involve measuring discontinuities in the Stokes parameter S_1 [65], observing changes in the radio frequency (RF) spectrum [93] or using an optimisation algorithm with a fitness function based on feedback from a range of diagnostics that record spectral and temporal laser output data [94]. An experimental exploration of different automation techniques will be presented in Chapter 4 of this thesis. One automation technique will then be expanded upon and fully implemented in Chapter 5.

1.7 Outline of Thesis

Chapter 1 gave an overview of this project's objectives and highlighted several previous passive mode-locked laser achievements from the literature. Applications for passively mode-locked laser sources at two micron including seed sources, soft x-ray generation and supercontinuum generation were described. An important takeaway message is that high peak powers and excellent stability are often advantageous for most mode-locking applications. Such factors re-enforce the appeal of an automated NLPR mode-locked fibre laser.

Chapter 2 covers a range of fundamental physics concepts that are crucial to understanding NLPR and the work presented in Chapters 3-5. It starts with an overview of optical fibres before exploring non-linear effects in optical fibres. There is also an overview of the fundamental limits driving pulse duration including gain bandwidth, the time-bandwidth product, dispersion and the Optical Kerr Effect. The chapter concludes with an introduction to non-ideal pulsing regimes for an NLPR source.

In Chapter 3, there is a discussion of measurement techniques for interpreting the lasing output mode-locked sources. The relative merits of each technique are explored. The chapter includes measurements taken for an erbium-doped NLPR fibre laser in several different regimes (an ideal output and two non-ideal outputs). This laser was fabricated to test measurement techniques before operating in the two-micron region.

Chapter 4 involves the characterisation of a thulium-doped NLPR mode-locked laser that has both a manual and electronic polarisation controller. Different measurements were taken for a variety of operating regimes. The main purpose of this source was to test a range of different automated mode-locking algorithms. Several diagnostic signals are explored including discontinuities in Stokes parameters using power measurements from a polarising beamsplitter, a two-photon absorption (TPA) signal, and amplitude modulation in the radio-frequency (RF) domain. The relative merits of each diagnostic metric are discussed.

In Chapter 5, one of the automation metrics from Chapter 4 is developed further. A novel outcome of this research was the demonstration of a fully automated diode-pumped holmium doped mode-locked laser. The automation algorithm enables near real-time identification of the current lasing regime and correction of the intracavity polarisation state if the regime is non-ideal. It can operate without human intervention and corrects any eventual drifts out of an ideal (continuously mode-locked) regime.

Chapter 6 reviews the capabilities and limitations of the automated mode-locked algorithm. Future research directions are noted, including fibre laser design improvements.

Chapter 2

Background

2.1 Introduction

This chapter focuses on the physical concepts that explain NLPR as a mode-locking technique and what limits the attainable pulse duration.

Section 2.2 provides an introduction to optical fibres and pumping schemes for the sources developed in Chapters 3, 4 and 5. Parametrising and controlling the polarisation state of light is the focus of Section 2.3. Section 2.4 begins by exploring the properties of pulses. Important physical phenomena that alter pulse duration are introduced including the time-bandwidth product, gain narrowing and dispersion.

In Section 2.5, a variety of non-linear effects are introduced. The Optical Kerr Effect and Non-linear Schrödinger Equation (NLSE) provide a starting point for introducing Self Phase Modulation (SPM) and Cross Polarisation Modulation (CPM). These non-linear effects aid with understanding Non-linear Polarisation Evolution in optical fibres. Mode-locking is introduced in Section 2.6 and Non-linear Polarisation Rotation (NLPR) is described.

Finally, in Section 2.7, we discuss the non-ideal regimes that NLPR mode-locked lasers can operate in.

2.2 Optical Fibres

2.2.1 Introduction to Fibres

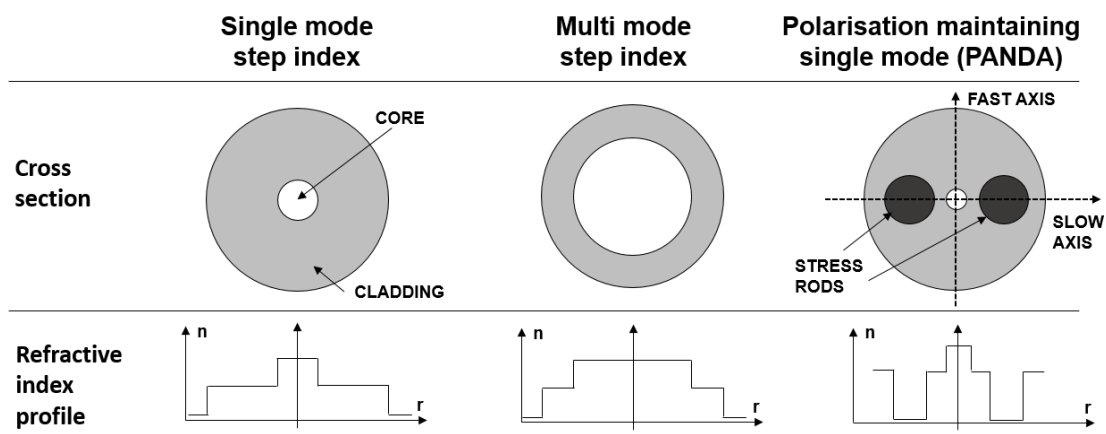
Optical fibres are waveguides used to transmit light [1]. Fibres typically consist of a core, cladding and coating. The signal light is generated and propagated in the core [2, 3]. The dielectric layers of a fibre waveguide determine the modes that are supported for propagation [4].

Dopants modify the refractive index difference between the core and cladding [5]. Germanium oxide (GeO_2) increases refractive index, whereas boron and fluorine decrease the refractive index [6].

NLPR fibre laser cavities often have a passive fibre (used to exploit non-linear effects) and an active fibre (a doped fibre that acts as the laser gain medium, discussed in Section 2.2.2).

Fibre waveguides can be single mode (SM) or multi-mode. Cross sections of each fibre type and their corresponding refractive index profile are presented in Table 2.1.

Table 2.1: Table featuring cross sections and the refractive index profile for a range of different fibre types.



SM fibres can only support the propagation of a fundamental mode at a particular wavelength. For the purpose of this research, the passive fibre is a single mode, step-index fibre at the lasing wavelength. However, some of the pump sources are multi-mode step index fibres. Passive SM fibres were used because different modes have different group velocities, which can inhibit stable pulse formation [5].

The number of modes supported by a step-index fibre is dependent on its V-number, which is also referred to as the V-parameter [6]. This characteristic parameter is defined by the geometry and properties of the optical fibre, as expressed in Equation 2.1 [6].

$$V = \frac{2\pi r NA}{\lambda} \quad (2.1)$$

where NA is the fibre's numerical aperture (related to the acceptance of light into a fibre), r is the core radius, and λ is the optical wavelength. For $V < 2.405$, the waveguide supports only a single mode [6].

Another important quantity is the mode field diameter (MFD). MFD is a measure of the spatial distribution of irradiance across the end face of a SM fibre. An empirical approximation for MFD, known as the Marcuse formula, is given by Equation 2.2 [6].

$$MFD \approx 2r \left(0.65 + \frac{1.619}{V^{\frac{3}{2}}} + \frac{2.87}{V^6} \right) \quad (2.2)$$

The effective mode area, A_{eff} is a related parameter that describes the transverse extent of a fibre waveguide mode [7,8]. It is given by Equation 2.3, where I is the intensity of the optical field, A is the cross sectional area of the fibre and dA is the differential cross section area element.

$$A_{eff} = \frac{(\int I dA)^2}{\int I^2 dA} \quad (2.3)$$

Splicing two fibres that have different mode field profiles together leads to losses as the coupling of optical fields from one geometry to another is imperfect. This is discussed at several stages throughout the thesis.

Polarisation describes the temporal evolution of an electromagnetic wave's electric field, \vec{E} .

Fibres can be polarisation maintaining (PM) or non-polarisation maintaining (non-PM). PM fibres maintain the polarisation state of light polarised in certain orientations (generally linear) as it propagates [2]. Preservation of the polarisation state occurs as a result of there being no or very little cross-coupling between polarisation modes [3]. This is achieved by introducing an induced linear birefringence such that the two polarisation modes propagate with different phase velocities (a concept introduced in Section 2.4.1) along a fast or slow axis of the fibre [2,3].

A common PM fibre design (known as the PANDA design) is presented in Table 2.1. Stress rods of silica doped with, generally, boron trioxide B_2O_3 , run parallel to the fibre core [3]. Light propagating along the fast and slow axes maintains its polarisation state [2,3].

A summary of typical properties for SM and PM fibres is presented in Table 2.2 where Δn is the refractive index difference between the fast and slow axes of the optical fibre. The beat length is the distance over which polarisation has made one rotation (i.e. the phase shift between two orthogonal polarisation modes in a fibre is 2π). Polarisation modes and polarisation rotation are discussed in Sections 2.5 and 2.6 [2,3].

Table 2.2: Table of typical properties for SM and PM fibres [2,3].

Property	SM	PM
Δn	10^{-6}	10^{-4}
Beat length	m	mm

2.2.2 Doped Fibres

Active fibres typically contain a rare-earth ion dopant, or dopants, within the core of the optical fibre. These ions are almost exclusively trivalent as their electronic transitions occur in the 4-f shell, which is shielded from the host material [9].

Optical pumping of a rare-earth active fibre aims to excite ions to a metastable state [7]. Ions transition and emit photons through stimulated emission, generating an optical signal at a different wavelength to the pump light [7]. From the laser rate equations, the generated light will be at a longer wavelength (lower energy) than the pump [7].

Additionally, dopants such as aluminium oxide (Al_2O_3) and phosphates are often added to core of active fibres to improve solubility of rare earth ions and preventing clustering [4].

This research focused on laser systems at a range of different wavelengths. Trivalent erbium ions were used to yield light at $1.5 \mu\text{m}$ (Chapter 3). To generate light near $2 \mu\text{m}$, transitions in trivalent thulium and holmium ions were used (Chapters 4 and 5 respectively). A schematic of the pumping schemes for erbium [10, 11], thulium [4, 12] and holmium [4, 13] is shown in Fig. 2.1.

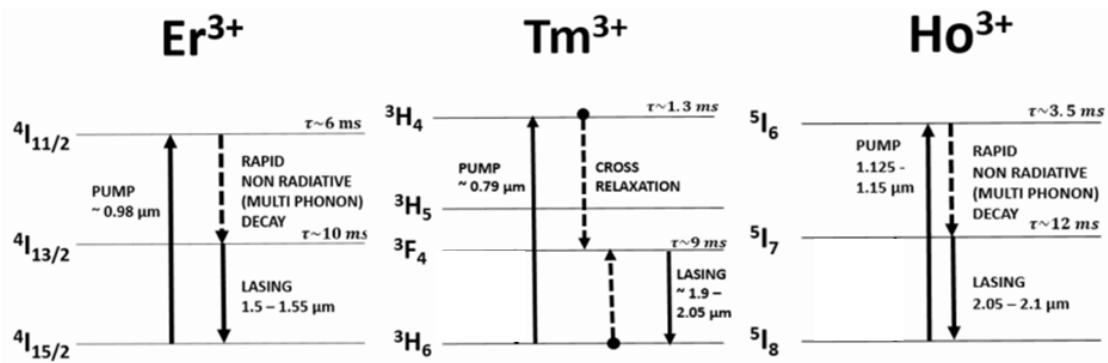


Figure 2.1: Energy level diagrams for trivalent erbium (Er), thulium (Tm) and holmium (Ho) ions in silica showing transitions that yield light around $1.5 \mu\text{m}$ and $2 \mu\text{m}$ [4, 10-13].

The gain medium has an associated gain profile that is representative of the stimulated emission cross-section of the medium [7]. The absorption and emission cross sections for erbium, thulium and holmium are presented in Fig. 2.2.

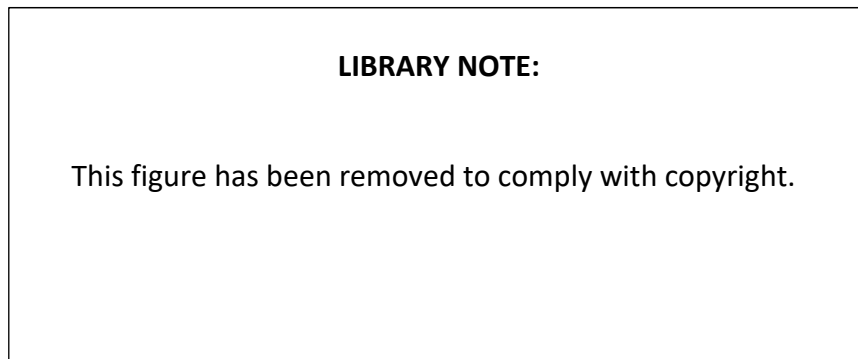


Figure 2.2: (a): Absorption and emission cross-section of erbium. Figure reproduced from [7]. (b): Absorption and emission cross-section of thulium and holmium. Figure reproduced from [13].

For this project, erbium ions were pumped at $0.98 \mu\text{m}$ to transition from the $4I_{15/2}$ state to the $4I_{11/2}$ state. A rapid, non-radiative decay results in a transition to the metastable $4I_{13/2}$ state. Non-radiative decays involve the release of energy in the form of phonons rather than electromagnetic radiation [14]. Lastly, erbium ions return to the scheme's ground state ($4I_{15/2}$) by emitting a photon with a wavelength of approximately $1.5 \mu\text{m}$.

The thulium transition used in this project is often utilised in highly-doped fibres [4]. Pumping at $0.79 \mu\text{m}$ results in a transition from the 3H_6 state to the 3H_4 state. A cross relaxation process is then exploited involving the exchange of energy between two ions. One excited state ion exchanges energy with a ground state ion resulting in both ions changing to the intermediate energy state (3F_4) [15]. A radiative transition back to the ground state results in a photon emission at around $2 \mu\text{m}$.

The scheme used to pump trivalent holmium ions in this project involved pumping at $1.15 \mu\text{m}$ [16]. Ions transition from the 5I_8 state to the 5I_6 state before decaying (through a non-radiative process) to the metastable 5I_7 state. A return to the ground state results in the emission of a photon with a wavelength around $2.1 \mu\text{m}$.

An alternate pumping pathway at $1.95 \mu\text{m}$ exists and has the benefit of a lower quantum defect. A quantum defect occurs due to the energy difference between pump and laser photons [16]. A larger quantum defect limits the power efficiency of a pumping approach [16]. Simplicity was the primary appeal of the $1.15 \mu\text{m}$ scheme presented in Fig. 2.1, as a range of compact and lightweight commercial diodes are available at that wavelength. Consequently, this specific scheme did not require noise from a pump laser to be fully characterised, as diodes often have excellent (known) stability compared to in-house thulium pump lasers at $1.95 \mu\text{m}$.

2.2.3 Pumping Schemes

There are two schemes for pumping a fibre laser – core and cladding pumping, as shown in Fig. 2.3. In the figure, black represents the pump light and red represents the output signal. A single mode fibre core is represented for both schemes.

Both the pump and signal light are generally launched into the fundamental mode in the core-pumped scheme. In the cladding pumped scheme, a multi-mode pump and single mode signal is represented. The diminishing thickness of the black arrows

represents the reduction in pump power [17].

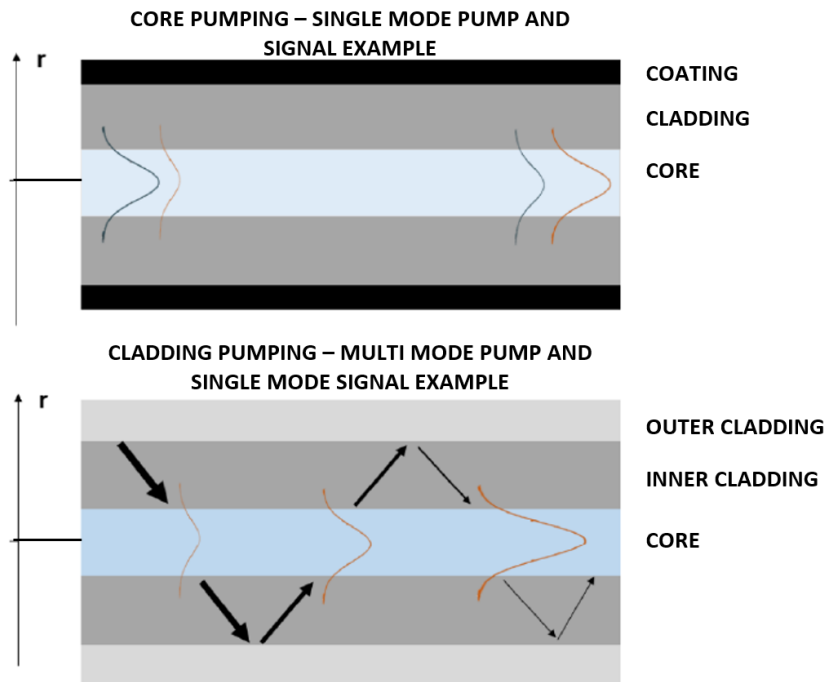


Figure 2.3: Refractive index profile and schematic of core-pumped (top), and cladding-pumped (bottom) fibre geometries. Black represents the pump input, and red represents the signal output. Pump light is converted to signal through transitions (as outlined in the previous section). Based off a similar image presented in [17].

Core pumping involves launching pump light into the core of the fibre. Pump light interacts with doped ions to generate an amplified signal. The signal and the pump light co-propagate through the core [17].

Cladding pumping utilises double-clad fibres that contain an inner and outer cladding. The outer cladding has a lower refractive index than that of the inner cladding. Light launched into the inner cladding is confined by the inner-cladding-outer-cladding interface [15, 16]. Pump light interacts with the signal when it propagates through the core [17, 18].

A summary of the advantages of each pumping scheme are presented in Table 2.3.

Table 2.3: Advantages of each of the pumping schemes.

Core pumped	Cladding pumped
<ul style="list-style-type: none"> ✓ Shorter fibre length needed so can reduce dispersion (discussed in Section 2.4.4) ✓ Higher inversion possible meaning lower noise [7] 	<ul style="list-style-type: none"> ✓ Enables high power applications as the pump light is of similar brightness to the generated signal [4, 17]

2.3 Polarisation

2.3.1 Polarisation States

Polarisation can be parameterised by a set of Stokes parameters [19]. A simple overview of polarisation and Stokes parameters is included in Appendix A.

The Poincarè sphere, shown in Fig. 2.4, is a representation for the polarisation state of a signal. It can be used to describe the polarisation of light or the transformation of a polarisation state. Any polarisation state can be uniquely represented by a point inside or on the surface of the sphere [30, 31]. Its three orthogonal axes are normalised Stokes Parameters (S_1 , S_2 , S_3). Linear polarisations are located along the equator, whereas circular polarisations are at the poles, as depicted in Fig. 2.4 [19, 20].

An arc or curve between two points on the sphere can represent a transformation in the polarisation state [20]. Stokes parameters can also be used as a diagnostic for assessing whether the laser output is pulsed or CW - as explored in Chapter 4.

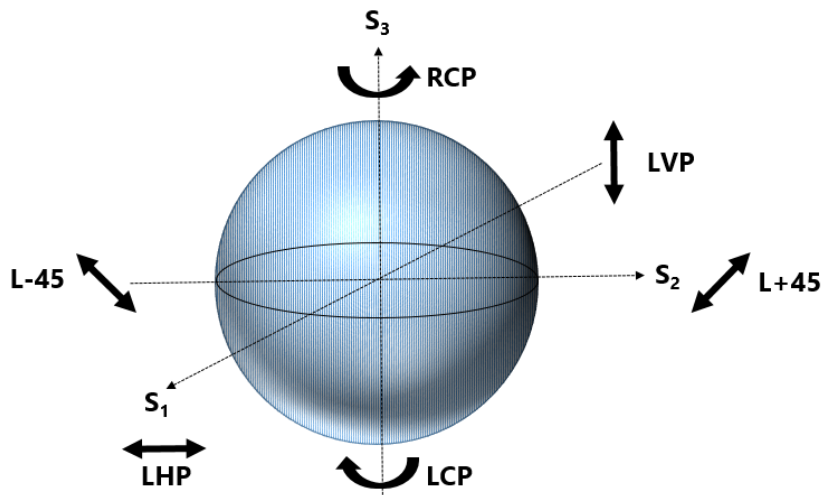


Figure 2.4: The Poincaré sphere with the three axes representing S_1 , S_2 and S_3 . Polarisation states at the poles and the equator correspond to circular and linear polarisations respectively. LCP = Left Circularly Polarised, RCP = Right Circularly Polarised, LVP = Linear Vertically Polarised, LHP = Linear Horizontally Polarised, L-45 = Linearly Polarised at -45° , L+45 = Linearly Polarised at $+45^\circ$.

2.3.2 Polarisation Controllers

Polarisation is sensitive to temperature and vibrational fluctuations. Additionally, it can be controlled/adjusted through induced birefringence, as will be demonstrated over the next few sections. Induced birefringence can be introduced to a cavity through applying strain to a fibre.

Several devices can be used to adjust the intra-cavity polarisation state of a fibre laser. Here we shall focus on two commercially available products.

A manual polarisation controller can introduce strain to a fibre using an actuator and fibre squeezer [21, 22]. Newport's manual fibre polarisation controller, as shown in Fig. 2.5, operates using the Babinet Soleil principle where one birefringent crystal is moveable and the other is fixed [21, 22]. Applying pressure to the fibre through the actuator induces a linear birefringence that is akin to a fibre waveplate [22]. The manual polarisation controller was used experimentally in an erbium NLPR laser (Chapter 3) and a thulium NLPR laser (Chapter 4).

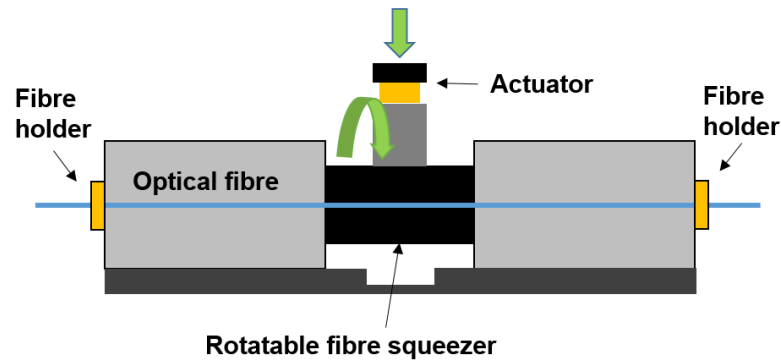


Figure 2.5: Schematic of the Newport manual polarisation controller. Image adapted from [22].

Electronic polarisation controllers can use voltage-driven actuators to introduce strain to a fibre. The General Photonics Polarite controller is one among many commercially available controllers [23]. It supports up to four independent channels for drive voltages. An accompanying piezoelectric driver supported three channels of 0-150V, so only three channels were used in experimentation [23]. Each of the channels on the driver corresponded to different intra-cavity actuators, as shown in Fig. 2.6. Each of the actuators is positioned to enable rotation about different axes and positions of the Poincarè Sphere. Squeezers 1 and 3 lead to clockwise rotation about the S_1 axis, and squeezer 2 leads to clockwise rotation about the S_2 axis. Voltages on the controller were configurable using knobs or via a BNC input [23].

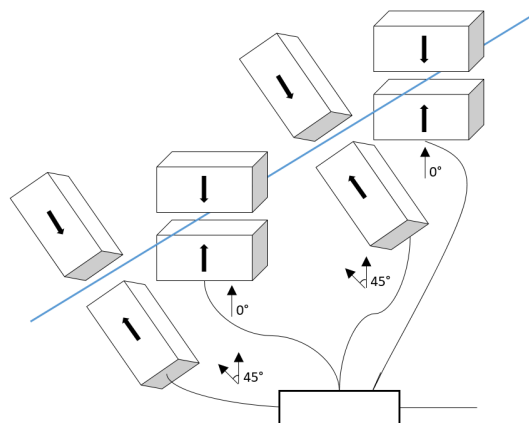


Figure 2.6: Schematic of the actuators inside the General Photonics electronic polarisation controller. Image adapted from [23]. Squeezers labelled from 1 (foreground) to 4 (background). Squeezer 4 was not included in the specific controller used in this project.

The electronic polarisation controller, with a custom-ordered fibre, was used experimentally in thulium (Chapter 4) and holmium (Chapter 5) NLPR mode-locked fibre lasers.

2.4 Optical Pulses

2.4.1 Introduction to Pulses

A pulse consists of a high-frequency carrier component and a broad envelope, as shown in Fig. 2.7. The envelope shape and phase of the pulse change at different rates while propagating.

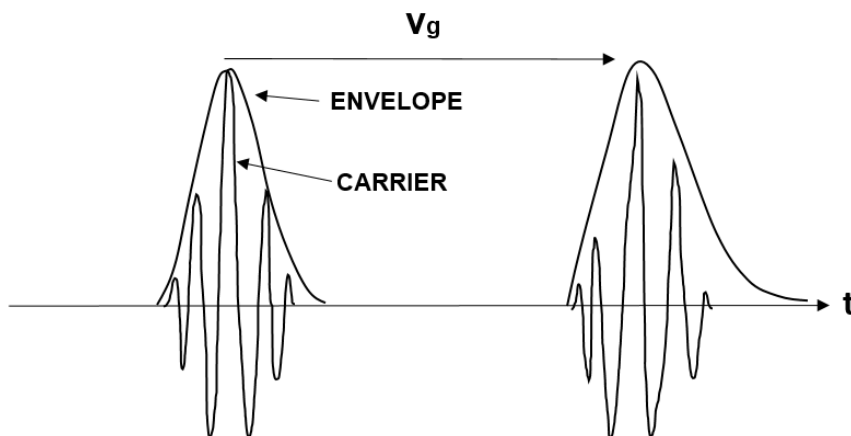


Figure 2.7: Carrier and envelope schematic for an optical pulse.

The speed of the envelope is the group velocity. Group velocity is the rate of change in the frequency of the wave, ω , with respect to its wavenumber, k . It can also be written in terms of group index, N , and the speed of light, c , as given in Equation 2.4 [7].

$$v_g = \frac{\partial \omega}{\partial k} = \frac{c}{N} \quad (2.4)$$

The wavenumber k can be related to wavelength λ by Equation 2.5.

$$k = \frac{2\pi}{\lambda} \quad (2.5)$$

For pulses, one often considers a central wavelength, λ_0 , and a central frequency, ω_0 . The group index is defined, in terms of λ_0 by Equation 2.6 [7].

$$N = n(\lambda_0) - \lambda_0 \frac{dn}{d\lambda_0} \quad (2.6)$$

where $n(\lambda_0)$ is refractive index at λ_0 and $\frac{dn}{d\lambda_0}$ is the rate at which refractive index changes as wavelength changes at a particular value of λ_0 [7].

Group velocity involves measuring the round trip time, τ , for a passive fibre of some length, L , as shown in Equation 2.7

$$v_g = \frac{L}{\tau} \quad (2.7)$$

Phase velocity is the rate of evolution of phase for the carrier component inside the pulse. It is given by Equation 2.8, where n is the refractive index of the medium [7].

$$v_p = \frac{c}{n} \quad (2.8)$$

The phase velocity differs from the group velocity [7]. It is calculated using the refractive index (rather than group index) and is often (not always) faster than the group velocity [7]. Over a 1 km distance in a silica medium, the difference in time taken for an object travelling at v_p compared to an object with speed v_g can be as much as 50 - 80 nanoseconds for NIR and MIR wavelengths. But it is important to recall that v_p is not a time of flight measure. What this result infers is that the phase of the carrier changes more than that of the envelope.

2.4.2 Time-Bandwidth Product

A Fourier transformation connects the temporal and frequency domains of optical pulses. Consequently, there is an inverse relationship between quantities (widths) - the temporal FWHM, τ , and the spectral FWHM, Δf .

Consequently, small temporal FWHM values manifest as large spectral FWHM values [7]. The converse is valid for a CW laser, which is spectrally narrow due to its broad temporal repetition features [24].

The product, $\tau\Delta f$, defined as the time-bandwidth product (TBP), depends on the pulses' profile. TBP can be expressed in terms of λ and c by Equation 2.9.

$$TBP = \Delta f\tau = \frac{\Delta\lambda c\tau}{\lambda^2} \quad (2.9)$$

The TBP has a limit, imposed by Fourier transformations, that depends on the shape of the pulse. Gaussian pulses have a limit of $\frac{2\ln 2}{\pi}$ (approximately 0.44), and hyperbolic secant squared pulses have a TBP limit of approximately 0.315 [24].

For example, a 1 ps (temporal FWHM) bandwidth-limited Gaussian pulse would have a minimum spectral width of 4.7 nm for $\lambda = 2 \mu\text{m}$ [7]. A pulse may not be bandwidth-limited due to chirp. Monotonically varying chirped pulses can be temporally compressed. Pulse durations are generally incompressible if the frequency is not monotonically varying. For example, a chirped 1 ps pulse can have a larger TBP than the limit [7].

2.4.3 Gain Bandwidth

Gain bandwidth is a phenomenon that can be explained using the gain profile (Section 2.2.2) and the time-bandwidth product (Section 2.4.2).

Gain narrowing can occur each time an optical pulse passes through a gain medium (active fibre) [7]. Different optical frequencies (wavelengths) experience different amounts of gain with a central wavelength experiencing the most amplification and the pulse's spectral wings experiencing the least [25]. Consequently, the width of the pulse's optical spectrum reduces every round trip [25]. As a result, optical pulse duration must increase if the pulse is near the time-bandwidth transform limit [25].

It should be noted that there are ways to configure a cavity to have no gain narrowing, although this is beyond the scope of this thesis.

Assuming a Gaussian fit, the pulse duration obtainable for a given gain bandwidth, $\Delta\lambda$, is given by Equation 2.10 [26].

$$\tau = \frac{2ln2}{\pi c} \frac{\lambda_a^2}{\Delta\lambda} \quad (2.10)$$

Here, λ_a is the central wavelength of the gain profile, and $\Delta\lambda$ is the wavelength FWHM of the line profile [26].

Gain bandwidths and the corresponding theoretical pulse duration, τ , are presented in Table 2.4.

Table 2.4: Table with gain bandwidth and corresponding pulse durations (Equation 2.10) for a range of rare-earth ion doped amplifiers – erbium, holmium and thulium.

Active dopant	Gain bandwidth, $\Delta\lambda$ (nm)	Central wavelength, λ (nm)	Pulse duration attainable, τ (fs)	Source ref
Er	80	1570	45	[27, 28]
Ho	100	2100	65	[29]
Tm	250	1900	20	[30]

Gain narrowing can be compensated in mode-locked fibre lasers. Introducing loss at the peak of the gain spectrum can offset the higher levels of gain. This modulation over the gain spectrum ensures that the pulse’s optical spectrum does not narrow considerably, which would temporally elongate pulses [26]. Additionally, non-linear effects (discussed in Section 2.5.3) provide gain that balances gain narrowing [26]. In practice, few-cycle (i.e. 1.3 cycles) erbium pulses have been demonstrated [31].

2.4.4 Dispersion

Dispersion is the temporal broadening of a pulse as it propagates through a medium [32]. It is a consequence of pulses consisting of multiple frequencies that experience different group velocities. Propagation phase constants, β , are parameters that describe dispersion. β_2 is the group velocity dispersion (GVD) parameter. It describes second-order chromatic dispersion effects in a waveguide that manifest as a result of different frequencies (that make up a pulse) propagating at different speeds [32]. β_2 can be quantified using Equation 2.11, where ω is optical frequency [32].

$$\beta_2 = \frac{1}{c} \left(2 \frac{dn}{d\omega} + \omega \frac{\partial^2 n}{\partial \omega^2} \right) \quad (2.11)$$

β_2 can take both positive and negative values. Its sign is indicative of the nature of pulse dispersion in a medium. Normal dispersion occurs for $\beta_2 < 0$ and hence

$\frac{\partial v_g}{\partial \omega} < 0$ [32]. The opposite is true for anomalous dispersion with $\beta_2 > 0$ and $\frac{\partial v_g}{\partial \omega} > 0$ [32].

Third-order (β_3) and higher-order dispersion coefficients also exist. Such coefficients impact the shape of a pulse – particularly near a zero-dispersion wavelength where there is a transition between normal and anomalous dispersion regimes [33].

Chromatic dispersion consists of two main constituents: waveguide and material dispersion [34]. Both constituents have a dispersion coefficient with units of ps/km/nm.

Material dispersion is the temporal spreading of a pulse due to interactions between light and the molecules in the medium through which light propagates [7]. It manifests from the optical frequency dependence in refractive index [34].

The increase in the pulse duration per unit length and unit bandwidth due to material dispersion is given by Equation 2.12 [34].

$$D_{material} = -\frac{\lambda_0}{c} \frac{d^2 n}{d\lambda_0^2} \quad (2.12)$$

Waveguide dispersion is caused by the geometry of the optical fibre through which the light is propagating. Interactions between light and the materials in the core and cladding of an optical fibre lead to a temporal distortion of a pulse [35].

The waveguide dispersion can be approximated by Equation 2.13 [35].

$$D_{waveguide} = -\frac{n_{cl}\Delta n V}{c\lambda} \frac{d^2}{dV^2}(\beta V) \quad (2.13)$$

where, β is a propagation constant for a particular mode, Δn is the refractive index contrast (difference between core and cladding), V is the V parameter and n_{cl} is

the refractive index of the cladding. $D_{\text{waveguide}}$ can take either positive or negative values.

A typical total dispersion curve for a standard single-mode silica fibre is given in Fig 2.8. The zero total dispersion crossing, at around $1.3 \mu\text{m}$, marks a transition between anomalous and normal dispersion regimes [35]. Minimum attenuation in silica fibres occurs around $1.5 \mu\text{m}$. Consequently, fibre optics that shift the zero-crossing wavelength are commercially available.

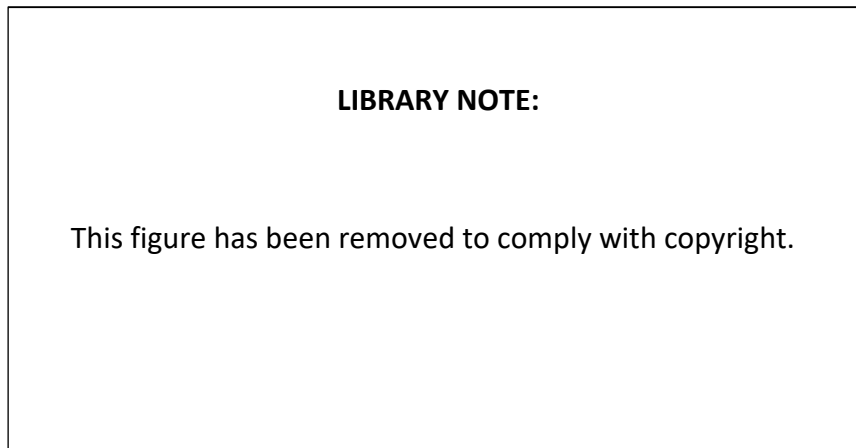


Figure 2.8: A plot of the material dispersion curve and waveguide dispersion curve for a silica optical fibre. Image initially presented in [36].

The sign and magnitude of group velocity dispersion (GVD) plays an important role in mode-locking. Mode-locked lasers with close to zero net dispersion are generally subject to less timing jitter and have larger spectral bandwidths [37]. Higher order dispersion does play a role near zero net dispersion.

2.5 Non-linear Effects

2.5.1 Non-linear Optical Propagation

In a linear regime, the polarisability, $P(\vec{r}, t)$, can be approximated by Equation 2.14, where \vec{E} is the incident electric field [32].

$$\vec{P}(\vec{r}, t) = \epsilon_0 \chi^{(1)} \vec{E}(\vec{r}, t) \quad (2.14)$$

Where ϵ_0 is the permeability of free space and $\chi^{(1)}$ is the first order susceptibility of a medium.

In non-linear regimes, the n^{th} order susceptibilities of a medium, $\chi^{(n)}$ become non-negligible. For an isotropic medium, such as silica glass, $\chi^{(2)} = 0$, however $\chi^{(3)}$ is non-zero. The polarisability can hence be approximated by Equation 2.15 [32]. Here, a scalar equation has been given. One could utilise this equation for a given direction in a fibre. The polarisability in different directions can be different, as will be seen shortly.

$$P(t) \approx \epsilon_0 [\chi^{(1)} E(t) + \chi^{(2)} E^2(t) + \chi^{(3)} E^3(t) + \dots] \quad (2.15)$$

These higher order terms in polarisability can lead to third harmonic generation (the generation of photons at $3\omega_0$ for a central frequency of ω_0) and also an intensity dependence in refractive index.

The Optical Kerr Effect is a refractive index change that manifests from the electric field of a light wave. This refractive index change has a dependence on intensity (total irradiance) of the light, as per Equation 2.16 [7, 38].

$$n(\lambda, |E|^2) = n_0(\lambda) + n_2|E|^2 \quad (2.16)$$

Here n_0 is the linear refractive index, n_2 is the non-linear refractive index (often called the Kerr coefficient) and $|E|^2$ is the square of the electric field amplitude (intensity) [17, 38]. A derivation for the Kerr coefficient in terms of the third-order, non-linear susceptibility is in Appendix B [32].

Not all parts of a pulse experience the same refractive index because intensity varies over the longitudinal/temporal profile of the pulse. A variable refractive index leads to a range of pulse propagation effects that alter a pulse's phase as it propagates down a fibre [32].

2.5.2 Non-linear Schrödinger Equation

The Non-linear Schrödinger Equation (NLSE) can be used to explain the evolution of an ultrashort pulse in a non-linear dispersive medium. One must first consider a standard wave equation in order to derive the NLSE [32]. The standard wave equation can have the non-linear and linear parts of the induced polarisation written as two separate terms (P_L and P_{NL}), as per Equation 2.17 [39].

$$\nabla^2 \vec{E} - \frac{1}{c^2} \frac{\partial^2 \vec{E}}{\partial t^2} = \mu_0 \frac{\partial^2 \vec{P}_L}{\partial t^2} + \mu_0 \frac{\partial^2 \vec{P}_{NL}}{\partial t^2} \quad (2.17)$$

Here μ_0 is the permeability of glass, which is similar to that of the permeability of air ($4\pi \times 10^7$ H/m).

The electric field propagating in the z-direction can be expressed in terms of wavenumber (k), time (t), position (\hat{r}) and frequency (ω) as per Equation 2.18. cc stands for complex conjugate [32].

$$\vec{E} = \frac{1}{2} \left(\vec{E}(\hat{r}) e^{i(kz - \omega_0 t)} + c.c \right) \quad (2.18)$$

where $\vec{E}(\hat{r})$ is the evolution of the optical field's slowly varying envelope. It is the product of the optical field amplitude in the longitudinal (propagation) direction ($\vec{A}(z, t)$) and the transverse direction ($F(x, y)$) that is perpendicular to the direction of propagation, and is given in Equation 2.19 [32, 39].

$$\vec{E}(\hat{r}) = F(x, y) \vec{A}(z, t) \quad (2.19)$$

A formal derivation of the NLSE involves solving eigenvalue equations, first-order perturbation theory and the slowly varying envelope approximation for the electric field amplitude (i.e. $\frac{\partial^2 A}{\partial z^2} \approx 0$) [39]. It relies on several simplifications and assumptions, as listed here:

- Non-linear polarisation contribution is assumed to be substantially less than the linear contribution – a reasonable assumption as non-linear refractive index changes are small relative to the linear refractive index.
- The weakly guiding approximation is valid. This assumes that the transverse refractive index contrast is small.
- Waves are also assumed to be quasi-monochromatic [32, 39]. This means that the spectral width ($\Delta\omega$) is smaller than the central optical frequency (ω_0) – true for most pulses except few-cycle pulses [32].
- Scattering in optical fibres (Rayleigh, Raman and Brillouin) is neglected, however these effects can be added if necessary [32]

Additionally, assuming no cross-coupling between polarisation modes, the amplitude, A , is a scalar. The final result is the NLSE, which is given in Equation 2.20.

Here, α is an attenuation coefficient of light in the fibre, and β_2 is the group velocity dispersion parameter (Section 2.4.4) [32, 39].

$$i\frac{\partial A}{\partial z} - \frac{\beta_2}{2}\frac{\partial^2 A}{\partial t^2} - i\frac{\alpha}{2}A + \gamma|A|^2A = 0 \quad (2.20)$$

The non-linear parameter, γ , is defined in Equation 2.21 and involves the effective mode area, A_{eff} .

$$\gamma = \frac{2\pi n_2}{\lambda A_{eff}} \quad (2.21)$$

In Equation 2.20, the second term on the LHS describes dispersion, the third term represents the loss, and the fourth term describes non-linearity [32].

For a non-PM fibre, a set of two coupled NLSEs are needed to describe the light field's temporal evolution. The non-linear term involves the phase shift between orthogonal polarisation modes in single-mode optical fibre [40]. This concept is introduced in Sections 2.5.4 and 2.5.5 when explaining cross-coupling and how it yields NLPR.

The coupled equations are given in Equation 2.22. The non-linear term on the RHS relates to cross polarisation modulation (CPM), which is explained in Section 2.5.4 [40]. Note the similarities between Equation 2.20 and 2.22.

$$\begin{aligned} \frac{\partial A_x}{\partial z} + \beta_{1x}\frac{\partial A_x}{\partial t} + \frac{i\beta_2}{2}\frac{\partial^2 A_x}{\partial t^2} + \frac{\alpha}{2}A_x = \\ i\gamma\left(|A_x|^2 + \frac{2}{3}|A_y|^2\right)A_x + \frac{i\gamma}{3}A_x^*A_y^2e^{-2i\Delta\beta z} \end{aligned} \quad (2.22)$$

$$\begin{aligned} \frac{\partial A_y}{\partial z} + \beta_{1y}\frac{\partial A_y}{\partial t} + \frac{i\beta_2}{2}\frac{\partial^2 A_y}{\partial t^2} + \frac{\alpha}{2}A_y = \\ i\gamma\left(|A_y|^2 + \frac{2}{3}|A_x|^2\right)A_y + \frac{i\gamma}{3}A_y^*A_x^2e^{2i\Delta\beta z} \end{aligned}$$

In Equation 2.22, $\Delta\beta$ accounts for the linear birefringence that optical fibres naturally exhibit due to differences between orthogonal polarisation modes [40]. It is given by Equation 2.23.

$$\Delta\beta = \beta_{0x} - \beta_{0y} \quad (2.23)$$

Where β_{0i} is the propagation constant of light in the fundamental mode in the i^{th} direction.

Additionally, β_1 accounts for polarisation mode dispersion as different polarisation components propagate with different velocities [40].

2.5.3 Self Phase Modulation

An optical pulse can modulate its phase due to the Optical Kerr Effect [7]. This phenomenon is known as self phase modulation (SPM) and manifests from the temporal dependence of intensity. A time-varying intensity creates a time dependent phase shift and can lead to pulse chirping. Chirp is the time dependence in a pulse's instantaneous frequency (ω) [41].

Consequently, an initially un-chirped optical pulse (i.e. one that has $\frac{d\omega}{dt} = 0$) can develop a chirp as it propagates due to SPM [32]. A central part of an initially unchirped pulse may develop a positive chirp, for example, as shown in Fig. 2.9.

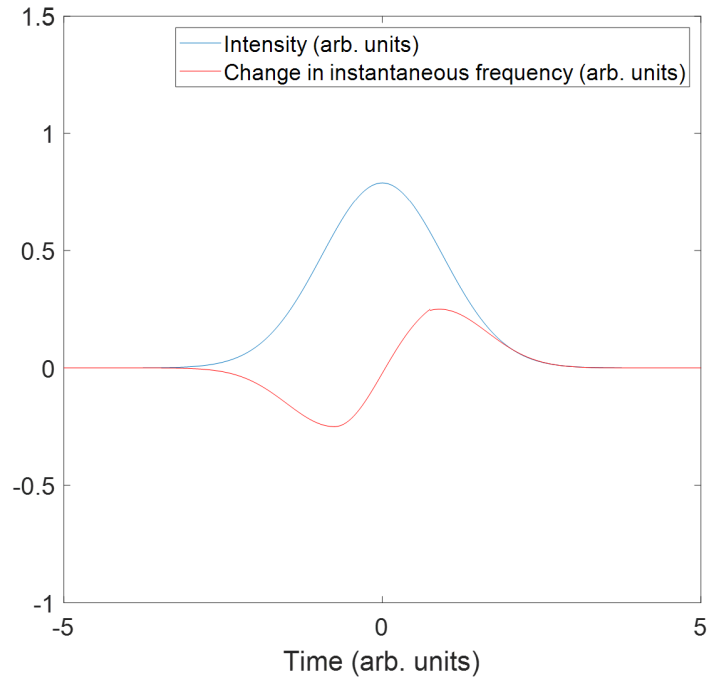


Figure 2.9: Temporal plot of pulse intensity for an initially unchirped pulse and the corresponding chirp it experiences due to self phase modulation. An upchirp is experienced at the centre of the pulse when $\frac{d\omega}{dt} = 0$. Note that the lower curve is the derivative of the upper curve. Image adapted from [7].

This ‘self-chirping’ process results in the formation of new frequencies introduced through four-wave mixing. New frequencies form because a differential phase shift takes place, and as $\Delta\phi = \Delta\omega\Delta t$, this implies that $\frac{\Delta\phi}{\Delta t} = \Delta\omega$.

A pulse subject to only SPM has an intensity profile that remains unchanged, but the pulse’s spectrum changes. Pulses, however, also experience GVD, which will lead to intensity profile changes due to newly introduced frequencies.

SPM can be counterbalanced by GVD. GVD occurs from the group velocity of light having a dependence on optical frequency and, unlike SPM, is not a non-linear effect. Solitons form when GVD and SPM are balanced in equilibrium [32]. A soliton is a pulse that maintains its temporal and spatial profile while propagating. Such behaviour is necessary to maintain pulse duration [38]. SPM sharpens pulses in the anomalous dispersion regime, whereas GVD acts to spread the pulse [41].

2.5.4 Cross Polarisation Modulation

In addition to a pulse modulating its own phase, orthogonally polarised components of light can interact and affect one another leading to cross polarisation modulation (CPM). In general, intense optical fields propagating down a fibre tend to have an arbitrary polarisation. It is hence necessary to analyse non-linear polarisation in terms of specific orthogonal polarisation components (x and y) [32, 40]. The electric field can hence be given by Equation 2.24, where cc stands for complex conjugate. Here, E_x and E_y are electric field amplitudes in the x and y direction respectively.

$$\vec{E}(\hat{r}, t) = \frac{1}{2}(\hat{x}E_x + \hat{y}E_y)e^{-i\omega_0 t} + cc \quad (2.24)$$

The scalar non-linear polarisation components, P_x and P_y , can hence be derived, using Equation 2.15, to yield Equations 2.25 and 2.26 [32, 40].

$$P_x^{(NL)} = \frac{3\epsilon_0}{4}\chi_{xxxx}^{(3)} \left[\left(|E_x|^2 + \frac{2}{3}|E_y|^2 \right) E_x + \frac{1}{3} (E_x^* E_y) E_y \right] \quad (2.25)$$

$$P_y^{(NL)} = \frac{3\epsilon_0}{4}\chi_{xxxx}^{(3)} \left[\left(|E_y|^2 + \frac{2}{3}|E_x|^2 \right) E_y + \frac{1}{3} (E_y^* E_x) E_x \right] \quad (2.26)$$

Consequently, by relating permittivity to refractive index, one can obtain an expression for the Kerr non-linear refractive index. The refractive index components for the orthogonal spatial co-ordinates are given in Equation 2.27 [32, 42].

$$n_{2x} = n_2 \left(|E_x|^2 + \frac{2}{3}|E_y|^2 \right), n_{2y} = n_2 \left(|E_y|^2 + \frac{2}{3}|E_x|^2 \right) \quad (2.27)$$

The first term of each expression is a contribution from the Optical Kerr Effect, covered in the last section. The second term of each expression depends on the intensity of the orthogonal polarisation component. Consequently, a coupling between orthogonal polarisation components is necessary for understanding non-linear pulse

propagation [32, 42]. CPM occurs in all fibres as two orthogonally polarised modes are supported and results in the refractive index of x and y polarised components of light differing, yielding a non-linear birefringence [40].

2.5.5 Non-linear Polarisation Evolution

An optical pulse has non-uniform intensity across its spatial profile [32]. Longitudinal and temporal intensity profiles often have the highest intensity at the centre of a pulse with lower power at the wings. The pulse experiences a non-linear temporal phase shift as it propagates through a length of non-PM fibre, as established throughout Section 2.5.3 and 2.5.4 [7, 32]. Consequently, polarisation states of different parts of the pulse evolve (rotate) to different extents, as depicted by Fig. 2.10. The peak of the pulse experiences the most rotation [41].

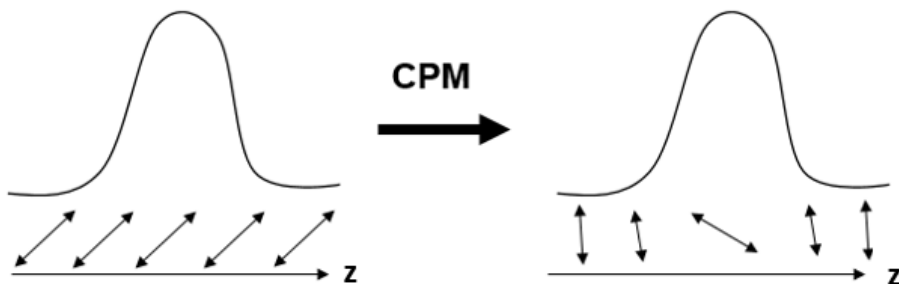


Figure 2.10: Graphic depicting polarisation rotation across the intensity profile of a pulse.

The amount of non-linear phase shift and rotation can be quantified. A polarised beam propagating down an optical fibre can be modelled by Equation 2.28. There are propagation constants (Section 2.4.4) for both orthogonal polarisation directions (β_x and β_y) due to non-linear birefringence (Section 2.5.4). Recall that $F(\vec{x}, y)$ is the amplitude of the envelope in the transverse propagation direction and $A(\vec{z}, t)$ is the envelope in the longitudinal direction (Section 2.5.2) [32].

$$\vec{E}(\hat{r}, t) = \vec{F}(x, y) [\hat{x}A_x(z, t)e^{i\beta_x z} + \hat{y}A_y(z, t)e^{i\beta_y z}] e^{-i\omega_0 t} \quad (2.28)$$

The two orthogonal components develop non-linear phase shifts that are readily obtained using Equation 2.27, which express the non-linear refractive index as the sum of an SPM and a CPM contribution. These phase shifts are given in Equation 2.29 [32, 38].

$$\phi_x = \gamma \left(|A_x|^2 + \frac{2}{3} |A_y|^2 \right) L, \phi_y = \left(|A_y|^2 + \frac{2}{3} |A_x|^2 \right) L \quad (2.29)$$

Obtaining the difference between the two components yields a relative phase difference between the orthogonal polarisation states, $\Delta\phi_{NL}$, due to CPM, as per Equation 2.30. The state of polarisation changes as this difference is non-zero [38, 40].

$$\Delta\phi_{NL} = \phi_x - \phi_y = \frac{1}{3}\gamma (|A_x|^2 - |A_y|^2) \quad (2.30)$$

NLPR and NALM mode-locked systems exploit this non-uniformity in polarisation states across a pulses' profile to mode-lock the cavity. An effective saturable absorber is produced in both cases [40].

2.6 Mode-locking

2.6.1 Introduction to Mode-locking

Mode-locking is a method to generate very short pulses with a high repetition rate. Pulses produced from mode-locking can be on the order of picoseconds or 10's of femtoseconds [43]. The repetition rate is governed by the length of the cavity as pulses are generally out-coupled once per round trip. This results in repetition rates on the order of MHz and GHz for cavities that have lengths of m and cm, respectively.

Laser cavities have modes separated by the free spectral range (FSR) [43]. These

modes are the result of the constructive and destructive interference of light propagating in a laser cavity [43].

The electric field can be written as a summation of the modes, as given in Equation 2.31 [41].

$$E(t) = \sum_{n=-N}^N E_n e^{i(\phi_n - \omega_n t)} \quad (2.31)$$

Here E_n , ϕ_n and ω_n are the amplitude, phase and frequency for the n^{th} mode [43].

For a multi-mode CW laser, there is typically no fixed phase relationship between any of the modes. Mode-locking occurs when longitudinal modes develop a phase relationship. The phase relationship becomes ‘locked’ as the phase difference between two neighbouring modes tends to some fixed value, ϕ_{ML} , as per Equation 2.32 [32].

$$\phi_n - \phi_{n-1} = \phi_{ML} \quad (2.32)$$

Consequently, the phase varies linearly with mode number due to the constant phase relationship, as given in Equation 2.33 [32, 43].

$$\phi_n = n\phi_{ML} + \phi_0 \quad (2.33)$$

Mode frequency for the n^{th} mode can hence be written in terms of the difference in frequency between modes, Δf , as given in Equation 2.34 [32, 44].

$$\omega_n = \omega_0 + 2n\pi\Delta f \quad (2.34)$$

Using a top hat approximation to assume that all modes have the same amplitude,

E_0 , the total intensity can be given by Equation 2.35 [32].

$$|E(t)|^2 = \frac{\sin^2 \left[(2N + 1)\pi\Delta ft + \frac{\phi_{ML}}{2} \right]}{\sin^2 \left(\pi\Delta f + \frac{\phi_{ML}}{2} \right)} E_0^2 \quad (2.35)$$

Equation 2.35 implies the CW energy is ‘forced’ into ultrashort pulses in the temporal domain. The resulting intensity is periodic with a period of $\frac{1}{\Delta f}$ [32]. Recalling that Δf is related to the FSR, the repetition time depends on the optical length of the cavity. The time taken for light to complete one round trip of the cavity is the round trip time, T_R [32]. Consequently, Equation 2.35 is analogous to having a single circulating pulse outcoupling part of its energy at intervals of T_R [32].

A continuously mode-locked (CML) regime occurs when:

- the output pulse energy does not vary with each round trip [7]
- the time between pulses is consistent with how long it takes light to propagate through the cavity
- all power is concentrated within the pulse (i.e. there are no persistent CW offset or noisy satellite pulse features) [7].

The pulse width is, approximately, the reciprocal of the gain bandwidth for all phase-locked modes [32]. Such a result is consistent with what one would expect from a Fourier transformation [7].

Mode-locked pulses are most stable when they form a soliton, discussed in Section 2.5.2. Consequently, any non-linear effects such as self-phase modulation (SPM) must balance GVD to obtain stable pulsing [42, 45]. This means GVD must take a small range of non-zero values to obtain soliton-like stability. Too much or too little GVD can lead to the tendency to generate multiple soliton pulses or the formation of incoherent pulses due to pulse-shaping issues [42, 45].

2.6.2 Non-linear Polarisation Rotation Mode-locking

NLPR in fibre lasers exploit the rotation of polarisation states to yield ultra-short optical pulses. Typical NLPR laser cavity designs consist of at least one polarisation controller, non-PM fibre and a polariser, as shown in Fig. 2.11 [7]. Non-PM fibre allows for non-linear phase shifts to occur during propagation. In essence, NLPR exploits the fact that the polarisation controller (either electronic or manual, as discussed in Section 2.3.3) can be configured in such a way that the central part of the pulse is linearly polarised when passing through the polarising element [41]. The element that provides polarisation discrimination, and hence enables mode-locking, is usually a linear polariser, non-PM isolator with an inline polariser or a PM isolator. For a ring cavity, an isolator is often used to ensure unidirectional light propagation [46].

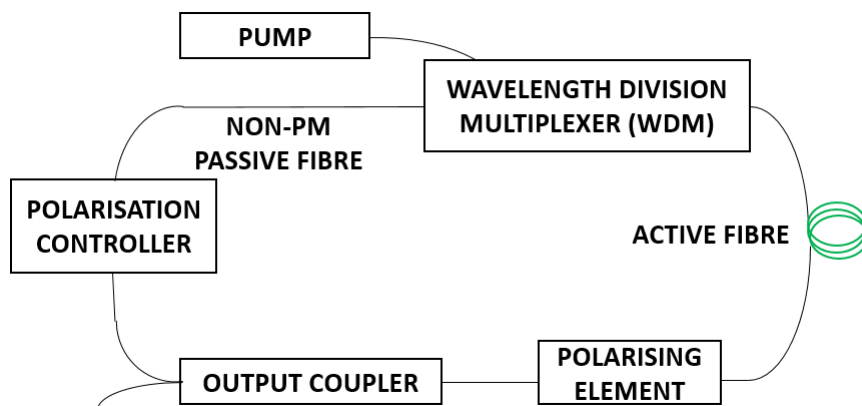


Figure 2.11: A general (theoretical) schematic for a NLPR mode-locked fibre laser. Non-PM passive fibre is spliced between all components and is spliced to the active fibre. An in-line polariser could be used in lieu of an isolator as the mode-locking element.

For an ideally-configured system, the most intense part of the pulse (the centre) is linearly polarised and can be extracted/outcoupled after the polarising element. This is the case as the high intensity, low loss configuration is favoured [41]. Wings of the pulse, which are not linearly polarised, are trimmed as they experience more considerable losses at the isolator [41, 46].

Environmental stability is one of the challenges with NLPR, as mentioned in Section 1.3. A sufficiently long length of non-PM fibre is required to yield a sizeable non-linear phase shift. Longer lengths of fibre are also more susceptible to vibrational fluctuations [41, 46]. Vibrations perturb polarisation and can lead to a drift or transition away from the optimum cavity configuration [46].

2.7 NLPR Regimes

This section presents a variety of temporal traces acquired from the lasers introduced in Chapters 3, 4 and 5 while operating in different regimes.

Recall, from Section 2.6.1, that a laser is continuously mode-locked (CML) if:

- the output pulse energy does not vary with each round trip [7]
- the time between pulses is consistent with how long it takes light to propagate through the cavity
- all power is concentrated within the pulse (i.e. there are no persistent CW offset or noisy satellite pulse features) [7].

An example temporal trace of a CML laser regime is presented in Fig. 2.12. The CML regime is often considered an ideal regime for most applications, although some applications such as machining have found benefit from other regimes [7]. For the purpose of this research, and in context of seeding an amplifier, the CML state is considered ideal and other regimes are considered as competing and non-ideal.

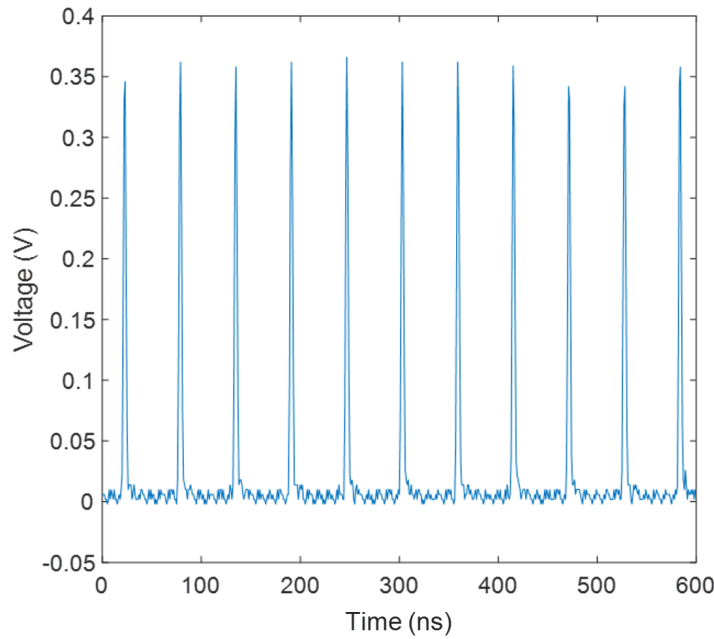


Figure 2.12: Temporal trace of a CML laser output

Several prominent regimes are observed for an NLPR laser when it is not CML.

These include:

- Q-switched mode-locked (QML)
- Multi-pulsed mode-locked (MPML)
- Background CW (non-pulsed)
- Continuous mode-locking with a CW component (CMLCW)

2.7.1 Q-switched Mode-locked

Unlike CML regimes, Q-switched mode-locked (QML) regimes have pulse trains whose amplitudes are modulated in the time domain, as shown in Fig. 2.13. Picosecond or femtosecond pulses are constituents of a much wider modulation envelope (μs or ms duration) [47]. QML regimes result from sizeable intra-cavity energy oscillations [7]. The regime occurs when there is a small increase in pulse

energy from a steady-state value resulting in absorber saturation [47]. For NLPR, the absorber is the polarising element, which can consist of a combination of non-linear fibre sections, waveplates and polarising elements [47]. Pulse energy grows exponentially until it is stopped when a certain level of gain saturation is reached [7].

In practice, QML regimes are most prevalent when weakly pumping a mode-locked laser. Low average power in the cavity makes it difficult to enter a stable CML regime [7]. This concept is discussed more in Section 6.3.2.

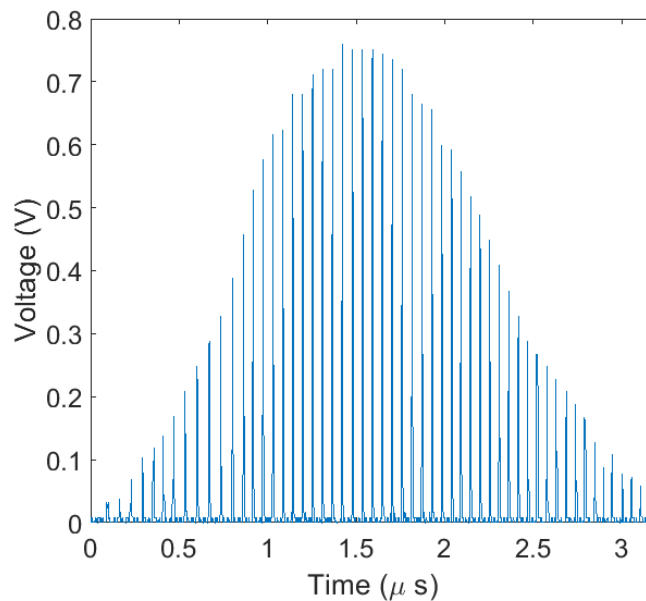


Figure 2.13: Temporal trace of a QML laser output

2.7.2 Multi-pulsed Mode-locked

Multi-pulsed mode-locking (MPML) occurs when multiple pulses are out-coupled from the cavity per round trip, as shown in Fig. 2.14. This results in multiple pulse trains that repeat at the PRF of the laser cavity. MPML regimes can be both stable (a mathematical solution to the Ginzburg-Landau equation) or unstable.

Stable MPML regimes out-couple light at fractions of τ . They are prevalent when

pulse power becomes high, and optical pulse frequency spans a wide range. Consequently, the circulating pulse splits into multiple pulses that can find a stable solution.

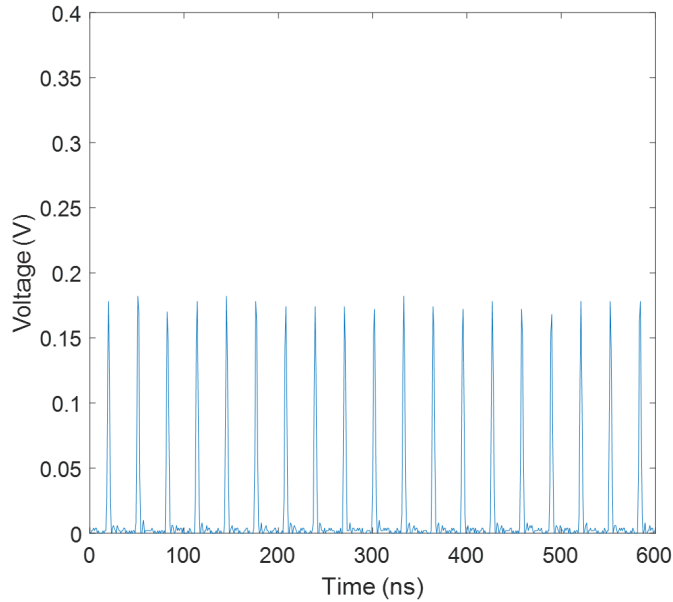


Figure 2.14: Temporal trace of a stable MPML laser output where pulses are out-coupled twice per round trip

NLPR dynamics and non-linear wave propagation can be modelled by the complex cubic-quintic Ginzburg-Landau (GL) equation. This equation describes many of the effects mentioned above (including SPM and CPM), bandwidth-limited gain saturation and cavity attenuation [48].

The GL equation has stationary solutions for double pulsed, triple pulsed and n^{th} order pulsing regimes [32, 48]. Cavity gain determines when solutions are prevalent. Multi-pulsing can be energetically favourable when a threshold gain is exceeded, leading to multiple pulses of smaller bandwidth [48].

Unstable MPML regimes are not stationary solutions of the GL equation. They are often transient and occur when a circulating pulse splits to yield another pulse train that is of lower power, as shown in Fig. 2.15. Spurious reflections from components in the cavity are a leading cause for this regime [49].

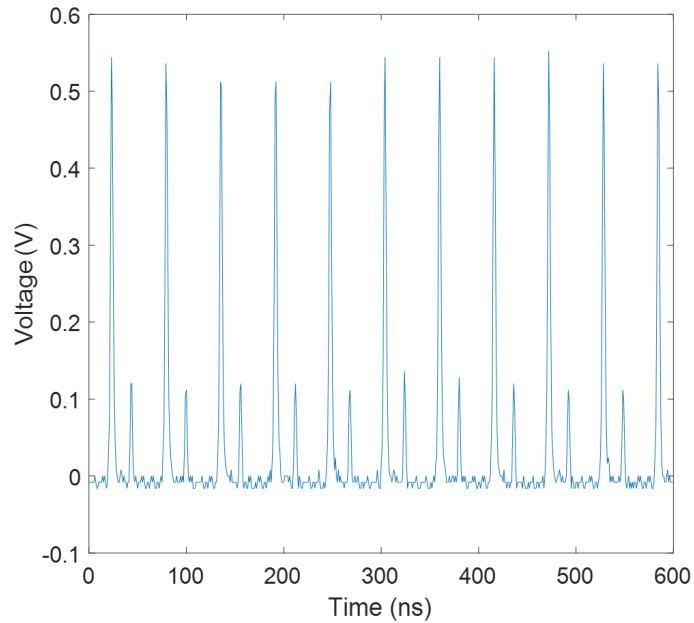


Figure 2.15: Temporal trace of an unstable MPML laser output

2.7.3 Background CW (non-pulsed)

Background CW regimes occur when the output power is effectively constant with time - implying that a pulse is not circulating in the cavity. Power is distributed over a larger time interval than a typical mode-locked pulse yielding an out-coupled signal of roughly constant average power [7]. The power level of the background CW signal is substantially lower than the peak power of optical pulses in a CML regime for a given pump power as the intra-cavity energy is effectively fixed [7]. A large amount of the polarisation parameter space operates CW as there is no valid pulsed solution to the GL equation [48].

2.7.4 Simultaneous CW and Continuously Mode-locked

CML regimes can have a persistent CW component in the time domain (CMLCW) that manifests as a result of intra-cavity energy bundling at some point slightly rather than being dispersed throughout the entire cavity. This behaviour often occurs in the transition from a CW to a CML regime and yields a temporal output

shown in Fig. 2.16. Regions of a slightly higher power often occur with a repetition rate consistent with the round trip time of the cavity.

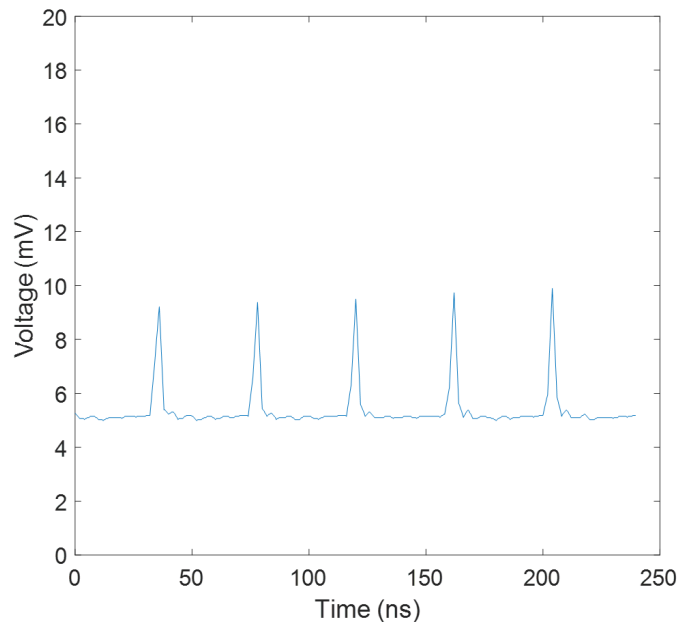


Figure 2.16: Temporal trace of a CMLCW laser output

Experimentally, both stable and unstable CMLCW regimes exist. Small pulse maxima can be observed in the temporal domain with a substantial CW background. Subtle adjustments to the intra-cavity polarisation state (using actuators) can increase the peak power of the pulses at the expense of the CW background power level.

Noisy CMLCW behaviour often occurs in the transition between a background CW and a CML regime, as shown in Fig. 2.17 and Fig. 2.18. Pulses manifest on top of the CW optical signal with pulse-like features that may or may not be separated by the cavity's PRF. The pulse train temporal output for these regimes is rarely reproducible.

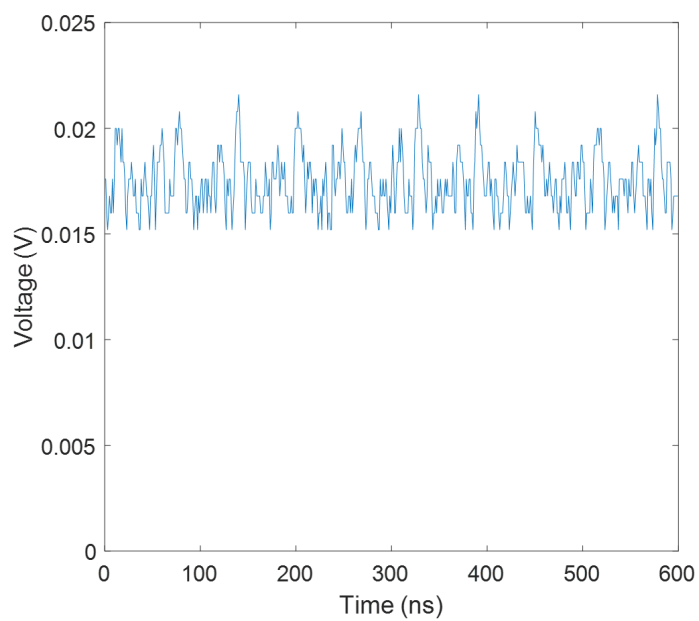


Figure 2.17: Temporal trace of a noisy CMLCW laser output

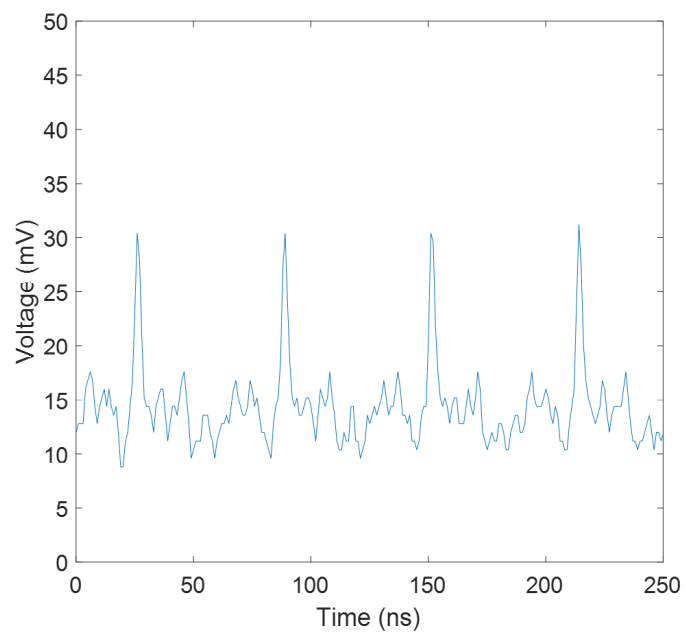


Figure 2.18: Temporal trace of another noisy CMLCW laser output

2.8 Summary

Several fundamental concepts were discussed in this chapter including fibre geometry, linear propagation, non-linear effects in optical fibres, pulse propagation and dynamics, and NLPR mode-locking. These ideas are necessary over the next few chapters with understanding how the constructed NLPR sources operate. The flowchart, Fig. 2.19, shows how these ideas are connected to one another. Notably, the idea of polarisation control is important as having the flexibility to finely control the polarisation is what enables the NLPR mode-locking results over the next three chapters. The next chapter focuses on the types of measurements needed to characterise the output of mode-locked lasers.

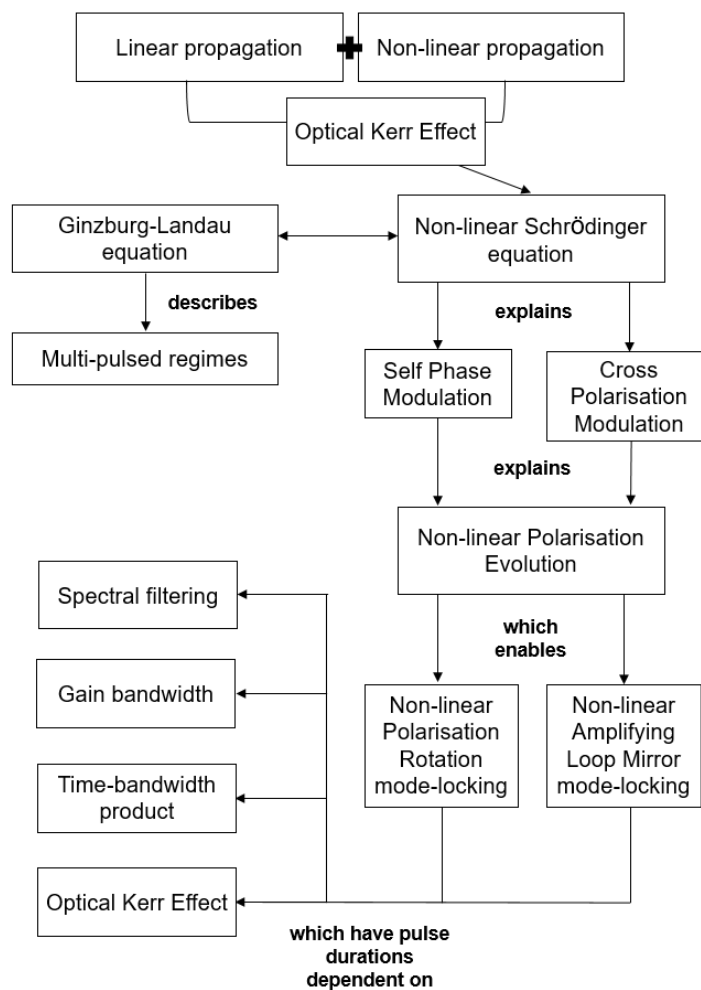


Figure 2.19: Flowchart outlining the connection between physical concepts and NLPR mode-locking, which forms the basis for the background information presented in this chapter.

Chapter 3

Mode-locking Measurement Techniques

3.1 Introduction

Mode-locked erbium fibre lasers at 1550 nm are vital for a range of applications including, but not limited to, atomic clock timekeeping, metrology, optical telecommunications and medical diagnostics [1,2].

This chapter focuses on the role that measurement techniques play in confirming that a laser is in a stable, continuously mode-locked (CML) state. Characterisation involves complementary frequency and time domain measurements to determine the lasing regime. Polarisation domain measurements involving Stokes parameters provide additional insight, as discussed in Section 4.4.2.

The aim of Chapter 3 is to understand how diagnostic measurements from multiple pieces of equipment can be used to quantify the lasing output of an NLPR source. In particular, we seek to focus on the differences between the measurements taken in stable and unstable pulsing regimes.

All data in this chapter was recorded using an in-house built erbium non-linear polarisation rotation (NLPR) fibre laser, as described in Section 3.2. An erbium source was selected because it could be readily core pumped using a range of commercially-available diodes and also because linear polarisers at $1.5 \mu\text{m}$ had greater extinction ratios than those for $2 \mu\text{m}$. It was thus anticipated that the laser could be stably mode-locked with relative ease and, potentially, with less competing and non-ideal regimes than at other wavelengths. This made it a good source for familiarisation with a range of measurement techniques.

An overview of the diagnostics investigated in this chapter is also described in Section 3.2. Examples of the information provided by an oscilloscope, radio-frequency (RF) spectrum analyser, optical spectrum analyser and an autocorrelator for CML, Q-switched mode-locked (QML) and multi-pulsed (MPML) mode-locked regimes are presented and discussed in Section 3.3. Additional diagnostics, including two photon absorption, will be explored in Chapter 4.

3.2 Erbium Fibre Laser

3.2.1 Cavity Configuration

A schematic of the erbium-doped fibre laser (EDFL) cavity is presented in Fig. 3.1. A 976 nm (Thorlabs BL976-PAG900) diode-pumped a 2 m length of the active fibre via a 980/1550 nm non-polarisation-maintaining (non-PM) wavelength division multiplexer (WDM). The diode operated over a current range of 400 – 800 mA (200-600 mW) producing output powers of up to 85 mW from the NLPR laser. The erbium fibre had a $6 \mu\text{m}$ core diameter, an Er^{3+} doping concentration of 0.3 wt.% and a 0.15 NA.

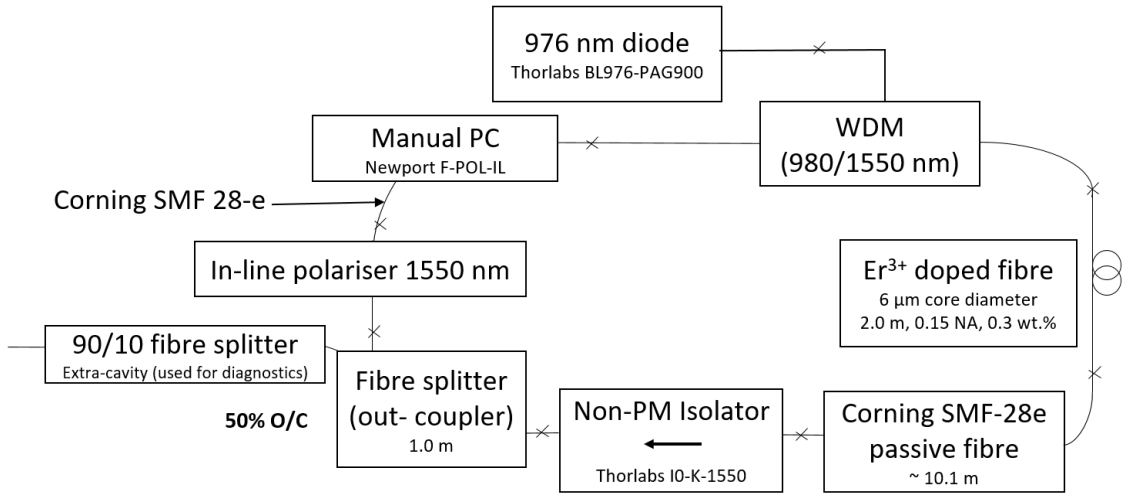


Figure 3.1: A schematic of the NLPR mode-locked EDFL cavity. WDM = wavelength division multiplexer, PC = polarisation controller and x marks the position of splices or fibre connectors.

The output of the active fibre was coupled into a non-PM passive fibre (Corning SMF-28e) passing through an isolator (Thorlabs IO-K-1550), an in-line polariser (Australian Fibre Works ILP-15-L-1-7-2-SA), that acted as the mode-locking element, and a manual polarisation controller (Newport F-POL-IL) [3]. The total fibre length of the cavity was estimated to be 12.1 m. A 50% output coupler was used.

Birefringence was adjusted using the Newport manual polarisation controller, which employs the Babinet-Soleil compensation mechanism to generate any polarisation state from an arbitrary input [3]. An actuator and rotatable fibre squeezer introduced strain to the fibre [4]. Altering the birefringence and changing pump powers enabled transitions between CW, QML, CML and MPML regimes, which were introduced in Section 2.7.

3.2.2 Characterisation Overview

The output of the NLPR EDFL was characterised using the diagnostics shown in Fig. 3.2. A 90/10 fused coupler (splitter) separated the output power into different components. The majority of the out-coupled power (90%) was launched into an

autocorrelator (APE Berlin, PulseCheck 150) via a parabolic mirror and a wire grid polariser. The wire-grid polariser would have added a small amount of dispersion to the pulsed output (due to the transparent substrate that the wires are suspended on) however this would have been relatively minimal given the thickness of the polariser.

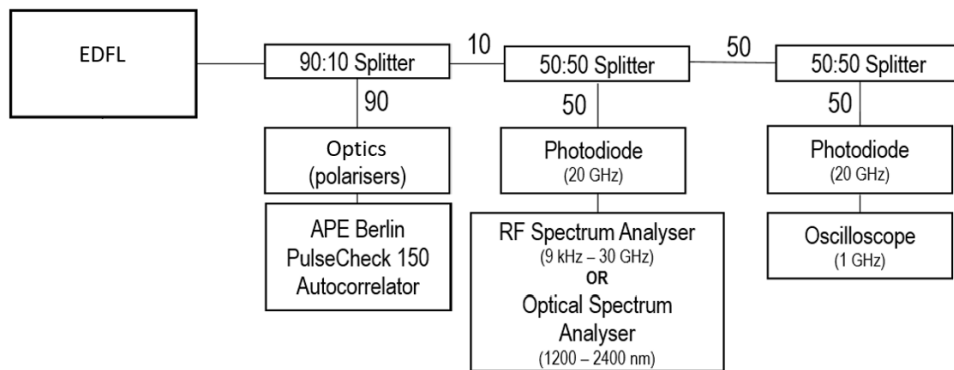


Figure 3.2: Diagnostics used for characterisation of the mode-locked EDFL. Connections from the laser are optical fibre splitters which launch light into the diagnostic instruments. The output of the second 50% splitter was beam dumped. The photodiode in the second arm was removed when using the OSA.

A parabolic mirror collimated light exiting the fibre and the polariser ensured that light from the output of the ring cavity was the correct orientation for phase matching with the autocorrelator. An optimum input polarisation for the autocorrelator was found by maximising the autocorrelation signal. Power meter measurements with a fibre beamsplitter revealed that the laser output was approximately 97% linearly polarised after passing through an additional 50 cm of extra-cavity fibre splitters to reach the diagnostics. Verification of the input polarisation was also confirmed using a Rochon prism.

The remaining 10% component was further split and launched into photodetectors connected to both an RF spectrum analyser (Rohde & Schwarz FSP30, 30 GHz) and a 100 MHz bandwidth oscilloscope (Rigol DS1102E, 1 Gs/second, 1 million record points). The photodetectors used were wideband extended-InGaAs photodiodes (Discovery Semiconductors, PD20, LabBuddy DSC2 (AC coupled), 20 GHz). An optical spectrum analyser (Yokogawa AQ6376) was also used to measure the optical

spectrum of the output and was connected in lieu of the photodetector/RF spectrum analyser after the necessary measurements were taken.

Other useful characterisation measurements, beyond the scope of this particular characterisation, include a ‘Frequency Resolved Optical Gating’ (FROG) trace which can be used to determine a unique intensity and phase profile for the pulse, as discussed in Appendix D [5,6,7].

3.3 Results

3.3.1 Temporal Characterisation

The temporal traces produced by the oscilloscope can be used as a preliminary tool to observe whether the laser is producing a pulsed output. Photons incident on a photodetector excite electrons in a material (such as extended InGaAs or silicon) to form an electron-hole pair [8]. The photocurrent produced generates a voltage signal that is proportional to the incident light power. While the bandwidth of the photodiode sensor and oscilloscope limits the resolution of the temporal measurements, the energy associated with the pulse is always captured in the trace provided the following conditions are met [9]:

- The incident light does not saturate the detector
- The regime across the entire pulse is linear
- There is no aliasing of the signal
- There are a sufficient number of points across the shape of the pulse

The polarisation parameter space of the laser predominantly consisted of regimes with CW operation; however, by changing the strain, one could obtain linear polarisation at the centre of the pulse (the condition needed for pulsed operation).

A CML pulse train observed on the oscilloscope is presented in Fig. 3.3. It reveals a small random amplitude variation (8%) over eleven consecutive peaks. There were no noticeable satellite pulses above the noise floor of the instrument. Extended time bases reveal a continuous train with no prominent amplitude modulation. Amplitude roll-off did not exceed 10% over twenty consecutive pulses. An enlarged trace of the signal noise between each out-coupled pulse is presented in Fig. 3.4.

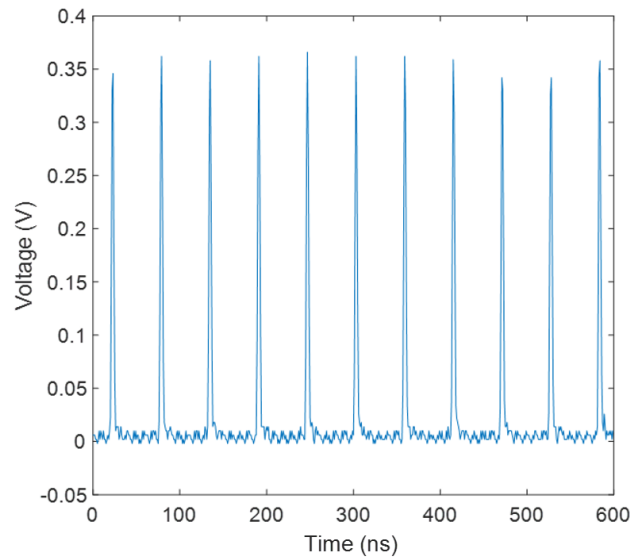


Figure 3.3: Oscilloscope trace of pulse train output in a CML regime. Amplitude variation between subsequent pulses was around 8% over eleven pulses.

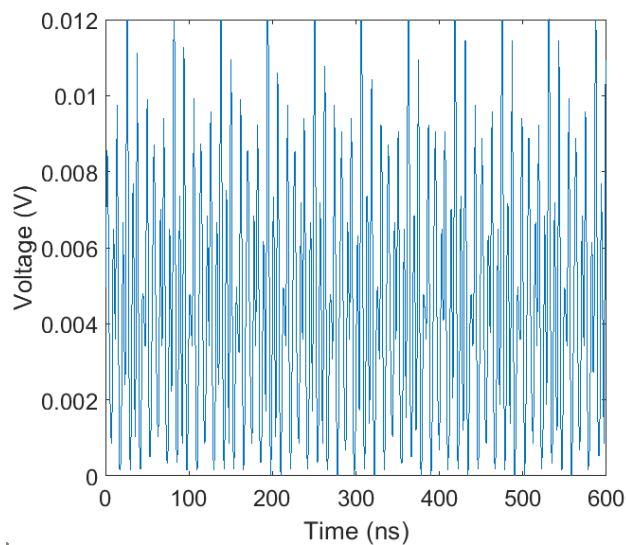


Figure 3.4: Oscilloscope trace of noise between pulses. Periodic patterns are evident albeit small, indicating fairly good stability.

This figure revealing the noise has the same time-span as Fig. 3.3 with pulses extending beyond the vertical axis in Fig. 3.4. Contributions to this noise include:

- Imperfect mode-locking of the laser signal
- Periodic noise from the oscilloscope
- Photodiode response and ringing effects

Tweaking the pump laser diode current and manual polarisation controller forced the laser into a QML regime. A trace of the Q-switched mode-locked envelope is shown in Fig. 3.5.

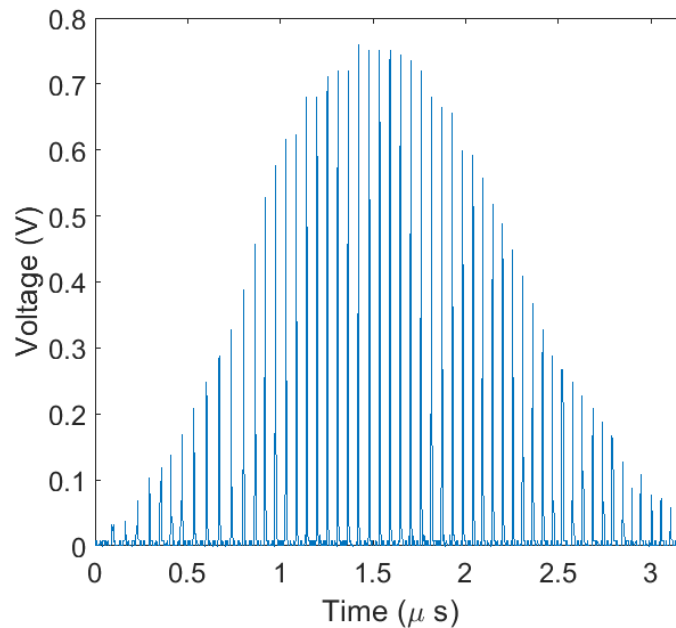


Figure 3.5: Oscilloscope trace of pulse train output in a QML regime.

Pulses that are further from the centre of the envelope have significantly lower peak power [10]. The primary difference lies in amplitude modulation over a train of many pulses, which becomes apparent in Fig. 3.5. Additionally, the average power of the QML regime varies with time more than the CML regime due to the oscillatory nature of intra-cavity energy in this regime.

Each Q-switched envelope had a temporal FWHM of approximately $1.5 \mu\text{s}$. The duration between pulse envelopes was found to vary with a peak-to-peak separation of $5 - 10 \mu\text{s}$. It was often the case that the envelope structures were asymmetric and the regime is unstable.

Further tweaking of the intra-cavity polarisation state and the pump current led to a persistent satellite MPML regime, as shown in Fig. 3.6. It is apparent from both Fig 3.6 and 3.7 that the MPML is continuous, but the amplitude of the satellite pulses also varies. Amplitude variation across pulses in the temporal domain was around 9% over 11 consecutive pulses. The lag time, between secondary (satellite) pulses and the primary pulse train, also varied slightly.

The MPML regime observed was unstable and would only persist for a few seconds at a time. Unlike stable MPML regimes, discussed in Chapter 2, the satellite pulse was transient. Satellite pulses maintained a separation that was approximately consistent with the PRF, however the time interval between primary and satellite pulses varied.

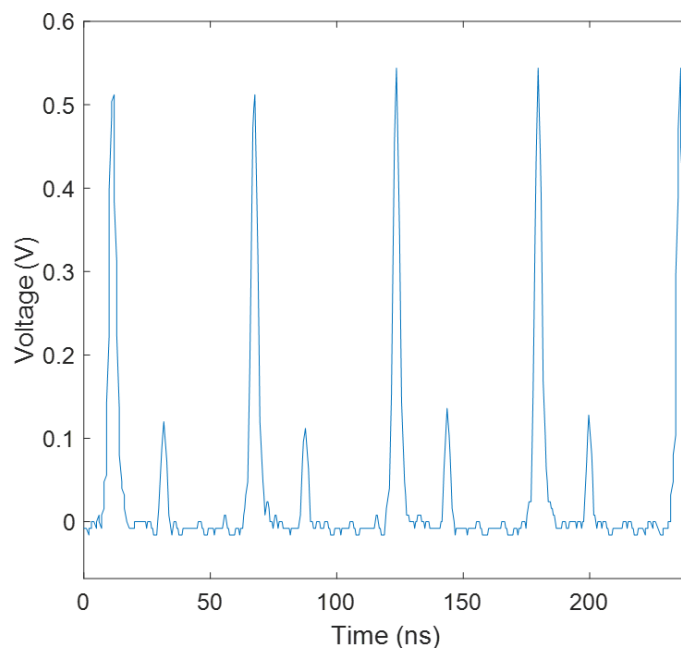


Figure 3.6: Oscilloscope trace of pulse train output in a MPML regime.

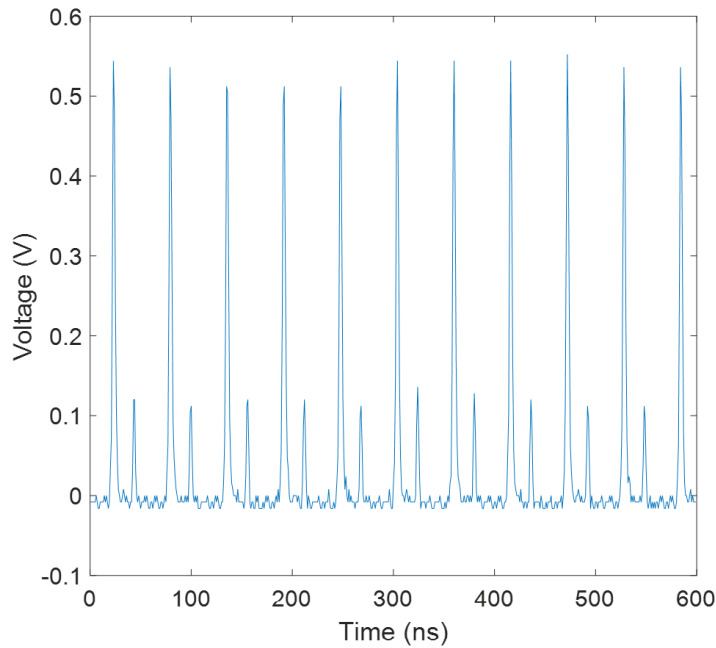


Figure 3.7: Oscilloscope trace of pulse train output in a MPML regime. Amplitude variation between subsequent pulses was of the order of 9% over eleven pulses.

In summary, different oscilloscope timebases can be used to explore different parts of the output train. A short time base, sufficient to observe three to five consecutive pulses, was used to look for any signs of satellite pulses or excess noise between pulses. This is limited, however, by the resolution of the oscilloscope (i.e. to within a couple nanoseconds).

Extended time bases, adequate to observe a dozen or more pulses, were used to look for a CW component to the optical signal output. The oscilloscope's main experimental benefit is the quick feedback it provided when attempting to manually bring the fibre laser into a pulsed state [11]. It cannot determine whether a laser is in a CML state alone due to the discretisation of voltages and the finite sampling rate of the instrument.

3.3.2 Radio Frequency (RF) Spectrum

The Fourier transform of the temporal signal, as displayed by an RF spectrum analyser, is also useful for diagnosing the pulse train [12].

Fast Fourier transform (FFT) analysers (such as Rohde and Schwarz FSP 30) use the Fourier connection between the temporal and RF domains to display the RF spectrum. The signal from the photodetector output is fed into an RF spectrum analyser using an SMA cable. A low-pass filter removes high frequencies that lead to aliasing. The filter is adjusted based on the Nyquist frequency, which depends on the chosen sampling rate (samples/second) [13]. The filtered signal is then sampled using an analogue to digital converter. An analyser calculates the corresponding FFT amplitude and phase [13].

Spectrum analysers have two important bandwidths - resolution bandwidth (RBW) and video bandwidth (VBW). RBW is related to the input bandpass filter's response curve. A narrower response curve yields better frequency resolution but also increases the sweep time [14]. The VBW is related to the video filtering applied to a signal when it is processed. Smaller video bandwidths, controllable via a low-pass filter, smooth out a noisy trace [14].

Mode-locked lasers generate pulses separated by round-trip time of the laser cavity, T_{rep} , as per Equation 3.1,

$$T_{rep} = \frac{LN}{c} \quad (3.1)$$

where L is the round trip length, c is the speed of light in a vacuum and N is the group index – related to the envelope propagation speed, as per Section 2.4.1 [14].

The Fourier transform of such a pulse train yields a frequency comb with separation given by the pulse repetition frequency (PRF). The PRF is the reciprocal of T_{rep} .

A Fourier transform of an ideal (CML) pulse train consisting of regularly spaced ultra-short pulses would yield an ideal frequency comb, as illustrated in Fig. 3.8 (a). Pulses of width, τ_p , in the train result in a frequency comb with an envelope width inversely related to the pulse width [4]. Thus, for example, a train of 1 ps pulses would have a THz envelope width in the RF domain.

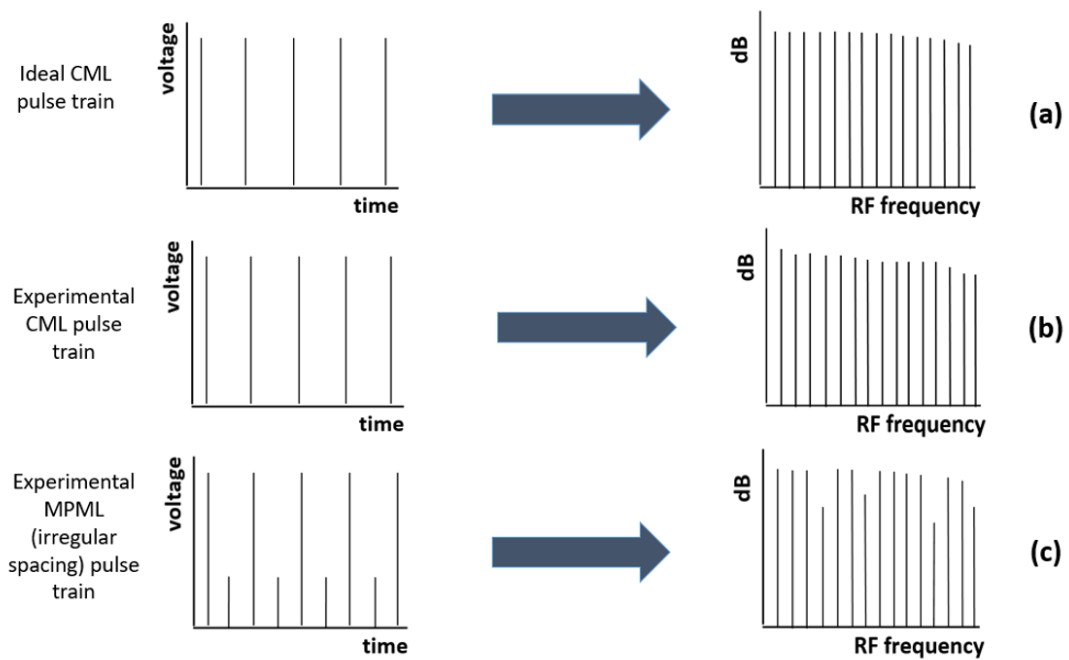


Figure 3.8: Diagram showing the relationship between time and frequency domains for (a) a theoretical CML regime, (b) an experimental CML regime with occasional instabilities and (c) a competing experimental (MPML) regime with irregular instabilities. Instabilities include amplitude noise and timing jitter.

Experimental CML pulse trains often have regular instabilities that increase amplitude modulation over the comb, as illustrated by Fig. 3.8 (b). The additional modulation manifests from amplitude noise and timing jitter in a mode-locked pulse train [15]. Timing jitter results in more power within bins either side of an exact multiple of the PRF - leading to harmonic broadening [15].

An RF spectrum was measured while the laser was in a CML state, as per Fig. 3.9. The spectrum span on the experimental trace was set to 600 MHz, which corresponded to around 35 RF harmonics. An RBW of 3 kHz and a VBW of 300 Hz were used resulting in a sweep time on the order of minutes. The PRF of the laser cavity was determined to be 17.9 MHz based on averaging the frequency distance between teeth in the frequency comb.

Amplitude modulation roll-off over the 35 peaks was around 8.5 dB, which is consistent with what other authors have reported for continuous mode-locking of sub-

ps pulses [16]. The ideal roll-off for a 600 fs pulse would be lower at just a few μ dB over 600 MHz based on a Fourier-transform limited conversion, as shown in Appendix E.

A quick sweep time, of a few seconds, using a lower RBW and VBW yielded behaviour closer to the Fourier-transform limited conversion. SMA cables attributed to around 0.75 dB of the roll-off attenuation at a 600 MHz frequency, based on documentation from the cable supplier [17].

The RF spectrum for the QML regime is shown in Fig. 3.10. Note that the vertical scale differs in this figure to that of Fig. 3.9. Smaller amplitude values are likely due to the large temporal separation between QML envelopes (on the order of several microseconds), which meant that no pulses were observed for extended durations reducing the power in the spectrum. The amplitude modulation across the spectrum was not reproducible due to differences between QML envelopes in the time domain, as the QML regime is a result of unstable intra-cavity energy oscillations, as discussed in Section 2.7.1. The variation between the harmonics was substantial with some harmonics as little as 5 dB above the instrument noise floor with others over 40 dB above.

Undesired multi-pulsing regimes have offset satellite pulses with an amplitude that is a small fraction of the main pulses in the train. In an ideal MPML regime, both the large-amplitude and satellite pulses are regularly spaced resulting in the two combs having the same maxima, but with a constant phase difference [18]. This yields a spectrum similar to the CML regime.

Experimentally, there are slight variations in timing between satellite pulses, and thus the phase shift varies randomly across the radio-frequency comb. Consequently, the amplitude of teeth in the frequency domain comb will be erratically modulated as the power at harmonics of the PRF can add or subtract, as shown in Fig. 3.8(c) and 3.11 [18, 19].

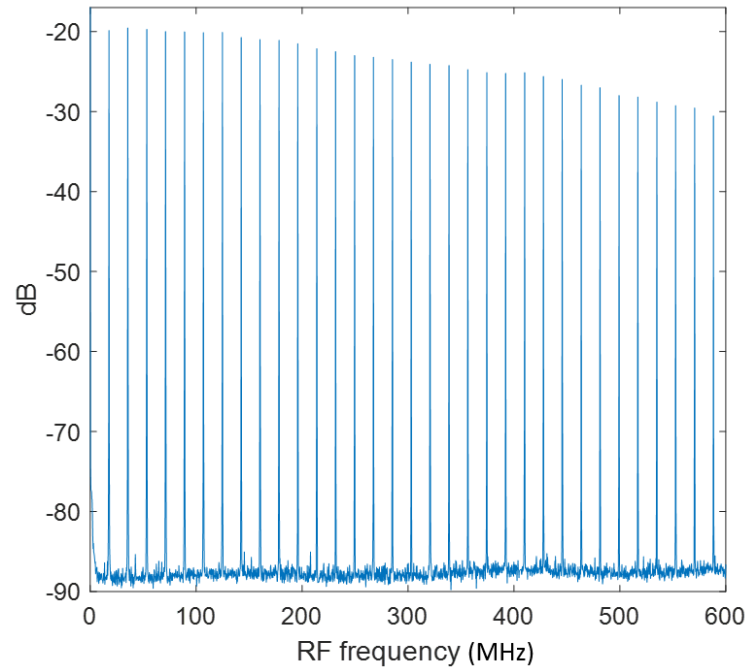


Figure 3.9: RF spectrum of erbium NLPR operating in CML regime.

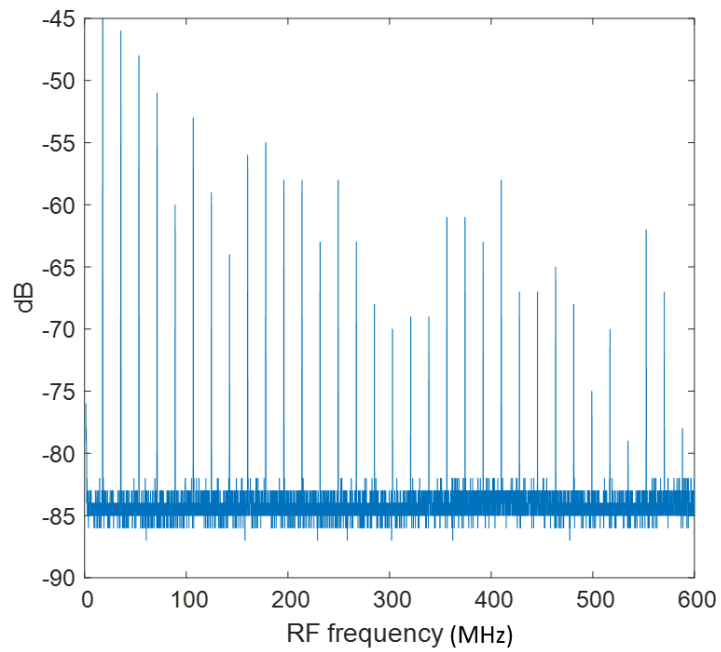


Figure 3.10: RF spectrum of erbium NLPR operating in QML regime.

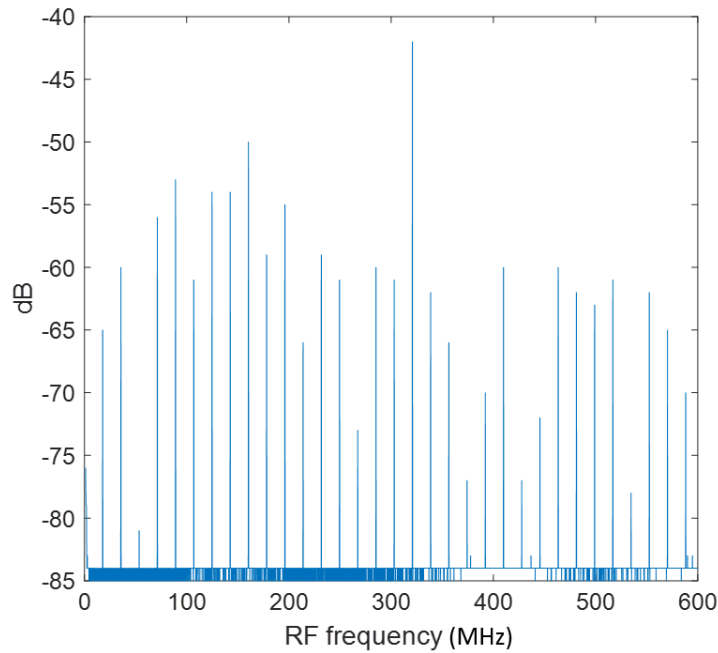


Figure 3.11: RF spectrum of erbium NLPR operating in a MPML regime.

Small temporal changes associated with MPML create large changes in the spectrum. The MPML regime will be explored in more detail in Chapter 4, and a stable MPML regime in which there is less amplitude modulation over the frequency comb will be analysed.

In summary, the sensitivity and dynamic range of the RF spectrum analyser make it a useful diagnostic for detecting lasing instabilities that may be less apparent in the time domain. Instabilities yield variable phase shifts in the radio-frequency domain leading to unique RF spectra that are not reproducible for every round trip.

3.3.3 Optical Spectrum

An optical spectrum analyser can be used to determine the central wavelength of the output and the associated optical FWHM [20]. Mode-locked pulses should have a broad spectrum in the frequency domain, as discussed in Section 2.4.2.

This project used a Yokogawa OSA (Yokogawa AQ6376), which incorporates a Czerny-Turner monochromator. Inside the OSA, light reflected by a collimating mirror onto a diffraction grating is dispersed at angles proportional to wavelength [21]. The diffracted light reflects off a secondary mirror and out an output slit, located at the focal point of the secondary mirror [22]. The rotation of the grating controls the wavelength of light that passes through the slit and onto a photodetector [22]. A ‘hold’ option that temporarily stops the grating at each wavelength was used and set to be 1 ms to improve the signal to noise. Sweeping too quickly reduces the integration time and can result in missing signal components in the final trace [23].

A CML optical spectrum is shown in Fig. 3.12. The OSA was operated with a resolution of 0.1 nm. The experimentally measured FWHM was 6.2 nm - consistent with the time-bandwidth product for a sub-ps Gaussian pulse [24].

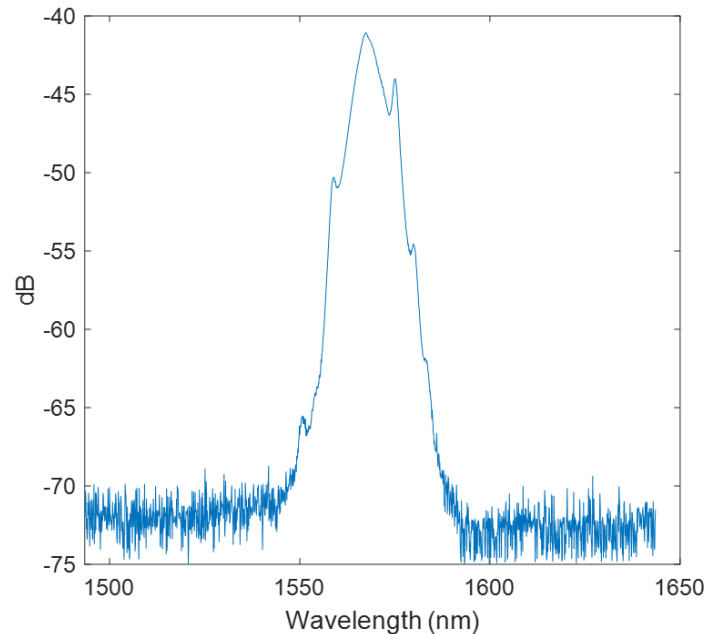


Figure 3.12: Optical spectrum of NLPR mode-locked EDFL operating in CML regime.

The structure evident on the leading and trailing edges of the optical spectrum, Fig. 3.12, are Kelly sidebands, which are associated with a periodic disturbance within the resonator [25]. Fibre lasers with high non-linearity and dispersion are

particularly more susceptible to this behaviour [25]. The periodic disturbance supports a dispersive wave in the cavity that propagates alongside a pulse [25]. Strong Kelly sidebands are an indicator that the pulse duration is near the minimum time-bandwidth product [26]. These sidebands can be problematic for amplification as they may be amplified more than the desired signal [27].

A QML optical spectrum is shown in Fig. 3.13. The Kelly sidebands are more prominent in the QML regime than the CML regime. The optical FWHM was similar to the CML regime at 6.1 nm. Additionally, there appears to be more power at shorter wavelengths in the QML trace at around 1530 nm.

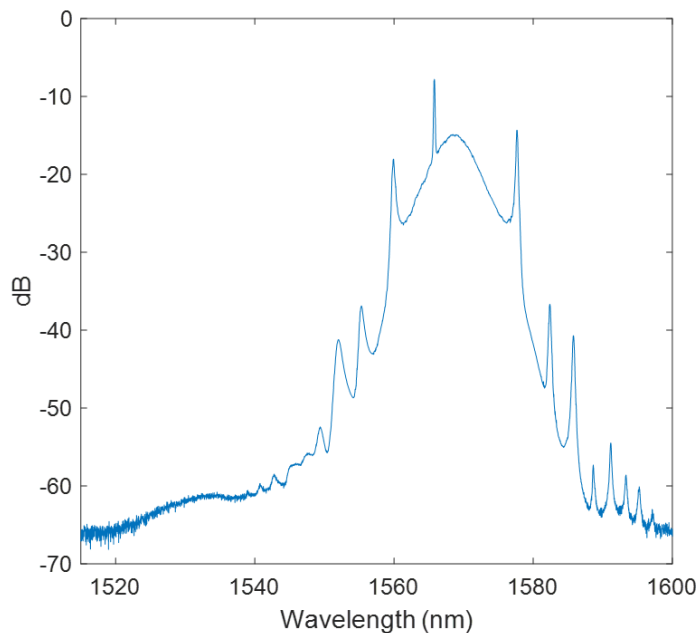


Figure 3.13: Optical spectrum of NLPR mode-locked EDFL operating in QML regime.

A trace of the laser output in the MPML regime is presented in Fig. 3.14. The optical spectrum contained a feature that had a similar optical FWHM to the characterised CML and QML regimes. There was also another structure at a shorter wavelength. The narrower nature of the other optical structure suggests that the satellite pulses may be temporally longer than the primary pulses in the train.

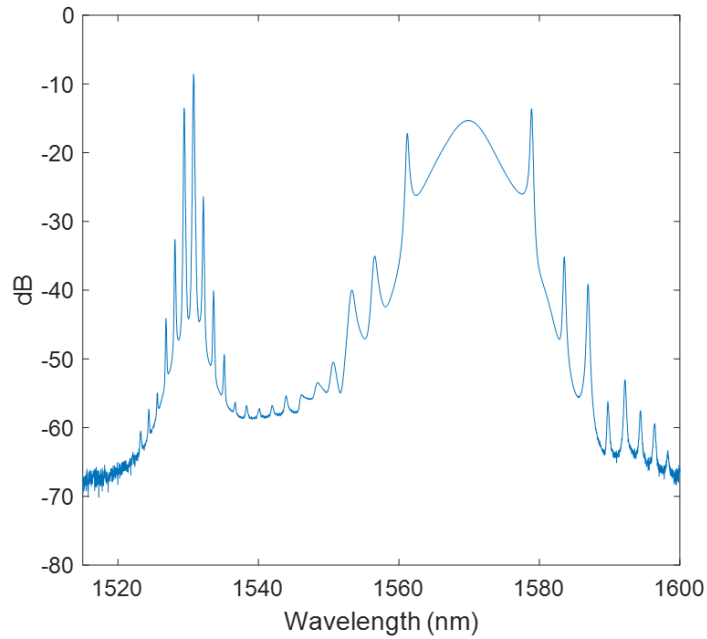


Figure 3.14: Optical spectrum of NLPR mode-locked EDFL operating in a MPML regime.

3.3.4 Autocorrelator

An autocorrelator measures the correlation between a signal and a version of a signal delayed by some time interval, τ [28]. One of the most basic autocorrelator designs is a field autocorrelator, which splits the pulse using a beam splitter and has a Michelson interferometer geometry, as shown in Fig 3.15 [29].

Changing the path length of one of the arms introduces a time delay [29]. The field autocorrelation trace, $A_F(\tau)$, is a plot of intensity as a function of the introduced delay as given in Equation 3.2 [30].

$$A_F(\tau) = \int_{-\infty}^{\infty} E(t)E^*(t - \tau)dt \quad (3.2)$$

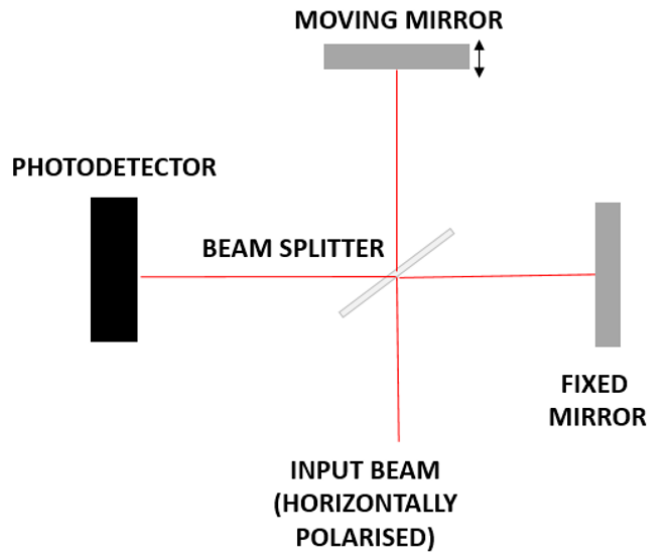


Figure 3.15: Schematic of a field autocorrelator

Field autocorrelation is inherently limited in the information it provides. It can not be used to extract the temporal extent of a short pulse – i.e. the FWHM of the pulse [30]. However, a Fourier transform of the field autocorrelation function yields the spectrum of the pulse [29].

A non-collinear second harmonic generation (SHG) autocorrelation geometry, as shown in Fig. 3.16, can (along with other geometries) be used to determine pulse width. In this instrument, the pulses reflected by the interferometer mirrors cross in a non-linear crystal producing a signal at the second harmonic (SH) if the pulses overlap [30]. A mirror prior to the SHG crystal is curved slightly to focus the beam waist to a location inside the crystal. The output of the SH generator is filtered to remove the unconverted fundamental and is then time-integrated by the photodetector to yield the intensity autocorrelation function (ACF), as given in Equation 3.3 [30].

$$A_I(\tau) = \int_{-\infty}^{\infty} I(t)I^*(t - \tau)dt \quad (3.3)$$

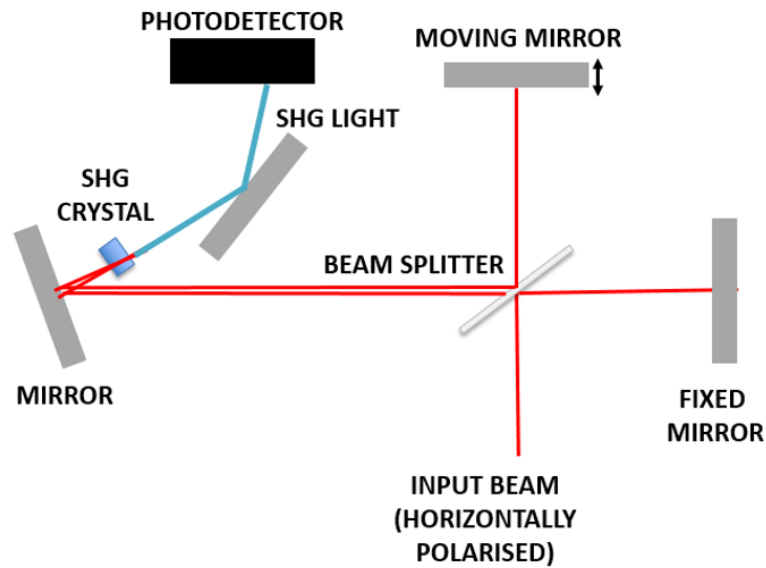


Figure 3.16: Schematic of a second harmonic generation (SHG) autocorrelator aligned for an intensity autocorrelation (non-collinear mode). A curved mirror is used to focus a beam waist in the SHG crystal.

Non-collinear intensity autocorrelations are background-free as only the overlap of the two pulses results in a SH propagating towards the photodetector, as discussed in Appendix F. That is, the photodetector measures none of the SH due to a single pulse. Consequently, SHG intensity declines for long delays between the two time-delayed beams. This is because the beams only overlap in the crystal, meaning that, for long delays, the incident light intensity is insufficient in generating SH light [31]. SHG ACF traces are also symmetric about the zero delay point.

The APE autocorrelator (PulseCheck 150) also has a collinear SHG setting that is used for aligning the input laser beam, as discussed in Appendix F. Alignment also depends on SHG phase matching, as discussed in Appendix G. Collinear autocorrelations yield a 1:8 ratio of noise to peak height that can be used as an additional alignment check.

Unfortunately, a unique pulse intensity and phase profile cannot be obtained from an autocorrelation measurement alone due to the one-dimensional phase-retrieval problem, a consequence of the fundamental theorem of algebra [30]. It is not possible

as autocorrelation only utilises Fourier transform magnitudes and not phases in the temporal domain. Ambiguities in the pulse's electric field lead to ambiguity in the unique profile of the pulse [30]. Consequently, a deconvolution factor is necessary to determine the pulse duration (FWHM) from the ACF FWHM. One must assume a specific pulse shape – such as Gaussian, squared hyperbolic secant or Lorentzian – to determine pulse width.

A few different pulse shapes that yield the same ACF are depicted in Fig. 3.17. The bottom row of traces reveals a pulse that has a third-order spectral phase [30]. This spectral phase, as a result of third-order dispersion, leads to intensity outside the primary pulse. The autocorrelation trace does not adequately reveal the structure of these smaller pulses. Instead, the trace has a small increase in intensity in its wings [30].

Nevertheless, non-collinear ACF's can distinguish between very noisy pulses, as depicted in Fig. 3.18. Such structures have an autocorrelation that appears as a coherence spike upon a broad background [30]. The spike is related to the pulse's spectrum, while the broad envelope feature is related to the actual width of the noisy intensity structure [30]. The FWHM of the autocorrelation (and hence the pulse) is meaningless for such regimes as noisy regimes may contain many pulses of variable amplitude under a small temporal envelope.

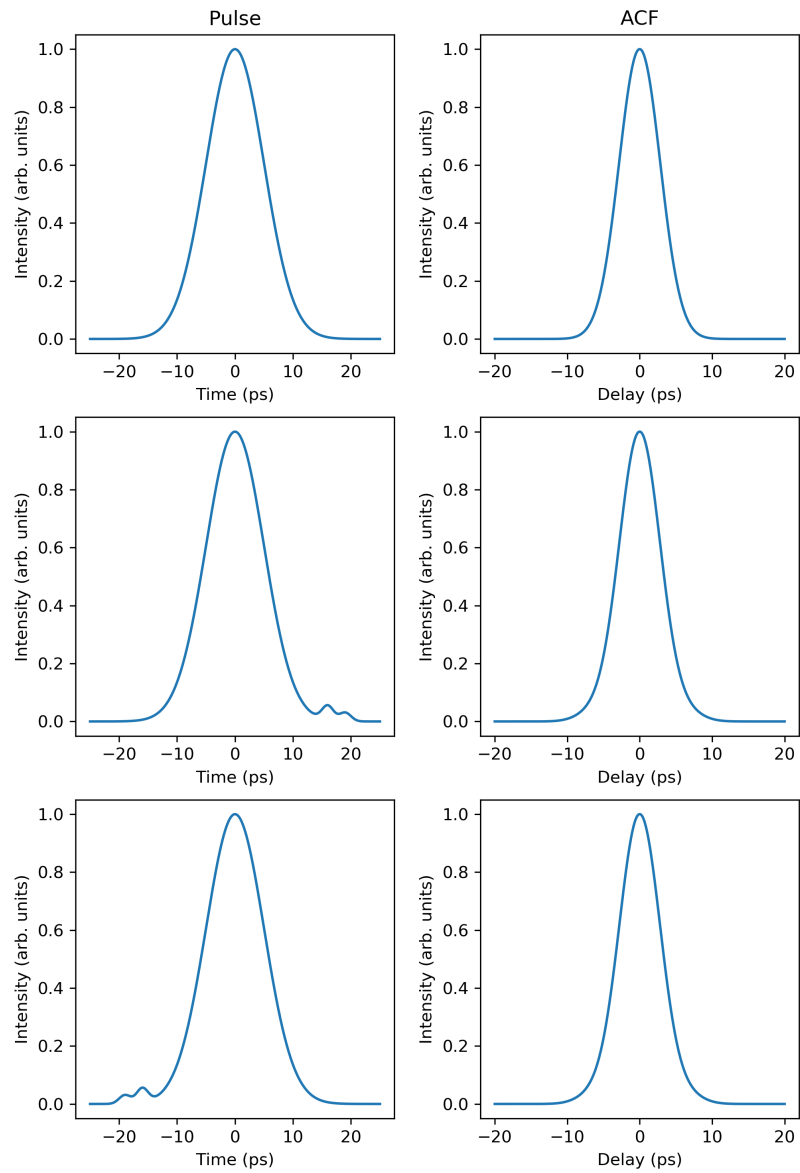


Figure 3.17: A set of different pulse intensity profiles that have similar autocorrelation functions.

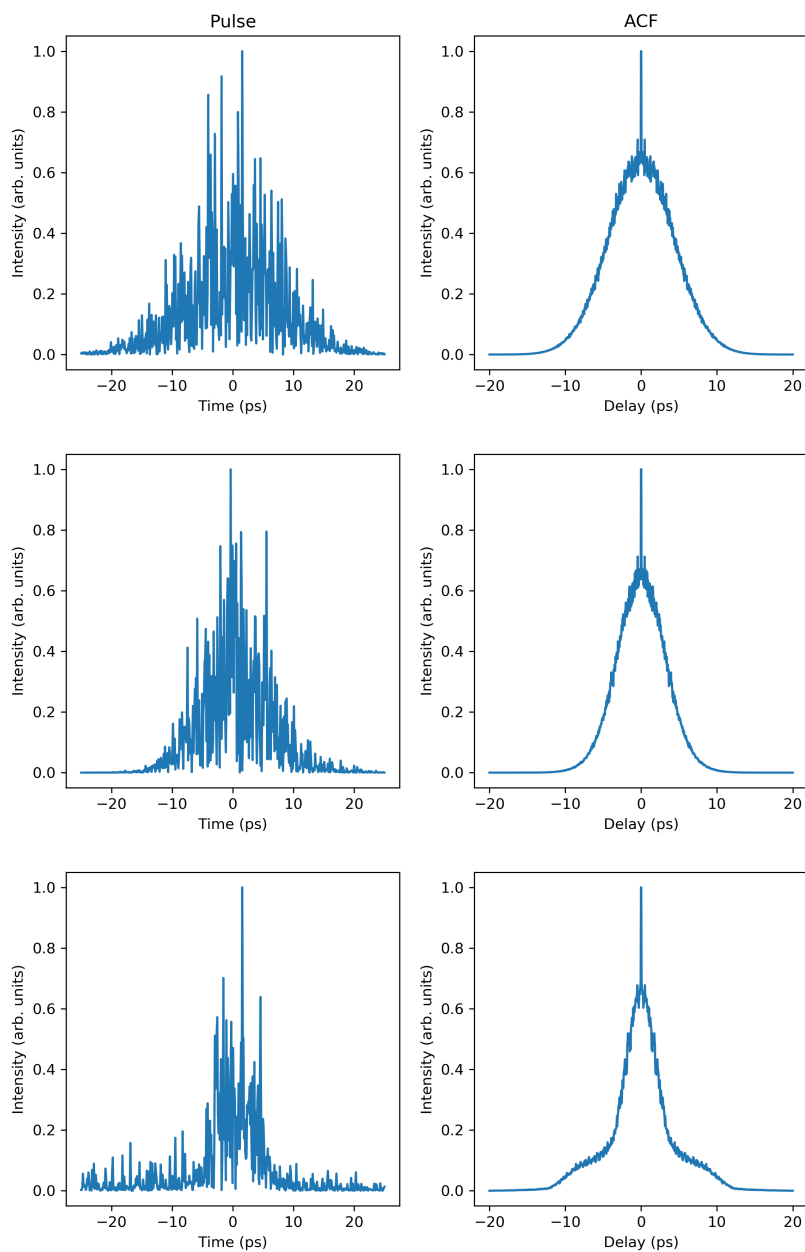


Figure 3.18: A set of noisy pulses and their corresponding autocorrelation traces. A pulse that has more noise tends towards a coherence spike upon an envelope.

The measured ACF with the NLPR mode-locked EDFL in the CML regime are plotted in Figs. 3.19 and 3.20. A long span (150 ps) trace reveals minimal optical power outside the pulse. A total of 256 points were sampled for each of these traces.

In the literature, most ultrashort pulses tend to correlate well with squared hyperbolic secant profiles [30]. A statistical mean square error (MSE) measure is a more

appropriate way to determine the optimum regression for the ACF trace. The autocorrelator used in this project measured across 1024 discrete intensity levels (with arbitrary units). An MSE value was attainable by simply calculating the difference in the arbitrary intensity units between the fitted profile and the ACF datapoints as the ‘error’. The units of MSE, for this Chapter and all future chapters is on the same arbitrary unit scale but summed across the trace.

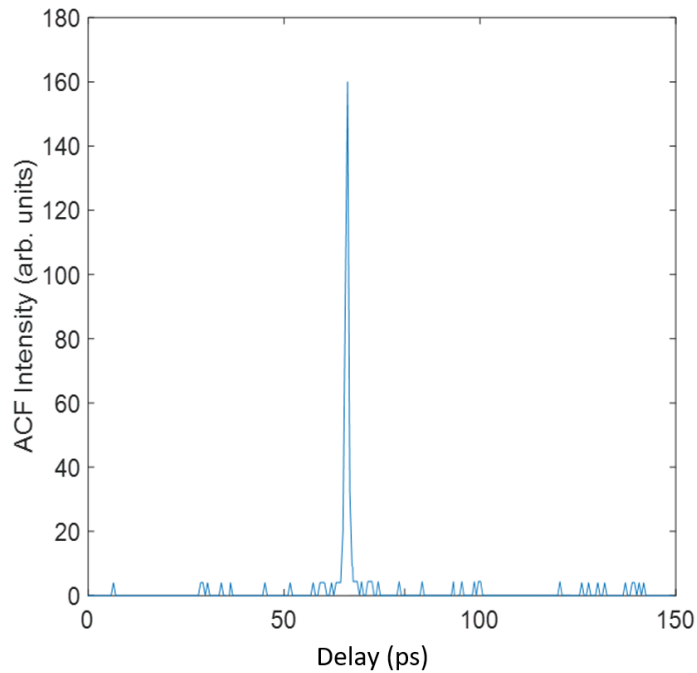


Figure 3.19: Autocorrelation trace (150 ps span) of NLPR mode-locked EDFL output operating in a CML regime with 70 mW average power.

A Gaussian fit on the 5 ps span ACF (Fig. 3.20) yielded an ACF FWHM of 880 fs and hence a pulse FWHM of 624 fs. The associated MSE was 8.071. Fitting the data to a square hyperbolic secant profile yielded a pulse FWHM of 579 fs with an MSE of 5.038. The hyperbolic secant profile was thus superior to the Gaussian profile due to the lower MSE (smaller difference between the fitted ACF profile and the experimental data).

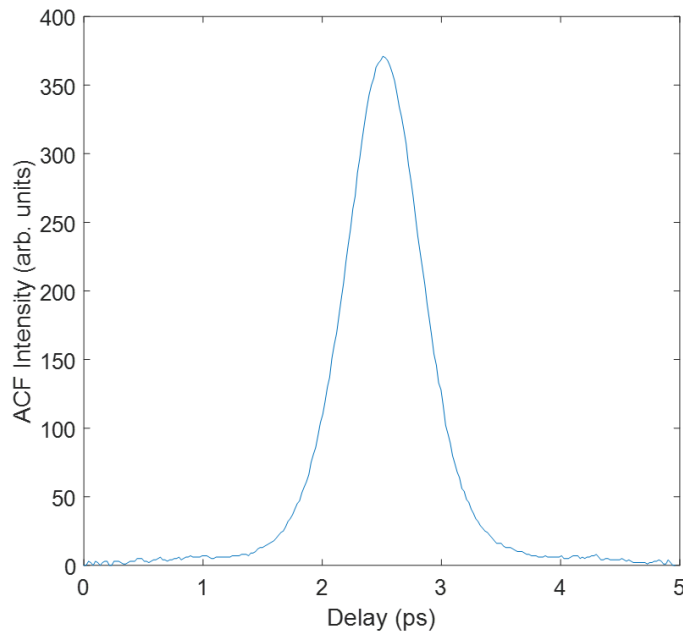


Figure 3.20: Autocorrelation trace (5 ps span) of NLPR mode-locked EDFL output operating in a CML regime with 70 mW average power.

Indeed, the wing shape of the pulse in Fig. 3.20 is consistent with this finding, as hyperbolic secant functions tend to have wider wings [32]. The fitted profiles are presented in Fig. 3.21.

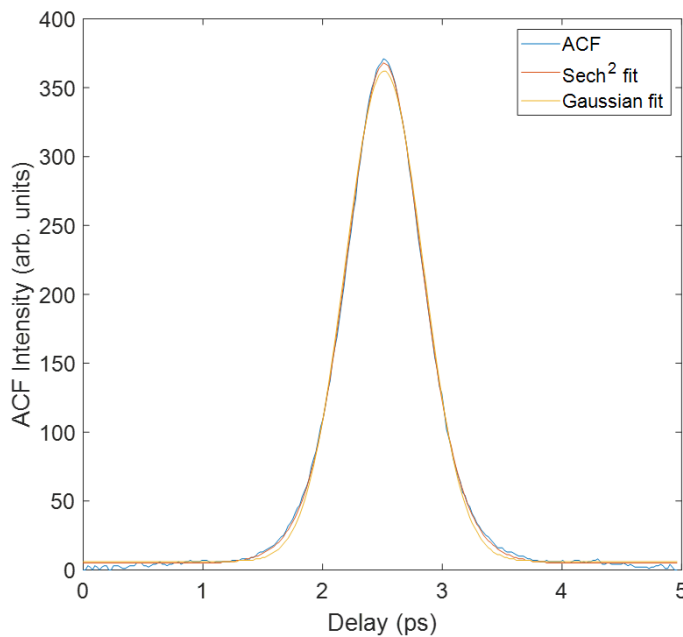


Figure 3.21: Fitted profiles for the ACF trace presented in Fig. 3.20.

A ratio of the background SHG intensity level (intensity above the instrument noise floor recorded when the laser was off) to the peak intensity level of the ACF trace yields the percentage of power contained in the pulse [33]. The background level varied between 0-8 arbitrary units on the instrument's intensity scale (Fig. 3.19) with an average value across the trace (excluding the pulse) of 4.5. From Fig. 3.20, the largest attained intensity was 378. Consequently, 98.8% of the power was within the pulse in this instance.

This metric complements measurements taken in other domains to validate the CML nature of the laser. It is important to note that this measurement was based only on a 150 ps scan (the maximum for the autocorrelator) and that it does not account for the remainder of the 59 ns between pulses. An oscilloscope trace can be used to look for additional noise between pulses over a longer time period.

The ACF in the QML regime, which occurred at lower pump powers with lower circulating power and reduced NLPR, is shown in Fig. 3.22 [34]. A Gaussian fit yielded the lowest MSE (9.32), for which the temporal FWHM was 740 fs.

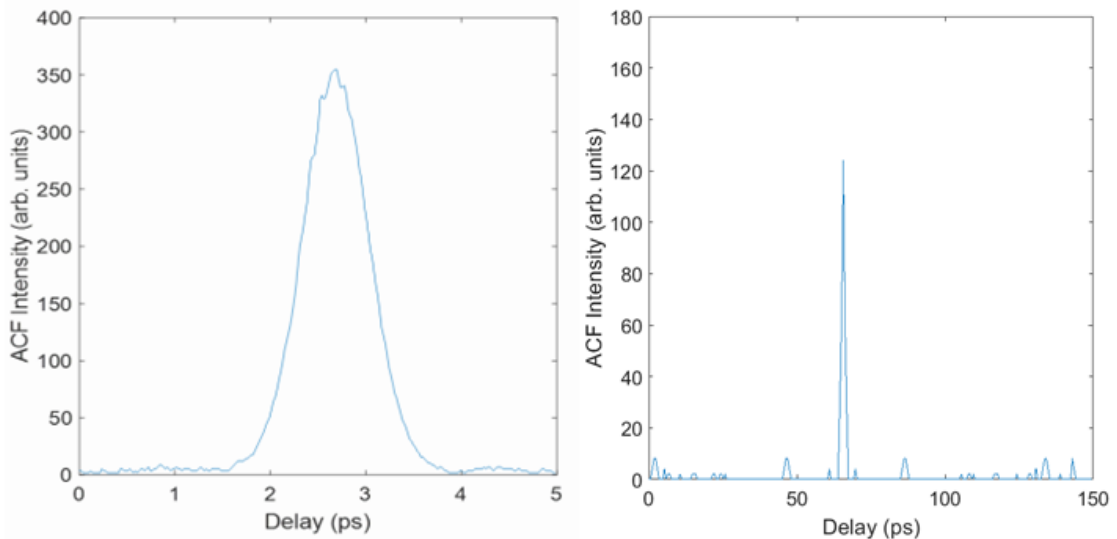


Figure 3.22: Autocorrelation trace (left: 5 ps span and right: 150 ps span) of NLPR mode-locked EDFL operating in a Q-switched mode-locked regime.

The ratio of background to peak ACF intensity yielded 94.1%, meaning that more power was outside the pulse than when the laser was operating in a CML regime.

More power outside the pulse would make the regime unsuitable for amplification as small deposits of optical power between PRF can dominate over the desired optical signal [35]. A lower ACF peak intensity on the 150 ps scan is attributable to both aliasing and the fact that an ensemble of pulses are sampled to attain an ACF.

A reliable autocorrelation could not be obtained for the unstable MPML regime observed as the trace was not readily reproducible due to excessive jitter instabilities.

3.4 Summary

This chapter investigated the information available from several diagnostics for a range of regimes. The key findings are summarised in Table 3.1.

Table 3.1: Table summarising the role of each diagnostic instrument.

Equipment	Measurements	Relative merits
Oscilloscope	Presence of a pulse train Amplitude of pulses	Can explore large scale temporal changes – i.e. looking for Q switched mode-locking envelope or CW component
Optical spectrum analyser	Central wavelength Kelly Sidebands FWHM (optical)	Can discriminate against small CW optical power components as device has a wide dynamic range Observe whether a pulse near Fourier transform bandwidth limit
RF spectrum analyser	Amplitude modulation	Sensitive to pulse train output as frequency domain trace heavily influenced by small perturbations in pulse train output
Autocorrelation	FWHM (temporal) Power within pulse	Determination of pulse duration assuming a functional form for the pulse's temporal profile

Additionally, unique pulse profiles are attainable using FROG measurements, as discussed in Appendix D.

The combination of diagnostics used here provided a consistent method for determining when the NLPR EDFL was operating in a CML regime. Pulse properties for the CML regime are summarised in Table 3.2.

Table 3.2: Table of summary characteristics for erbium source in a CML state.

Central wavelength (nm)	Optical FWHM (nm)	Pulse duration (fs)	Repetition rate (MHz)	Average power (mW)	Peak power (kW)	Pulse energy (nJ)
1567	6.2	579	17.9	70	5.93	3.9

The aim of this chapter was to investigate the merits of different characterisation equipment and explore how measurements differed between an ideal (CML) regime and an non-ideal pulsed regime. The RF spectrum analyser provided a clear distinction between CML and other regimes. There were also notable differences in the optical spectrum. Oscilloscope traces were useful when non-ideal lasing behaviour was apparent (i.e. large satellite pulses or QML) however smaller satellite pulses and noise may be more difficult to detect using this diagnostic alone.

The measurement techniques applied to the EDFL output are transferable to any NLPR laser. The following chapters will focus on what diagnostic tool provides the best discrimination on its own.

Chapter 4

Automation Metric Testing using a Thulium NLPR Fibre Laser

4.1 Introduction

This chapter focuses on the characterisation and automation of an NLPR mode-locked thulium-doped fibre laser (TDFL). The source lases at 1990 nm, which differs from that of the EDFL source in Chapter 3. Thulium was chosen based on its lasing transition near 2 μm . The purpose of this Chapter is to explore a range of possible automation metrics to assess the lasing output of the NLPR laser. In addition to a manual polarisation controller (PC), an electronic polarisation controller was added to provide an alternative mechanism for varying the intra-cavity polarisation state, as shown in Section 4.2. A characterisation, in Section 4.3, revealed several additional non-ideal lasing regimes that the laser could operate in under incorrect polarisation settings.

The key aim of the chapter was to conduct preliminary feasibility studies for several automatic diagnostic metrics, as presented in Section 4.4, including discontinuities in Stokes Parameters, two-photon absorption (TPA) signals and amplitude modulation in radio frequency (RF) spectra. As mentioned in Section 1.6, these suggested techniques are common in the literature, and this chapter aims to identify some mer-

its for each technique. A robust automation diagnostic is critical to ensuring the laser can stably remain mode-locked and be adjusted as necessary. As mentioned in Chapter 2, small vibration and temperature perturbations can have substantial impacts on intra-cavity polarisation state altering the lasing output. For seeding or amplification purposes, a stable and non-noisy output is of substantial importance.

4.2 Mode-locked Thulium Fibre Laser

4.2.1 Cavity Configuration

A schematic of the NLPR mode-locked TDFL laser cavity is presented in Fig. 4.1. A 793 nm diode (LIMO, 35F100DL790EX1677) pumped a 4.5 m length of 8.5 wt.% thulium-doped active fibre via a multi-mode coupler. The diode was water-cooled at 20 °C and mounted on a copper block. It was operated over a current range of 14-25 A, yielding output powers of 2-6 W.

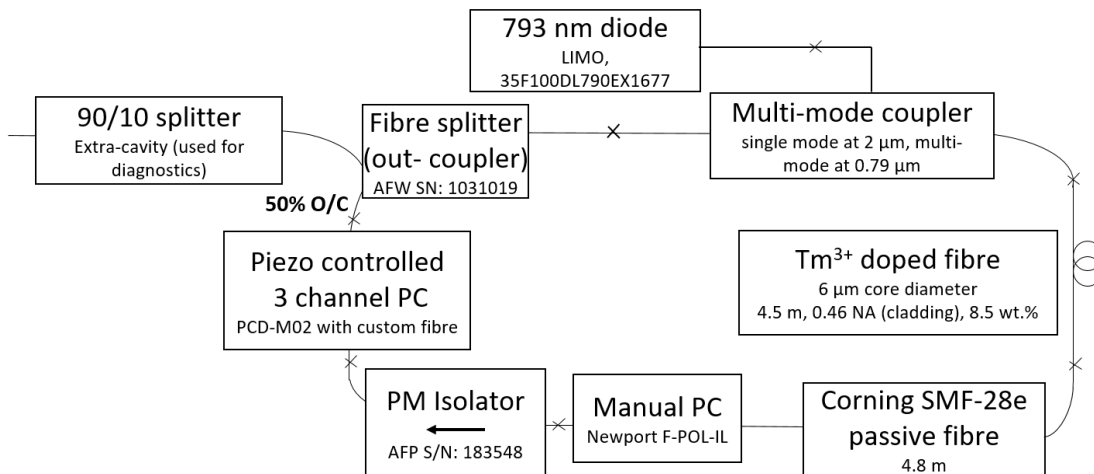


Figure 4.1: A schematic of the NLPR mode-locked TDFL cavity. WDM = wavelength division multiplexer, PC = polarisation controller and x marks the position of splices or fibre connectors.

The thulium fibre had a 6 μm core diameter with an NA of 0.2 and an octagonal cladding with a flat-to-flat diameter of 125 μm and an NA of 0.46. This system was cladding-pumped, as discussed in Section 2.2.3.

The output of the active fibre was spliced to a non-PM passive fibre (Corning SMF-28e) passing through a manual polarisation controller and an isolator (AFP S/N: 183548). A three-channel piezo-electric polarisation controller was placed at the output of the PM isolator. The controller had a customised fibre suited to wavelength operation at $2\ \mu\text{m}$. Fibre specifications included a $15\ \mu\text{m}$ core diameter with a $250\ \mu\text{m}$ cladding and 0.1 NA. Each channel controlled three intra-cavity actuators to introduce strain to the optical fibre. Each channel corresponded to a different actuator which were positioned at different angles and could hence yield different polarisation state transitions on the Poincarè Sphere, as per Section 2.3.2. Both the electronic and manual controllers worked in tandem to provide control over the intra-cavity polarisation state.

4.3 Results

Several mode-locked regimes were attainable by adjusting the polarisation controllers and altering the pump diode currents, including states that were:

- Continuous mode-locked (CML)
- Q-switched mode-locked (QML)
- Continuous mode-locked with a CW component (CMLCW)
- Stable and unstable multi-pulsed mode-locked regimes (MPML)

Characterisation of these regimes are reported in Sections 4.3.1 to 4.3.4 respectively. The diagnostics used are the same as Fig. 3.2.

Both the TDFL and EDFL could operate in CW regimes. Each diagnostic trace in such a regime differs substantially from what was observed with a pulsed regime. Consequently, the characterisation results of this regime are not presented.

4.3.1 Continuously Mode-locked (CML)

The TDFL source had a stable CML regime that produced a stable pulse train as shown in Fig. 4.2. The amplitude variation over eleven consecutive peaks was 10.9 %. There were no prominent satellite pulses or noisy features.

A broadband RF spectrum of the CML pulse train, with the same bandwidths used in the last chapter (RBW of 3 kHz and VBW of 300 Hz) is shown in Fig. 4.4. Amplitude roll-off over 600 MHz is around 9 dB, as observed for the EDFL for a long sweep time RF trace (200 seconds).

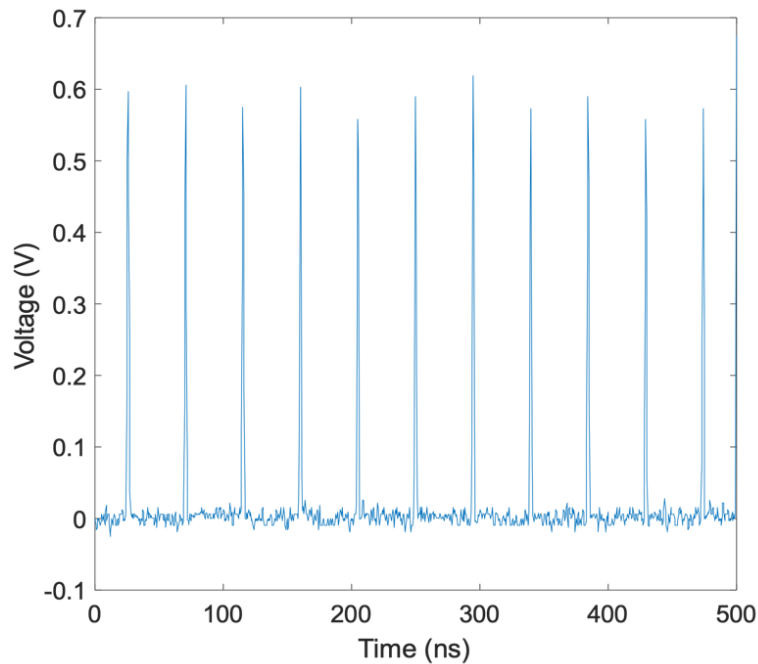


Figure 4.2: Temporal trace of a CML pulse train

The maximum attainable average power of the continuously mode-locked (CML) output was 120 mW, which required a pump power of 6.5 W. Thus, the average pulse energy was around 5.4 nJ, which is an increase from the EDFL pulse energy of 3.9 nJ.

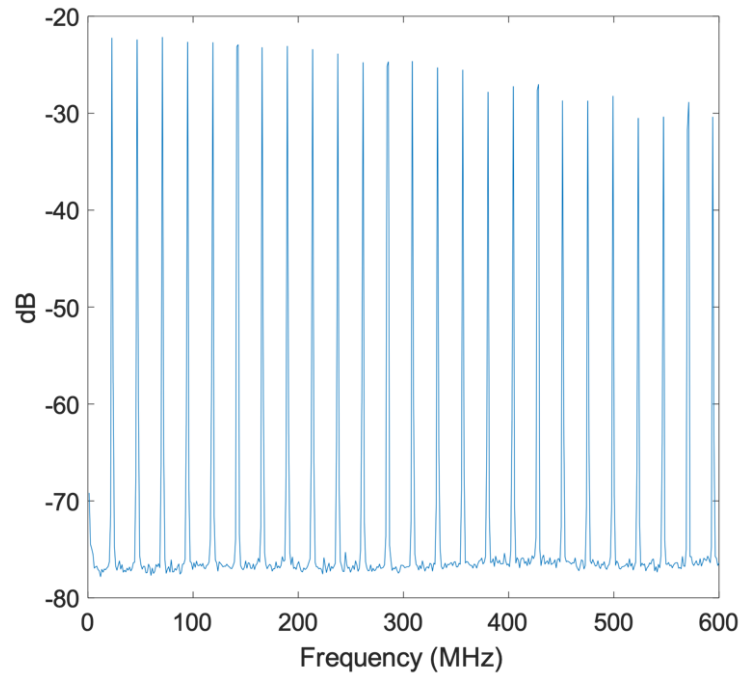


Figure 4.3: Broadband RF spectrum of a CML pulse train

A CML optical spectrum is shown in Fig. 4.4. The OSA trace had a resolution of 0.1 nm, as per Chapter 3. The measured FWHM is 4.7 nm, which would suggest a Gaussian pulse with a width of around 1 ps .

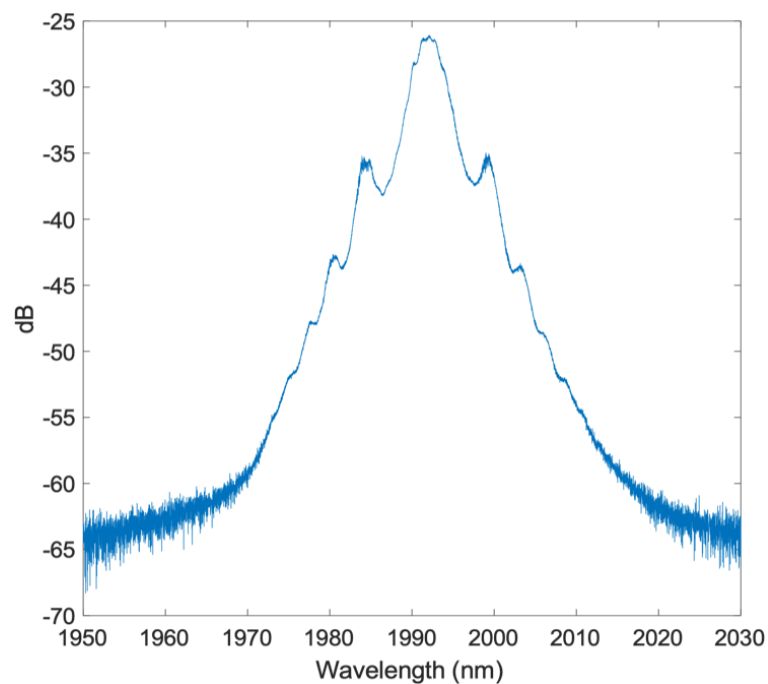


Figure 4.4: Optical spectrum for a CML regime

A long span (150 ps) AC trace is shown in Fig. 4.5. An optical filter was removed from the IR photodetector as it reduced the intensity of the SH signal [2]. A reliable estimate for the percentage of power contained in the pulse was unobtainable due to the additional noise that manifested as a result of removing the filter. A background trace taken with the filter installed was subtracted from the trace presented in the figure.

A 5 ps scan and 256 sample points were recorded in the trace in Fig. 4.6. A Gaussian fit yielded a ACF FWHM of 1.62 ps and hence a pulse FWHM of 1.15 ps, which is consistent with the optical spectrum, given in Fig. 4.4. The associated mean square error (MSE) was 17.98.

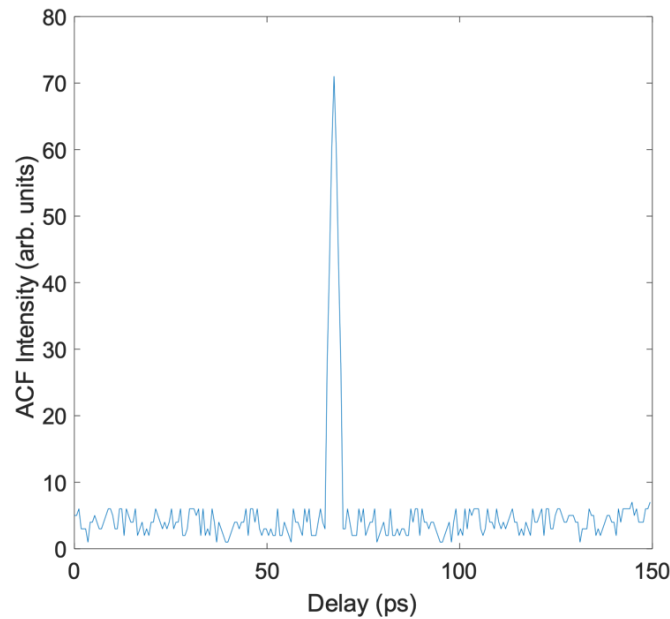


Figure 4.5: Autocorrelation trace (150 ps span) taken while operating in a CML regime. Trace collected after removing a filter from the photodetector module. Average power of CML output launched into autocorrelator was 80 mW.

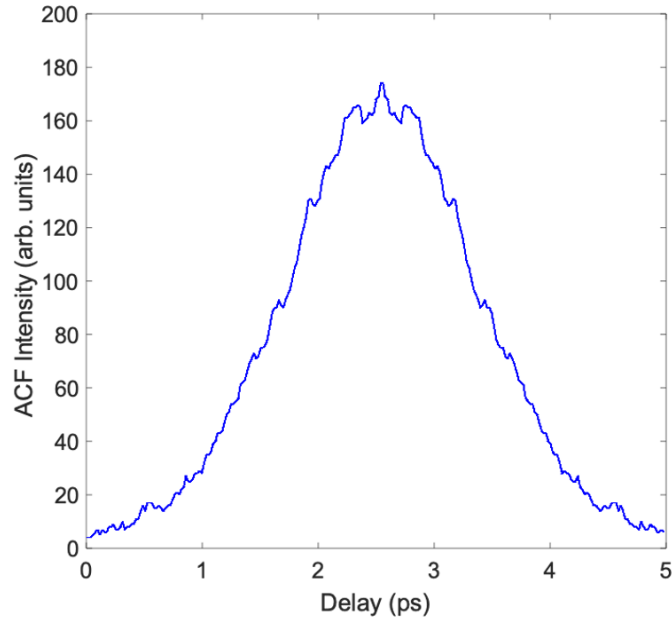


Figure 4.6: Autocorrelation trace (5 ps span) taken while operating in a CML regime. Average power of CML output launched into autocorrelator was 80 mW.

4.3.2 Q-switched Mode-locked (QML)

A QML regime, as discussed in Chapters 2 and 3, results from an unstable oscillation in intra-cavity energy. A characterisation profile of this regime is critical to avoid false identification of a CML regime. The QML pulse train is presented in Fig. 4.7. The figure covers the entire asymmetric Q-switched envelope (with a FWHM of around $2 \mu\text{s}$). While the Q-switched envelope was not reproducible, it had a similar shape and maintained its asymmetrical nature. The separation between Q-switched envelopes was around $100 \mu\text{s}$.

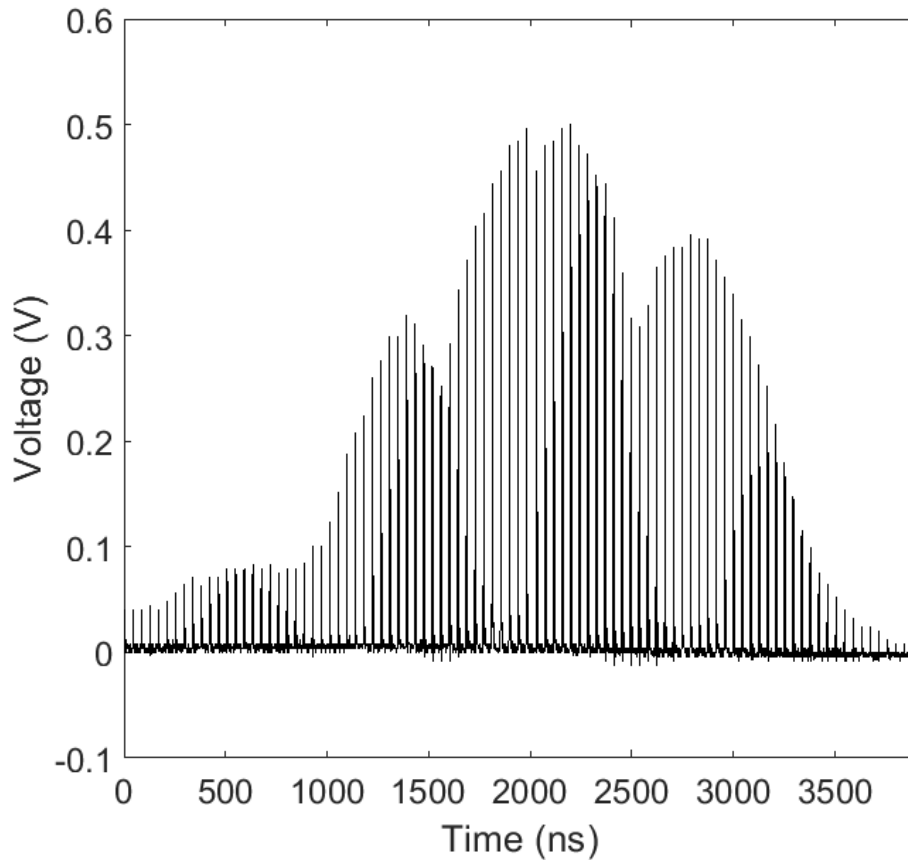


Figure 4.7: Oscilloscope traces of a QML envelope. The output intensity varies with time considerably. The plot is produced from stitching 4 shorter temporal windows together.

A broadband RF spectrum analyser trace is shown in Fig. 4.8. Additional amplitude modulation of the harmonics, relative to the CML trace (Fig. 4.3), is present over the frequency comb. Fluctuations in out-coupled pulse power led to variable amplitudes across the harmonics. The trace was not constant between sweeps but had a somewhat similar shape.

A QML optical spectrum is shown in Fig. 4.9. The measured FWHM was 3.5 nm. The decreased spectral width implied that the QML pulses had a slightly longer duration than the CML pulses, as is consistent with the behaviour observed when operating the EDFL in Chapter 3.

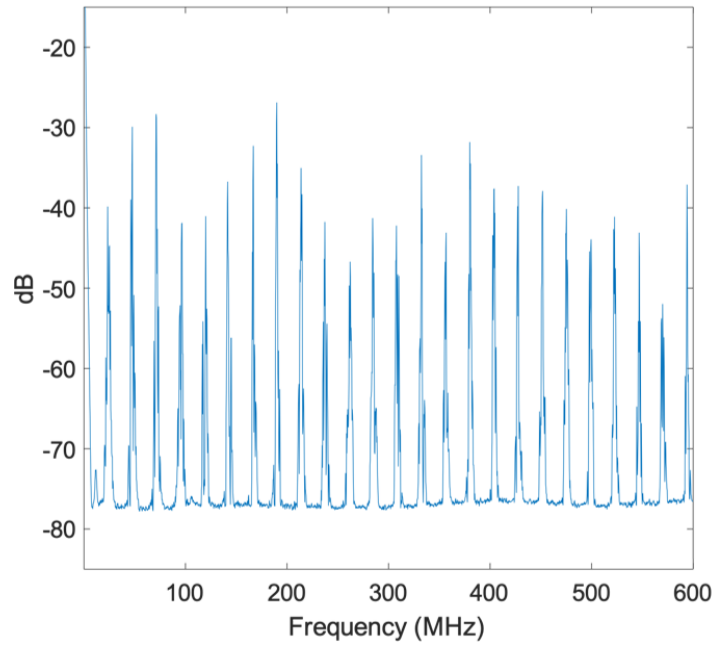


Figure 4.8: Broadband RF spectrum of the QML pulse train.

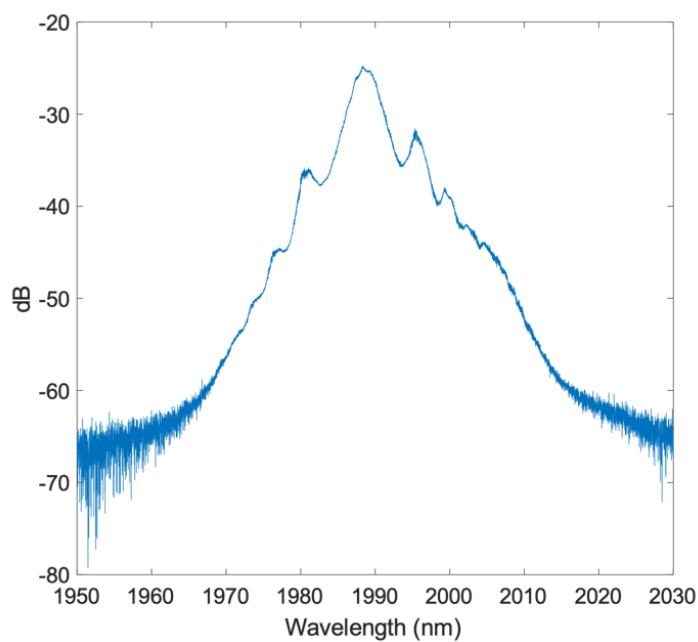


Figure 4.9: Optical spectrum for a QML regime.

A long span (150 ps) AC trace with the filter removed is shown in Fig. 4.10.

A span of 15 ps was used to obtain an ACF FWHM of 2.75 ps and hence a pulse FWHM of 1.95 ps, as per Fig. 4.11. A Gaussian fit was used with an MSE of 19.26, which was larger than the MSE associated with the CML fit.

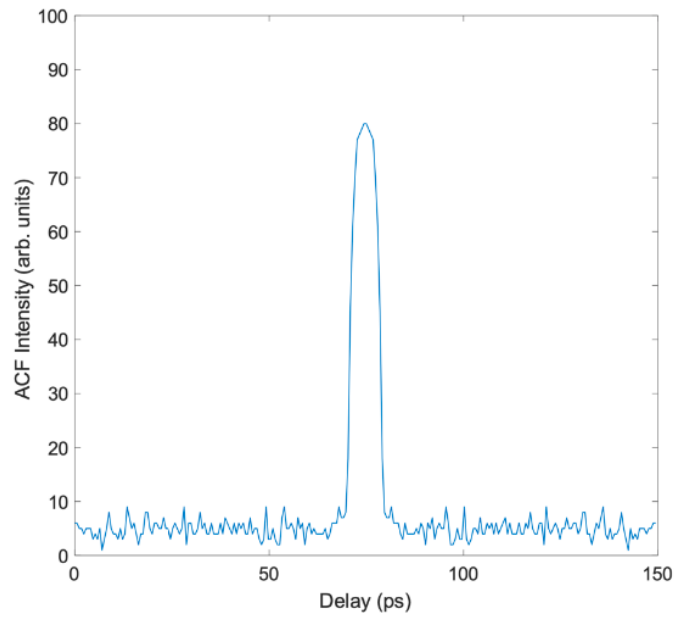


Figure 4.10: Autocorrelation trace (150 ps span) taken while in a QML regime.

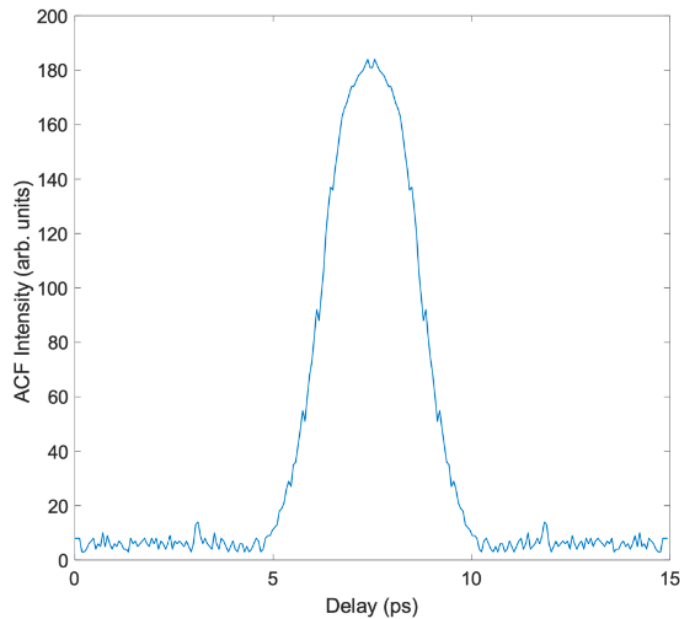


Figure 4.11: Autocorrelation trace (15 ps span) taken while in a QML regime.

4.3.3 Continuously Mode-locked with CW Background (CMLCW)

The TDFL source had a non-ideal regime with small pulses on top of a CW component (a CMLCW regime), as shown in Fig. 4.12. This regime was characterised using a DC-coupled detector. There was minimal amplitude modulation ($< 10\%$)

across 15 consecutive pulses.

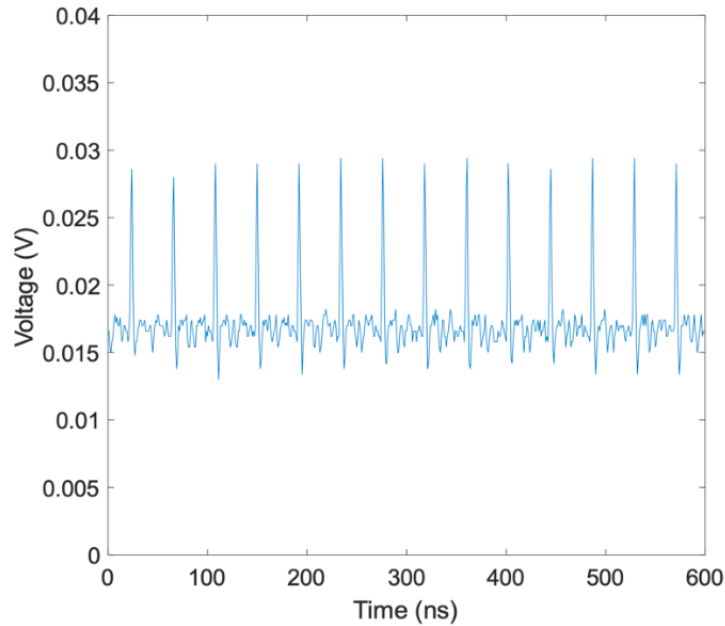


Figure 4.12: Temporal trace of a CML pulse train with a CW optical power component.

A broadband RF spectrum analyser trace is shown in Fig. 4.13. Additional amplitude modulation, relative to the CML regime, is present over the frequency comb. The modulation appears prevalent at lower frequencies where the broad comb should be flat. There is also a low-frequency peak at about 10 MHz which is probably due to modulation of the pulse peaks observed in the temporal trace, Fig. 4.12.

A CMLCW optical spectrum (Fig. 4.14) reveals a spike feature atop a broader envelope, which is likely due to the optical CW component in this competing regime. The broader envelope is associated with the optical pulses in the pulse train. A pulse envelope FWHM of 14 nm was measured with a 30 dB SNR. The narrow spike had a 3.1 nm FWHM.

A span of 5 ps was used to record the trace in Fig. 4.15. A Gaussian fit yielded an ACF FWHM of 0.371 ps and hence a pulse FWHM of 0.263 ps, which is much less than the 1.15 ps observed for the CML regime. The MSE was around 17.4.

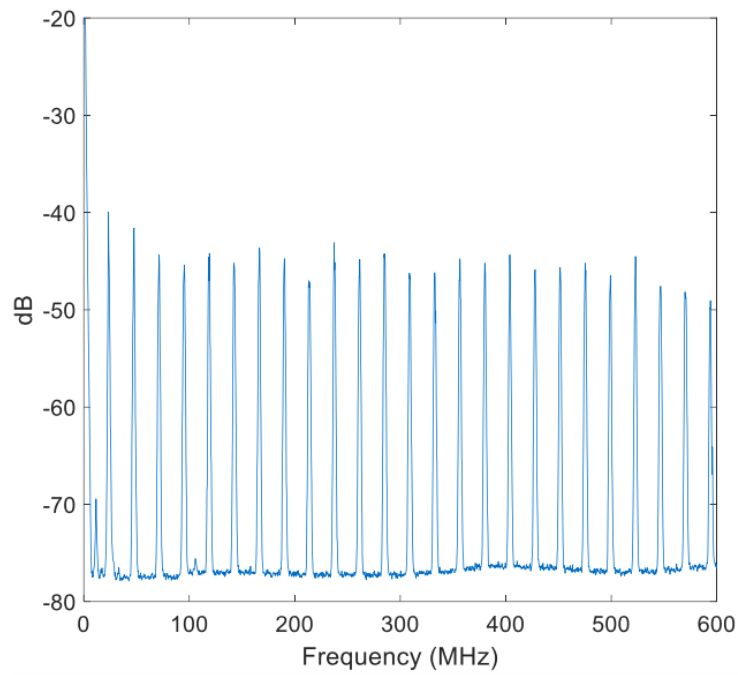


Figure 4.13: Broadband RF spectrum of the CML mode-locked pulse train with an optical CW component.

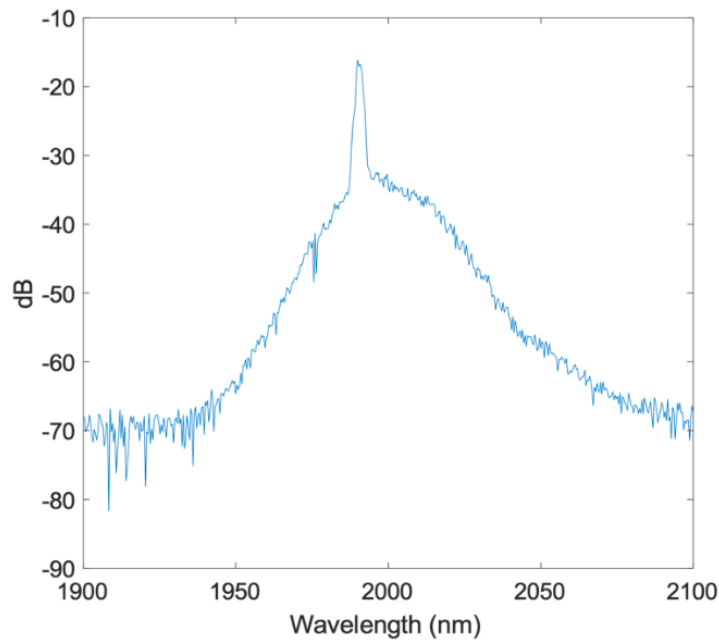


Figure 4.14: Optical spectrum for a CML regime with a CW optical power component.

However, the CW background makes this regime unsuitable for optical amplification as the CW would saturate the gain of the amplifier.

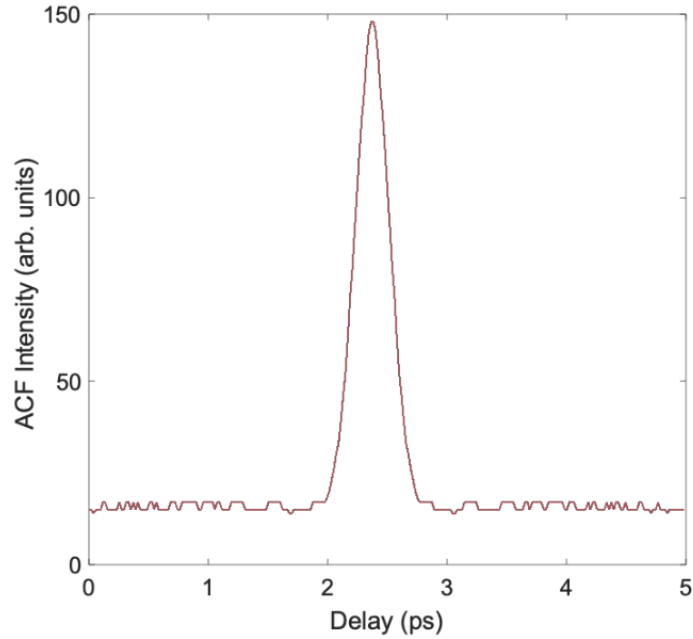


Figure 4.15: Autocorrelation trace (5 ps span) taken while laser operating in a CML regime with an optical CW component.

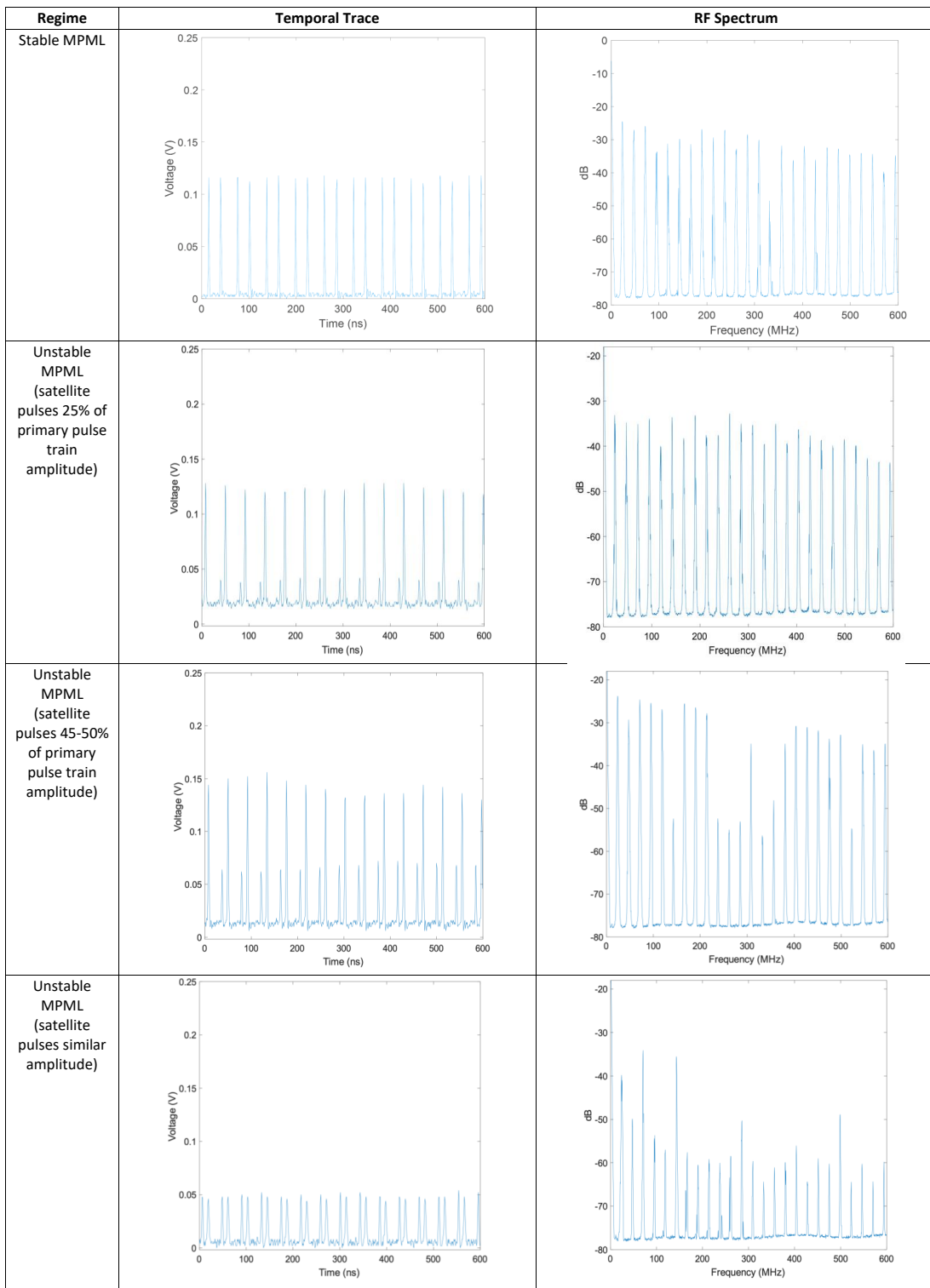
4.3.4 Multi-pulsed Mode-locked (MPML)

The NLPR mode-locked TDFL operated in several MPML states. Temporal and RF traces of the pulse train in stable and unstable MPML regimes are presented in Table 4.1. Some states were stable and could be predicted from the Ginzburg-Landau equation, as described in Section 2.7.2. Others were unstable with satellite pulses containing substantially less power than pulses in the primary train. The stable MPML regime persisted for several minutes, whereas the unstable regimes typically did not persist for longer than 20-40 seconds before transitioning to a CW or noisy pulsed regime. An optical CW component was also observed in unstable MPML regimes to varying extents.

A MPML optical spectrum for the stable regime is shown in Fig 4.16. There is an asymmetry towards longer wavelengths with some prominent Kelly sidebands on both the leading and trailing edge of the spectrum. The optical FWHM is around 4.9 nm, which is consistent with the CML regime. Unlike the EDFL MPML regime in Section 3.3.3, there only appears to be one peak feature.

A long span autocorrelation for any of the pulses in the stable MPML is shown in Fig. 4.17. A 5 ps scan autocorrelation of the stable MPML regime is shown in Fig 4.18. A hyperbolic fit yielded an ACF FWHM of 1.79 ps, and hence a pulse FWHM of 1.16 ps, which is similar to that observed in the CML regime. The MSE was 18.2.

Table 4.1: Side-by-side depiction of temporal and RF traces for a range of stable and unstable MPML regimes.



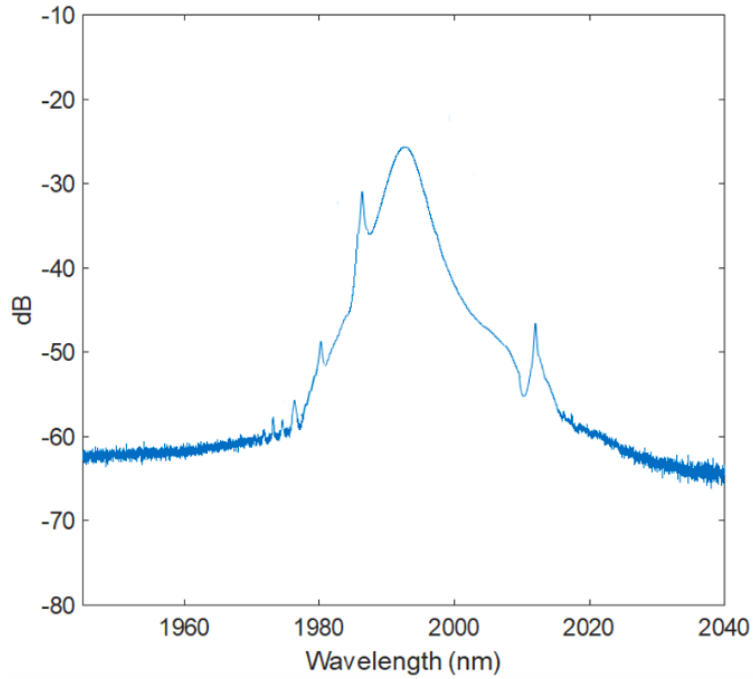


Figure 4.16: Optical spectrum for the stable MPML regime.

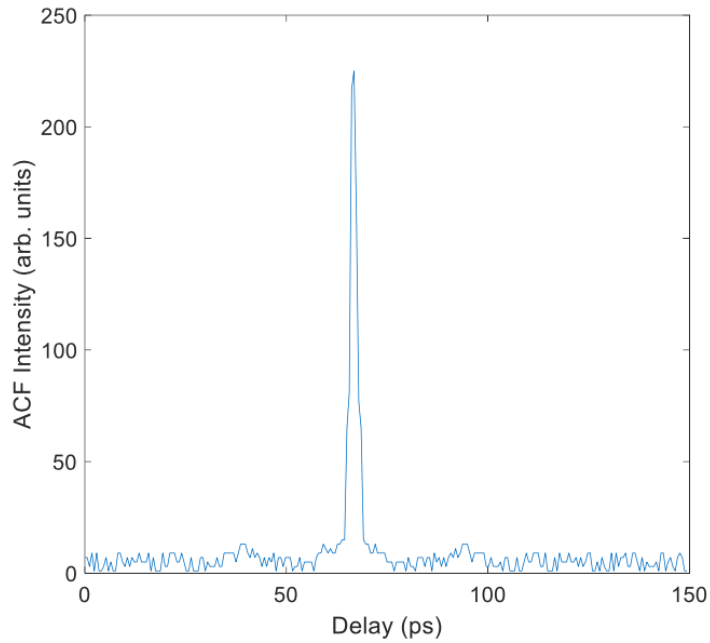


Figure 4.17: Autocorrelation trace (150 ps span) taken while in a stable MPML regime.

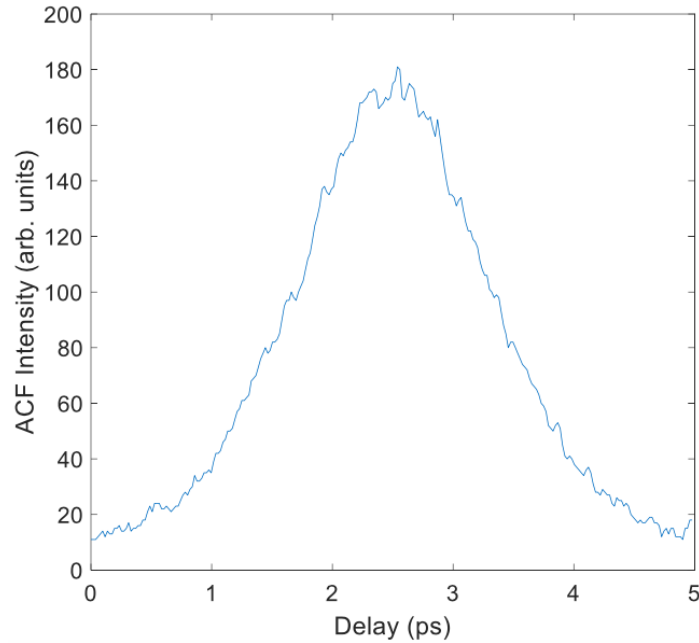


Figure 4.18: Autocorrelation trace (5 ps span) taken while in a stable MPML regime.

4.4 Automation Techniques Investigation

4.4.1 Literature Review

A range of pulse train characteristics have been used to automate CML NLPR mode-locking including RF spectra [4, 5, 6], Stokes parameters [7] and two-photon absorption (TPA) [8].

Winters *et al.* utilised the RF spectrum [4]. Their approach involved using a bandpass filter at the PRF of the laser cavity. A complete polarisation parameter space scan was performed by varying the voltages applied to the intra-cavity liquid crystal retarders used to alter polarisation state, which yielded 22,000 unique mode-locked states. A threshold for the power of the fundamental RF harmonic was used to determine if the laser was CML or CW (when the laser out-couples power from the cavity constantly with no pulses) [4]. QML behaviour was accounted for by measuring the power contained in the RF spectrum multiple times in a row to

check for significant variation as a result of modulation in laser output power in the time domain [4]. Radnatarov *et al.* also used a similar approach to determine when an NLPR laser was stably mode-locked [5].

Woodward *et al.*'s approach to automating an NLPR fibre laser involved a fitness function that was a weighted expression of the temporal trace, optical spectra and RF spectra. This genetic algorithm approach took more than 30 generations on average to obtain an optimum CML state [6].

Olivier *et al.* automated an NLPR mode-locked EDFL using abrupt discontinuities in the time-averaged Stokes Parameters, $\langle S_1 \rangle$, $\langle S_2 \rangle$ and $\langle S_3 \rangle$, that occur when entering a mode-locked regime. Stokes parameters describe the polarisation state of light, as discussed in Appendix C. The $\langle S_1 \rangle$ parameter can be calculated using the average powers in orthogonal polarisation states:

$$\langle S_1 \rangle = \frac{P_x - P_y}{P_x + P_y} \quad (4.1)$$

where, P_x and P_y are the average power values for light polarised in the x and y direction [7].

Olivier *et al.*'s experimental results are presented in Fig. 4.19. The red curve represents $\langle S_1 \rangle$ when varying the angle of the fibre in a motorised polarisation controller. Blue and black curves are from cases where a polarisation perturbation is introduced before and after the active fibre, respectively [7]. In each of the marked transitions, there is a clear jump in the $\langle S_1 \rangle$.

The observed Stokes discontinuities were likened to thermodynamic phase transitions where the cavity goes from a disordered to ordered state [9]. Unlike a thermodynamic phase transition, however, the swept parameter is actuator voltage or polariser angle, rather than temperature [7].

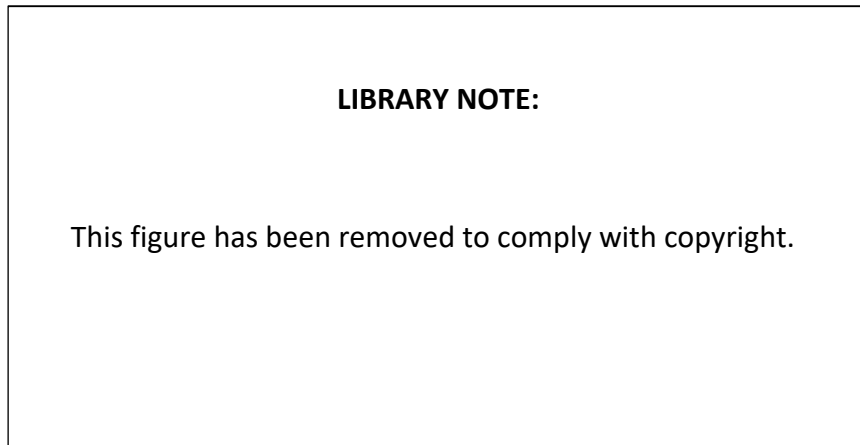


Figure 4.19: Plot of $\langle S_1 \rangle$ as a function of angle relative to the polariser axis, θ . Entire figure reproduced including the original caption from [7]. The authors have used the abbreviation EDF for erbium doped fibre (the active fibre).

Hellwig *et al.* used two photon absorption (TPA) in an NLPR mode-locked EDFL with an extra-cavity photodetector to detect the resulting short wavelength photons [10]. Two-photon absorption (TPA) occurs when two photons are simultaneously absorbed, as depicted in Fig. 4.20 [10]. This quantity can be measured by a photodetector on the output of a laser cavity. TPA increases with the square of the incident optical intensity, I^2 [10]. For a laser source at $2 \mu\text{m}$, each photon would have a wavelength of $1 \mu\text{m}$.

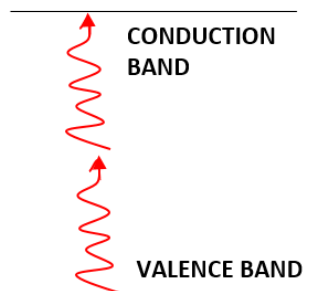


Figure 4.20: Two-photon absorption energy level diagram showing how two photons can bridge the energy gap in a semiconductor.

To characterise this metric, Hellwig *et al.* investigated the relationship between the TPA signal and the operating regime of the NLPR laser [8]. It was noted that some non-ideal pulsed regimes could have large peak powers, and hence large TPA signals, which may lead to the false identification of a CML regime - a QML regime being a prime example [8]. The authors invoked a numerical filtering technique to detect irregular pulses [8].

The following sections will explore these techniques in practice. One of these techniques will be implemented in Chapter 5.

4.4.2 Stokes Parameters

The setup shown in Fig 4.21 was used to investigate Stokes parameter discontinuities as a mode-locking automation metric for our TDFL source.

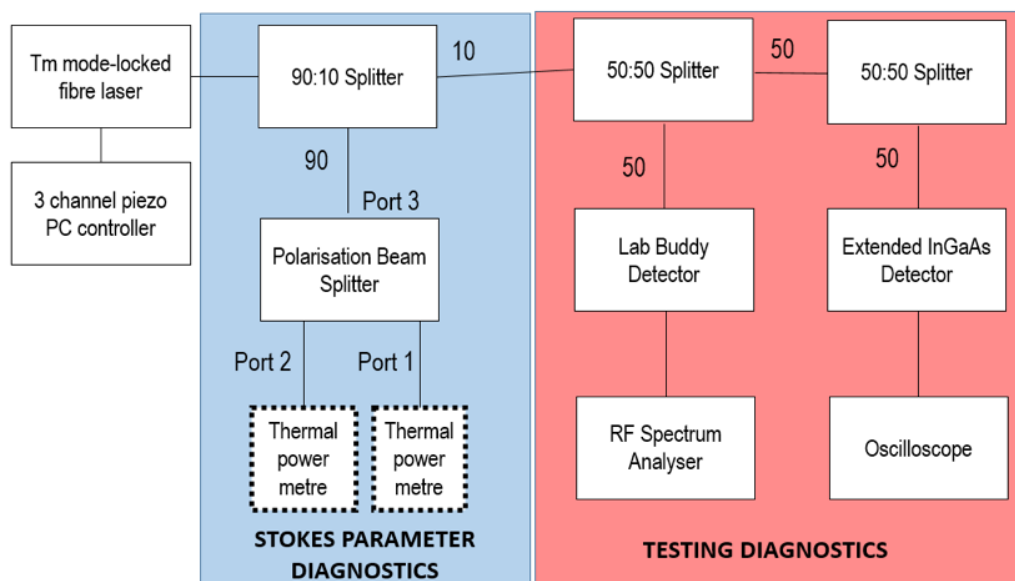


Figure 4.21: Schematic diagram of measurement and diagnostic equipment for Stokes Parameter discontinuities. The remaining 50% power from the second splitter was beam-dumped.

This setup was a preliminary test to observe whether a discontinuity could be detected using a low temporal resolution thermal power meter. A polarising beam-

splitter (AFW POBS-15-3-22ER) was used to divide the power into two orthogonal polarisation components while providing almost complete extinction in the orthogonal linear polarisation.

The iterative process used to automate continuous mode-locking (CML) is shown in Fig. 4.22.

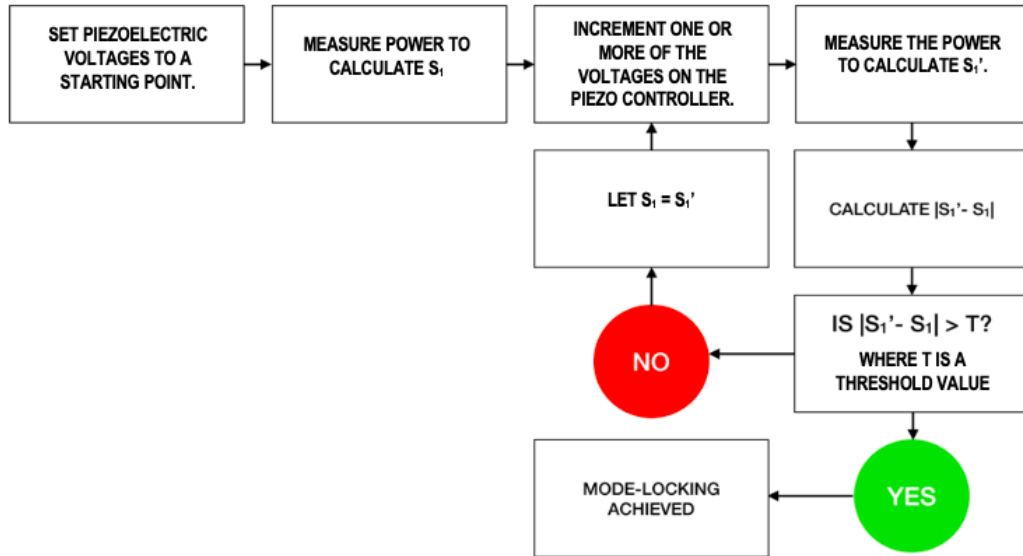


Figure 4.22: A flowchart with an iterative process to determine when mode-locking is achieved based on changes in the Stokes parameter $\langle S_1 \rangle$. S_1' is simply the new value of S_1 at some given point in time when analysing the signal.

To test the procedure, the voltages on the three-channel PC were set to values known to be conducive to mode-locking. CH1 was chosen arbitrarily to be the actuator that had variable strain while transitioning into the pulsed regime from a CW state. The starting position had $V_2 = 77.5$ V and $V_3 = 2.1$ V with the voltage on CH1 incremented in 0.3 V steps starting at 40.4 V. The CH1 step size was reduced to 0.1 V when nearing a pulsing regime.

The results are shown in Fig. 4.23. An abrupt change in $\langle S_1 \rangle$ at $V_1 = 56.30$ V corresponds to the transition from CW to a QML regime. As the QML regime approaches, the power in one of the two orthogonal linear polarisations increased rapidly, as per Appendix H. This reveals that the strain imparted to the fibre by the actuators forced the central part of the pulse to be linearly polarised in a single

orientation. The laser exited the QML regime at 61.0 V on CH1.

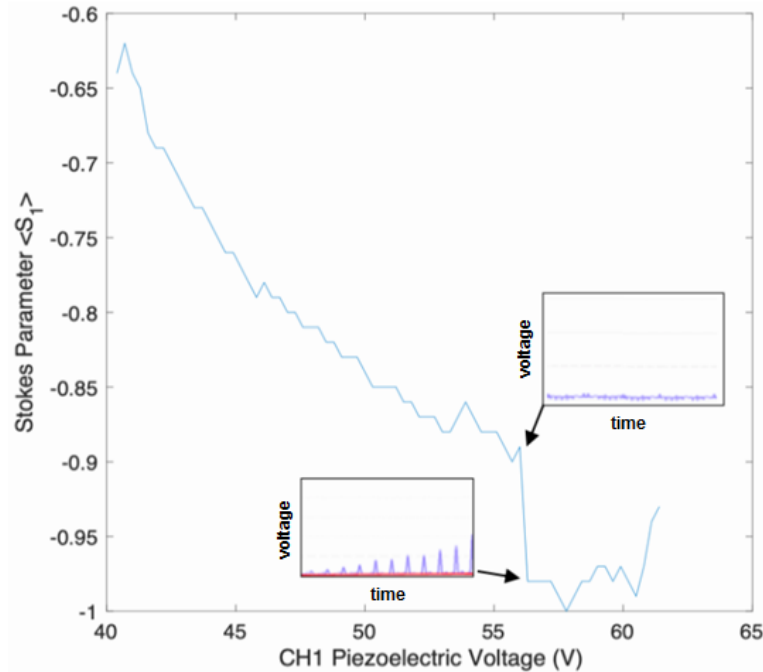


Figure 4.23: Plot of $\langle S_1 \rangle$ as a function of voltage on CH1. The insets show the pulse train temporal trace before and after entering the QML regime. A discontinuity in $\langle S_1 \rangle$ was found to coincide with a regime transition (background CW regime to QML).

The results above show that a Stokes parameter discontinuity can be observed when transitioning into a pulsed regime using an average power measurement. However, Olivier *et al.* obtained a $\langle S_1 \rangle$ discontinuity without mode-locking, as noted for the black curve in the caption of Fig. 4.19.

The power meter was replaced by photodetectors to explore the Stokes parameters with a higher temporal resolution. This would enable an investigation of how S_1 varies over the structure of a pulse rather than having to rely on an average power measurement.

Two extended InGaAs photodetectors (LabBuddy 20 GHz and ElectroOptic Systems EOT 5000F) were used. The oscilloscope would be the limiting factor in displaying and visualising the output as it had a bandwidth of only 1 GHz with a 1 Gs/second sampling rate. A calibration curve relating the voltage measured on the

oscilloscope to the average power incident on each detector was produced in order to calculate S_1 .

The time dependence of the observed photodetector voltages and S_1 are plotted in Figs. 4.24-4.29 for $V_2 = 104.1$ V, $V_3 = 83.7$ V and various CH1 voltages. These voltages were selected because the other diagnostics shown in Fig. 4.21 indicated that the laser would transition from CW to CML over the V_1 range. This sequence of figures clearly shows that there was an observed rapid transition in S_1 during a CML pulse.

Note that there appears to be a rapid fluctuation in the magnitude of the S_1 parameter as voltages are steadily incremented. This can be attributed to the rapidly changing CW power level for the CMLCW regime. Experimental plots of S_1 from the literature, such as Fig. 4.19, have also shown some rapid changes in this parameter near discontinuities.

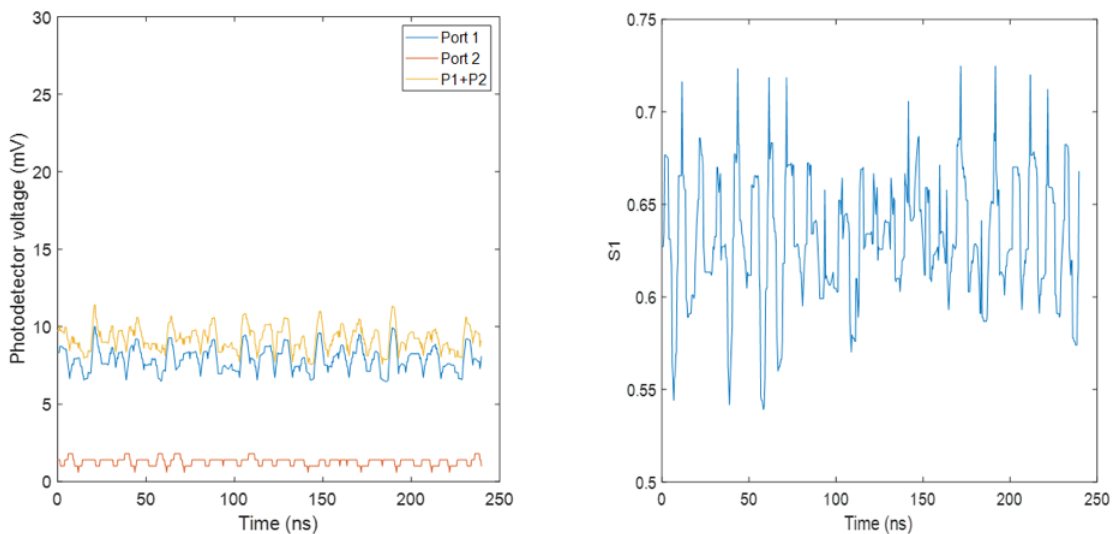


Figure 4.24: A plot of photodetector voltages (left) and S_1 parameter (right) for CH1 voltage: 64.5 V.

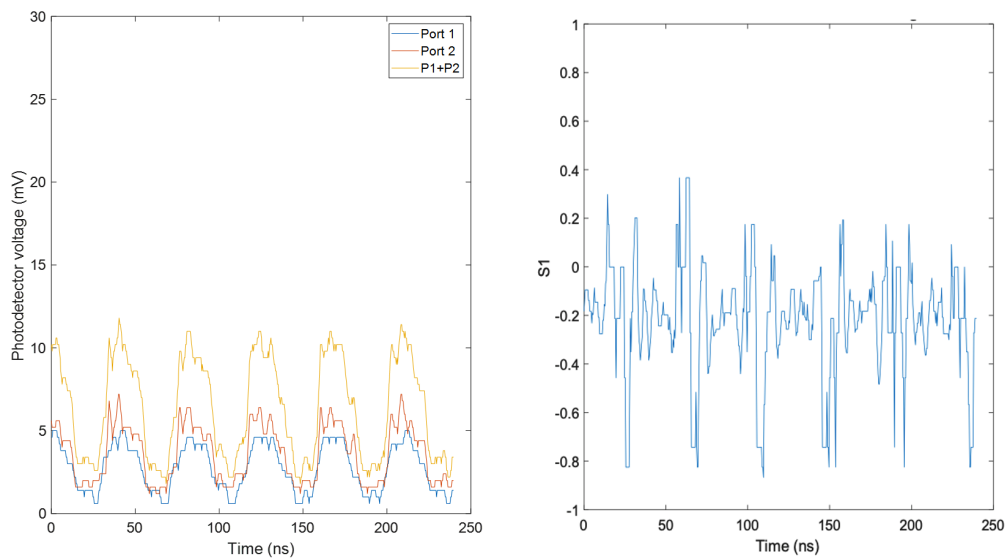


Figure 4.25: A plot of photodetector voltages (left) and S_1 parameter (right) for CH1 voltage: 64.6 V.

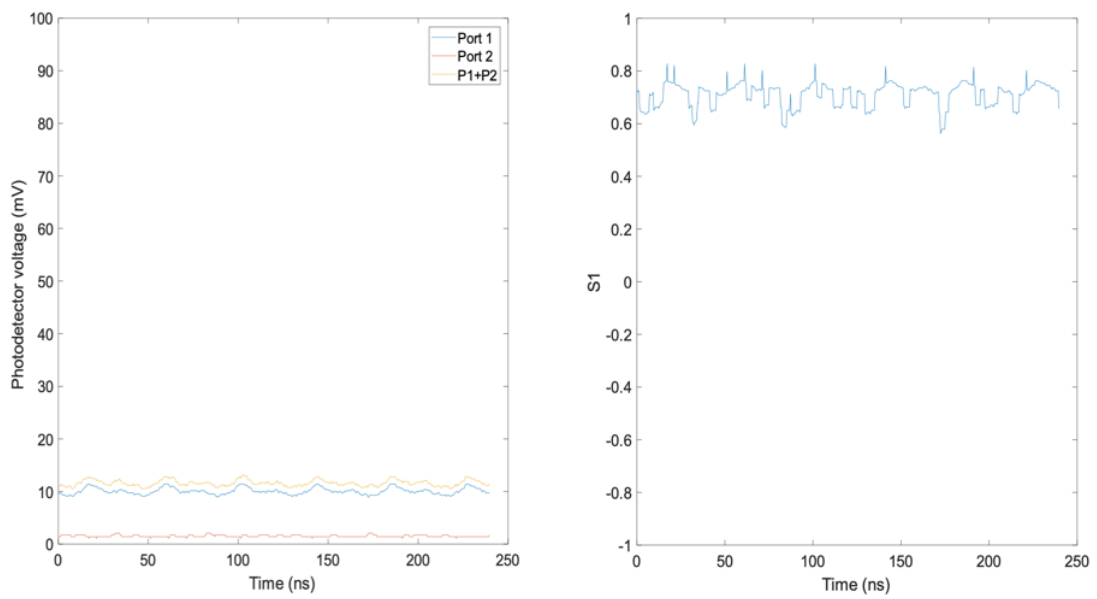


Figure 4.26: A plot of photodetector voltages (left) and S_1 parameter (right) for CH1 voltage: 64.7 V.

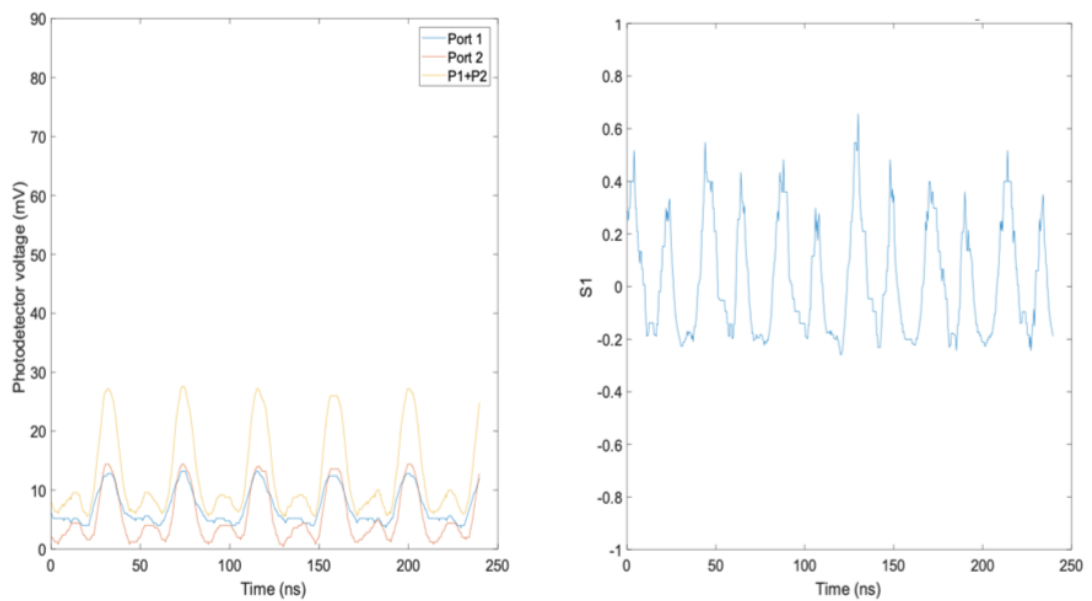


Figure 4.27: A plot of photodetector voltages (left) and S_1 parameter (right) for CH1 voltage: 64.8 V.

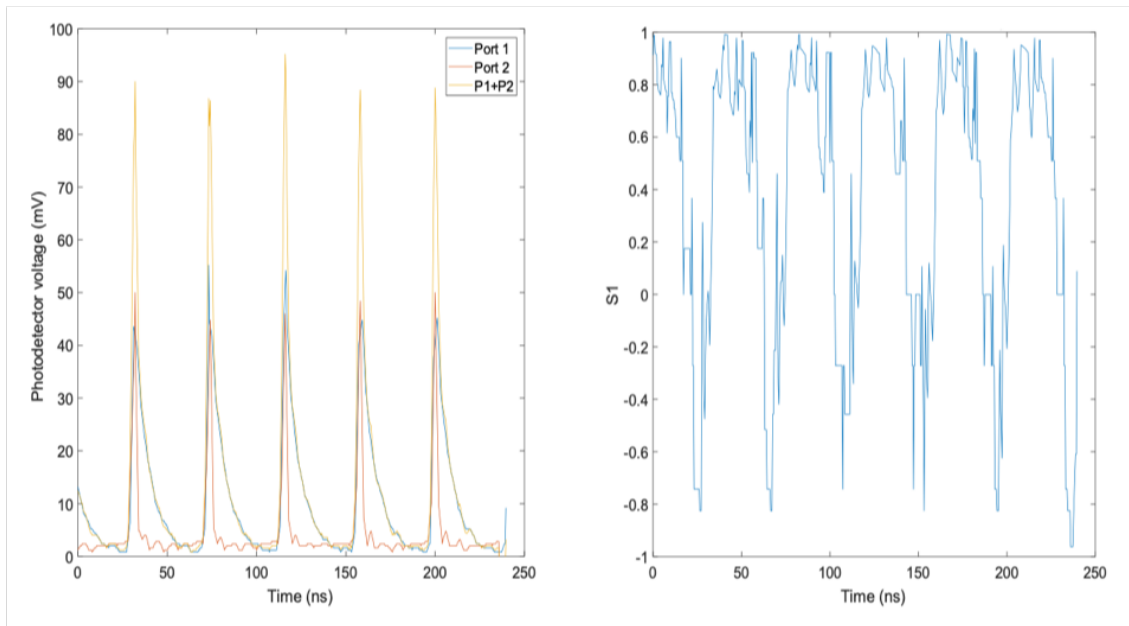


Figure 4.28: A plot of photodetector voltages (left) and S_1 parameter (right) for CH1 voltage: 65.0 V.

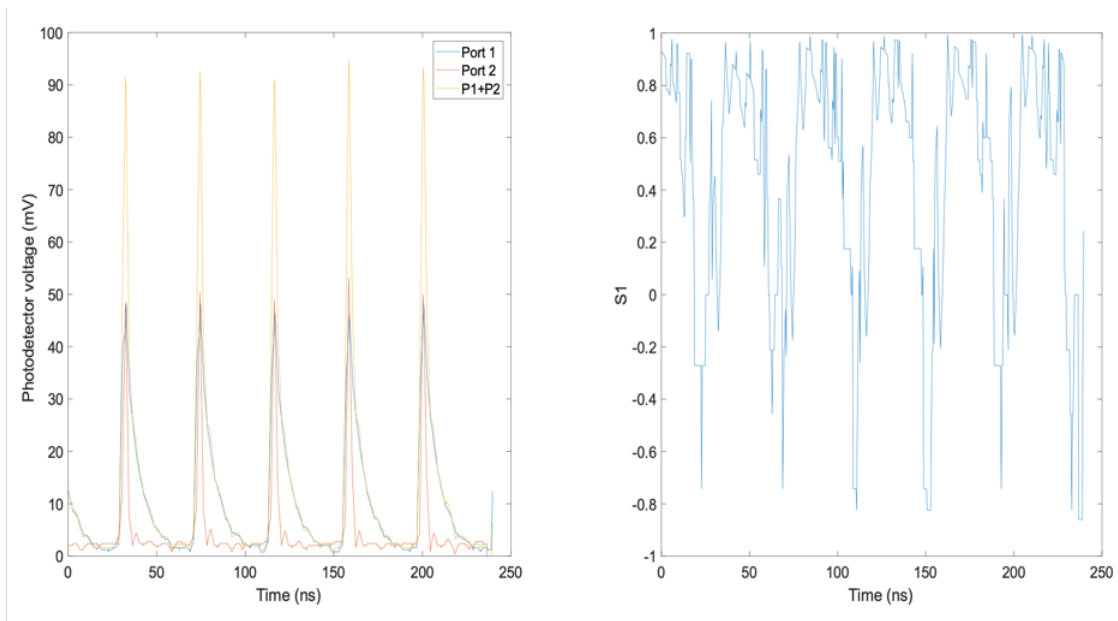


Figure 4.29: A plot of photodetector voltages (left) and S_1 parameter (right) for CH1 voltage: 65.1 V.

This technique was also used to investigate the S_1 response when transitioning into a QML regime. Changes in the photodetector voltages and S_1 for $V_1 = 68.8$ V, $V_2 = 70.3$ V and two adjacent values of V_3 are plotted in Fig. 4.30 and 4.31. CH1 and CH2 voltages on the controller remained at 68.8 V and 70.3 V respectively while CH3 was incremented.

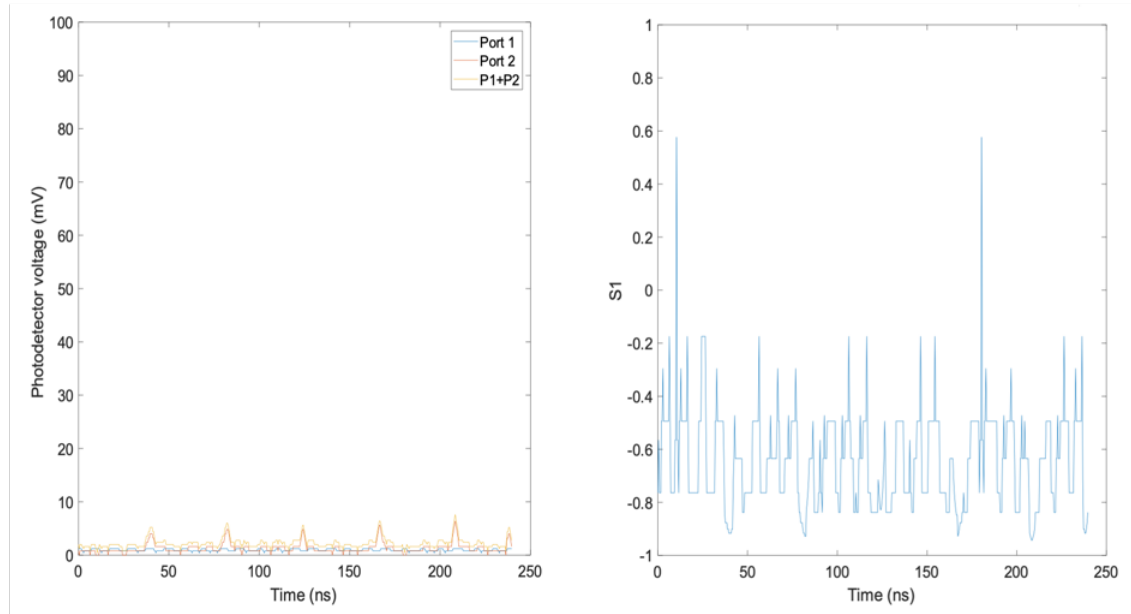


Figure 4.30: A plot of photodetector voltages (left) and S_1 parameter (right) for CH3 voltage: 6.3 V.

Rapid changes in S_1 occur for pulses in the QML regime. The magnitude of the change in the S_1 parameter during a QML pulse is less than for a CML pulse. It may therefore be possible to hence find a threshold value, T, for the automation process outlined in Fig. 4.22, however a detailed characterisation of each regime would be necessary.

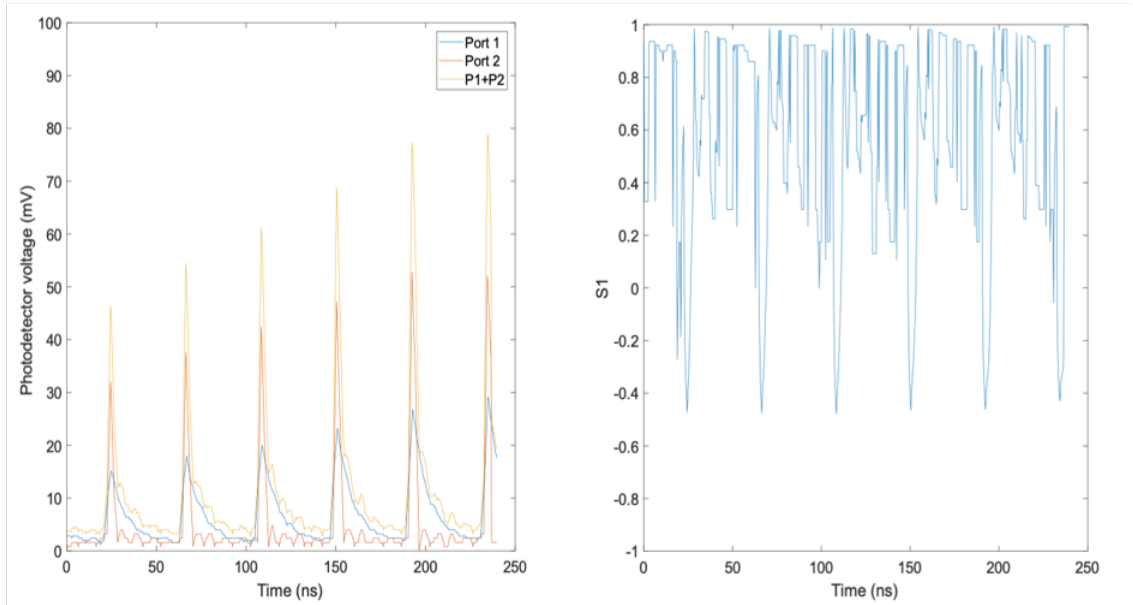


Figure 4.31: A plot of photodetector voltages (left) and S_1 parameter (right) for CH3 voltage: 6.4 V.

From the preliminary tests conducted, Stokes parameter discontinuities appear to be a potential automation diagnostic. A brief table summarising the advantages and disadvantages is presented below in Table 4.2.

Table 4.2: Advantages and disadvantages of using $\langle S_1 \rangle$ discontinuity measurement as a diagnostic for automated mode-locking.

Advantages	Disadvantages
✓ Simple numerical processing to obtain S_1 from measurements	✗ Requires either two photodetectors or power meters which may affect the compactness of the fibre laser design and/or portability
✓ Clear discontinuities observed from pulsing behaviour	✗ A full temporal trace requires the calculation of S_1 at all points across a trace which may take some time depending on the sampling rate
✓ Only requires a small portion of the light out-coupled from the cavity	✗ May not be easy to determine if a regime is CML or an unideal pulsed regime from first glance

4.4.3 Two Photon Absorption (TPA) Diagnostic

A schematic of the TPA characterisation system is shown in Fig 4.32.

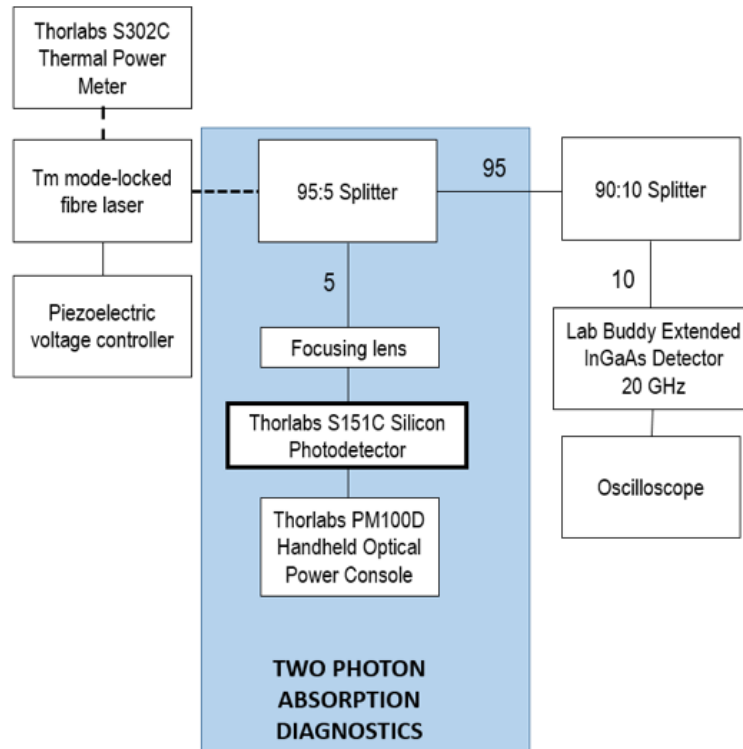


Figure 4.32: Schematic diagram of measurement and diagnostic equipment for two-photon absorption.

A Thorlabs S151C fibre-connected silicon photodiode was used to measure TPA. The responsivity of the photodiode is shown in Fig. 4.33. It is thus clear that the photodiode would respond to the TPA wavelength but not the lasing wavelength.

Different regimes were accessed by changing the intra-cavity polarisation state. The average output power for each regime was measured using a Thorlabs S302C thermal power meter to confirm that each regime had a similar average power.

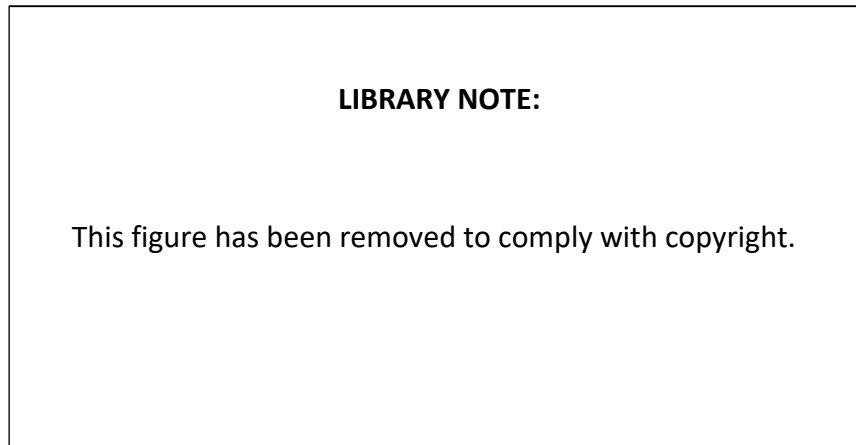


Figure 4.33: Responsivity curve for a silicon photodetector. Diagram originally from [11].

A list of the measured powers for a range of different regimes is shown in Table 4.3. The TPA signal provides good discrimination between CW operation and the mode-locked regimes. Average TPA powers are similar for CML, MPML and NML regimes making it difficult to identify the lasing regime based on this metric alone.

Table 4.3: Average 2 μm and TPA power for different regimes

Regime type	Average laser output power on thermal power meter (mW)	TPA average power from Silicon detector (nW)
Laser off	0	0.1
Continuous wave (CW)	35	1.0
Continuously mode-locked (CML)	40	41-43
Q-switched mode-locked (QML)	32	25-38
Multi pulsed mode-locked (MPML)	42	40-44
Noisy mode-locked (NML)	39	37-43

An alternative approach would be to monitor the temporal evolution of the TPA signal from the 2 μm pulses. This would require a wideband silicon photodiode however, which was not available.

To demonstrate that such an approach should provide a useful diagnostic, pulse trains were recorded in CML and QML regimes. As expected, from Section 3.3.1,

the QML pulses had a larger amplitude near the centre of the Q-switched envelope than the CML pulses. Thus, when squared to simulate the TPA process (a second order process), the amplitude for the TPA pulses is much larger than for QML compared to CML, as shown in Figs. 4.34 and 4.35. Additionally, QML pulses have a finite extent.

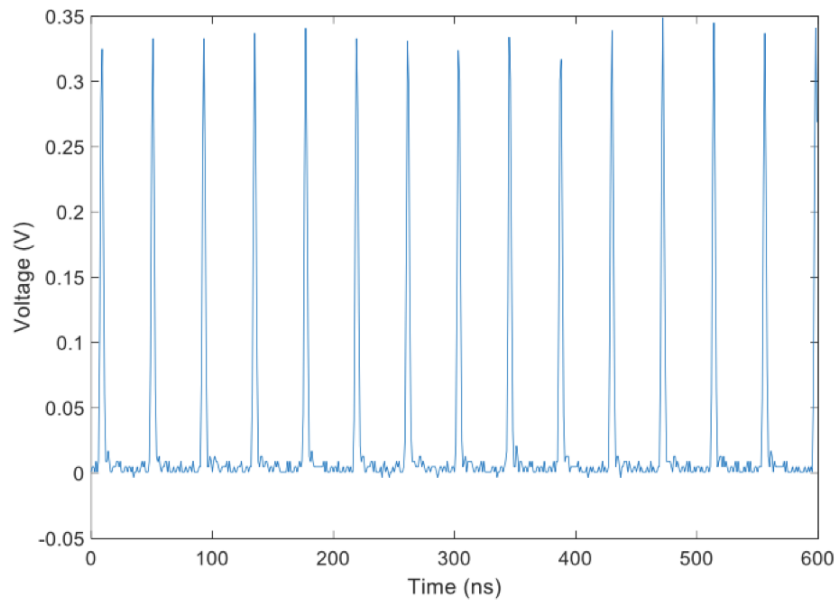


Figure 4.34: Simulation of TPA pulses in the CML regime using a 2 μm trace.

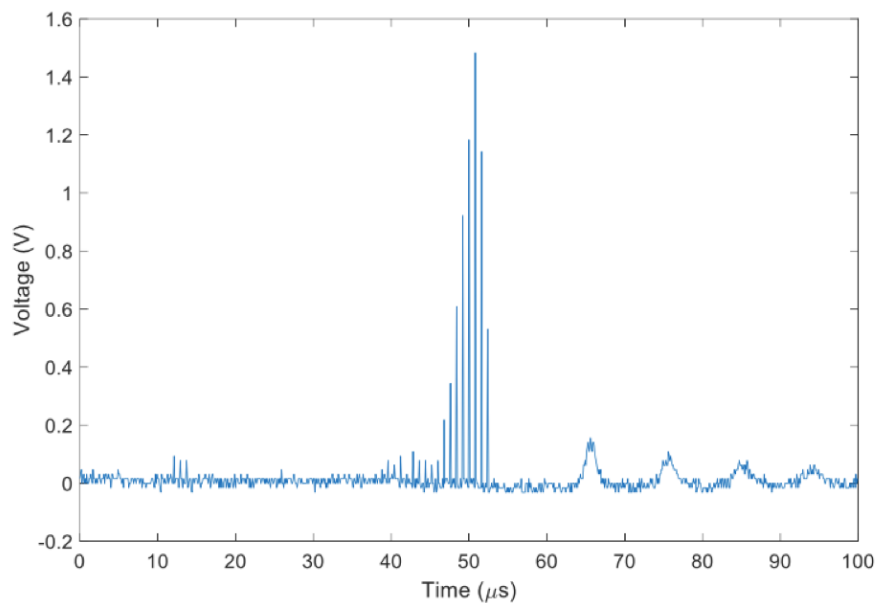


Figure 4.35: Simulation of TPA pulses in the QML regime based on a 2 μm trace. Note that there were oscillations outside the main envelope.

It may not be possible to use this TPA approach to discriminate against MPML or NML pulses however as they do not have a finite temporal extent.

The shape of the QML envelope was transient with asymmetry due to the laser being in an unstable parameter space based on the cubic-quintic Ginzburg-Landau equation.

A brief table summarising the advantages and disadvantages of TPA is below in Table 4.4.

Table 4.4: Advantages and disadvantages of using a TPA power measurement as a diagnostic for automated mode-locking.

Advantages	Disadvantages
✓ Easy to distinguish between CW and a pulsed regime based on a single metric	✗ Can't readily distinguish between CML and some multi or noisy pulsed mode-locked regimes based on average power measurements alone
✓ Single real-time measurement using affordable equipment	✗ Utilising TPA temporal traces may require a system-specific (lasing wavelength-dependent) high-speed photodetector which is potentially expensive
✓ Unlike Stokes Parameter discontinuities, only need one photodiode power metre	

4.4.4 RF Spectrum Diagnostic

Section 3.3.2 and RF spectra of the various mode-locked regimes in this chapter suggest that information within these spectra should be useful for distinguishing the lasing regime.

This section investigates how amplitude modulation within the RF frequency comb can be used to distinguish between CML, MPML, NML, QML and other lasing regimes. The approach is to compare the RF spectrum of the output with a known 'baseline' CML measurement. RF spectra for the different regimes are in Table 4.5.

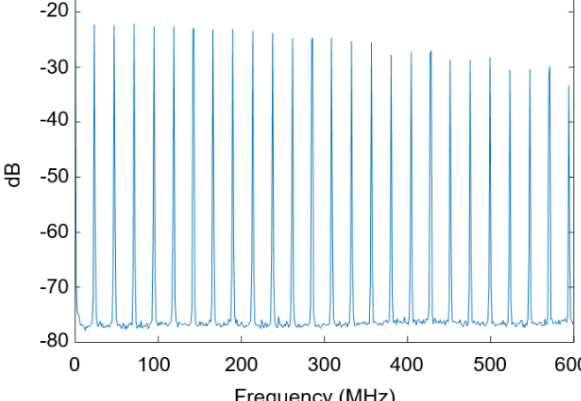
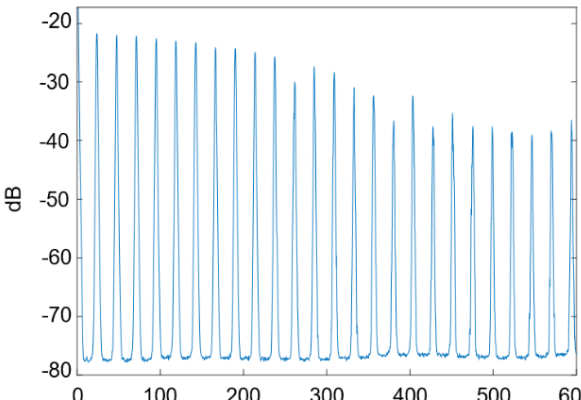
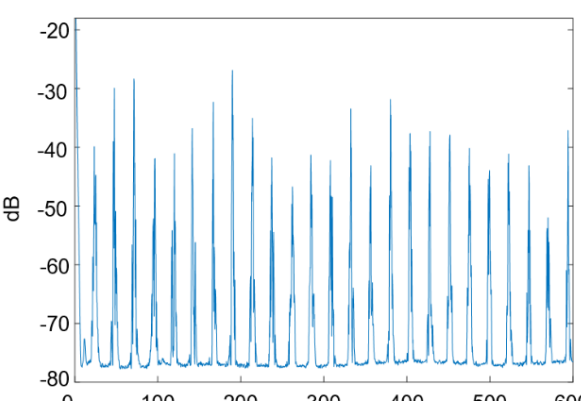
Baseline measurement/characterisation (only performed once)

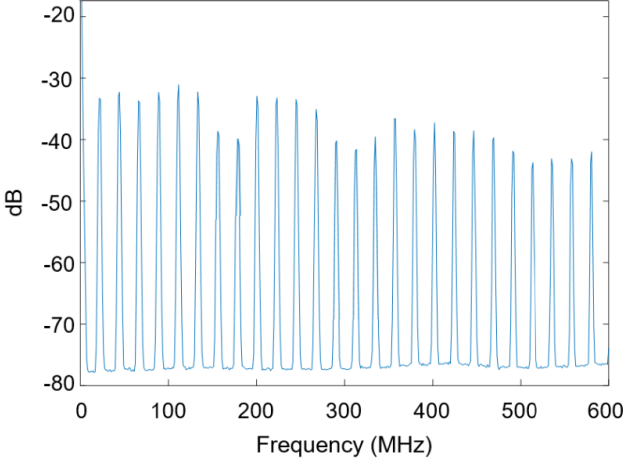
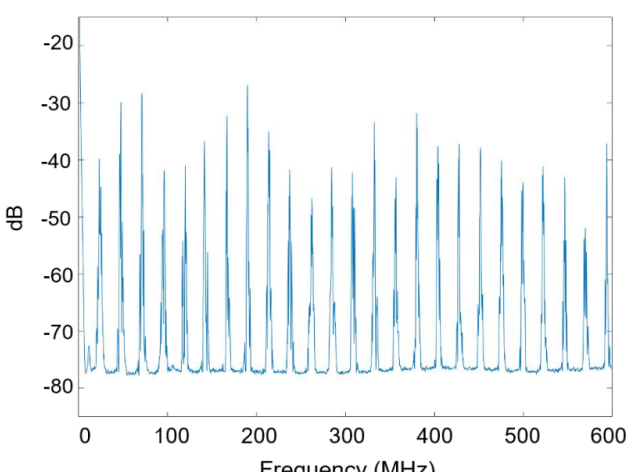
- Acquire an RF spectrum when the laser is known to have an ideal CML output (this can be assessed using the diagnostics mentioned in Chapter 3)
- Obtain a baseline measurement for amplitude modulation across the RF frequency comb by:
 - Recording the amplitude of all harmonic peaks across the spectrum
 - Dividing the spectrum into groups of 3 non-overlapping peaks
 - Calculating the amplitude difference (the difference between the harmonic peaks of smallest and largest amplitude) for each group

Regime categorisation measurement (performed whenever you want to assess laser output)

- Acquire an RF spectrum for the laser operating in some state
- Repeat the three bulletpoints under the baseline measurement section but for the current trace
- Compare the peak-height differences between the current spectra and the baseline for each group. A value of 0 is assigned if a group has the same or less amplitude modulation than the CML regime (within some tolerance) otherwise a 1 is assigned.
- Categorise the regime
 - If a value of 0 is assigned for all groups, then it is inferred that the laser is operating in a CML state.
 - If a value of 1 is assigned for one or more groups, then it is inferred that the laser is not operating in a CML state and that the intra-cavity polarisation state must be adjusted.

Table 4.5: Table containing RF spectrum traces of the laser train output for different regimes and the amplitude modulation (peak-height) metric across groups of harmonics.

Regime type	RF spectrum trace	AM test results
CML		<p data-bbox="1086 427 1254 450">[0;0;0;0;0;0;0;0]</p> <p data-bbox="1142 461 1198 483">PASS</p>
CML with some (large) amplitude modulation		<p data-bbox="1086 875 1254 898">[0;1;1;1;1;1;1;0]</p> <p data-bbox="1142 909 1198 931">FAIL</p>
NML		<p data-bbox="1086 1350 1254 1373">[1;1;1;1;1;1;1;1]</p> <p data-bbox="1142 1384 1198 1406">FAIL</p>

<p>Unstable MPML with small satellite pulses</p>		<p>[1;1;1;1;0;0;0]</p> <p>FAIL</p>
<p>QML</p>		<p>[1;1;1;1;1;1;1;1]</p> <p>FAIL</p>

A sweep time of 200 seconds was used for this test. A reduced sweep time, at the expense of video bandwidth (VBW) and resolution bandwidth (RBW) will be explored in Chapter 5.

A brief summary of the advantages and disadvantages of RF spectrum amplitude modulation analysis is shown in Table 4.6.

Table 4.6: Advantages and disadvantages of using RF spectrum amplitude modulation as a diagnostic for automated mode-locking.

Advantages	Disadvantages
✓ A distinct signal between different regimes with results predictable by Fourier theory simulation	✗ Requires an RF spectrum analyser – costly and bulky
✓ Relatively computationally inexpensive	✗ Speed limited by interfacing between spectrum analyser and computer
✓ Multiple checks by discretising peaks into several batches across the frequency comb	

4.5 Automation Discussion

A range of automation techniques were investigated in this Chapter including Stokes Parameter discontinuities, TPA signals and RF spectra. Preliminary tests were conducted for each of these diagnostics with the relative merits of each metric considered.

Stokes Parameter discontinuities provided insight into the behaviour of the lasing output, however the change in the S_1 was not necessarily a good indicator of the state the laser was operating in. Large changes in S_1 were obtained when the laser was brought into a pulsed state but a large amount of characterisation would be needed to distinguish between QML and CML regimes, both of which have large changes in the power between orthogonal polarisation components. Modelling and/or empirical evidence would need to be recorded to determine a suitable threshold.

Furthermore, as documented in Section 4.4.2, previous attempts to use this parameter have shown that discontinuities or large changes in the parameter can occur without stable mode-locking being achieved [4]. This behaviour is apparent from the caption of Fig. 4.20 [4]. Consequently, it is possible that a potential threshold for discontinuity size to distinguish between CML and non-CML regimes may not even exist.

TPA signals were an alternative metric of interest that has been in the literature. Taking average power measurements of the TPA signal did not provide adequate discrimination between CML and different non-ideal regimes. This was because noisy or CW behaviour can still contribute to TPA, as the signal is proportional to the square of the intensity incident on the photodetector. Additionally, one would need to characterise the signal for multiple pump currents/powers as this influences the average output power from the cavity [8].

Temporal TPA traces can be acquired either by squaring the temporal output of the laser or from direct measurement using a high speed photodetector that is sensitive to TPA photons. In testing, integrating the TPA signal over a long time window yielded different results for CML and QML regimes. It is important to sample for a duration of time that captures most of the QML envelope, otherwise it may be more difficult to discern between the two regimes. This is because QML pulses near the centre of the envelope will have similar or slightly larger amplitudes than CML pulses. Consequently, a similar time-integrated quantity could be returned if only sampling over a few pulses.

One deterrent to pursuing this approach was the cost of acquiring a high speed Silicon photodetector. Silicon would be suitable for the NLPR sources as it is sensitive to the two-photon wavelength. Pump wavelengths that are within the responsivity curve of Silicon may lead to measurement confusion as the output signal may also contain pump leakage.

Lastly, an RF spectrum diagnostic was explored. As more RF data was captured for a range of regimes, it became more apparent how sensitive a broadband RF spectrum trace was to intensity noise, timing jitter and satellite pulses in the temporal domain. The broadband trace provided the best indication of whether the EDFL output was CML or not out of all the measurement techniques in Chapter 3. Optical spectra and the autocorrelation traces only changed small amounts between regimes. Similarly, temporal traces taken on an oscilloscope were bandwidth and sampling rate limited and also had discretised voltages. The advantage of the RF metric is its intuitive nature as results can be predicted from Fourier theory. A high dynamic range attainable from most RF spectrum analyser instruments was another advantage.

Traces from non-ideal regimes revealed that amplitude variation can occur in multiple places across the RF spectrum. Typical RF approaches in the literature have only used the amplitude of the first harmonic to determine whether a source is mode-locked. RF spectra presented across Chapters 3 and 4 revealed that this can often be misleading, which is why the metric devised uses information across many harmonics.

4.6 Summary

This chapter reported on the demonstration of an NLPR mode-locked TDFL and an investigation of various diagnostics that might be used to determine the operating regime. Typical properties of the laser operating in a CML regime are summarised in Table 4.7. While these may appear similar to the NLPR mode-locked EDFL reported in Chapter 3, it was substantially more difficult to obtain a clean mode-locked state with the TDFL. Cladding pumping, instead of core pumping, is proposed as a possible reason for the additional noise and stability issues.

Table 4.7: Table of summary statistics for thulium source in highest power, stable CML state.

Central wavelength (nm)	Optical FWHM (nm)	Pulse duration (ps)	Repetition rate (MHz)	Average power (mW)	Peak power (kW)	Pulse energy (nJ)
1992	4.7	1.15	22.3	120	4.40	5.38

The cladding-pumped thulium mode-locked NLPR source demonstrated had pulse energies and profiles that compare favourably with the literature. Li *et al.* demonstrated a thulium NLPR laser that stably mode-locked at a 5th harmonic (a solution based on Ginzburg-Landau equation) and lased around 1787 nm [12]. The optical spectra obtained suggest a Fourier-transform limited duration of 750 fs [12]. An output power of 3 mW suggests the source yielded pulse energies of 0.02 nJ [12].

Jia *et al.* reported on a thulium NLPR mode-locked laser pumped by a erbium/ytterbium co-doped fibre amplifier [13]. The output train was characterised in a harmonic mode-locked regime and QML regime. A pulse duration of 617 ps with a 3.2 MHz repetition rate was recorded [13]. The authors noted that noisy pulse bunch regimes existed for certain pump powers [13].

Tao *et al.* reported on a thulium NLPR mode-locked laser operating at 1978 nm. A pulse width of 560 fs and a repetition rate of 55 MHz was achieved [14]. An average output power for the source was not given [14].

Liu *et al.* reported on a higher pulse energy (12 nJ) however their autocorrelation had a wide temporal feature of fairly constant intensity (around 100 ps) [15]. A narrow coherence spike (indicative of a 406 fs pulse feature) was presented on top of the wide feature [15]. This noisy pulse structure may not necessarily be ideal for amplification and the other applications discussed in Chapter 1.

Stability of the cladding pumping scheme was an issue and is discussed in Section 6.2.1.

The diagnostics investigated included Stokes parameter discontinuities, two-photon absorption (TPA) signals and changes in the RF spectra.

TPA and Stokes Parameter Discontinuities were found to yield results that may not discriminate between CML and other non-ideal regimes. This observation is consistent with that of Woodward *et al.* who noted that two-photon absorption (TPA) or second harmonic generation (SHG) a QML regime may be mistaken as a CML regime due to high peak power [6].

Two key benefits of the RF spectrum analyser as an automation metric are the large dynamic range and substantially different response in its output between different regimes. This particular diagnostic appears promising and this preliminary investigation has warranted further exploration. Chapter 5 will focus on implementing the RF spectrum amplitude modulation diagnostic into an NLPR fibre cavity.

Chapter 5

Automation of a Diode-pumped Holmium NLPR Fibre Laser

5.1 Introduction

This chapter focuses on the characterisation and automation of a diode-pumped NLPR mode-locked holmium doped fibre laser (HDFL). An overview of the source is presented in Section 5.2. The source utilised the same electronic polarisation controller as the thulium source in Chapter 4. Unlike the sources from the previous chapters, the Newport manual polarisation controller was not spliced in to the cavity – resulting in an intra-cavity polarisation state that was fully controllable electronically.

A characterisation of the source in a continuously mode-locked (CML) state is reported in Section 5.3. Automation of the NLPR laser was achieved using the process outlined in Section 4.4.4. A detailed description is given in Section 5.4.

The broadband RF spectrum approach provided good discrimination between CML states and competing regimes, such as Q-switched mode-locked (QML), continuous mode-locked with a CW component (CMLCW) and multi-pulsed mode-locked (MPML). Our amplitude variation approach differs from other standard RF ap-

proaches in the literature, discussed in Section 4.4.1, which often only use a single harmonic. Additionally, unlike Stokes Parameter measurements, discussed in Section 4.4.2, this method only relied on a single photodetector and an RF spectrum analyser.

Lastly, results from the automation diagnostic are presented in Section 5.5.

Several authors have reported on holmium NLPR mode-locked lasers in recent years. Li *et al.* reported on a holmium fibre laser that was used to seed a Ho:YLF amplifier. The NLPR seed source produced pulses with a 920 fs duration and pulse energy of 800 pJ [1]. Kelly sidebands in the optical spectrum were suppressed during amplification as they were at wavelengths that were not part of the amplifier's gain profile [1]. A relative intensity noise of 0.13% was obtained from the pump and oscillator, making it a good source for seeding [1].

Kamynin *et al.* developed an all-fibre holmium NLPR mode-locked laser pumped by a 1125 nm ytterbium doped fibre laser. They reported on stable harmonic (multi-pulsed) mode-locking with an average output power of around 5 mW [2]. An autocorrelation measurement was not taken however there was a 52 ps upper bound on the pulse duration [2].

Diode-pumped holmium sources have a few attractive advantages including size and weight benefits. Additionally, diode-pumping eliminates the need to perform a comprehensive characterisation for instabilities that would exist if you used another laser as a pump.

Sorokina *et al.* have demonstrated diode-pumped holmium doped mode-locked fibre lasers that use a combination of semiconductor saturable absorber mirrors (SESAMs) and non-linear amplifying loop mirrors (NALMs) [3,4]. To the best of our knowledge, the source introduced in this Chapter is the first diode-pumped NLPR mode-locked holmium laser at 2 μm .

5.2 Mode-locked Holmium Fibre Laser

5.2.1 Cavity Configuration

A schematic of the NLPR mode-locked HDFL laser cavity is presented in Fig. 5.1. An 1150 nm (Innolume, LD-1152-FBG-300) diode pumped a 1.2 m length of the active fibre (0.5 wt.% holmium-doped fibre) via a 1150/2050 nm non-polarisation maintaining (non-PM) wavelength division multiplexer (WDM). The 1150 nm pumping scheme, from Section 2.2.2, was used due to the availability of commercial diodes and the four-level nature of the transition.

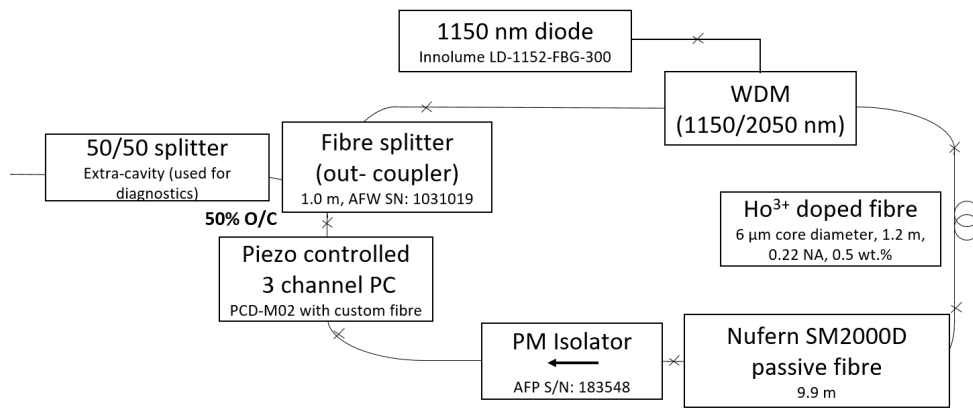


Figure 5.1: A schematic of the NLPR mode-locked HDFL cavity. WDM = wavelength division multiplexer, PC = polarisation controller and x marks the position of fibre splices or fibre connectors.

The holmium fibre had a 6 μm core diameter with an NA of 0.22. This holmium-doped silica fibre has a long lifetime and achieved a record slope efficiency [5]. The system was core-pumped, as discussed in Section 2.2.3, yielding output powers of up to 6 mW from the mode-locked ring cavity.

The output of the active fibre was coupled into a non-PM passive fibre (Nufern SM 2000D). Light passed through a PM isolator. The total fibre length of the cavity was estimated to be 12.1 m - the same as the erbium cavity from Chapter 3.

Birefringence within the cavity was adjusted using an electronically controlled 3-axis piezo polarisation controller (PCD-001 3 channel piezo driver voltage unit with

a PCD-M02 polarisation controller, PC). The output coupler was a 50/50 wide-band splitter rated for 1550 nm. Fibre splitter testing revealed approximately 62% of power was outcoupled per round trip at the HDFL lasing wavelength of approximately 2060 nm.

5.2.2 Results

The purpose of this characterisation was to see whether a clean CML regime could be obtained with the HDFL source. A low doping concentration and weaker pump compared to the previous EDFL and TDFL sources meant it was necessary to evaluate the performance of the source.

Characterisation diagnostics were the same as in Fig. 3.2, however a 50% splitter was used as the primary splitter rather than the 90% splitter. The reason behind the change was the lower average power from the HDFL when continuously mode-locked compared to the TDFL and EDFL - mainly due to the weaker pump.

A CML pulse train in the temporal domain is presented in Fig. 5.2. This regime was obtained using a pump power of 220 mW and a net cavity fibre length of 12.1 m (as per Section 5.2). The output power of this regime was 4.2 mW. The amplitude variation over eleven consecutive peaks was 6.5%. This level of temporal domain amplitude variation is similar to that observed with the TDFL in Chapter 4. There were no prominent satellite pulses or CW components.

A 600 MHz, long sweep time RF spectrum, acquired while the laser was operating in a CML regime, is shown in Fig. 5.3. A resolution bandwidth (RBW) of 30 kHz and video bandwidth (VBW) of 100 Hz provided ample resolution to assess variation between harmonics. These RBW and VBW settings resulted in a sweep time of 200 seconds. The observed roll off over 600 MHz was 8.6 dB, which is consistent with experimental results obtained from long sweep time, high-resolution RF traces for other CML sources [6].

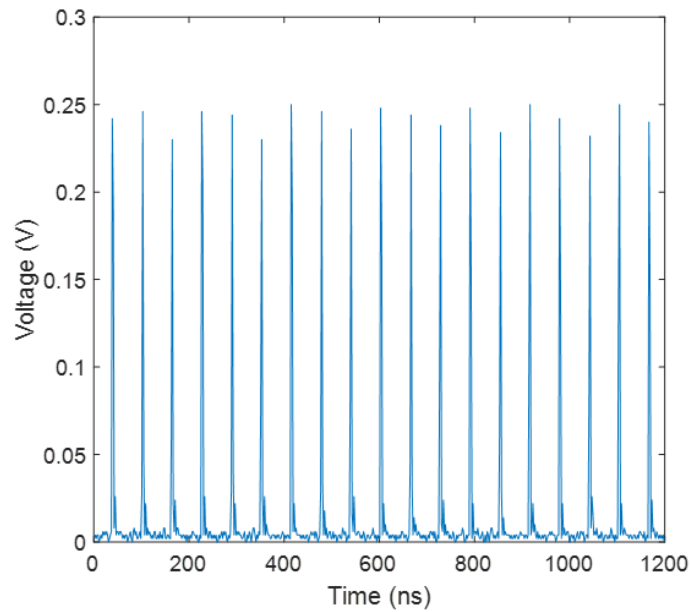


Figure 5.2: Temporal trace of a CML pulse train.

The laser output had a pulse repetition frequency (PRF) of 17 MHz, which corresponded to a 59 ns round trip time.

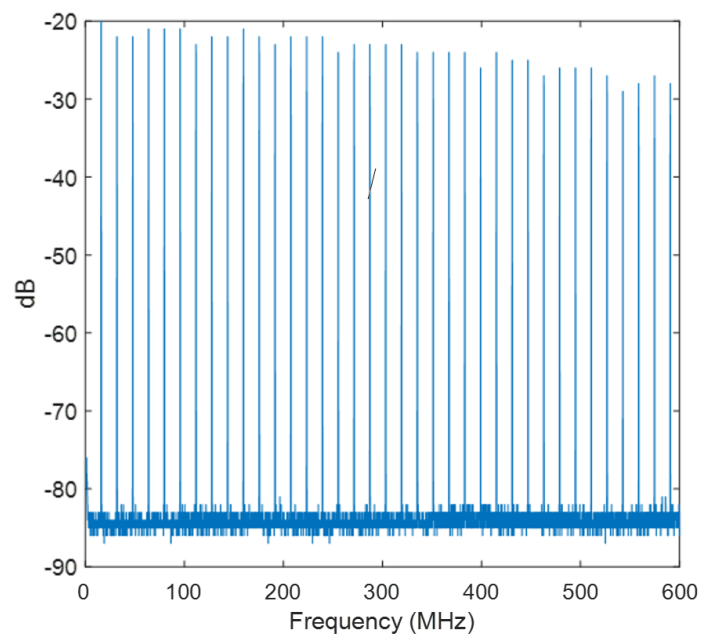


Figure 5.3: Broadband RF spectrum of a CML pulse train with 200 s sweep time.

A CML optical spectrum is shown in Fig. 5.4. The optical FWHM is 8.6 nm based on the centre of the spectrum although the strong Kelly sidebands exceed

the power of the broad central peak. These sidebands would need to be taken into consideration when using the HDFL as a seed source for an amplifier to avoid an undesirable signal.

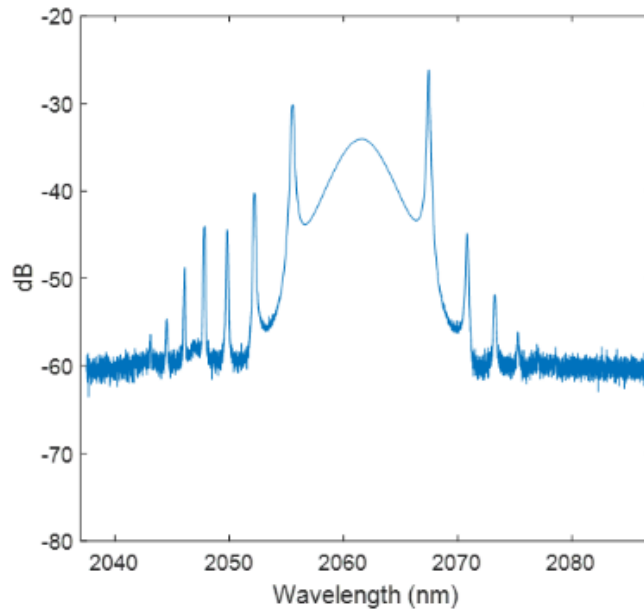


Figure 5.4: Optical spectrum for the holmium NLPR operating in a CML regime.

An autocorrelation measurement, shown in Fig. 5.5, resulted in a 770 fs pulse FWHM from a 1.1 ps Gaussian fit. The fit had an MSE of 1.78. A 150 ps scan revealed no key pedestal, satellite pulses or noisy features, as shown in Fig. 5.6.

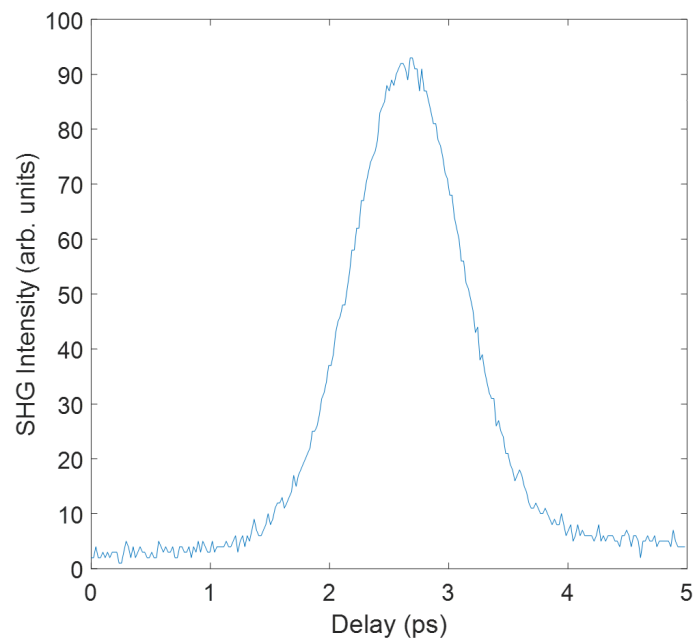


Figure 5.5: Autocorrelation trace (5 ps span) for holmium NLPR operating in a CML regime taken for an average power of 4.2 mW.

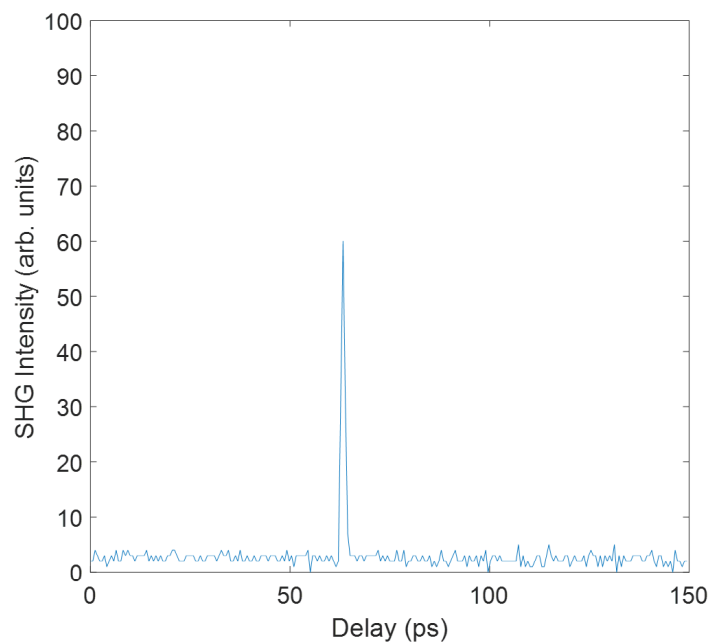


Figure 5.6: Autocorrelation trace (150 ps span) for holmium NLPR operating in a CML regime.

5.2.3 Discussion

The NLPR mode-locked HDFL demonstrated stable sub-ps pulsing. There are a range of improvements to the system that could be made, as discussed in Chapter 6. Mode-locking was achieved solely using the electronic polarisation controller, which reduced the degrees of freedom in the system. Lack of a manual polarisation controller did increase the difficulty of finding a stable CML state for characterisation. The automation algorithm outlined in the next section eased this difficulty somewhat.

A time-bandwidth product of 0.468 was attained, which is close to the theoretical limit of 0.44 for a Gaussian pulse.

5.3 Automation

5.3.1 Overview

Section 4.4.4 discussed the automation of a mode-locked fibre laser using its RF spectrum. This method was identified in Chapter 4 as being the most robust for discriminating between non-ideal regimes (including QML) and CML regimes. A flowchart for this process is shown in Fig. 5.7.

A schematic of the RF diagnostic is presented in Fig. 5.8. A 95:5 splitter was used with the 5% tap fed into an extended InGaAs photodetector (EOT 5000F). An SMA cable connected the detector and RF analyser.

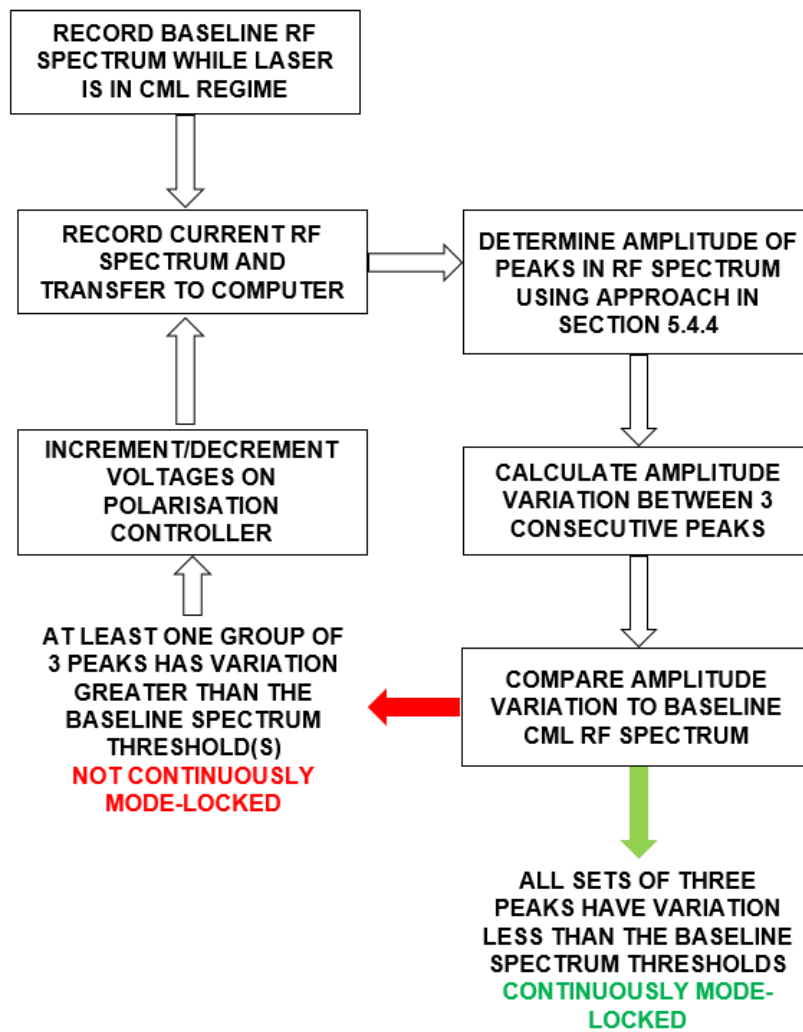


Figure 5.7: A flowchart of an iterative process to determine when mode-locking is achieved based on amplitude variation in radio-frequency (RF) spectra of the pulsed train laser output.

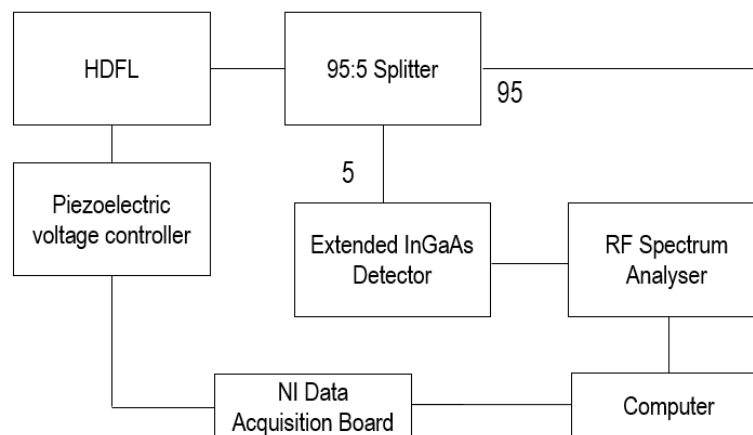


Figure 5.8: Diagnostics used for the automation of an NLPR mode-locked HDFL using RF spectrum analyser metrics.

5.3.2 RF Spectrum Collection

A Rhode and Schwarz RF Spectrum Analyser (FSP30) was used to collect the RF spectra. Communication between a computer and the analyser was via a RS232 serial port. The MATLAB Instrument Control toolbox ensured that the appropriate drivers were installed for communication. Code used to interface the computer to the FSP30 is included in Appendix I. The script used standard interfacing commands to obtain an ASCII text file with amplitudes for each frequency bin across the RF spectrum. An example of the ASCII output is shown in Appendix J. Interfacing and collecting the trace takes around 5 seconds.

5.3.3 Baseline RF Spectrum

A baseline RF spectrum measurement acts as a reference when comparing the current laser output to a CML regime.

A two second sweep time ($RBW = 300$ kHz, $VBW = 1$ kHz) was used to record the broadband RF spectra. A typical CML spectrum is shown in Fig. 5.9. The noise floor for the measurement increased significantly, as expected, but it did not appear to substantially affect the stability of the spectral peaks. Note that the reduction in the power of the peaks was due to using the 5% tap of the power splitter rather than the 50% tap used for Fig. 5.4. The lower power was also a result of operating at a different pump current.

Less amplitude roll-off (1.2 dB) across the RF spectrum was obtained for the 2-second trace than the 200-second trace (9.4 dB). This can be attributed to the change in resolution bandwidth and how power is distributed between neighbouring frequency bins [7]. The two second sweep time led to a 5 second acquisition time.

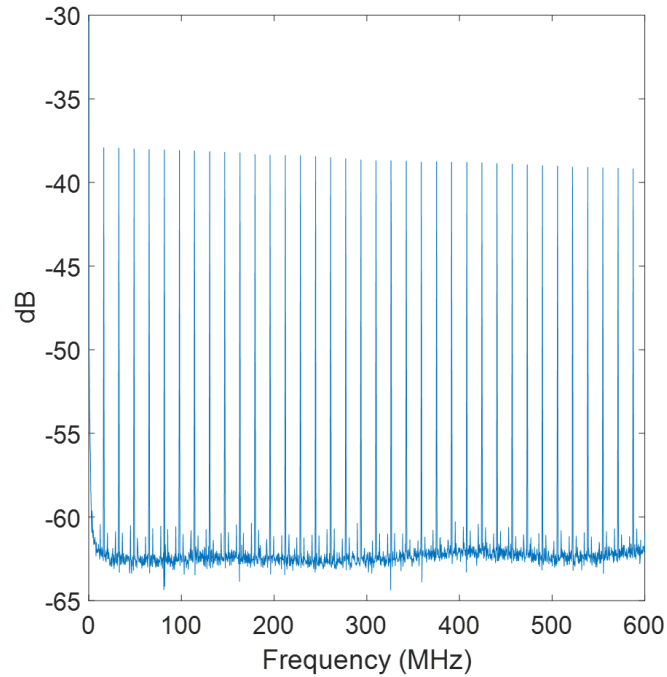


Figure 5.9: Broadband RF spectrum of a measured CML pulse train with 2-second sweep time. The PRF was 17 MHz.

5.3.4 Categorising the Laser Output using RF Spectra

The amplitudes of the peaks in the RF spectra were determined and compared as discussed in Section 4.4.4 using the MATLAB script in Appendix K. The operation of the script, which takes approximately 1 second to run, is described below:

- *Determine the amplitude of the comb peaks in the RF spectrum*

A custom peak finding routine was devised to obtain the amplitude of the comb peaks. The script used information about the approximate PRF of the laser to identify only the peaks that were at multiples of the PRF. In particular, this approach avoided the first few datapoints at very low frequencies that often exceed all the other measured amplitudes and peaks that do not occur at multiples of the PRF, such as those observed due to timing jitter or in some MPML regimes.

To ensure the appropriate maxima are found, ten datapoints either side of a multiple of the PRF are considered (for a total of 21 datapoints) and the in-built MATLAB maximum function finds the largest value from this subset.

This process is repeated for each harmonic. In the case of the final harmonic, there may be less than 10 datapoints from the suspected peak to the end of the captured data. If this is the case, the script will only consider points up to the final element of the amplitude array to avoid indexing errors.

- *Calculate the amplitude difference for each group of harmonics*

As per section 4.4.4, spectral peaks are divided into non-overlapping, adjacent groups of 3 peaks and the difference between the largest and smallest amplitude is calculated for each group.

- *Compare the difference to threshold values from a CML baseline characterisation*

The difference between the largest and smallest amplitude for each group in the newly acquired spectrum is compared to that for the baseline CML spectrum. A value of 1 is assigned if the difference for a group exceeds the baseline difference, otherwise a value of 0 is assigned.

- *Classify the regime*

There are two possible outcomes – CML or not-CML. A CML outcome is inferred when **every** group has a value of 0. The regime is not-CML if one or more batches is assigned the value 1.

- *Check that the CML output is of reasonable power*

An additional test is included to check the average power of the CML regime. The amplitude of the first harmonic must be larger than a pre-set value, otherwise a non-CML result is obtained. This test is to ensure that an optimum CML regime has been obtained rather than a low power CML pulse train.

5.3.5 Adjusting Polarisation Controller Voltages

The final stage of this automation technique is to update the intra-cavity polarisation state. The state of the piezo-controlled polarisation controller (PCD-001 3 channel piezo driver voltage unit with a PCD-M02 PC) was adjusted by a Na-

tional Instruments data acquisition board (NI-DAQ USB 6341), as per the setup in Fig. 5.8, and the MATLAB code in Appendix L. Its two analogue voltage outputs are connected to the PCD-001 driver, enabling computer-controlled adjustment on two of the three channels of the PC. The third channel was fixed during operation, which prevented complete control over the polarisation state. Future work would involve updating the hardware used for this system by obtaining a board with three analogue voltage outputs.

Each channel of the PCD-001 controller accepts an external 0-10 V input for which a 0-150V output is produced. The NI-DAQ USB 6341 output has a 12 bit controller, resulting in a PCD-M02 minimum output voltage step size of 0.037 V. The specified drift of the PCD-001 is $< 0.01\%$ over five hours [8].

5.3.6 Automation GUI

A graphical user interface (GUI) was developed using MATLAB Application Builder to simplify user interaction with the automation script. A screenshot of the program developed is featured in Fig. 5.10.

The GUI includes the ability to:

- Set initial piezo voltages
- Set the voltage step size for each channel with settings for no increment (0 V), fine (0.074 V on 150V scale), medium (0.296 V) and coarse (0.555 V)
- Set the increment direction for each channel independently
- Manually start the automation script or set it to run repeatedly until a CML state is reached
- Capture RF spectra and store to a directory on the computer

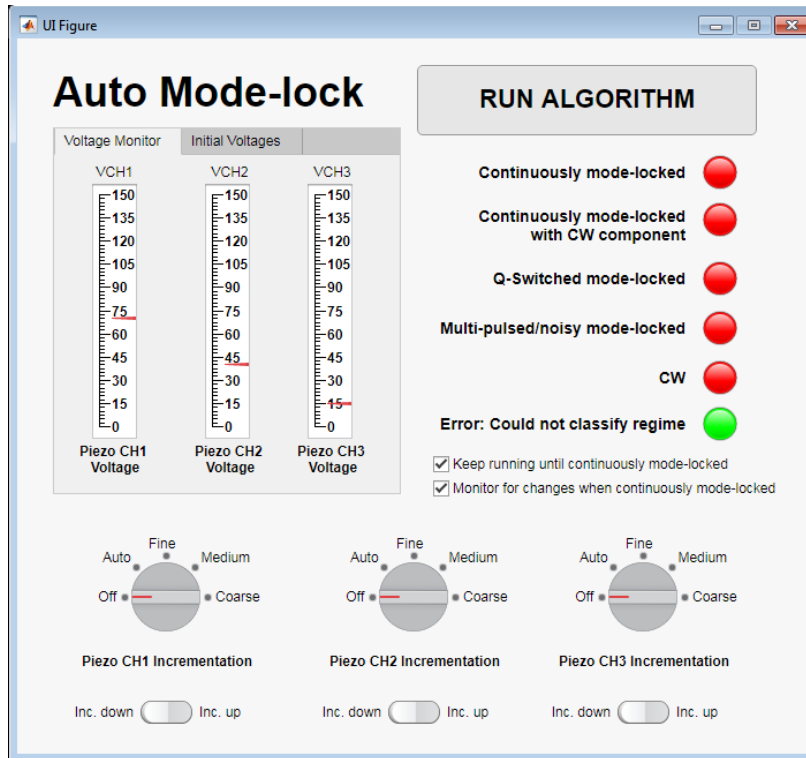


Figure 5.10: A screenshot of the MATLAB GUI used for automation.

- Identify whether the regime is CML or not-CML using status lights. Future work may enable the program to indicate the specific non-ideal regime from the RF spectrum

5.4 Automation Results

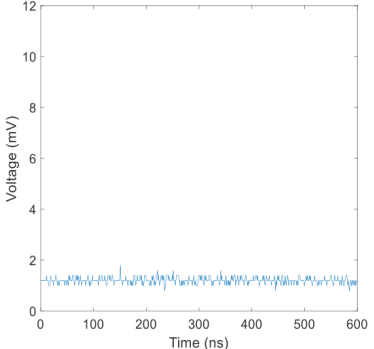
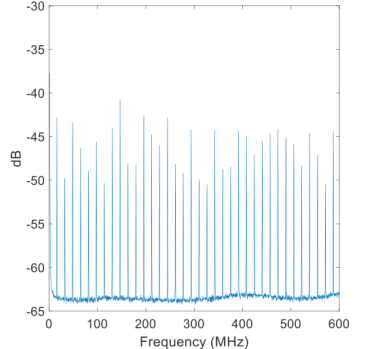
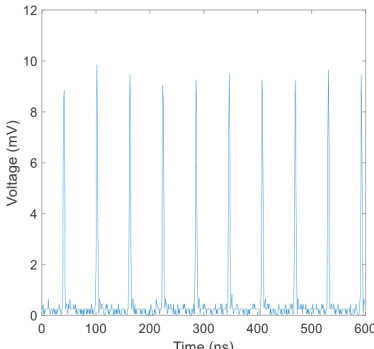
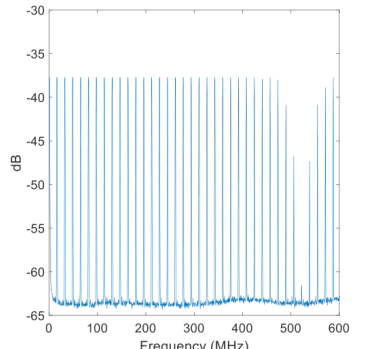
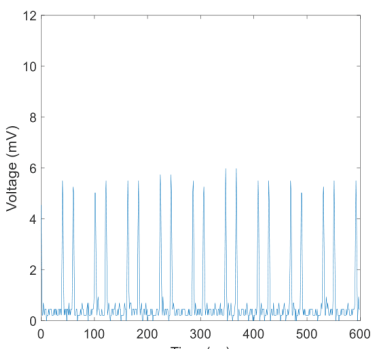
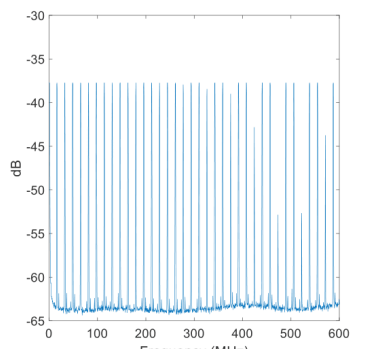
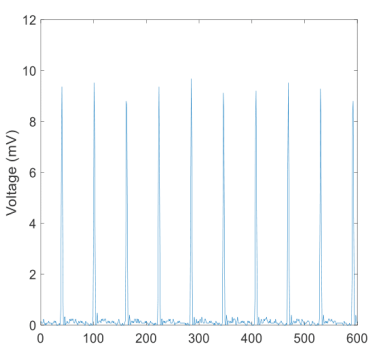
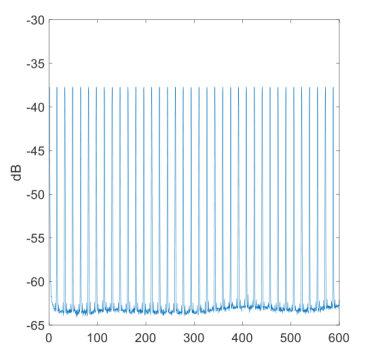
The automation process outlined in Section 5.4 was tested for a variety of initial (not-CML) settings and search strategies:

- CH1 voltage was incremented while CH2 and CH3 voltages were held constant. This scan did not result in a CML regime and was stopped after 15 steps. Temporal and RF traces for each step are shown in Appendix M.
- CH1 and CH2 voltages were incremented alternatively while CH3 was held constant. This scan terminated when a CML state was achieved but amplitude differences were still calculated routinely to detect whether the CML state was

exited. The CML regime persisted for 3 minutes and 29 seconds. A selection of the temporal and RF spectra are presented in Table 5.1. Traces for each step are presented in Appendix N.

- CH3 voltage was increased slightly and then, starting with the voltages attained from the previous (successful) CML state, CH1 and CH2 were alternately decreased until a CML state was re-established. These results are shown in Appendix O.

Table 5.1: Table featuring temporal and RF spectrum traces as the piezoelectric controller is changed to sweep into a CML regime.

Piezo Voltages (V)			Temporal Domain Trace	RF Domain Trace
CH1	CH2	CH3		
113.3	88.1	106.7		
113.5	88.4	106.7		
114.1	88.8	106.7		
114.7	89.4	107.1		

5.4.1 Automation Discussion

The results presented in the previous subsection, alongside those presented in Section 4.4.4, confirm that this automated mode-locking approach can discriminate between non-ideal and CML states.

A workable RF spectrum was attainable from just 5% (0.2 mW) of the power out-coupled from the HDFL cavity. Consequently, 95% of the power out-coupled was available for use. The TDFL and EDFL had larger average powers meaning an even smaller portion of the output power could be sampled for this automation metric.

However, it is apparent that the initial voltage settings may be far from those required to produce a CML output, and may not allow CML for some CH3 voltages. Thus, we propose creating a database of PC voltages that have previously resulted in a CML state and then using the automation code to maintain such a state.

As discussed in Chapter 2, vibrational and temperature effects may change the voltages at which CML occur. Consequently, any voltage values previously attained may act as a good starting point but will not guarantee a CML state.

Interestingly, the automation enabled the HDFL to enter a CML state with less amplitude modulation than the baseline characterisation. Getting a better understanding of the regimes in the entire polarisation space may allow for tweaking to threshold values based on the desired amount of acceptable pulse train noise.

Each step/increment in the automation process took approximately 10-12 seconds. Consequently, the full 15 steps taken to obtain the CML state was just under three minutes. Three minutes was suitable for the laser stability of the HDFL tested where vibrational and temperature perturbations often occurred over large timescales. For example, the HDFL was able to remain in a CML state for more than three minutes at a time.

5.5 Summary

This chapter focused on the demonstration, characterisation and automation of the first diode-pumped holmium doped NLPR mode-locked laser. A stable, low-noise CML regime was attained with sub-ps duration.

Pulse characteristics for the CML regime are summarised in Table 5.2.

Table 5.2: Summary of holmium source in highest power, stable CML state.

Central wavelength (nm)	Optical FWHM (nm)	Pulse duration (fs)	Repetition rate (MHz)	Average power (mW)	Peak power (kW)	Pulse energy (nJ)
2061	8.6	770	17	7	0.50	0.41

Sorokina *et al.* have also produced diode-pumped holmium sources using different mode-locking techniques, as discussed in Section 5.1 [3,4]. A comparison of this NLPR mode-locked source to these other sources is presented in Table 5.3.

Table 5.3: Summary of diode-pumped mode-locked holmium sources.

Source	Central wavelength (nm)	Optical FWHM (nm)	Pulse duration (fs)	Repetition rate (MHz)	Average power (mW)	Pulse energy (nJ)
NLPR (this Chapter)	2061	8.6	770	17	7	0.41
NALM & SESAM [2]	2094	15.3	2230	7.8	28	3.7
NALM & SESAM [3]	2134	4.3	1260	15.2	2	0.41

An automation mechanism using information from the broadband RF spectrum was implemented. Several automation regime sweeps were performed. This mechanism is a step towards combining the stability one would usually expect from a polarisation maintaining (PM) fibre laser with the benefit of having NLPR as a mode-locking technique (i.e. a pulse duration that is independent of material properties of a semiconductor saturable absorber mirror – for example).

Chapter 6

Conclusion

6.1 Introduction

Stable mode-locked fibre lasers are critical for a variety of medical and defence applications. There are many techniques that can be used to mode-lock a laser, as discussed in Section 1.2. This thesis explored NLPR mode-locked lasers and the challenges associated with developing a stable source. Characterisation and analysis of different mode-locking regimes was performed to develop an automation mechanism that could yield a stable laser output.

The key objectives addressed in this thesis include:

- A detailed characterisation of NLPR sources operating in different (ideal and non-ideal) regimes at a variety of different wavelengths – erbium (1560 nm), thulium (1990 nm) and holmium (2060 nm).
- An exploration of appropriate metrics to automate mode-locking of an NLPR laser around two micron.
- Demonstration of the first diode-pumped NLPR holmium-doped mode-locked source at $2\ \mu\text{m}$
- The development of a fully automated NLPR source.

This research resulted in, to the best of our knowledge, the development of the first automated NLPR mode-locked holmium fibre laser.

In Chapter 1, there was an overview of state of the art passive mode-locking results along with a concise overview of some of the applications enabled by stable mode-locked sources. Some techniques that have been reported in the literature to automate erbium NLPR lasers were also identified. These techniques formed the basis for an investigation into a robust automation algorithm that could work for an NLPR source at $2\ \mu\text{m}$.

Chapter 2 reviewed physical concepts critical to understanding NLPR mode-locked fibre lasers including a brief overview of optical fibres, the non-linear effects that enable NLPR mode-locking and the physical phenomena that limit pulse duration.

Chapter 3 focused on an erbium-doped fibre laser (EDFL) to investigate the merits of different measurement devices and techniques. Four measurements that aid in characterising an NLPR laser were explored. These measurements were a temporal domain trace, a RF spectrum analyser trace, an optical spectrum and an autocorrelation. Other techniques such as Frequency Resolved Optical Gating (FROG) were mentioned but not investigated in this thesis. The relative merits of each measurement tested were summarised. Characterisation included measurements taken in three different regimes (continuously mode-locked - CML, multi-pulsed mode-locked - MPML and Q-switched mode-locked - QML). The CML regime produced 620 fs pulses with over 98% of the power contained in the pulse (from taking power ratios with a 150 ps autocorrelation).

Chapter 4 focused on the advantages and disadvantages of different automation metrics for a NLPR mode-locked thulium-doped fibre laser (TDFL). The fibre laser cavity featured both electronic and manual polarisation controllers. In a CML state, the laser operated with a pulse duration of 1.15 ps. One automation technique investigated involved measuring discontinuities in the Stokes parameter S_1 around

a mode-locking regime. Such a measurement involved acquiring either an average power or the temporal evolution of signals (optical power) in orthogonal polarisation states. Another technique involved the measurement of a two-photon absorption (TPA) signal based on either average power measurements or the time evolution of the laser output. The best regime discrimination occurred from the testing of a third metric – amplitude variation from a pulse train’s RF spectrum. Any amplitude variation beyond values measured for a baseline (threshold) trace implied that the source was not-CML.

In Chapter 5, a holmium-doped fibre laser (HDFL) was characterised and automated. This led to the demonstration of the first diode-pumped NLPR mode-locked holmium fibre laser at 2 μm . Work featured in this chapter was a culmination of what was explored with the erbium and thulium sources in Chapters 3 and 4, respectively. An autocorrelation recorded a 770 fs pulse duration for the HDFL while CML.

6.2 Summary

6.2.1 Sources Developed and Characterised

Three different NLPR mode-locked fibre lasers operating at different wavelengths were developed. Each source provided unique insight into what non-ideal regimes were attainable, which enabled a robust automation method to be devised. The stability and power attainable for each design varied, as shown in Table 6.1.

Table 6.1: Table of summary statistics for holmium source in highest power, stable CML state.

Active Fibre Dopant	Observed Temporal CML Amplitude Modulation (%)	CML Regime Persistence (minutes)	RF Spectrum Roll-off (dB)	Average CML Power (mW) - depends on pump current
Er	5-8	20-30	8.5	20-80
Tm	7-11	0.6-4.5	9	15-150
Ho	5-9	0.5-5.4	8.6	2-7

A comparison of the pulse characteristics attained for each of the different sources is presented in Table 6.2.

Table 6.2: Summary of CML state performance of all laser sources developed.

Source	Central wavelength (nm)	Optical FWHM (nm)	Pulse duration (fs)	Repetition rate (MHz)	Average power (mW)	Peak power (kW)	Pulse energy (nJ)
Er	1567	6.2	579	17.9	70	5.93	3.9
Tm	1992	4.7	1150	22.3	120	4.40	5.38
Ho	2061	8.6	770	17	7	0.50	0.41

The TDFL described in Chapter 4 served as a testbed for exploring mode-locked regimes at longer wavelengths. It was cladding pumped using a more powerful diode than the butterfly diode packages used with the erbium and holmium sources. Consequently, a substantially larger CML average power was achievable.

As per Table 6.1, the thulium source experienced the most CML amplitude modulation in the time domain and often had additional noise between pulses. One potential explanation for this behaviour is the fact that the source was cladding pumped. Cladding pumping typically results in a lower inversion, as documented in Section 2.2.3. Consequently, it is more susceptible to noise [1].

The thulium source was difficult to mode-lock for large pump currents. This is consistent with the literature that suggests that non-ideal regimes may be more prevalent for larger pulse energies due to noise outbursts [1,2]. Noise outbursts are documented to occur beyond a critical pulse energy as a result of a dependence of non-linear effects on intensity noise [2].

Consequently, the source was characterised at the highest output power that still had a stable CML state (i.e. one that could persist for tens of seconds without substantial noise).

The piezo PC was also incorporated into the HDFL investigated in Chapter 5 and a range of non-ideal regimes were once again encountered. Mode-locking was readily

attainable at high pump currents, which was likely due to the lower intra-cavity pulse energies than the thulium source [2].

A lower output average power was obtained for the HDFL than the other sources for several reasons including:

- Large intra-cavity losses due to mode-field diameter mismatch between fibre components
- A lower average power pump diode than the TDFL and EDFL
- A lower pump absorption in active fibre - primarily due to its shorter length

6.2.2 Automation Metric Summary

The RF amplitude variation metric was implemented in a HDFL, as outlined in Chapter 5. Several sweeps were conducted starting from fairly arbitrary polarisation controller settings. The algorithm consistently distinguished between non-CML states and CML states. The RF spectrum provided more discrimination for cases where the temporal oscilloscope trace appeared almost CML, as evident from Table 5.1.

A test and discussion of different mode-locking techniques was presented in Sections 4.4 and 4.5 respectively. Additionally, a discussion for the fully-implemented algorithm is presented in Section 5.6.

Currently, the HDFL source is fully automated. The ‘auto’ function in the software (Section 5.4.6) increments channels on a medium setting while the laser is CW (non-pulsed) and switches to the fine setting when nearing a CML regime. There are further improvements and adjustments that can be made to the algorithm, some of which will be discussed in Section 6.3.

6.3 Future Work

The research summarised in Sections 6.1 and 6.2 demonstrated automated NLPR mode-locking of Tm and Ho-doped silica fibre lasers. The acquisition of a mode-locked regime and its stability was compromised, however, by: a wide range of non-ideal pulsing regimes, choice of components that were readily available, the lack of dispersion management and likely the lack of environmental isolation.

Future work towards improving the fibre lasers constructed and the automation process is discussed in this section.

6.3.1 Component Selection

There are several component limitations that may have adversely impacted the performance of the NLPR mode-locked fibre lasers built and characterised for this thesis.

Notably, the mode field diameter (MFD) was mismatched between active and passive fibres in each cavity. Mismatch often leads to losses in optical power. SMF-28e has a MFD of $10.4 \mu\text{m}$ at 1550 nm [3], which differs substantially from the $8 \mu\text{m}$ MFD of the holmium doped fibre used for this project (Chapter 5). The other active fibres also have a similar mismatch. An alternative optimisation method would be to use a tapered fibre as an adaptor to reduce losses.

The pump intensity could also be increased (in the holmium source in particular) as one method for increasing the output power. Presently, the HDFL produced a 5 mW output when in a CML state with the pump diode at its maximum current.

Additionally, the PM isolators used in the holmium and thulium NLPR sources had a lower extinction ratio than the non-PM isolator used in the erbium source.

The erbium NLPR mode-locked laser utilised a Thorlabs I0-K-1550 that has a return loss of > 50 dB with 36 dB isolation [4]. An in-line polariser, that acted as a mode-locking element for the Er^{3+} cavity, had an extinction ratio of > 28 dB [5]. The PM isolator in the thulium and holmium cavities had a return loss of > 50 dB, 28 dB isolation and > 20 dB extinction ratio [6]. Selecting components that provide better polarisation discrimination may enable more stable mode-locking in NLPR laser systems.

6.3.2 Removing Q-switched Instabilities

The most prevalent non-ideal state encountered from the laser cavities in Chapters 3-5 was the Q-switched mode-locked (QML) regime. QML instabilities can be eliminated by operating a laser system with an appropriate set of parameters [7]. Hönninger *et al.* formulated the stability criterion for stable passive mode-locking using saturable absorber mirrors [7]. The stability criterion manifests as the inequality in Equation 6.1

$$E_p \left. \frac{dR(E_p)}{dE_p} \right|_{\bar{E}_p} < \frac{T_R}{\tau_L} + \frac{E_p}{E_{sat,L}} \quad (6.1)$$

Here, E_p is the energy of the mode-locked pulse in the cavity at any given location and point in time and $R(E_p)$ is the non-linear reflectivity, τ_L represents the lifetime of the upper state medium and T_R represents the round trip time. The $E_{sat,L}$ term is the saturation energy of the gain, which can be obtained by multiplying the gain medium saturation fluence ($F_{sat} = h\nu/(m\sigma_L)$) and effective laser mode area. Where, m is 1 for a ring cavity and σ_L is the emission cross section at the lasing wavelength [8]. This inequality must hold at all points throughout the cavity to ensure continuous mode-locking prevails and that Q-switched mode-locked instabilities are not prevalent.

NLPR is a form of artificial saturable absorber mode-locking. Although the reflec-

tivity term of the mirror is not necessarily analogous to NLPR mode-locking, there is still a relationship between QML instabilities and physical parameters for such sources. Equation 6.1 suggests there is a definite dependence between intra-cavity pulse energy and the ability to obtain a CML regime. Low pump currents, yielding low intra-cavity energies, cause an increased prevalence of QML.

6.3.3 Dispersion Management

The effect dispersion has on regime stability and pulse duration, particularly at wavelengths away from the silica fibre zero dispersion crossing, was discussed in Section 2.4.4.

Dispersion-compensating fibres (DCF) can reduce the total chromatic dispersion of a fibre laser. DCF fibres have a significant refractive index difference between the core and cladding, which yields large, negative waveguide dispersion coefficients at long wavelengths [9]. The magnitude of the waveguide dispersion coefficient offsets the positive material dispersion that can only be slightly changed by introducing different dopants [9].

Typical dispersion profiles for standard, dispersion-shifted and dispersion-compensating fibres are in Fig. 6.1.

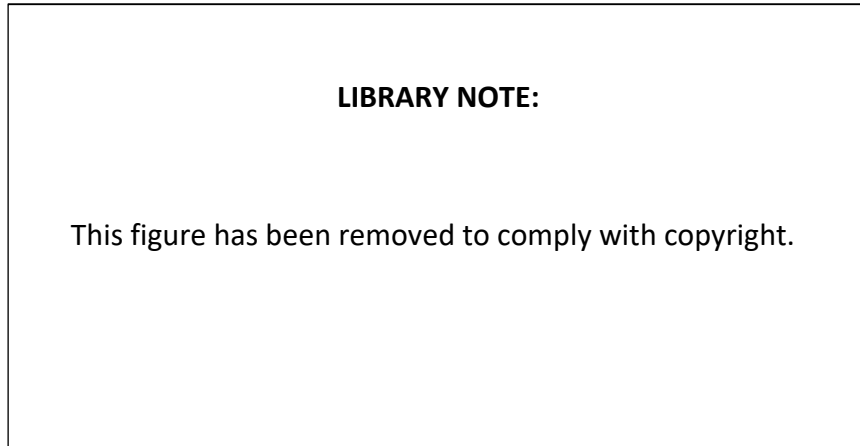


Figure 6.1: A plot of the total dispersion curves for a variety of different optical fibres – standard single-mode, non-zero dispersion-shifted and dispersion-compensating. Image from [10].

Dispersion compensation may involve splicing a calculated length of DCF into a cavity to yield close to zero net dispersion. Cavities contain multiple types of fibre including an active (doped) fibre and passive fibre. Under such circumstances, the equation for net dispersion is given by Equation 6.2.

$$D_p l_p + D_a l_a + D_d l_d = D_{net} \quad (6.2)$$

where D_p is the total chromatic dispersions coefficient (sum of waveguide and material dispersion coefficients) in the passive fibre, D_a is the total chromatic dispersion coefficient in the active fibre and D_d is the total dispersion coefficient in the DCF. l_p is the length of passive fibre used, l_a is the length of active fibre and l_d is the length of DCF. Note that D_d is negative. By knowing all other quantities, one can rearrange for l_d to determine the length of DCF needed to mitigate dispersion.

However, as discussed in Section 2.5.3, stable mode-locking requires a balance of GVD and SPM. Consequently, the optimum DCF length will result in a non-zero GVD with a small magnitude whose sign depends on whether you are in the normal

or anomalous dispersion regime. A methodical way of splicing in different lengths of fibre or a mechanism to measure GVD would allow for an optimum cavity configuration to be attained.

A few authors have reported on DCF installations in passively mode-locked erbium, holmium and thulium lasers, as discussed in Appendix P. A range of extra-cavity techniques have also been utilised to compress pulses by managing dispersion including using gratings, mirrors and prisms.

Pulses that are near the transform limit, such as the holmium laser demonstrated in Chapter 5, require the compensation of both group delay dispersion and higher-order dispersion terms [11]. Chirped mirrors and gratings are often useful to precisely control this.

Chirped fibre Bragg gratings can also be used to manage dispersion within the laser cavity. The installation of this component often requires adjustment of the laser cavity and the use of a circulator [12]. Authors have reported on the use of intra-cavity and extra-cavity chirped fibre Bragg gratings to reduce dispersion, as discussed in Appendix P.

Silica fibres were used for NLPR sources throughout this thesis. ZBLAN glasses have lower material dispersion than silica at longer wavelengths, as shown in Fig. 6.2. This could make them suitable for use in mode-locked laser sources around $2\ \mu\text{m}$ [13]. NLPR mode-locked ZBLAN sources have been demonstrated in the literature [14].

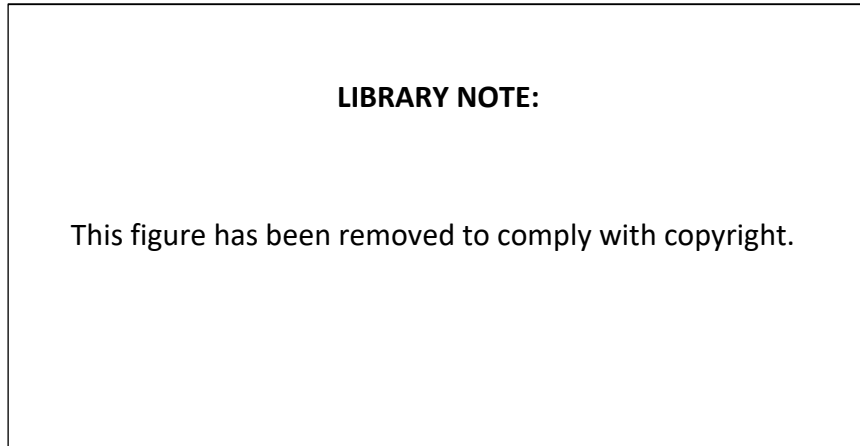


Figure 6.2: A plot of material dispersion coefficient as a function of wavelength for silica and ZBLAN glasses. Figure originally presented in [14].

6.3.4 Automation Algorithm Refinements

The mode-locked HDFL developed was automated using the RF spectrum amplitude variation test and could distinguish between a CML regime and a non-CML regime. Further work could provide classification of the current regime as CML, MPML, QML or continuously mode-locked and simultaneous CW (CMLCW).

A Fourier theory simulation of RF spectra due to different noisy or multi-pulsed temporal pulse trains could be used as a comparison to classify experimental data. This regime classification could also aid in the algorithm determining which channels to adjust voltages on and the voltage step needed based on a back-catalogue of previous mode-locking attempts. Such an analysis could lead to an ‘auto’ setting for incrementation that could obtain a CML regime with far fewer increments. Commonalities or patterns in behaviour could be identified using machine learning algorithms from large data sets taken by spanning the entire intra-cavity polarisation parameter space [15].

Difficulties would arise if one required an automation method that could respond

quicker to external stimuli. For example, an NLPR mode-locked laser on a moving platform or subject to a fairly rapid changes in temperature would likely not perform well with the automation metric in its current state. Improvements that could be tested to make the RF amplitude variation approach more suitable for systems subject to short time-scale perturbations include:

- A reduction in time taken to acquire spectra - perhaps through removing the need to interface with the RF analyser
- Processing data on a computer system with a faster processor or processing data on a device that can directly output voltages rather than requiring communication with a data acquisition board

One could also explore the calculation of an RF spectrum from a high-bandwidth photodetector and series of voltage controlled oscillators (VCO's). This configuration would be in lieu of an RF spectrum analyser, which is a bulky and (often) expensive instrument. A known pulse repetition frequency (PRF) means that each VCO can be set to capture the intensity for a specific RF harmonic. One separate VCO would be used for each of the 30 (or so) harmonics. The feedback loop from the oscillator would enable a measurement to be made even in the presence of timing jitter in the laser output [16].

The VCO measurement approach would directly measure the amplitude of the peaks in the RF spectrum rather than processing the entire RF trace and using a peak finding tool. This would remove the biggest inefficiency that still exists in the automation method presented in Chapter 5. Consequently, there would be a reduction in the time taken to collect and process data – reducing the time taken between increments.

6.4 Final Remarks

This section has provided a comprehensive overview of future work and improvements for this project. Each of the original objectives, stated in Chapter 1 and the beginning of this Chapter, have been addressed. The work presented demonstrated a good platform that could be further explored through a faster control system and optimised cavity components. The 2.06 μm lasing wavelength of the diode-pumped holmium source demonstrated would make it suitable for seeding Ho:YLF. Some adjustments to the system could push this to longer wavelengths and make seeding Ho:YAG at 2.09 μm possible.

Appendix A

Stokes Parameters

Linear polarisation implies that \vec{E} is confined to a single plane coincident with the wave's propagation direction. Circular polarisation occurs when orthogonal linear components of equal amplitude have a phase difference of $\pi/2$ [1].

The resultant \vec{E} rotates along a circular path in the direction of propagation. The rotation direction determines whether light is left-hand (LH) or right-hand (RH) circularly polarised [1]. Elliptical polarisation is when the field traces out an ellipse in the direction of propagation. An ellipse is formed when two orthogonal linear components have different amplitudes, and the phase difference between them is not $\pi/2$ [1]. An unpolarised light source is one that vibrates in more than one plane.

Stokes parameters form a vector that spans all possible polarisation states (completely polarised, partially polarised and unpolarised) for light. Each parameter is a measurable quantity associated with an optical field [2].

S_0 describes the total intensity of an optical field. It is the incident irradiance. It is the sum of two orthogonal polarisation components, as given in equation A.1 [2].

$$S_0 = E_{0,x}^2 + E_{0,y}^2 \tag{A.1}$$

S_1 describes the proportion of left-hand (LH) polarised light relative to right-hand (RH) polarised light. It takes values between -1 and 1. $S_1 < 0$ implies that vertical polarisation components are preponderant over horizontal components. If $S_1 > 0$ then the converse is true [1]. S_1 is written in terms of the \vec{E} field in each of the orthogonal spatial co-ordinates as given in equation A.2.

$$S_1 = E_{0,x}^2 - E_{0,y}^2 \quad (\text{A.2})$$

S_2 describes the proportion of light polarised at 45° relative to light polarised at -45° . $S_2 < 0$ value implies the polarisation state is more similar to that of polarisation at -45° , whereas $S_2 > 0$ implies it is more similar to polarisation at 45° [1]. S_2 is written in terms of the components of \vec{E} and δ , the phase difference between the two orthogonal field components, as given in equation A.3.

$$S_2 = 2E_{0,x}E_{0,y}\cos\delta \quad (\text{A.3})$$

S_3 describes the proportion of light that is RH circularly polarised relative to LH circularly polarised. $S_3 < 0$ implies a tendency toward LH and a $S_3 > 0$ implies a RH tendency. S_3 is defined in equation A.4.

$$S_3 = 2E_{0,x}E_{0,y}\sin\delta \quad (\text{A.4})$$

A dimensionless (normalised) version of S_1 and S_2 is often obtained by using the ratio S_1/S_0 and S_2/S_0 , respectively [1].

For dimensionless Stokes parameters, equation A.5 holds. Equality occurs for completely polarised light [1].

$$S_0^2 \geq S_1^2 + S_2^2 + S_3^2 \quad (\text{A.5})$$

A Stokes vector has components given by $\vec{S} = [S_0, S_1, S_2, S_3]$

- Linear (horizontal): $\vec{S} = [1, +1, 0, 0]$
- Linear (vertical): $\vec{S} = [1, -1, 0, 0]$
- Linear (diagonal, 45°): $\vec{S} = [1, 0, +1, 0]$
- Linear (diagonal, -45°): $\vec{S} = [1, 0, -1, 0]$
- Circular (RH): $\vec{S} = [1, 0, 0, +1]$
- Circular (LH): $\vec{S} = [1, 0, 0, -1]$
- Unpolarised: $\vec{S} = [1, 0, 0, 0]$

References

- [1] Goldstein, D 2010, Polarised light, CRC Press, Boca Raton.
- [2] Collett, E 2003, Polarised light in fiber optics, Polawave Group, New Jersey.

Appendix B

Kerr Coefficient Derivation

This derivation is adapted from [1, 2].

Consider a fast responding non-linear medium and neglect any effects of Stimulated Raman Scattering. We also assume that the non-linear susceptibility tensor has no frequency dependence. Under such conditions, the third order non-linear polarisation in the i^{th} direction can be written as:

$$P_i^{(3)}(t) = \epsilon_0 \sum_{j=1}^3 \sum_{k=1}^3 \sum_{l=1}^3 \chi_{ijkl}^{(3)} E_j(t) E_k(t) E_l(t) \quad (\text{B.1})$$

If the field is a single, linearly polarised field, then this collapses to:

$$P_x^3(t) = \epsilon_0 \chi_{xxxx}^{(3)} E_x(t) E_x(t) E_x(t) \quad (\text{B.2})$$

The Optical Kerr Effect pertains to electric fields that are modulated with time. Namely, the \vec{E} field can be modelled by:

$$\vec{E} = \vec{E}_0 e^{-i\omega t} \quad (\text{B.3})$$

For a single, linearly polarised field, we remove the vector nature of the equation.

Upon substituting the scalar version of B.3 into B.2, one obtains:

$$P_x^{(3)}(t) = \epsilon_0 \chi_{xxxx}^{(3)} \left[\frac{1}{2} E(t) e^{-i\omega_0 t} + c.c. \right]^3 \quad (\text{B.4})$$

$$P_x^{(3)}(t) = \epsilon_0 \chi_{xxxx}^{(3)} \frac{1}{8} [E(t) e^{-i\omega_0 t} + E(t) e^{i\omega_0 t}]^3 \quad (\text{B.5})$$

And hence upon expanding, one obtains:

$$P_x^{(3)}(t) = \chi_{xxxx}^{(3)} \epsilon_0 \frac{1}{8} [(E(t) e^{-i\omega_0 t} + E(t) e^{i\omega_0 t})(E(t) e^{-i\omega_0 t} + E(t) e^{i\omega_0 t})(E(t) e^{-i\omega_0 t} + E(t) e^{i\omega_0 t})] \quad (\text{B.6})$$

$$P_x^{(3)}(t) = \chi_{xxxx}^{(3)} \epsilon_0 \frac{1}{8} [(E(t)E(t)e^{-2i\omega_0 t} + 2E(t)E(t) + E(t)E(t)e^{2i\omega_0 t})(E(t)e^{-i\omega_0 t} + E(t)e^{i\omega_0 t})] \quad (\text{B.7})$$

$$P_x^{(3)}(t) = \chi_{xxxx}^{(3)} \frac{\epsilon_0}{8} [(E^3(t)e^{-3i\omega_0 t} + 3|E(t)|^2 E(t)e^{-i\omega_0 t} + E^3(t)e^{3i\omega_0 t} + |E(t)|^2 E(t)e^{i\omega_0 t})] \quad (\text{B.8})$$

And hence by recognising the terms that appear with their complex conjugate, the polarisation can be written as:

$$P_x^{(3)}(t) = \chi_{xxxx}^{(3)} \frac{\epsilon_0}{8} [(E^3(t)e^{-3i\omega_0 t} + 3|E(t)|^2 E(t)e^{-i\omega_0 t} + c.c.)] \quad (\text{B.9})$$

Neglecting the third harmonic term, this can be rewritten as:

$$P_x^{(3)}(t) = \frac{1}{2} \left[\chi_{xxxx}^{(3)} \frac{\epsilon_0}{4} 3|E(t)|^2 E(t) \right] (e^{-i\omega_0 t} + c.c.) \quad (\text{B.10})$$

And using a general form for the polarisation of $P_x^{(3)}(t) = \frac{1}{2}[P(t)e^{-i\omega_0 t} + c.c.]$ and $P(t) = \epsilon_0 \epsilon_{NL} E(t)$, one can obtain:

$$\epsilon_{NL} = \frac{3}{4} \chi_{xxxx}^{(3)} |E(t)|^2 \quad (\text{B.11})$$

And using $\epsilon_L + \epsilon_{NL} = (n + \Delta_n)^2$, one obtains:

$$\Delta n = \frac{\epsilon_{NL}}{2n} = \frac{3}{8n} \chi_{xxxx}^{(3)} |E(t)|^2 = n_2 |E(t)|^2 \quad (\text{B.12})$$

Hence the Kerr coefficient in terms of the third order non-linear susceptibility is:

$$n_2 = \frac{3}{8n} \chi_{xxxx}^{(3)} \quad (\text{B.13})$$

References

- [1] New, G 2011, Introduction to Nonlinear Optics, Cambridge University Press, Cambridge.
- [2] Agrawal, G 2015, 'Polarisation phenomena in nonlinear optical fibers', lecture notes distributed in OPT 467 Nonlinear optics, University of Rochester, on April 2015.

Appendix C

Tensor Simplification

For an isotropic medium, such as silica, the tensor can be rewritten with delta functions.

Hence, an expression for polarisation in the i^{th} direction can be written as:

$$\chi_{ijkl}^{(3)} = \chi_{xxyy}^{(3)} \delta_{ij} \delta_{kl} + \chi_{xyxy}^{(3)} \delta_{ik} \delta_{jl} + \chi_{xyyx}^{(3)} \delta_{il} \delta_{jk} \quad (\text{C.1})$$

And hence, the polarisation in the i^{th} direction can be obtained using equation 2.24.

$$P_i = \frac{3\epsilon_0}{4} \sum_{j=x,y} (\chi_{xxyy}^{(3)} E_i E_j E_j^* + \chi_{xyxy}^{(3)} E_j E_i E_j^* + \chi_{xyyx}^{(3)} E_j E_j E_i^*) \quad (\text{C.2})$$

Using the fact that for an isotropic medium, $\chi_{xxyy}^{(3)} = \chi_{xyxy}^{(3)} = \chi_{xyyx}^{(3)} = \frac{1}{3} \chi_{xxxx}^{(3)}$, one obtains the expressions for P_x and P_y in Chapter 2.

Appendix D

Frequency Resolved Optical Gating (FROG)

FROG traces are measurements of a pulsed laser output taken in the time-frequency domain. The time-frequency domain is a hybrid domain where the spectrogram of a pulse is measured [1]. An optical pulse has a low frequency leading edge that is of relatively weak intensity [2]. The leading edge is a gate for the pulse, which is measured as a function of delay, τ [1]. A spectrogram is a set of instantaneous frequencies as a function of delay for the gated portion of the pulse's electric field [1]. The key difference between FROG and autocorrelation is the spectral resolution of the measurement. SHG autocorrelation involves measuring signal energy as a function of delay, whereas a FROG trace is an autocorrelation style measurement with a spectrally resolved signal beam [2].

SHG FROG is a standard geometry for measurement. For this geometry, the FROG trace is effectively a recording of the SHG signal spectrum as a function of delay, as per equation D.1 [3].

$$I_{FROG}^{SHG}(\omega, \tau) = \left| \int_{-\infty}^{\infty} E(t)E(t - \tau)\exp(-i\omega t)dt \right|^2 \quad (D.1)$$

The FROG technique solves a two-dimensional phase-retrieval problem that has a unique solution for intensity and phase apart from a few small ambiguities (such as an absolute phase factor) [2].

An interesting nuance of the time-frequency domain is the fact that there is an ideal temporal width for the gate pulse - a result of the uncertainty principle in the time-frequency domain [1]. A balance must be struck between temporal and spectral resolution to produce an accurate spectrogram [1]. For SHG FROG, the gate pulse is the time width of the measured pulse [2].

A FROG trace is constructed from an $N \times N$ array of points that map time to frequency. From this, N intensity and N phase points are used to determine the pulse's structure uniquely [4]. An algorithmic approach is used to determine the complex electric field from a FROG trace as given below [4].

- Start with an initial guess for the $E(t, \tau)$ field
- Fourier transform the field with respect to t to obtain $E(\omega, \tau)$ – the field in the frequency domain
- Use the measured FROG trace (spectrogram measurements) to get a better signal field for $E(\omega, \tau)$
- Inverse Fourier transform the field to obtain $E(t, \omega)$
- Repeat until a solution converges

References

- [1] Kane, D & Trebino, R 1993, 'Characterisation of arbitrary femtosecond pulses using frequency resolved optical gating', *Journal of Quantum Electronics*, vol. 29, no. 2, pp. 571 – 579.
- [2] Trebino, R 2000, *Frequency Resolved Optical Gating*, Chapter 5: FROG, Springer, Germany.

- [3] Yabushita, A, Fuji, T & Kobayashi, T 2001, 'SHG FROG and XFROG methods for phase/intensity characterization of pulses propagated through an absorptive optical medium', *Optics Communications*, vol. 193, no. 3, pp. 227 – 232.
- [4] Trebino, R 2000, *Frequency Resolved Optical Gating*, Chapter 7: FROG Algorithm, Springer, Germany.

Appendix E

Theoretical roll-off

For simplicity, this calculation of RF spectrum roll-off assumes a 1 ps pulse. The RF envelope width is related to the temporal pulse width by an inverse proportionality due to the nature of a Fourier transform [1]. For the sake of this calculation, assume that a 1 ps pulse yields an RF spectrum FWHM of 1 THz.

Assuming that the envelope over the RF spectrum is Gaussian and centred at 0 Hz, the envelope can be modelled by:

$$y = \frac{1}{\sigma\sqrt{2\pi}} e^{-\frac{f^2}{2\sigma^2}} \quad (\text{E.1})$$

where f is the RF frequency and σ is the standard deviation of the envelope.

Using the FWHM value of 1 THz and the origin, two expressions can be written in terms of the amplitude, A , of the frequency comb, as illustrated by Fig. E.1 and the proceeding equations:

$$A = \frac{1}{\sigma\sqrt{2\pi}} e^{-0} = \frac{1}{\sigma\sqrt{2\pi}} \quad (\text{E.2})$$

$$\frac{A}{2} = \frac{1}{\sigma\sqrt{2\pi}} e^{-\frac{(1 \times 10^{12})^2}{2\sigma^2}} \quad (\text{E.3})$$

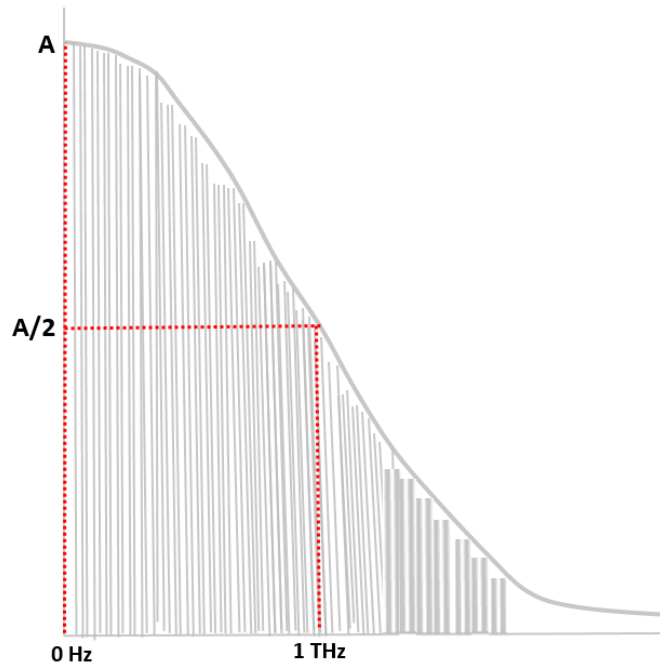


Figure E.1: Diagram of an RF spectrum envelope for a mode-locked pulse train with two points documented.

Substituting equation E.2 into equation E.3 yields:

$$\frac{1}{2\sigma\sqrt{2\pi}} = \frac{1}{\sigma\sqrt{2\pi}} e^{-\frac{(1 \times 10^{12})^2}{2\sigma^2}} \quad (\text{E.4})$$

And hence:

$$\frac{1}{2} = e^{-\frac{(1 \times 10^{12})^2}{2\sigma^2}} \quad (\text{E.5})$$

Taking the log of both sides yields:

$$\ln\left(\frac{1}{2}\right) = \frac{-(1 \times 10^{12})^2}{2\sigma^2} \quad (\text{E.6})$$

And hence:

$$\ln 2 = \frac{(1 \times 10^{12})^2}{2\sigma^2} \quad (\text{E.7})$$

And upon rearranging for σ one obtains:

$$\sigma = \sqrt{\frac{(1 \times 10^{12})^2}{2 \ln 2}} \quad (\text{E.8})$$

Hence at 600 MHz, the RF amplitude is:

$$y(600 \text{ MHz}) = A e^{\frac{-(600 \times 10^6)^2}{2(0.849 \times 10^{12})^2}} = 0.99999975 A \quad (\text{E.9})$$

And hence, in terms of roll-off in decibels from the maximum amplitude:

$$dB = 10 \log \left(\frac{1}{0.99999975} \right) = 1.086 \times 10^{-6} = 1.086 \mu dB \quad (\text{E.10})$$

References

- [1] Mittleman, D 2018, 'Theory of ultrashort laser pulse generation', lecture notes distributed in ENGN 2911T: Ultrafast optics, Brown University, on April 10th 2018.

Appendix F

Alignment of an autocorrelator using collinear and non-collinear mode

Correct alignment of the autocorrelator for measurement purposes relies on:

- The input beam being well collimated (achieved using a parabolic mirror at the input)
- The appropriate lateral displacement of the two beams
- Ensuring the waist of the two beams overlap in the non-linear crystal

The autocorrelator alignment procedure involves both the collinear mode and a non-collinear mode.

The interferometric autocorrelation has beams overlapping outside the SHG crystal, as shown in Fig. F.1. This differs from Fig. 3.15 where beam overlap is localised to inside the crystal.

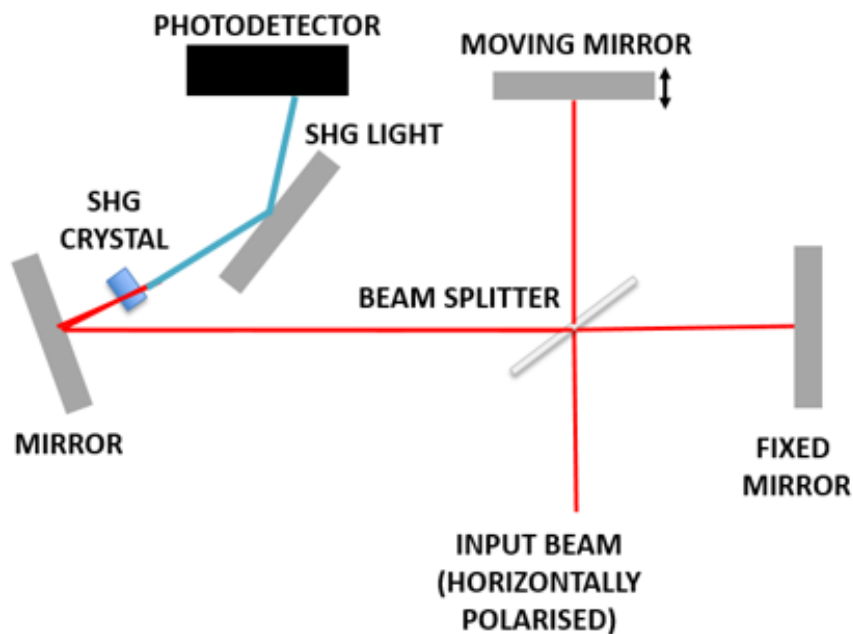


Figure F.1: Schematic of a second harmonic generation (SHG) autocorrelator aligned for an interferometric autocorrelation (collinear mode). Note that the beams overlap outside the crystal (along the path to the mirror after the beamsplitter).

The following notes can be made about collinear mode (interferometric autocorrelation):

- Useful for an initial signal search during instrument alignment due to higher sensitivity
- Larger SNR than non-collinear mode
- Beams at detector surface are overlapping
- Qualitative information is captured in the trace – such as pulse chirp nature
- Sum of intensity autocorrelation and electric field interference for incident and SH light

Adjusting the beam distance and focus enables a transition from non-collinear mode to collinear mode [1].

The following notes can be made about non-collinear mode (intensity autocorrelation):

- Beam localised to overlap entirely in crystal
- Suitable for temporal FWHM measurements

The general procedure for testing the alignment of the APE autocorrelator is presented below:

- Set polarisers in front of the autocorrelator to ensure light from laser output is horizontally polarised. This polarisation discrimination is needed to ensure that the SH light observed by the detector comes from the overlap of the two beams and not just from one beam.
- Steer the collimated laser beam into autocorrelator entry port
- Set the 'beam distance' micrometer to a known non-collinear setting (look at exit port on the front of the instrument for when the two beams overlap). The beam distance setting corresponds to movement of the fixed mirror in the autocorrelator.
- Insert an appropriate SH crystal into the autocorrelator path
- Check that the fundamental light passes through the crystal. Adjust the autocorrelator mirror, as necessary, to steer light to the centre of the crystal.
- Connect the photodetector module
- Turn on the electronics unit connected to the autocorrelator
- Run the device in FREE RUN mode on ZERO scan
- Adjust the sensitivity setting for the photodetector (three levels – 1, 10, 30 with 30 being most sensitive). The appropriate sensitivity will depend on the peak power and average power of the laser output being measured.

- Increase the gain setting using the knob control on the electronics unit
- Use the control buttons to change the tuning angle for SHG phase matching and aim to maximise the signal on-screen. Phase matching is briefly outlined in Appendix G.
- Perform a shutter test to check the alignment. In collinear mode, one shutter closed should halve the signal and both shutters closed should yield no signal above the baseline.
- Tweak beam steering and repeat shutter test until the desired behaviour is observed
- Use the beam distance micrometer to move the fixed mirror and bring the autocorrelator into non-collinear mode
- Perform another shutter test to check alignment. In non-collinear mode, one shutter closed should yield no signal as the signal will only form from overlap in the crystal.
- Recall that signals similar to that of Fig. 3.18 are indicative of a noisy pulse structure and are hence not meaningful for pulse width measurements.

References

- [1] APE Berlin GmbH 2017, Pulse check autocorrelator, APE, viewed 12th September 2018, < <https://www.ape-berlin.de/en/autocorrelator/pulsecheck/> >

Appendix G

Angular Acceptance of Type I Phase Matching with SHG

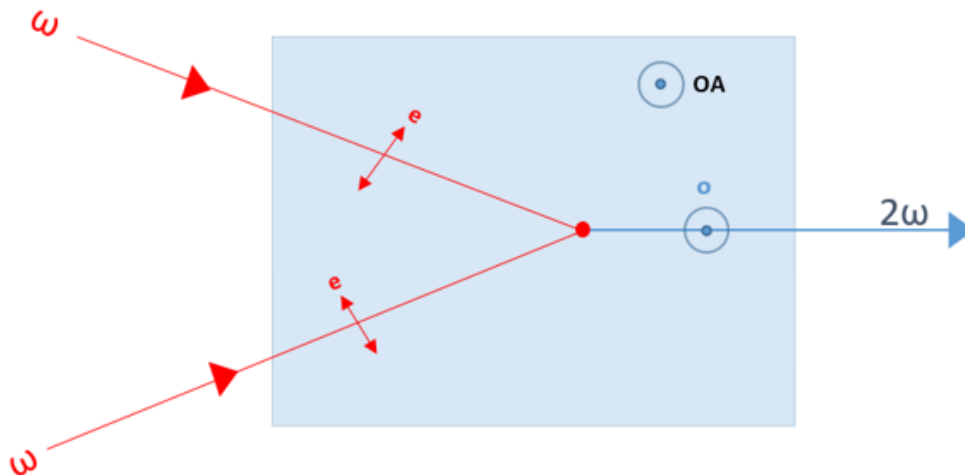


Figure G.1: Schematic of type-I phase matching in a non-linear crystal

Measuring an SHG autocorrelation relies on phase matching, as shown in Fig. G.1. The autocorrelator used required type I phase matching. In type I phase matching, the two fundamental beams from the laser output are at a frequency $\omega_1 = \omega_2$ and have the same polarisation. In the case of the APE autocorrelator, this is horizontal polarisation. The incident light consisted of extraordinary rays as the crystal was negative uniaxial. The generated light (SH light at a higher frequency ω_3) has a polarisation state that is perpendicular to the incident state [1].

Thin crystals are used in SHG autocorrelation to yield greater phase-matching bandwidth and to maximise conversion efficiency [1].

The angular acceptance of the crystal, $\Delta\theta$, is defined as the FWHM of a plot of SHG intensity as a function of crystal tuning angle. $\Delta\theta$ depends on the mismatch angle between the two fundamental beams, θ , the thickness of the non-linear crystal, L , and refractive indices associated with light at ω_3 as per equation G.1 [2].

$$\Delta\theta = \frac{2.783c}{L\omega_3|n^3(\omega_3, \theta)[n_e^{-2}(\omega_3) - n_o^{-2}(\omega_3)]\sin\theta\cos\theta|} \quad (\text{G.1})$$

where

$$n(\omega_3, \theta) = \sqrt{\frac{n_o^2(\omega_3)n_e^2(\omega_3)}{n_o^2(\omega_3)\sin^2\theta + n_e^2(\omega_3)\cos^2\theta}} \quad (\text{G.2})$$

With e and o subscripts denoting the refractive index of ordinary and extraordinary rays.

Insertion of representative values into equation G.1 yields an acceptance range that is of the order of 0.1° , highlighting the difficulty in obtaining an optimum autocorrelator alignment [2].

References

- [1] Boyd, R 2003, *Nonlinear Optics*, University of Rochester, United States.
- [2] Pattelli, L 2018, *Imaging light transport at the femtosecond scale: a walk on the diffusion side of life*, Firenze University Press, Italy.

Appendix H

Power Measurements from Polarising Beamsplitter

CH1 Piezoelectric Voltage (V)	P_x (mW)	P_y (mW)	Stokes Parameter S_1
52.4	0.68	9.47	-0.87
52.7	0.63	9.39	-0.87
53.0	0.61	9.27	-0.88
53.3	0.57	8.77	-0.88
53.6	0.58	8.39	-0.87
53.9	0.60	8.18	-0.86
54.2	0.54	8.06	-0.87
54.5	0.53	7.99	-0.88
54.8	0.50	7.83	-0.88
55.1	0.47	7.53	-0.88
55.4	0.46	7.88	-0.89
55.7	0.39	7.51	-0.90
56.0	0.43	7.58	-0.89
56.1	0.40	7.65	-0.90
56.2	0.32	9.85	-0.94
56.3	0.22	18.43	-0.98
56.4	0.23	18.67	-0.98
56.5	0.21	18.88	-0.98
56.6	0.21	18.95	-0.98
56.7	0.20	18.45	-0.98
56.8	0.19	17.98	-0.98
56.9	0.18	17.29	-0.98
57.2	0.13	16.96	-0.98
57.5	0.09	16.77	-0.99
57.8	0.02	16.24	-1.00

Appendix I

Interfacing MATLAB Code

Start and span frequencies for the FSP30 are checked while interfacing. These values are updated if the span is not 600 MHz and the starting frequency is not 9 kHz (the minimum frequency resolvable by the instrument). The number of data points displayed on the screen is also set to an appropriate value (often 2001). The 600 MHz span was mainly arbitrary but was selected to ensure that a decent amount of the frequency comb was measured with at least 20-30 harmonic peaks.

```
1 % Find a serial port object.
2 obj1 = instrfind('Type', 'serial', 'Port', 'COM15', 'Tag', '');
3 tic
4 start_frequency = 10000; % Hz
5 span_frequency = 600e6; % Hz
6
7 % Create the serial port object if it does not exist
8 % otherwise use the object that was found.
9 if isempty(obj1)
10     obj1 = serial('COM15');
11 else
12     fclose(obj1);
13     obj1 = obj1(1);
14 end
15
```

```
16 obj1.InputBufferSize = 2048;
17 obj1.Timeout = 5;
18
19 % Connect to instrument object, obj1.
20 fopen(obj1);
21
22 fprintf(obj1, 'INIT:SEL SAN'); %set in standard RF spectrum
    analyser mode
23 fprintf(obj1, 'SYST:DISP:UPD ON'); %keep display on
24 fprintf(obj1, 'SWE:POIN 501'); %set number of sweep points
25 fprintf(obj1, 'INIT:CONT OFF'); %single sweep (not continuous)
26 fprintf(obj1, 'INIT;*WAI'); %synchronisation
27
28 %Check to see if start frequency is in range of 9kHz to 30GHz
29 if(start_frequency >=9000) && (start_frequency <=30e9)
30     fprintf(obj1, ['FREQ:STAR ' start_frequency 'HZ']);
31 else
32     warndlg('The input value is out of range','Error!');
33 end
34
35 %Check to see if start frequency is in range of 9kHz to 30GHz
36 if(span_frequency >=100) && (span_frequency <=29e9)
37     fprintf(obj1, ['FREQ:SPAN ' span_frequency 'HZ']);
38 else
39     warndlg('The input value is out of range','Error!');
40 end
41
42 % Trigger the instrument to take a trace and save data
43 fprintf(obj1, 'DISP:TRAC:Y:RLEV 10dBm')
44
45 fprintf(obj1, 'FORMAT REAL, 32');
46 fprintf(obj1, 'TRAC1? TRACE1');
47 fread(obj1,1);
```



```
48 number = fread(obj1,1);
49 number_value = str2num(char(number));
50
51 result = fread(obj1,number_value);
52 data_length = int32(str2num(char(result')));
53 mod_part = mod(data_length, 2048);
54 mod_number = mod_part/4;
55
56 data = fread(obj1,double(mod_number),'single');
57 trace_data=reshape(data,1,mod_number);
58
59 step = span_frequency/length(trace_data);
60
61 x_freq = linspace(start_frequency, start_frequency+
        span_frequency, length(trace_data));
62
63 % Disconnect from instrument object, obj1.
64 fclose(obj1);
```


Appendix J

RF Spectrum Output File

Saved RF spectrum output files contained a semi-colon delimiter with a header outlining measurement conditions. An exemplar of the RF spectrum analyser datafile is in Figure J.1.

```

Type;FSP;
Version;3.70;
Date;24.Oct 19;
Mode;ANALYZER;
Center Freq;300000000,000000;Hz
Freq Offset;0,000000;Hz
Span;600000000,000000;Hz
x-Axis;LIN;
Start;0,000000;Hz
Stop;600000000,000000;Hz
Ref Level;-15,800000;dBmV
Level Offset;-61,800000;dB
Ref Position;96,000000;%
y-Axis;LOG;
Level Range;100,000000;dB|
Rf Att;30,000000;dB
RBW;300000,000000;Hz
VBW;1000,000000;Hz
SWT;2,000000;s
Trace Mode;AVERAGE;
Detector;AVERAGE;
Sweep Count;0;
Trace 1;;;
x-Unit;Hz;
y-Unit;dBmV;
Values;501;
0;-18,980606079101563;
1200000;-60,760604858398437;
2400000;-79,139419555664063;
3600000;-81,514854431152344;
4800000;-81,820236206054687;
6000000;-81,965469360351563;
7200000;-82,135124206542969;
8400000;-82,188911437988281;
9600000;-82,220794677734375;
10800000;-82,175285339355469;
12000000;-82,132171630859375;
13200000;-82,177162170410156;
14400000;-82,216270446777344;
15600000;-81,334060668945313;
16800000;-44,820564270019531;
18000000;-52,638717651367188;
-----

```

Figure J.1: ASCII output of the RF spectrum trace.

Appendix K

Regime Classification Code

```
1 % Prepare frequency and amplitude as vectors
2 Frequency = x_freq;
3
4 Amplitude = trace_data';
5
6 % Memory management
7 vars={'filedata','fid'};
8 clear(vars{:})
9
10 % Determine number of points in amplitude measurement array
11 AmplitudeArraySize = size(Amplitude, 1);
12
13 %% Quantity definitions
14 % Define pulse repetition frequency (an estimate will suffice)
15 PRF = 22; % MHz
16
17 % Define broadband RF spectrum range
18 RFrage = 600; % MHz
19
20 % Define the resolution bandwidth of the measurement
21 RBW = 1; % kHz
22
```

```

23 % Define the number of sampled datapoints set as 501 or 2001
24 DataPoints = AmplitudeArraySize;
25
26 % Define number of peaks per bin for analysis FIXED for v1.0
27 NumPB = 3;
28 NumPB = int8(NumPB);
29
30 %% Location of maxima
31 % Calculation of expected number of peaks across spectrum
32
33 NumPeaks = floor(RFrange./PRF);
34
35 MaxAmp = [];
36
37 if(DataPoints == 501)
38     ScanNumber = 8;
39 elseif(DataPoints == 2001)
40     ScanNumber = 20;
41 else
42     disp('Error, set number of sampled datapoints to 501 or
43         2001')
44 end
45 % Identify the first maxima
46 EstimatedMax = (PRF./RFrange).*AmplitudeArraySize;
47 MaxAmp = [MaxAmp; max(Amplitude(ScanNumber:EstimatedMax+
48     ScanNumber,:))];
49
50 % Identify maxima around the pulse repetition frequency for
51     subsequent
52 % peaks
53 for i = 2:NumPeaks 1
54     EstimatedMax = i*(PRF./RFrange).*AmplitudeArraySize;

```

```

53 MaxAmp = [MaxAmp; max( Amplitude( EstimatedMax ScanNumber :
    EstimatedMax+ScanNumber , : ) ) ];
54 end
55
56 % Consider the last case separately to avoid exceeding matrix
    dimensions
57 i = NumPeaks;
58 EstimatedMax = i*(PRF./RFRange).* AmplitudeArraySize;
59 MaxAmp = [MaxAmp; max( Amplitude( EstimatedMax ScanNumber : end , : ) )
    ];
60
61 % Memory management
62 vars={'EstimatedMax', 'i'};
63 clear( vars{:})
64
65 %% Temporary Plot the RF spectrum to check maxima have indeed
    been found
66
67 %plot( Frequency , Amplitude );
68
69 %% Statistical analysis
70
71 % Determine the size of MaxAmp and cast it to an integer
72 MaxAmpSize = size( MaxAmp , 1 );
73 MaxAmpSize = int8( MaxAmpSize );
74
75 % Determine number of times loop needs to run i.e. how many
    bins?
76 LoopCount = int8( MaxAmpSize ./ NumPB );
77
78 % Set range for first bin based on number of peaks per bin
79 Lowbound = 1;
80 Upbound = NumPB;

```

```

81
82 % Calculate the first value in the vector of amplitude
    variations
83 AmpVar = [];
84
85 AmpVar(1) = max(MaxAmp(1:Upbound))    min(MaxAmp(1:Upbound));
86
87 % Consider whether the number of peaks divided by number of
    peaks per bin
88 % has a remainder
89 if (rem(MaxAmpSize, NumPB) == 0)
90
91     % Loop over and populate the amplitude variation array
92     for i = 2:LoopCount
93         Lowbound = Upbound + 1;
94         Lowbound = int8(Lowbound);
95         Upbound = Lowbound + (NumPB - 1);
96         Upbound = int8(Upbound);
97         AmpVar = [AmpVar; max(abs(MaxAmp(Lowbound:Upbound))) ...
98                 min(abs(MaxAmp(Lowbound:Upbound)))];
99     end
100
101     vars = { 'Lowbound', 'Upbound', 'LoopCount' };
102     clear(vars{:})
103
104 else
105     % Loop over and populate amplitude variation array
106     LoopCount = floor(LoopCount);
107
108     for i = 2:LoopCount
109         Lowbound = Upbound + 1;
110         Lowbound = int8(Lowbound);
111         Upbound = Lowbound + 2;

```



```

112     Upbound = int8(Upbound);
113     AmpVar = [AmpVar; max(abs(MaxAmp(Lowbound:Upbound))) ...
114             min(abs(MaxAmp(Lowbound:Upbound)))];
115 end
116
117 vars={'Lowbound', 'Upbound', 'LoopCount'};
118 clear(vars{:})
119
120 end
121
122 %% Regime categorisation
123 % Characterise regimes based on critical values. Must obtain a
124 % passing
125 % grade of 1 for all values to be continuously mode locked.
126 % Categorisation
127 % thresholds are subject to change.
128
129 % Import a set of threshold values this data set will depend
130 % on peaks/bin
131
132 fide=fopen('thresholds3peaksperbin.txt');
133
134 filedata=textscan(fide, '%s', 'HeaderLines', 2);
135
136 fclose(fide);
137
138 % Prepare thresholds as a vector
139
140 Thresholds = str2double(filedata{1});
141
142 vars={'filedata', 'fid'};
143 clear(vars{:})
144
145 % Initialise VarOutcome vector
146
147 VarOutcome = [];

```

```
142
143 % Determine the size of the thresholds and amplitude variation
      array
144 ThresholdsArraySize = size(Thresholds, 1);
145 AmpVarArraySize = size(AmpVar, 1);
146
147
148 % Does the regime meet the minimum amplitude requirement of 28
      dB?
149 if(AmpVarArraySize <= ThresholdsArraySize)
150     for i = 1:AmpVarArraySize
151         VarOutcome = [VarOutcome; any(AmpVar(i)>Thresholds(i))];
152     end
153 else
154     disp('Error. Amplitude variation vector exceeds threshold
          vector size.')
155 end
156
157 % Classify the regime outcome
158 if(VarOutcome==0)
159     if(MaxAmp(1) > 28)
160         disp('Continuously mode locked')
161     else
162         disp('NOT Continuously mode locked')
163     end
164 else
165     disp('NOT Continuously mode locked')
```

Appendix L

Interfacing with Piezoelectric Polarisation Controller

```
1 %% Interfacing to piezoelectric controller
2
3 if exist('Newrun')==1
4     % Do nothing
5 else
6     Newrun=1;
7     % Set initial piezoelectric controller settings in volts on
8         0 10 V scale. This is controllable via textfield input
9         for the GUI version of the autoML code
10
11     c1 = 1.3;
12     c2 = 1.3;
13 end
14
15 % Prepare data for RS232 to increment voltage channels CH1,
16     CH2, CH3
17
18 % Increment channels by set amount. GUI version has this
19     controllable via a series of knobs
20
21 i1 = 0.1;
22 i2 = 0.3;
```

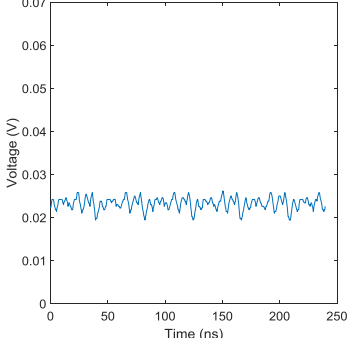
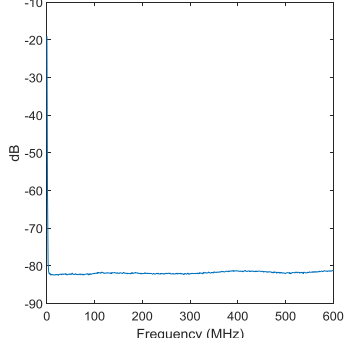
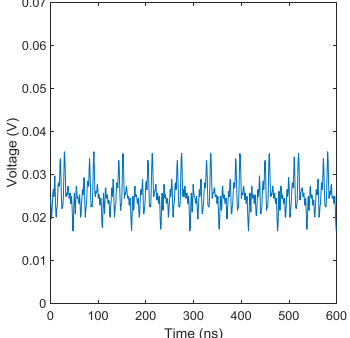
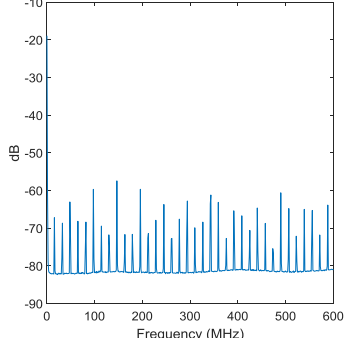
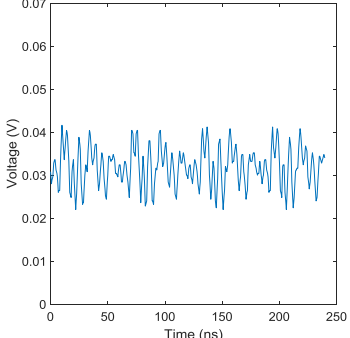
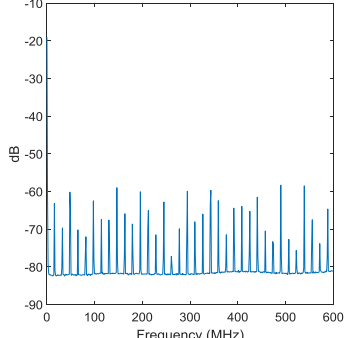
```
17 i3 = 0.001;
18
19 c1 = c1+i1;
20 c2 = c2+i2;
21 c3 = c3+i3;
22
23 % Send data to piezoelectric channels
24
25 devices = daq.getDevices();
26 s = daq.createSession('ni');
27 ch0 = addAnalogOutputChannel(s, 'Dev1', 0, 'Voltage');
28 ch1 = addAnalogOutputChannel(s, 'Dev1', 1, 'Voltage');
29
30 outputSignal1 = c1;
31 outputSignal2 = c1;
32 queueOutputData(s, [outputSignal1 outputSignal2]);
33 s.startForeground;
34
35 toc
36 plot(x_freq, trace_data);
37 set(gca, 'FontSize', 20);
38 xlabel('Frequency (Hz)')
39 ylabel('dB')
40 title('RF spectrum')
41
42 c1o = c1;
43 c2o = c2;
44 c3o = c3;
```

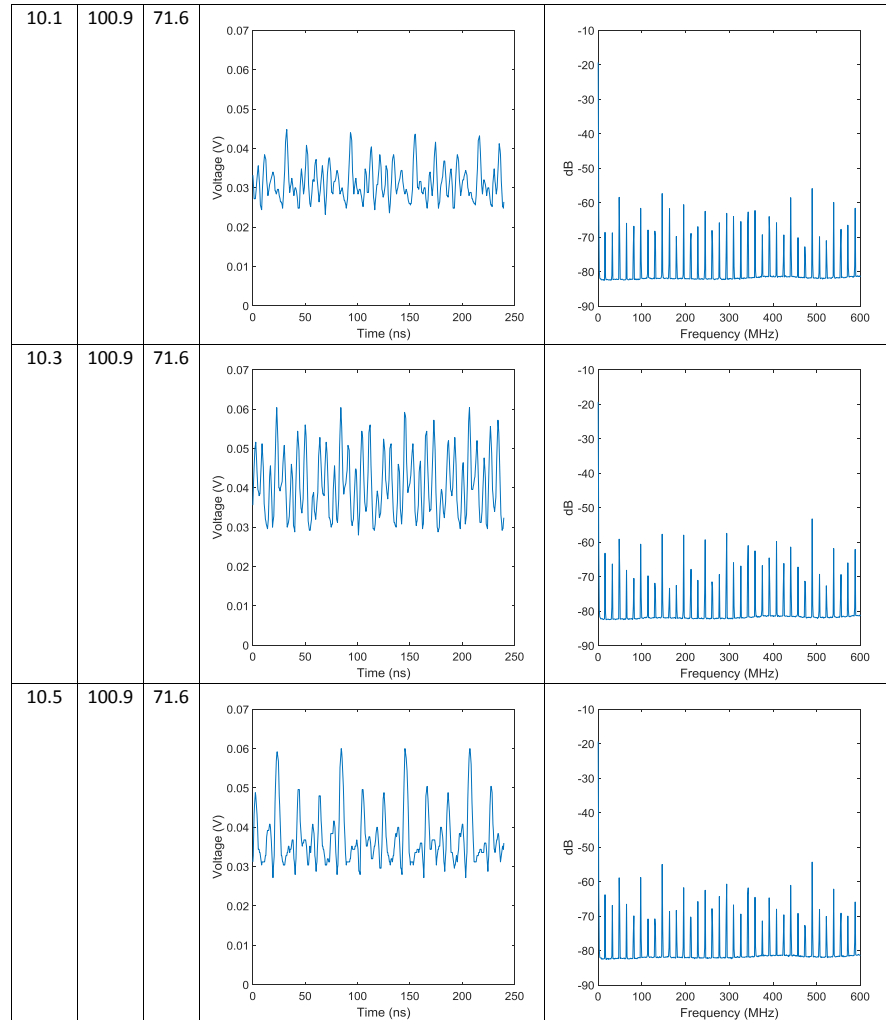
Appendix M

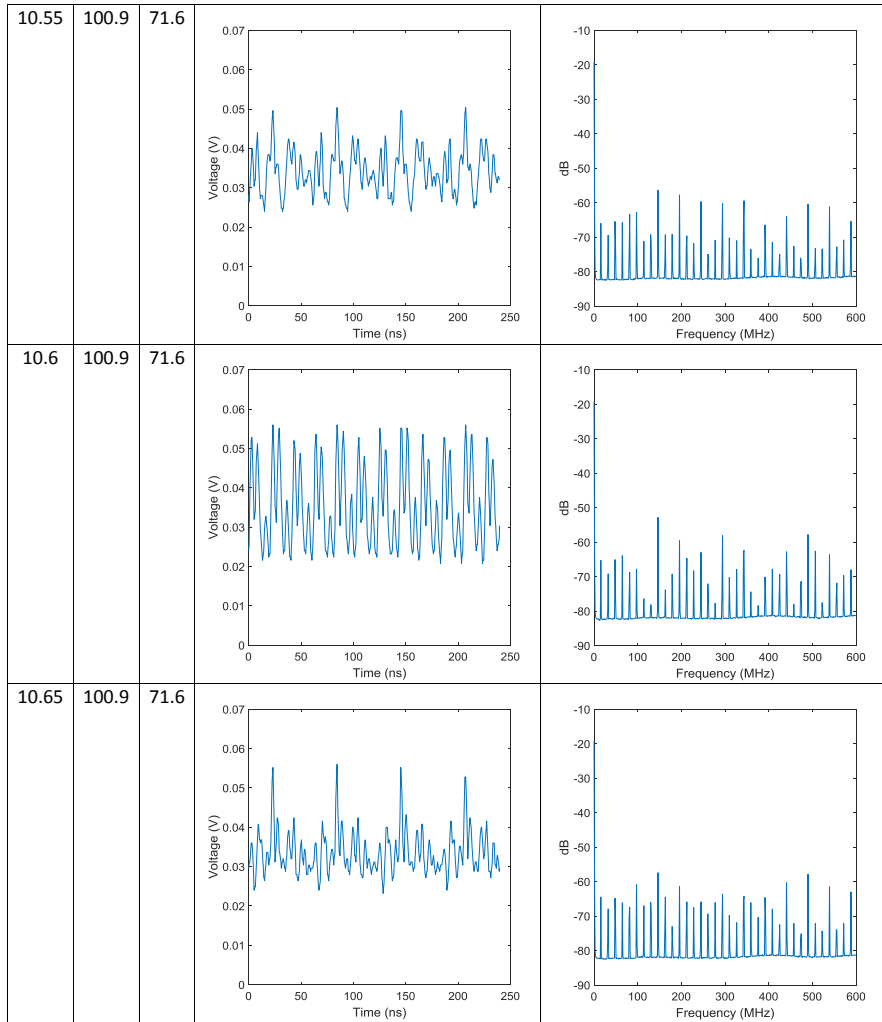
Q-switched Mode-locked Piezo Incrementation

The proceeding table contains time and radio-frequency domain measurements taken while sweeping into a regime using the automation algorithm.

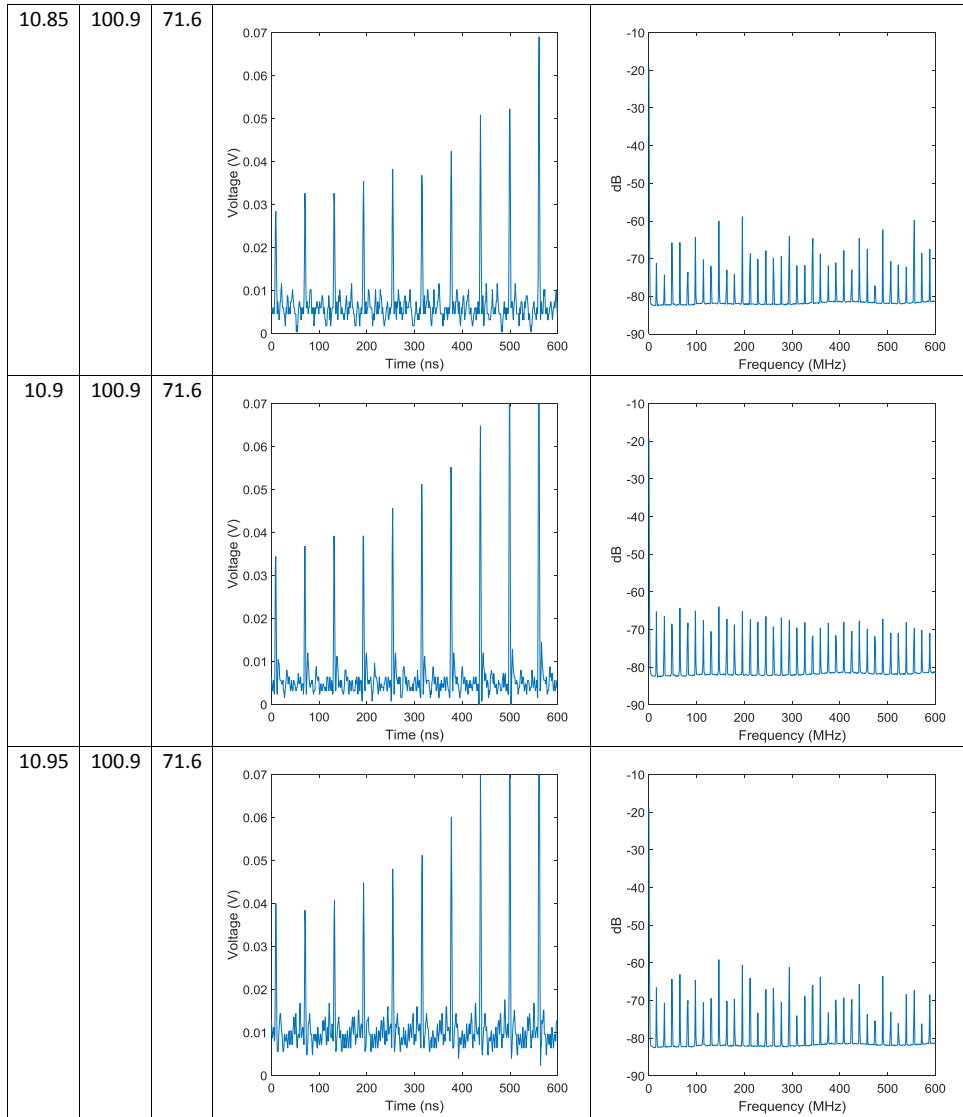
Table M.1: Table featuring temporal and RF spectrum traces for every step of the piezoelectric voltages while sweeping into a QML regime.

Piezoelectric Voltages (V)			Temporal Domain Trace	RF Domain Trace
CH1	CH2	CH3		
9.3	100.9	71.6		
9.6	100.9	71.6		
9.9	100.9	71.6		





10.7	100.9	71.6		
10.75	100.9	71.6		
10.8	100.9	71.6		



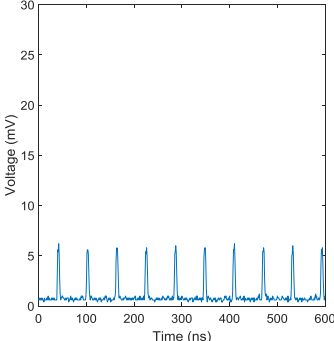
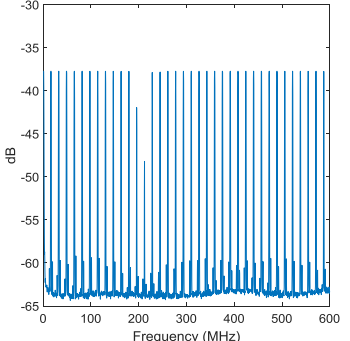
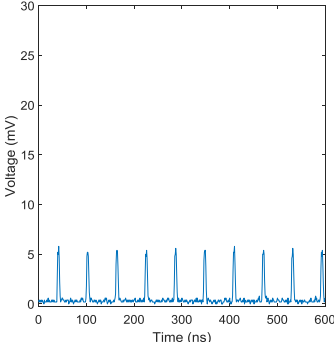
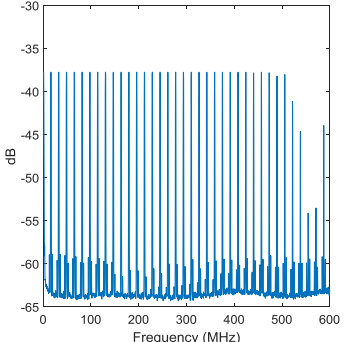
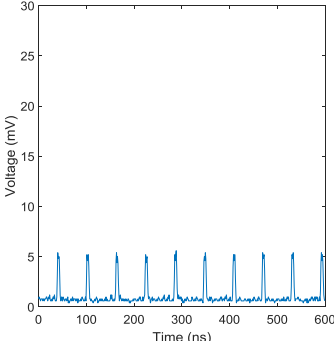
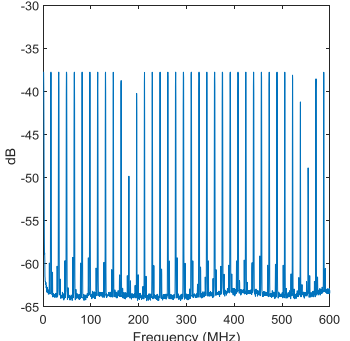
Appendix N

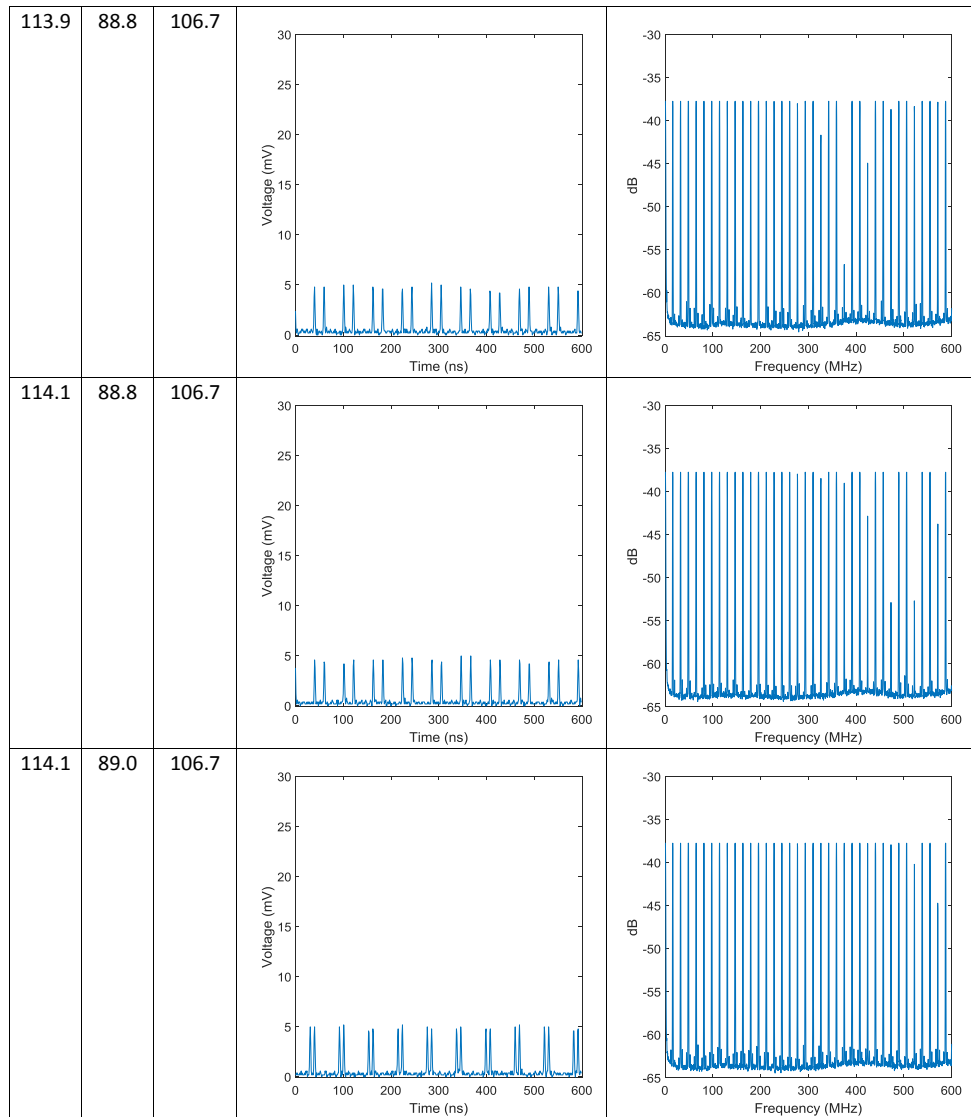
Continuous Mode-locked Piezo Incrementation

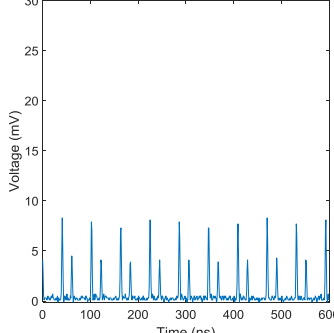
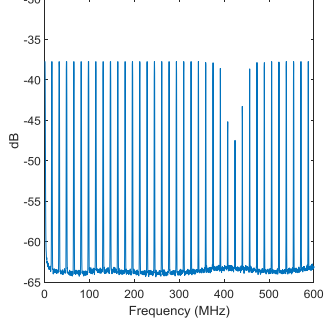
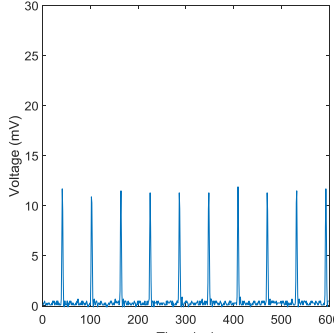
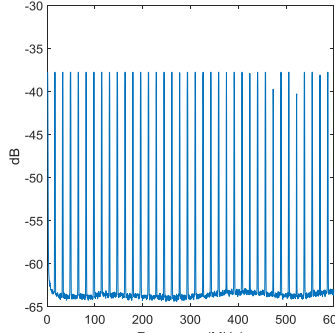
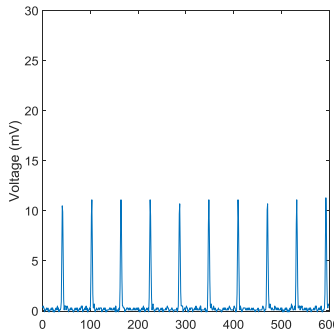
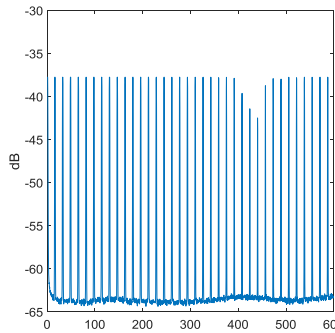
The proceeding table contains time and radio-frequency domain measurements taken while sweeping into a regime using the automation algorithm.

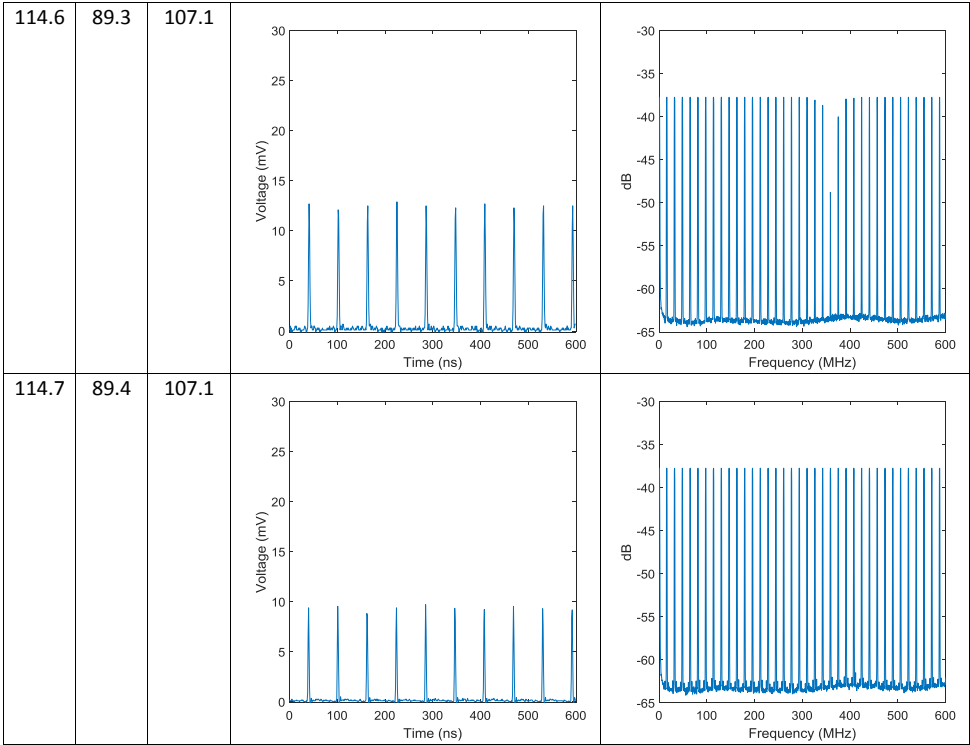
Table N.1: Table featuring temporal and RF spectrum traces for every step of the piezoelectric voltages while sweeping into a CML regime.

Piezoelectric Voltages (V)			Temporal Domain Trace	RF Domain Trace
CH1	CH2	CH3		
113.3	88.1	106.7		
113.5	88.1	106.7		
113.5	88.4	106.7		

113.7	88.4	106.7		
113.7	88.6	106.7		
113.9	88.6	106.7		



114.3	89.0	106.7		
114.3	89.0	107.1		
114.5	89.2	107.1		



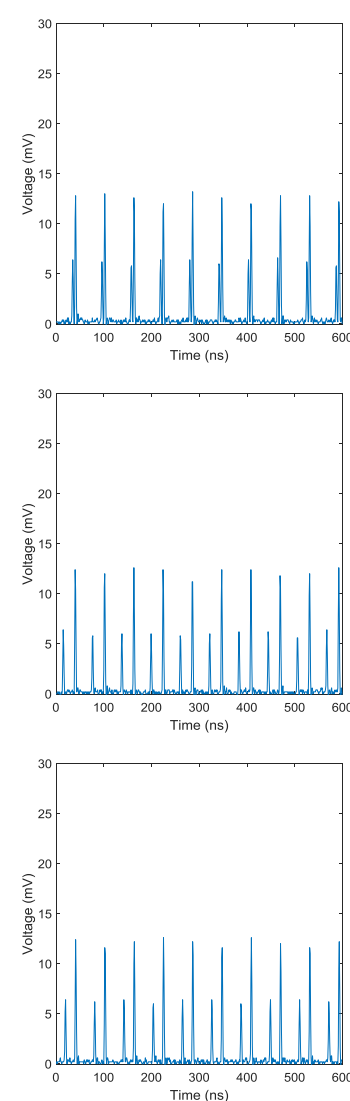
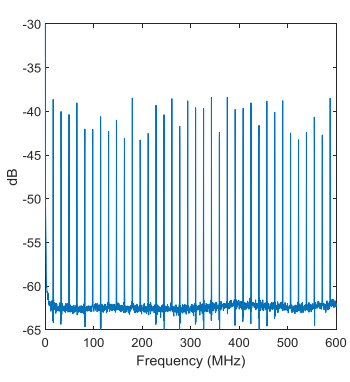
Appendix O

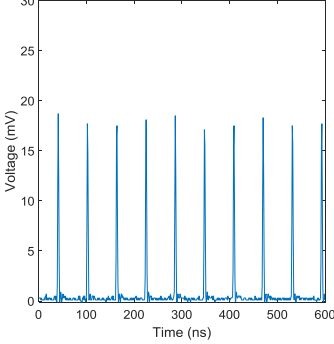
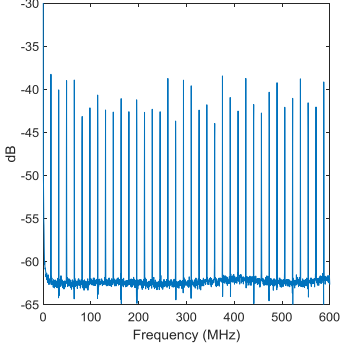
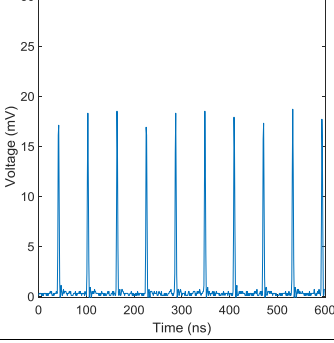
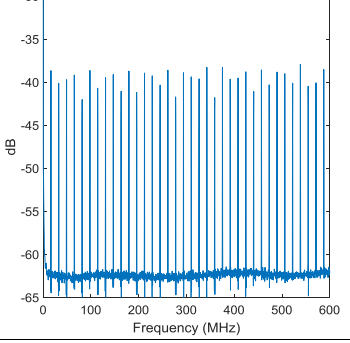
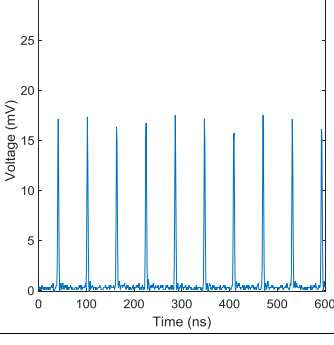
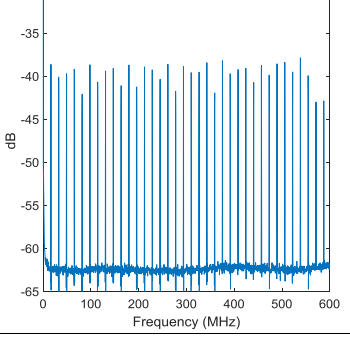
Continuous Mode-locked Piezo Incrementation Part II

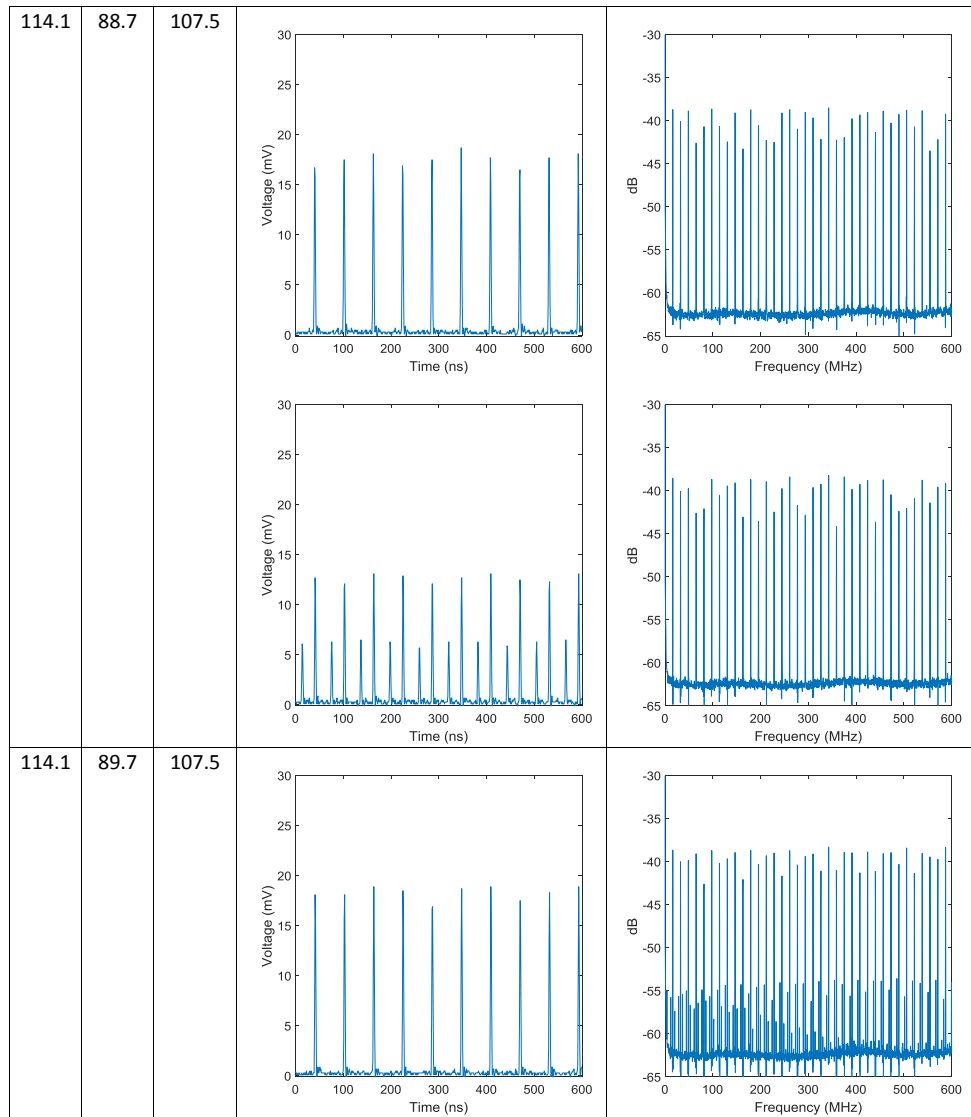
The proceeding table contains time and radio-frequency domain measurements taken while re-sweeping into a stable CML regime using the automation algorithm.

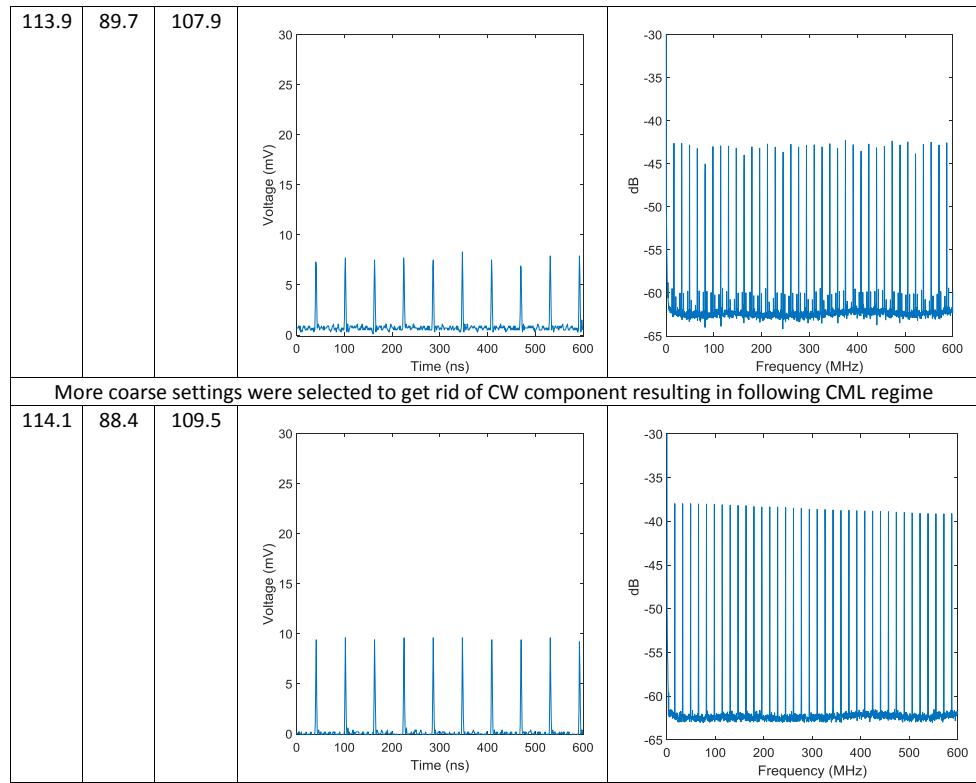
Some voltage settings had multiple corresponding oscilloscope traces and RF spectrum analyser traces due to dynamic (transient) changes in the regime.

Table O.1: Table featuring temporal and RF spectrum traces as the piezoelectric controller is changed to sweep back into a CML regime upon previously exiting.

Piezoelectric Voltages (V)			Temporal Domain Trace	RF Domain Trace
CH1	CH2	CH3		
114.7	89.4	107.1		

114.7	89.4	107.5		
114.7	89.1	107.5		
114.4	89.1	107.5		





Appendix P

Dispersion Compensation in the Literature

Dispersion Compensating Fibres

Jia *et al.* reported on an NLPR mode-locked TDFL which produced 617 ps pulses [1]. The installation of 4 m of DCF reduced the pulses to 48 ps, however it introduced a satellite pulse into the pulse train [1]. Zheng *et al.* reported on an NALM mode-locked EDFL that utilised DCF fibres to reduce the pulse duration of a 571 fs chirped pulse to 167 fs [2].

Pawlizewska *et al.* inserted DCF into a holmium laser cavity that was mode-locked using a graphene SESAM. Nufern's Ultra-high Numerical Aperture (UHNA) fibres were used to provide a positive GVD and reduce pulses to 190 fs. [3]

Grating and Prism Pair Compensation

Tokurakawa *et al.* demonstrated a single pass grating pair to compress pulses from a thulium ZBLAN fibre laser. Each fibre in the cavity had normal (positive) dispersion at the lasing wavelength (1880 nm) [4]. The output from the cavity was 860 fs, which

was compressed to 107 fs using a single pass grating pair. The autocorrelation of the pulse had a small pedestal, indicating incomplete compensation of higher-order dispersion [4]. The authors reported that a transform-limited pulse would have had a 99 fs FWHM [4].

Zhang *et al.* also reported on compressing pulses using grating pairs [5]. They reduced 8.7 ps pulses from a soliton nanotube mode-locked laser to 118 fs [5].

Chirped Mirrors and Gratings

Yang *et al.* used an intra-cavity chirped fibre Bragg grating with an optical circulator in the ring cavity. Authors reported that this lead to a noticeable improvement in regime stability and served as a good mechanism for dispersion compensation [6]. The FWHM of pulses out-coupled from the Yb-doped fibre cavity was 6.2 ps with a hyperbolic secant squared fit [6].

Liu *et al.* reported on using an extra-cavity chirped mirror pair for compression. The output from their mode-locked Ti: sapphire laser had an FWHM of 26 fs, which was shortened to 17 fs after mirrors [7].

References

- [1] Jia, Q, Wang, T, Ma, W, Liu, P, Zhang, P, Bo, B & Zheng, Y 2016, 'Passively harmonic mode-locked pulses in thulium-doped fiber laser based on nonlinear polarisation rotation', *Optical Engineering*, vol. 55, no. 10, pp. 1-6.
- [2] Zeng, Y, Zhou, Y & Xu, K 2018, 'All polarisation-maintaining, figure-of-9 dispersion-managed Er: fiber laser', presented at 10th International Conference on Information Optics and Photonics, Beijing, 15th November 2018.
- [3] Pawliszewska, M, Martynkein, T, Przewłoka, A & Sotor, J 2018, 'Dispersion-managed Ho-doped fiber laser mode-locked with a graphene saturable absorber',

Optics Letters, vol. 43, no 1, pp. 38-41.

[4] Tokurakawa, M, Sagara, H & Tunnermann, H 2019, 'All-normal-dispersion non-linear polarization rotation mode-locked Tm:ZBLAN fiber laser', Optics Express, vol. 27, no. 14, pp. 19530-19535.

[5] Zhang, Z *et al.* 2015, 'All-fiber nonlinearity – and dispersion-managed dissipative soliton nanotube mode-locked laser,' Applied Physics Letters, vol. 107, no. 241107, pp. 1-4.

[6] Yang, H, Li, W & Chen, G 2019, 'A chirped fiber Bragg grating with triple functions for stable wavelength-tunable Yb-doped fiber laser', Infrared Physics and Technology, vol. 102, no. 103008, pp. 1-4.

[7] Liu *et al.* 2019, 'Diode-pumped Kerr-lens mode-locked Ti:sapphire laser with broad wavelength tunability', Chinese Physics Letters B, vol. 28, no. 9, pp. 1-5

Appendix Q

List of Publications

Q.1 Conference Presentation and Proceedings

McAfee, D, Boyd, K, Carmody, N, Ganija, M, Simakov, N, Hemming, A, Veitch, P, Munch, J & Haub, J 2018, 'An electronically controlled mode-locked thulium all-fibre laser at 1.990 μm ,' paper presented at 43rd Australian Conference on Optical Fibre Technology, University of Western Australia, 10 December.

McAfee, D, Boyd, K, Ganija, M, Simakov, N, Carmody, N, Munch, J, Hemming, A, Veitch, P & Haub, J 2019, 'Mode-locked holmium fibre laser,' paper presented at 44th Australian Conference on Optical Fibre Technology, Royal Melbourne Institute of Technology, 10 December.

References

Chapter 1

- [1] Smith, P, Duguay, M & Ippen, E 1974, Mode-locking of lasers, Elsevier Science & Technology Books, Germany.
- [2] Knight, J & Wadsworth, W 2010, 'Silica fibres for supercontinuum generation', in JM Dudley & JR Taylor (eds), Supercontinuum generation in optical fibers, Cambridge Press, England, pp. 62-81.
- [3] Lee, J, Lee, J, Lee, S, Kim, S & Kim, Y 2012, 'High precision laser ranging by time-of-flight measurement of femtosecond pulses', Measurement Science and Technology Journal, vol. 23, no. 6, pp. 1-8.
- [4] Liu, J & Yang, L 2012, 'Femtosecond fibre lasers for biomedical solutions', SPIE Photonics Asia, vol. 8551, pp. 5-7.
- [5] Chichkov, B, Momma, C, Nolte, S, Alvensleben, F & Tunnerman, A 1996, 'Femtosecond, picosecond and nanosecond laser ablation of solids', Applied Physics Journal A, vol. 63, no. 2, pp. 109-115.
- [6] Surapaneni, R, Rohini, P, Vobbilireddi, S & Mounika, G 2012, 'Ultrafast spectroscopy: a review', International Journal of Pharmacy, vol. 2, no. 1, pp. 187-194.
- [7] Paschotta, R 2008, Encyclopedia of laser physics and technology, Wiley, Germany.
- [8] Agrawal, G 2008, Applications of non-linear fibre optics, Academic Press, United States.
- [9] Peters, G & Allen, L 1972, 'Spectral linewidth in laser amplifiers and amplified spontaneous emission, and its relevance to the interstellar medium', Physics Letters A, vol. 39, no. 4, pp. 259-260.

- [10] Woodward, R 2018, ‘Dispersion engineering of mode-locked fibre lasers’, *Journal of Optics*, vol. 20, no. 3, pp. 1-16.
- [11] Zimet, E & Mann, C 2009, *Directed energy weapons – are we there yet?*, Center for Technology and National Security Policy National Defense University, United States Government, Washington DC.
- [12] Antoncini, C 2013, ‘Ultrashort laser pulses’, paper presented at the University of Reading Physics Department Seminar, University of Redding.
- [13] Ruggiero, A, Scherer, N, Mitchell, G, Fleming, G & Hogan, J 1991, ‘Regenerative amplification of picosecond pulses in Nd:YAG at repetition rates in the 100-kHz range’, *Journal of Optical Society of America B*, vol. 8, no. 10, pp. 2061-2067.
- [14] Ueffing, M, Lange, R, Pleyer, T, Pervak, V, Metzger, T, Sutter, D, Major, Z, Nubbemeyer, T & Ferenc, K 2016, ‘Direct regenerative amplification of femtosecond pulses to the multi-millijoule level’, *Optics Letters*, vol. 41, no. 16, pp. 3840-3843.
- [15] Hinkelmann, M, Wandt, D, Morgner, U, Neumann, J & Kracht, D 2018, ‘Ultrashort pulse CPA-free Ho:YLF linear amplifier’, presented at the 27th Solid State Lasers Conference, San Francisco, 15th February 2018.
- [16] Rezvani, S, Suzuki, M, Malevich, P, Livache, C, Vincent de Montgolfier, J, Nomura, Y, Tsurumachi, N, Baltuska, A & Fuji, T 2018, ‘Millijoule femtosecond pulses at 1937 nm from a diode-pumped ring cavity Tm:YAP regenerative amplifier’, *Optics Express*, vol. 26, no. 22, pp. 29460-29470.
- [17] Solarz, R & Paisner, J 1986, *Laser spectroscopy and its applications*, CRC Press, New York.
- [18] Haag, G, Munz, M & Marowsky, G 1983, ‘Amplified spontaneous emission (ASE) in laser oscillators and amplifiers’, *IEEE Journal of Quantum Electronics*, vol. 19, no. 6, pp. 1149-1160.
- [19] Backus, S, Durfee, C, Murnane, M & Kapetyn, H 1998, ‘High power ultrafast lasers’, *Review of Scientific Instruments*, vol. 69, no. 3, pp. 1207-1223.
- [20] Boyd, R 2008, *Nonlinear optics*, Academic Press, London.
- [21] Johnson, A, Austin, D, Wood, D & Brahms, C 2018, ‘High-flux soft x-ray harmonic generation from ionisation-shaped few-cycle laser pulses’, *Science Advances*, vol. 4, no. 5, pp. 201 - 210.

- [22] Chini, M, Zhao, K & Chang, Z 2014, ‘The generation, characterization and applications of broadband isolated attosecond pulses’, *Nature Photonics*, vol. 8, no. 3, pp. 178-186.
- [23] Marangos, J 2019, ‘The measurement of ultrafast electronic and structural dynamics with x-rays’, *Philosophical Transactions of The Royal Society of America Mathematical, Physical and Engineering Sciences*, vol. 377, no. 20170481, pp. 1-9.
- [24] Bucksbaum, P, Betti, R, Collier, J, Dimauro, L, Garmire, E, Gish, J, Glover, E, Jones, M, Kapteyn, H, Lankford, A, Milchberg, H, Milton, S, Moulton, P & Patel, C 2018, *Opportunities in intense ultrafast laser physics*, National Academic Press, Washington.
- [25] Richard, H & Adra, C 2018, *Industrial applications of ultrafast lasers*, World Scientific, United States.
- [26] Pertot, Y, Schmidt, C, Matthews, M, Chauvet, A, Huppert, M, Svoboda, V, von Conta, A, Tehlar, A, Baykusheva, D, Wolf, J & Wörner, H 2017, ‘Time-resolved x-ray absorption spectroscopy with a water window high-harmonic source’, *Science*, vol. 335, no. 6322, pp. 264-267.
- [27] Genty, G 2013, ‘Supercontinuum generation in optical fibres: 40 years of non-linear optics in one experiment’, paper presented at the Tampere University of Technology Finland Optics Laboratory Seminars, Tampere University of Technology, April.
- [28] Agrawal, G 2014, ‘Supercontinuum generation in optical fibers and its biomedical applications (presentation video)’, presented at 12th conference on Optical Biopsy, California, 4th May 2014.
- [29] Blom, H & Widengren, J 2017, ‘Stimulated emission depletion microscopy’, *Chemical Reviews*, vol. 117, pp. 7377-7427.
- [30] Oracz, J, Westphal, V, Radzewicz, C, Sahl, S & Hell, S 2017, ‘Photobleaching in STED nanoscopy and its dependence on the photon flux applied for reversible silencing of the fluorophore’, *Scientific Reports*, vol. 7, no. 11354, pp. 1-14.
- [31] Wang, C, Kim, J, Jin, C, Leong, P & McEwan, A 2011, ‘Near infrared spectroscopy in optical coherence tomography’, *Journal of Near Infrared Spectroscopy*, vol. 20, no. 1, pp. 237-247.

- [32] Liang, H, Cheung, C, Daniel, J, Tokurakawa, M, Clarkson, W & Spring, M 2015, ‘High resolution Fourier domain optical coherence tomography at 2 micron for painted objects’, vol. 9527, no. 952705, pp. 1-6.
- [33] Bokobza, L 1998, ‘Near infrared spectroscopy’, *Journal of Near Infrared Spectroscopy*, vol. 6, no. 1, pp. 3-17.
- [34] Khodabakhsh, A, Pan, Q, Eslami, K & Harren, F 2018, ‘Mid-infrared spectroscopy using supercontinuum sources: towards field applications’, *Light Energy and the Environment Congress*.
- [35] Baker, M *et al.* 2015, ‘Using Fourier transform IR spectroscopy to analyze biological materials’, *Nature Protocols*, vol. 9, no. 8, pp. 1771-1791.
- [36] Kilgus, J, Duswald, K, Langer, G & Brandstetter, M 2017, ‘Mid-infrared stand-off spectroscopy using a supercontinuum laser with compact Fabry-Perot filter spectrometers’, *Applied Spectroscopy*, vol. 72, no. 4, pp. 634-642.
- [37] O’Donnell, S, Demshemino, I, Yahaya, M, Nwadike, I & Okoro, L 2013, ‘A review on the spectroscopic analyses of biodiesel’, *European International Journal of Science and Technology*, vol. 2, no. 7, pp. 137-146.
- [38] Grassani, D, Tagkoudi, E, Guo, H, Herkommer, C, Yang, F, Kippenberg, T & Bres, C 2019, ‘Mid infrared gas spectroscopy using efficient fiber laser driven photonic chip-based supercontinuum’, *Nature Communications*, vol. 10, no. 1553, pp. 1-8.
- [39] Wilks, P 2006, ‘NIR versus mid-IR: how to choose’, *Spectroscopy*, vol. 21, no. 4, pp. 43-46.
- [40] Fuerbach, A, Hudson, D, Jackson, S, Antipov, S, Woodward, R, Li, L, Alamgir, I, Amraoui, M, Messaddeq, Y & Rochette, M 2018, ‘Mid-IR supercontinuum generation’, paper presented at 5th speciality optical fibres conference, Zurich, 2nd – 5th July.
- [41] Gan, F 1995, ‘Optical properties of fluoride glasses: a review’, *Non Crystal Solids*, vol. 184, pp. 9-20.
- [42] Zhang, F, Yan, W, Liang, S, Tan, C & Tang, P 2019, ‘Numerical study on the soliton mode-locking of Er^{3+} doped fluoride fiber laser at $\sim 3 \mu\text{m}$ with nonlinear polarisation rotation’, *Photonics*, vol. 6, no. 1, pp. 1-7.

- [43] Majewski, M, Woodward, R & Jackson, S 2018, 'Dysprosium-doped ZBLAN fiber laser tunable from 2.8 μm to 3.4 μm , pumped at 1.7 μm ', Optics Letters, vol. 43, no. 5, pp. 971-974.
- [44] Henderson-Sapir, O, Bawden, N, Majewski, M, Woodward, R, Ottaway, D & Jackson, S 2020, 'Mode-locked and tunable fiber laser at the 3.5 μm band using frequency-shifted feedback', Optics Letters, vol. 45, no. 1, pp. 224-227.
- [45] Haus, H 2000, 'Mode-locking of lasers', IEEE Journal of Selected Topics in Quantum Electronics, vol. 6, no. 6, pp. 1173-1185.
- [46] Nikodem, M, Sergeant, H, Kaczmarek, P & Abramski, K 2020, 'Actively mode-locked fiber laser using acousto-optic modulator', paper presented at 16th Polish-Slovak-Czech Optical Conference, Polanica Zdroj, March 2020.
- [47] Lei, X, Wieschendorf, C, Firth, J, Ladouceur, F, Silvestri, J & Fuerbach, A, 'All-in-One fiber laser based on a liquid crystal transducer,' IEEE Photonics Technology Letters, vol. 31, no. 17, pp. 1409-1412.
- [48] Hudson, D, Holman, K, Jones, R, Cundiff, S & Ye, J 2005, 'Mode-locked fiber laser frequency-controlled with an intra-cavity electro-optic modulator', Optics Letters, vol. 30, no. 21, pp. 2948-2950.
- [49] Jakubczak, K 2011, Laser system for applications, InTech, Croatia.
- [50] Paschotta, R & Keller, U 2001, 'Passive mode locking with slow saturable absorbers', Applied Physics B, vol. 73, no. 7, pp. 653-662.
- [51] Repgen, P *et al.* 2020, 'Mode-locked pulses from a thulium-doped fiber Mamyshhev oscillator', Optics Express, vol. 28, no. 9, pp. 13837 - 13844.
- [52] Kobtsev, S & Smirnov, S 2011, 'Fiber laser mode-locked due to nonlinear polarization evolution: golden mean of cavity length', Laser Physics, vol. 21, no. 2, pp. 272-276.
- [53] Wang, X, Peng, X & Zhang, J 2018, 'Multistate passively mode-locked thulium-doped fiber laser with nonlinear amplifying loop mirror', Applied Optics, vol. 57, no. 13, pp. 3410-3414.
- [54] Hansel, W, Hoogland, H, Giunta, M, Schmid, S, Steinmetz, T, Doubek, R, Mayer, P, Dobner, S, Cleff, C, Fischer, M & Holzwarth, R 2018, 'All polarisation-maintaining fibre laser architecture for robust femtosecond pulse generation', in

T Esslinger, N Picque & T Udem (eds), Enlightening the world with the laser, Germany, pp. 331-430.

[55] Keller, U 2003, 'Recent developments in compact ultrafast lasers', *Nature*, vol. 424, pp. 831-838.

[56] Song, R, Chen, H, Chen, S, Hou, J & Lu, Q 2011, 'A SESAM passively mode-locked fiber laser with a long cavity including a band pass filter', *Journal of Optics*, vol. 13, no. 3, pp. 1-5.

[57] Li, P *et al.* 2016, '980-nm all-fiber mode-locked Yb-doped phosphate fiber oscillator based on semiconductor saturable absorber mirror and its amplifier', *Chinese Physics B*, vol. 25, no. 8, pp. 1-6.

[58] Liu, W, Liao, J, Cui, J, Song, Y, Wang, C & Hu, W 2019, 'Femtosecond Mamyshev oscillator with 10-MW-level peak power', *Optica*, vol. 6, no. 2, pp. 194-197.

[59] Liu, Z, Ziegler, Z, Wright, L & Wise, F 2017, 'Megawatt peak power from a Mamyshev oscillator', *Optica*, vol. 4, no. 6, pp. 649-654.

[60] Vinegoni, C, Wegmuller, M, Huttner, B & Gisin, N 2000, 'Measurement of nonlinear polarization rotation in a highly birefringent optical fibre using a Faraday mirror', *Journal of Pure & Applied Optics*, vol. 2, pp. 3140-318.

[61] Serebryakov, V, Boiko, E, Petrishchev, N & Yan, A 2010, 'Medical applications of mid-IR lasers – problems and prospects', *Journal of Optical Technology*, vol. 77, no. 1, pp. 6-17.

[62] Thomson, R, Leburn, C & Reid, D 2013, *Ultrafast non-linear optics*, Springer, Edinburgh (UK).

[63] Zhang, M 2019, *Handbook of graphene*, Wiley, Florida.

[64] Rose, A, Feat, N & Etzel, S 2003, 'Wavelength and temperature performance of polarization-transforming fiber', *Applied Optics*, vol. 42, no. 34, pp. 6897 – 6904.

[65] Olivier, M, Gagnon, M & Habel, J 2016, 'Automation of mode locking in a nonlinear polarization rotation fiber laser through output polarization measurements', *Journal of Visual Experiments Canada*, vol. 108, no. 1.

[66] Barbec, T, Spielmann, C, Curley, P & Krausz, F 1992, 'Kerr lens mode-locking', *Optics Letters*, vol. 17, no. 18, pp. 1292-1294.

- [67] Akbari, R & Major, A 2017, ‘Kerr-lens mode-locked femtosecond Yb:KGW laser’, presented at Photonics North 2017, Ottawa, 7th June 2017.
- [68] Sotor, J *et al.* 2016, ‘All-fiber Ho-doped mode-locked oscillator based on a graphene saturable absorber’, *Optics Letters*, vol. 41, no. 11, pp. 2592-2595.
- [69] Hinkelmann, M, Wandt, D, Morgner, U, Neumann, J & Kracht, D 2017, ‘Ultrafast mode-locked Ho-doped all-fibre laser operating at 2.05 μm ’, *Conference on Lasers and Electro-optics*.
- [70] Grzes, P, Michalska, M & Swiderski, J 2018, ‘Picosecond mode-locked Tm-doped fibre laser and amplifier system providing over 20W of average output power at 1994 nm’, *Metrology and Measurement Systems*, vol. 25, no. 4, pp. 649-658.
- [71] Lin, H, Lin, Z, Bai, R, Zhang, L, Lin, Z, Zhang, G & Chen, W 2018, ‘69 fs SESAM mode-locked Yb:GdYCOB oscillator’, presented at the Optical Society Laser Congress, 8th November 2018.
- [72] Wang, J, Liang, X, Hu, G, Zheng, Z, Lin, S, Ouyang, D, Wu, X, Yan, P, Ruan, S, Sun, Z & Hasan, T 2016, ‘152 fs nanotube-mode-locked thulium-doped all-fiber laser’, *Scientific Reports*, vol. 6, no. 28885, pp. 1-7.
- [73] Wang, Y *et al.* 2019, ‘52-fs SESAM mode-locked Tm,Ho:CALGO laser’, presented at the 2019 Laser Congress, 29th September 2019.
- [74] Pawliszewska, M, Przewłoka, A & Sotor, J 2018, ‘Stretched-pulse Ho-doped fiber laser mode-locked by graphene based saturable absorber’, paper presented at the 25th Fiber Lasers Technology and Systems conference, San Fransisco, January 2018.
- [75] Tolstik, N, Sorokin, E, Bugar, I & Sorokina, I 2016, ‘Compact diode-pumped dispersion-managed SESAM mode-locked Ho: fiber laser’, presented at High Brightness Sources and Light Driven Interactions conference, California, 21 March 2016.
- [76] Voropaev, V, Donodin, A, Voronets, A, Lazarev, V, Tarabin, M, Karasik, V & Krylov, A 2018, ‘High-power passively mode-locked thulium-doped all-fiber ring laser with nonlinearity and dispersion management’, paper presented at the International Conference of Laser Optics, June 2018.
- [77] Nomura, Y & Fuji, T 2014, ‘Sub-50-fs pulse generation from thulium-doped ZBLAN fiber laser oscillator’, *Optics Express*, vol. 22, no. 10, pp. 12461-12466.

- [78] Chen, L, Huynh, J, Zhou, H, Chyla, M, Smrz, M & Mocek, T 2019, 'Generating 84 fs, 4 nJ directly from an Yb-doped fiber oscillator by optimization of the net dispersion', *Laser Physics*, vol. 29, no. 6, pp. 1-6.
- [79] Li, J, Xia, H, Du, W, Li, H & Liu, Y 2018, 'Direct generation of 62-fs pulses in an erbium-doped fiber laser', paper presented at 6th International Conference on Optical and Photonic Engineering, Shanghai, July 2018.
- [80] Gao, C, Wang, Z, Luo, H & Zhan, L 2017, 'High energy all-fiber Tm-doped femtosecond soliton laser mode-locked by non-linear polarisation rotation', *Journal of Lightwave Technology*, vol. 35, no. 14, pp. 2998 – 2993.
- [81] Lin, P, Wang, T, Ma, W, Liu, R & Zhao, D 2019, 'Generation of dispersion-managed solitons with sidebands in a 2- μm mode-locked fiber laser', *Optical Engineering*, vol. 58, no. 11, pp. 1-6.
- [82] Li, P, Ruehl, A, Grosse-Wortmann, U, Hartl, I 2014, 'Sub-100 fs passively mode-locked holmium-doped fiber oscillator operating at 2.06 μm ', *Optics Letters*, vol. 39, no. 24, pp. 6859-6862.
- [83] Haxsen, F *et al.* 2012, 'Monotonically chirped-pulse evolution in an ultrashort pulse thulium-doped fibre laser', *Optics Letters*, vol. 103, no. 6, pp. 1014-1016.
- [84] Li *et al.* 2015, 'Subpicosecond SESAM and nonlinear polarization evolution hybrid mode-locking ytterbium-doped fiber oscillator', *Applied Physics B*, vol. 118, no. 4, pp. 561-566.
- [85] Wu *et al.* 2019, 'Wavelength-tunable passively mode-locked all-fiber laser at 1.5 μm ', *Applied Optics*, vol. 58, no. 19, pp. 5143-5147.
- [86] Dvoretzkiy, D *et al.* 2016, 'Dispersion-managed soliton generation in the hybrid mode-locked erbium-doped all-fiber ring laser', presented at the International Conference for Laser Optics, June 2016.
- [87] Chen, T *et al.* 2018, 'Incorporating MoS₂ saturable absorption with nonlinear polarization rotation for stabilized mode-locking fibre lasers', *Laser Physics Letters*, vol. 15, no. 7, pp. 1-10.
- [88] Liu, G, Jiang, X, Wang, A, Chang, G, Kaertner, F & Zhang, Z 2018, 'Robust 700 MHz mode-locked Yb: fiber laser with a biased nonlinear amplifying loop mirror', *Optics Express*, vol. 26, no. 20, pp. 26003-26009.

- [89] Deng, D, Zhang, H, Gong, Q, He, L, Li, D & Gong, M 2020, ‘Energy scalability of the dissipative soliton in an all-normal-dispersion fiber laser with nonlinear amplifying loop mirror’, *Optics and Laser Technology*, vol. 125, no. 106010, pp. 1-7.
- [90] Guo, Z, Hao, Q, Peng, J & Zeng, H 2019, ‘Environmentally stable Er-fiber mode-locked pulse generation and amplification by spectrally filtered and phase-biased nonlinear amplifying long-loop mirror’, *High Power Laser Science and Engineering*, vol. 7, no. 47, pp. 1-7.
- [91] Khegai, A, Melkumov, M, Riumkin, K, Khopin, V, Firstov, S & Dianov, E 2018, ‘NALM-based bismuth-doped fiber laser at 1.7 μm ’, *Optics Letters*, vol. 43, no. 5, pp. 1127-1130.
- [92] Michalska, M & Swiderski, J 2019, ‘Noise-like pulse generation using polarisation maintaining mode-locked thulium-doped fiber laser with nonlinear amplifying loop mirror’, *IEEE Photonics Journal*, vol. 11, no. 5, pp. 1-10.
- [93] Radnatarov, D, Khripunov, S, Kobtsev, S, Ivanenko, A & Kukarin, S 2013, ‘Automatic electronic-controlled mode locking self-start in fibre lasers with nonlinear polarisation evolution’, *Optics Express*, vol. 21, pp. 20626 – 20631.
- [94] Woodward, R & Kelleher, J 2016, ‘Towards ‘smart lasers’: self-optimisation of an ultrafast pulse source using a genetic algorithm’, *Scientific Reports*, vol. 6., no. 37616, pp. 1-9.
- [95] Chen, Y, Kärtner, F, Morgner, U, Cho, S, Haus, H, Ippen, E & Fujimoto, J 1999, ‘Dispersion managed mode-locking’, *Journal of the Optical Society of America B*, vol. 16, no. 11, pp. 1999-2004.

Chapter 2

- [1] Agrawal, G 1997, *Fibre-optic communication systems*, Wiley, University of Michigan.
- [2] Decusatis, C & Decusatis, C 2005, *Fibre optic essentials*, Academic Press, United States.
- [3] Sheekey, A 1994, *Optical fibres and applications*, Information Gatekeeping, Boston.

- [4] Simakov, N 2017, ‘Development of components and fibres for the power scaling of pulsed holmium-doped fibre sources’, PhD thesis, University of Southampton, England.
- [5] Ding, E, Lefrançois, S, Kutz, J & Wise, F 2011, ‘Passive mode-locking using multi-mode fiber,’ paper presented at 8th Fiber Lasers: Technology, Systems and Applications Conference, 10th February 2011.
- [6] Marcuse, D 1978, ‘Gaussian approximation of the fundamental modes of graded-index fibers’, Journal of Optical Society of America, vol. 68, no. 1, pp. 103-109.
- [7] Paschotta, R 2008, Encyclopedia of laser physics and technology, Wiley, Germany.
- [8] Dong, L, Li, J, McKay, H, Fu, L & Thomas, B 2009, ‘Large effective mode area for high power lasers’, Proceedings of SPIE, no. 7195.
- [9] Dong, L & Samson, B 2016, Fiber lasers: basics, technology and applications, CRC Press, Boca Raton.
- [10] Nakandakari, M, Kuroda, K & Yoshikuni, Y 2017, ‘Metastable-state lifetime of erbium ions measured in the fiber propagation direction: expansion of measurable fiber length’, Japanese Journal of Applied Physics, vol. 56, no. 112501, pp. 1-3.
- [11] Pollnau, M & Jackson, S 2001, ‘Erbium 3- μm fiber lasers’, IEEE Journal on Selected Topics in Quantum Electronics, vol. 7, no. 1, pp. 30-40.
- [12] Kakkar, C, Monnom, G, Thyagarajan, K & Dussardier, B 2005, ‘Segmented-clad fiber design for inherently gain-flattened L-band TDFA’, IEEE Photonics Technology Letters, vol. 17, no. 9, pp. 1833-1835.
- [13] Kurkov, A, Dvoyrin, V & Marakulin, A 2010, ‘All-fiber 10W holmium lasers pumped at $\lambda = 1.15 \mu\text{m}$ ’, Optics Letters, vol. 35, no. 4, pp. 490-492. [14] Bowman, S, O’Connor, S, Condon, N, Friebele, E, Kim, W, Shaw, B & Quimby, R 2013, ‘Non-radiative decay of holmium-doped materials’, presented at 6th Laser Refrigeration of Solids Conference, 11th March 2013.
- [15] Jackson, S 2004, ‘Cross relaxation and energy transfer upconversion processes relevant to the functioning of 2 μm Tm^{3+} -doped silica fibre lasers’, Optics Communications, vol. 230, no. 3, pp. 197-203.
- [16] Seaton, M 1983, ‘Quantum defect theory,’ Reports on Progress in Physics, vol.

46, no. 2, pp. 167-177.

- [17] Fiberlabs 2009, Core and cladding pumping, Fiberlabs Incorporated, viewed 15th August 2019, <<https://www.fiberlabs.com/glossary/core-pumping-and-cladding-pumping/>>
- [18] Snitzer, E 1989, Optical fiber lasers and amplifiers, United States patent 4815079.
- [19] Collett, E 2003, Polarised light in fiber optics, Polawave Group, New Jersey.
- [20] Goldstein, D 2010, Polarised light, CRC Press, Boca Raton.
- [21] Hecht, E 2001, Optics, Addison-Wesley, Essex.
- [22] Newport Corporation 2019, Manual polarisation controllers, Newport, viewed 20th August 2019, <<https://www.newport.com/f/polarization-controllers-manual>>
- [23] Laser Components 2019, Polarite electrically controlled polarisation controller, PolaRITE, viewed 22nd August 2019, <<https://lasercomponents.com/de-en/product/polarite-electrically-operated-polarization-controller/>>
- [24] VanderLugt, A 2005, Optical signal processing, Wiley, United States.
- [25] Ter-Mikirtychev, V 2013, Fundamentals of fiber lasers and fiber amplifiers, Springer, California.
- [26] Chang, Z 2011, Fundamentals of attosecond optics, Taylor and Francis CRC Group, Boca Raton.
- [27] Zhang, A, Chen, X, Yan, J, Guan, Z, He, S & Tam, H 2005, 'Optimization and fabrication of stitched long-period gratings for gain flattening of ultrawide-band EDFAs', IEEE Photonics Technology Letters, vol. 17, no. 12, pp. 2559-2561.
- [28] Vázquez-Córdova, S, Aravazhi, S, Grivas, C, Yong, Y, Garcia-Blanco, S, Herek, J & Pollnau, M 2018, 'High optical gain in erbium-doped potassium double tungstate channel waveguide amplifiers', Optics Express, vol. 26, no. 5, pp. 6260-6266.
- [29] Simakov, N, Li, Z, Jung, Y, Daniel, J, Barua, P, Shardlow, P, Liang, S, Sahu, J, Hemming, A, Clarkson, A, Alam, S & Richardson, D 2016, 'High gain holmium-doped fibre amplifiers', Optics Express, vol. 24, no. 13, pp. 13946-13956.
- [30] Wang, J, Liang, S, Kang, Q, Jung, Y, Alam, S & Richardson, D 2016, 'Broad-band silica-based thulium doped fiber amplifier employing multi-wavelength pumping', Optics Express, vol. 24, no. 20, pp. 23001-23008.

- [31] Krauss, G, Lohss, S, Hanke, T, Sell, A, Eggert, S, Huber, R & Leitenstorfer, A 2010, ‘Synthesis of a single cycle of light with compact erbium-doped fibre technology’, *Nature Photonics*, vol. 4, no. 1, pp. 33-36.
- [32] Agrawal, G 2012, *Non-linear fibre optics*, Academic Press, New York.
- [33] Wen-Cheng, X, Qi, G & Song-hao, L, ‘Higher-order dispersion and soliton pulse compression in dispersion-decreasing fibres’, vol. 14, no. 4, pp. 298-306.
- [34] Metha, N 2008, *Textbook of engineering physics: part 1*, PHI Learning, Varanasi.
- [35] Saleh, B & Teich, M 1991, *Fundamentals of photonics*, Wiley, United States.
- [36] Lin, W 2008, ‘Physically aware agile optical networks’, PhD thesis, Montana State University, Montana.
- [37] Woodward, R 2018, ‘Dispersion engineering of mode-locked fibre lasers [Invited]’, *Journal of Optics*, vol. 20, no. 033002, pp. 1-18.
- [38] New, G 2011, *Introduction to non-linear optics*, Cambridge University Press, Cambridge.
- [39] Huang, J 2018, ‘Non-linear Schro“dinger equation’ in Lembrikov, B (eds), *Non-linear optics – novel results in theory and applications*, Intechopen, United States, pp. 1-20.
- [40] Agrawal, G 2015, ‘Polarization phenomena in non-linear optical fibers’, lecture notes distributed in topic *Non-linear Fibre Optics*, University of Rochester.
- [41] Agrawal, G 2012, *Applications of non-linear fibre optics*, Academic Press, New York.
- [42] Mollenauer, L & Gordon, J 2006, *Solitons in optical fibers*, Academic Press, United Kingdom.
- [43] Paschotta, R 2008, *Field guide to laser pulse generation*, Society for Optical Engineering SPIE, United States.
- [44] Hannaford, P 2005, *Femtosecond laser spectroscopy*, Springer, New York.
- [45] Lu, W & Yan, L 2002, ‘Dispersion effects in an actively mode-locked inhomogeneous broadened laser’, *Journal of Quantum Electronics*, vol. 38, no. 10, pp. 1317 – 1324.
- [46] Gong, Q, Cui, Y, Lessard, R & Hui, Z 2005, *Non-linear optical phenomena and applications*, SPIE, Beijing.

- [47] Fermann, M, Galvanauskas, A & Sucha, G 2002, *Ultrafast lasers: technology and applications*, CRC Press, New York.
- [48] Shlizerman, E, Ding, E, Williams, M & Kutz, J 2011, 'Characterizing and suppressing multi-pulsing instabilities in mode-locked lasers', *Proceedings of SPIE*, vol. 7933, *Physics and Simulation of Optoelectronic Devices XIX*, 79331L.
- [49] Rühl, A 2008, *The normal dispersion regime in passively mode-locked fiber oscillators*, Cuviller Verlag, Germany.

Chapter 3

- [1] Xu, X *et al.* 2014, 'Passively mode-locking erbium-doped fiber lasers with 0.3 nm single-walled carbon nanotubes', *Scientific Reports*, vol. 4, no. 6761, pp. 1-4.
- [2] Nakazawa, M 2010, 'Recent progress on ultrafast/ultrashort/frequency-stabilized erbium-doped fiber lasers and their applications', *Frontiers of Optoelectronics in China*, vol. 3, no. 1, pp. 38-44.
- [3] Newport Corporation 2019, *Manual polarisation controllers*, Newport, viewed 11th February 2019, <<https://www.newport.com/f/polarization-controllers-manual>>
- [4] Agrawal, G 2009, *Applications of non-linear fibre optics*, Academic Press, United States.
- [5] Hönninger, C *et al.* 1999, 'Q-switching stability limits of CW passive mode locking', *Journal of the Optical Society of America B*, vol. 16, no. 1, pp. 46-59.
- [6] Kane, D & Trebino, R 1993, 'Characterisation of arbitrary femtosecond pulses using frequency resolved optical gating', *Journal of Quantum Electronics*, vol. 29, no. 2, pp. 571 – 579.
- [7] Anderson, M, Monmayrant, A, Gorza, S, Wasylczyk, P & Walmsley, I 2008, 'SPIDER: A decade of measuring ultrashort pulses', *Laser Physical Letters*, vol. 5, no. 4, pp. 259 – 266.
- [8] Melchior, H 1973, 'Sensitive high speed photodetectors for demodulation of visible and near infrared light', *Journal of Luminescence*, vol. 7, pp. 390 – 414.
- [9] Oldfield, D 1986, 'A data acquisition system for a 1 GHz digitising oscilloscope', *Hewlett Packard Journal*, vol. 37, no. 4, pp. 4 – 10.
- [10] Haboucha, A *et al.* 2014, 'Fiber Bragg grating stabilization of a passively

modelocked 2.8 μm Er^{3+} : Fluoride glass fiber laser', *Optics Letters*, vol. 39, no. 11, pp. 3294-3297.

[11] Olivier, M, Gagnon, M & Piche, M 2015, 'Automated mode locking in nonlinear polarization rotation fiber lasers by detection of a discontinuous jump in the polarization state', *Optics Express*, vol. 23, no. 5, pp. 6738 – 6746.

[12] Engelson, M 1984, *Modern spectrum analyser theory and applications*, Artec House, United States.

[13] Kularatna, N 2008, *Digital and analogue instrumentation: testing and measurement*, IET, United Kingdom.

[14] Gorbunkov, M, Maslova, Y, Petukhov, V, Semenov, M, Shabalin, Y & Tunkin, V 2017, 'Harmonic mode-locking and sub-round-trip time nonlinear dynamics of electro-optically controlled solid state laser', presented at European Conference on Nonlinear Maps and Applications, 28th June 2017.

[15] Ferrera, M *et al.* 2014, 'CMOS compatible integrated all-optical radio frequency spectrum analyzer', *Optics Express*, vol. 22, no. 18, pp. 21488 - 21498.

[16] Luo, Z, Li, Y, Zhong, M & Huang, Y 2015, 'Nonlinear optical absorption of few-layer molybdenum diselenide (MoSe_2) for passively mode-locked soliton fiber laser', *Photonics Research*, vol. 3, no. 3, pp. 79-86.

[17] Thorlabs Corporation GmbH 2019, SMA to SMA cables, Thorlabs, viewed 1st February 2019, < <https://www.thorlabs.com/newgrouppage9.cfm?objectgroupid=2888>>

[18] James, J 2002, *A student's guide to Fourier transforms: with applications in physics and engineering*, Cambridge University Press, United Kingdom.

[19] Nallathambi, G & Principe, J 2016, 'Signal processing with pulse trains: an algebraic approach - part I', ArXiv.

[20] Thomas, C 1966, 'Optical spectrum analysis of large space bandwidth signals', *Applied Optics*, vol. 5, no. 11, pp. 1782 – 1790.

[21] Yokogawa Test and Measurement Corporation, AQ6375B long wavelength optical spectrum analyzer 1200 - 2400 nm, Yokogawa, viewed 1st May 2019, < <https://tmi.yokogawa.com/au/solutions/products/optical-measuring-instruments/optical-spectrum-analyzer/aq6375b-optical-spectrum-analyzer/>>

- [22] Shafer, A, Megill, L & Droppleman, L 1964, 'Optimisation of a Czerny-Turner spectrometer', *Journal of the Optical Society of America*, vol. 54, no. 7, pp. 879-887.
- [23] Yao, X, Zhang, B, Chen, X & Willner, A 2008, 'Real-time optical spectrum analysis of a light source using a polarimeter', *Optics Express*, vol. 16, no. 22, pp. 17854-17863.
- [24] Klopff, F, Deubert, S, Reithmaier, J & Forchel, A 2002, 'Correlation between the gain profile and the temperature-induced shift in wavelength of quantum-dot lasers', *Applied Physics Letters*, vol. 81, no. 2, pp. 217-219.
- [25] Kelly, S 1992, 'Characteristic sideband instability of periodically amplified average soliton', *Electronic Letters*, vol. 28, no. 8, pp. 806-812.
- [26] Jones, D, Chen, Y, Haus & Ippen, E 1998, 'Resonant sideband generation in stretched-pulse fiber lasers', *Optics Letters*, vol. 23, no. 19, pp. 1535-1543.
- [27] Wan, P, Yang, L & Liu, J 2013, 'High power 2 μm femtosecond fiber laser', *Optics Express*, vol. 21, no. 18, pp. 21374 – 21379.
- [28] Broersen, P 2006, *Automatic autocorrelation and spectral analysis*, Springer, Germany.
- [29] Dubois, A 2016, *Handbook of full-field optical coherence microscopy: technology and applications*, CRC Press, United States.
- [30] Trebino, R 2000, *Frequency Resolved Optical Gating*, Chapter 4: Autocorrelation, Springer, Germany.
- [31] Urisui, T & Mizushima, Y 1982, 'Simplified theory of mode-locking process for evaluating SHG autocorrelation pulse width', *The Japan Society of Applied Physics*, vol. 21, no. 2, pp. 434 – 436.
- [32] Qian, L, Nakkeeran, K & Wai, P 2014, 'Ultrashort pulse train generation using nonlinear optical fibers with exponentially decreasing dispersion', *Journal of the Optical Society of America B*, vol. 31, no. 8, pp. 1786-1792.
- [33] Linde, D 1986, 'Characterization of the noise in continuously operating mode-locked lasers', *Applied Physics B*, vol. 39, no. 4, pp. 201 – 217.
- [34] Nolte, S, Schrepel, F & Dausinger, F 2015, *Ultrashort pulse laser technology: laser sources and applications*, Springer, Germany.

[35] Glass, A *et al.* 2000, ‘Advances in optical fibres’, Bell Labs Technical Journal, vol. 2000, pp. 168-187.

Chapter 4

[1] Thorlabs Corporation GmbH 2019, SMA to SMA cables, Thorlabs, viewed 1st February 2019, <https://www.thorlabs.com/newgrouppage9.cfm?object_group_id=2888>

[2] APE Berlin GmbH 2018, PulseCheck autocorrelator, APE, viewed 16th June 2018, <<https://www.ape-berlin.de/en/autocorrelator/pulsecheck/>>

[3] APE Berlin GmbH 2016, PulseCheck S/N S04028, APE instrumentation manual, APE, Berlin.

[4] Olivier, M, Gagnon, M & Piche, M 2015, ‘Automated mode-locking in nonlinear polarisation rotation fiber lasers by detection of a discontinuous jump in the polarisation state’, Optics Express, vol. 23, no. 5, pp. 6738 – 6746.

[5] Hellwig, T, Walbaum, T, Groß, P & Fallnich, C 2010, ‘Automated characterization and alignment of passively mode-locked fiber lasers based on nonlinear polarization rotation’, Applied Physics B, vol. 101, no. 3, pp. 565-570.

[6] Woodward, R & Kelleher, E 2016, ‘Towards smart lasers: self optimisation of an ultrafast pulse source using a genetic algorithm’, Scientific Reports, vol. 6, no. 37616, pp. 1-9.

[7] Winters, D, Kirchner, M, Backus, S & Kapteyn, H 2017, ‘Electronic initiation and optimization of nonlinear polarization evolution mode-locking in a fiber laser’, Optics Express, vol. 25, no. 26, pp. 33216 – 33225.

[8] Radnatarov, D, Khripunov, S, Kobtsev, S, Ivanenko, A & Kukarin, S 2013, ‘Automatic electronic-controlled mode-locking self-start in fibre lasers with nonlinear polarisation evolution’, Optics Express, vol. 21, no. 18, pp. 20626–20631.

[9] Gordon, A & Fischer, B 2003, ‘Phase transition theory of pulse formation in passively mode-locked lasers with dispersion and Kerr nonlinearity’, Optical Communications, vol. 223, no. 3, pp. 151-156.

[10] Tkachenko, N 2006, Optical spectroscopy: methods and instrumentations, Elsevier, Tampere.

- [11] Thorlabs Corporation GmbH 2019, Fiber photodiode power sensors, viewed 20th August 2019, < https://www.thorlabs.com/NewGroupPage9.cfm?ObjectGroup_ID=3328>
- [12] Li, C, Wei, Tan, S, Chen, N, Kang, J & Wong, K 2017, ‘Short wavelength mode-locked thulium-doped fiber laser based on nonlinear polarization rotation’, presented at the Conference on Lasers and Electro Optics US, San Jose, 16th May 2017.
- [13] Jia, Q, Wang, T, Ma, W, Liu, P, Zhang, P, Bo, B & Zhang, Y 2016, ‘Passively harmonic mode-locked pulses in thulium-doped fiber laser based on nonlinear polarization rotation’, *Optical Engineering*, vol. 55, no. 10, pp. 1-7.
- [14] Tao, Z, Lou, Y, Zhao, D, Ma, W, Liu, R & Wang, T 2019, ‘Thulium doped fiber laser with a limited pulse width of 560 fs,’ presented at the 17th International Conference on Optical Communications and Networks, Zhuhai, 14th February 2019.
- [15] Liu, S, Yan, F, Li, Y, Zhang, L, Bai, Z, Zhou, H & Hou, Y 2016, ‘Noise-like pulse generation from a thulium-doped fiber laser using nonlinear polarization rotation with different net anomalous dispersion’, *Photonics Research*, vol. 4, no. 6, pp. 318-321.

Chapter 5

- [1] Li, P, Ruehl, A, Bransley, C & Hartl, I 2016, ‘Low noise, tunable Ho: fiber soliton oscillator for Ho:YLF amplifier seeding’, *Laser Physics Letters*, vol. 13, no. 6, pp. 1-5.
- [2] Kamynin, V, Filatova, S, Zhluktova, I & Tsvetkov, V 2016, ‘Picosecond holmium fibre laser pumped at 1125 nm’, *Quantum Electronics*, vol. 46, no. 12, pp. 1082 - 1084.
- [3] Tolstik, N, Sorokin, E, Bugar, I & Sorokina, T 2016, ‘Compact diode-pumped dispersion-managed SESAM-mode-locked Ho: fiber laser’, presented at conference on High-Brightness Sources and Light-Driven Interactions, California, 21st March 2016.
- [4] Tolstik, N, Sorokin, E, Bugar, I & Sorokina, T 2017, ‘Diode-pumped mode-locked holmium fiber laser at 2.138 μm ’, Munich, 27th March 2017.
- [5] Hemming, A, Simakov, N, Oermann, M, Carter, A & Haub, J 2016, ‘Record

efficiency of a holmium-doped silica fiber laser’, presented at the 2016 Conference on Lasers and Electro Optics, San Jose, 7th June 2016

[6] Luo, Z, Li, Y, Zhong, M & Huang, Y 2015, ‘Nonlinear optical absorption of few-layer molybdenum diselenide (MoSe₂) for passively mode-locked soliton fiber laser’, *Photonics Research*, vol. 3, no. 3, pp. 79-86.

[7] Ferrera, M *et al.* 2014, ‘CMOS compatible integrated all-optical radio frequency spectrum analyzer’, *Optics Express*, vol. 22, no. 18, pp. 21488 – 21498.

[8] General Photonics Corporation, 3-Channel Piezo Driver, Hikari Trading, viewed 12th October 2019, <http://www.hikari-trading.com/opt/gp/file/modules/0039_pcd.001.pdf>.

Chapter 6

[1] Budunođln, I, Ülgüdüür, C, Oktem, B & Ilday F 2009, ‘Intensity noise of mode-locked fiber lasers’, *Optics Letters*, vol. 34, no. 16, pp. 2516-2518.

[2] Budunođln, I, Ülgüdüür, C, Gürel, K, Şenel, Ç & Ilday F 2009, ‘Observation of noise outburst in mode-locked fibre lasers’, presented at Advances in Optical Science Congress, Honolulu, 15th July 2009.

[3] Corning 2014, ‘Corning SMF-28 ultra optical fiber’, Corning, viewed 23rd December 2019, < <https://www.corning.com/media/worldwide/coc/documents/Fiber/SMF-28%20Ultra.pdf>>

[4] Thorlabs 2016, ‘IO-K-1550 - fiber isolator’, Thorlabs GmbH, viewed 14th April 2020, < <https://www.thorlabs.com/thorproduct.cfm?partnumber=IO-K-1550>>

[5] AFW 2010, ‘In line polarizer - 1310nm/1550nm’, Australian Fibre Work PTY LTD, viewed 14th April 2020, <http://www.afwtechnologies.com.au/in_line_polarizer.html1310'1550nm>

[6] AFW 2011, ‘Polarization maintaining PM isolator - 1310nm or 1480nm or 1550nm’, Australian Fibre Work PTY LTD, viewed 14th April 2020, < http://www.afwtechnologies.com.au/pm_isolator.html1310-1480>

[7] Hönninger, C, Paschotta, R, Morier-Genound, F, Moser, M & Keller, U 1999, ‘Q-switching stability limits of continuous-wave passive mode locking’, *Journal of*

Optical Society of America B, vol. 16, no. 1, pp. 46-56.

[8] Paschotta, R 2008, Encyclopedia of laser physics and technology, Wiley, Germany.

[9] Grüner-Nielsen, L, Knudsen, S, Edvold, B, Veng, T, Magnussen, D, Larsen, C & Damsgaard, H 2000, 'Dispersion compensating fibres', Optical Fiber Technology, vol. 6, no. 2, pp. 164-180.

[10] Thorlabs Corporation 2017, Dispersion compensating fibre, Thorlabs GmbH, viewed 30th August 2019, <<https://www.thorlabs.com/catalogpages/obsolete/2017/DCF38.pdf>>

[11] Chen, L, Zhang, M & Zhang, Z 2010, Frontiers in guided wave optics and optoelectronics, Intech, Croatia.

[12] Kartner, F, Matuschek, N, Schibli, T & Keller, U 1997, 'Design and fabrication of double-chirped mirrors', vol. 22, no. 11, pp. 831-833.

[13] Gan, F 1995, 'Optical properties of fluoride glasses: a review', Non Crystal Solids, vol. 184, pp. 9-20.

[14] Wang, Y *et al.* 2019, 'Ultrafast Dy³⁺:fluoride fiber laser beyond 3 μm ', Optics Letters, vol. 44, no. 2, pp. 395-398.

[15] Kokhanovskiy, A, Ivanenko, A, Kobtsev, S, Smirnov, S & Turitsyn, S 2019, 'Machine learning methods for control of fibre lasers with double gain nonlinear loop mirror', Scientific Reports, vol. 9, no. 2916, pp. 1-7.

[16] McNeill, J 2012, 'VCO fundamentals,' presented at Worcester Polytechnic Institute, United States, 5th December 2012.